

Heat Transfer between the Superconducting Cables of the LHC Accelerator Magnets and the Superfluid Helium Bath

THÈSE N° 5411 (2012)

PRÉSENTÉE LE 29 AOÛT 2012

À LA FACULTÉ DES SCIENCES DE BASE

LABORATOIRE DE PHYSIQUE DES ACCÉLÉRATEURS DE PARTICULES

PROGRAMME DOCTORAL EN PHYSIQUE

ÉCOLE POLYTECHNIQUE FÉDÉRALE DE LAUSANNE

POUR L'OBTENTION DU GRADE DE DOCTEUR ÈS SCIENCES

PAR

Pier Paolo GRANIERI

acceptée sur proposition du jury:

Prof. M. Q. Tran, président du jury

Prof. L. Rivkin, directeur de thèse

Dr B. Baudouy, rapporteur

Dr S. Sanfilippo, rapporteur

Dr D. Tommasini, rapporteur



ÉCOLE POLYTECHNIQUE
FÉDÉRALE DE LAUSANNE

Suisse
2012

A Viola

Abstract

In this thesis work we investigate the heat transfer through the electrical insulation of superconducting cables cooled by superfluid helium. The cable insulation constitutes the most severe barrier for heat extraction from the superconducting magnets of the CERN Large Hadron Collider (LHC). We performed an experimental analysis, a theoretical modeling and a fundamental research to characterize the present LHC insulation and to develop new ideas of thermally enhanced insulations. The outcome of these studies allowed to determine the thermal stability of the magnets for the LHC and its future upgrades.

An innovative measurement technique was developed to experimentally analyze the heat transfer between the cables and the superfluid helium bath. It allowed to describe the LHC coil behavior using the real cable structure, an appropriate thermometry and controlling the applied pressure.

We developed a new thermally enhanced insulation scheme based on an increased porosity to superfluid helium. It aims at withstanding large heat loads, as needed for the High Luminosity LHC upgrade (HL-LHC). Experimental measurements of the new insulation showed a major improvement of heat extraction compared to the present *state-of-the-art* used in the LHC.

We developed a theoretical heat transfer model quantitatively explaining the experimental results of the LHC and HL-LHC insulations. We identified the heat extraction mechanisms, mainly occurring through superfluid helium micro-channels. The average micro-channels dimensions were estimated to vary between few and dozens of μm , depending on the insulation scheme. In the model we considered the known laws describing the dynamic regimes of superfluid helium. However such laws were never demonstrated to be valid in the narrow channels typical of the cable insulation.

We developed a new experimental device to investigate heat transport through micro-channels. Micro-fabrication techniques were used to etch the channels down to a depth of $16\text{ }\mu\text{m}$. We measured the classical laminar and turbulent regimes, thus demonstrating the validity of such heat transport laws independently from the channel geometrical shape and size down to these dimensions.

To conclude, we used the obtained experimental and theoretical heat transfer results to determine the LHC and HL-LHC magnets stability. We estimated their quench margin and compared it to the beam induced heat deposit. The resulting difference allows a safe operation of the magnets.

Keywords: accelerator superconducting magnets, cable insulation, heat transfer, High Luminosity LHC upgrade, LHC, narrow channels, quench margin, superfluid helium.

Résumé

Dans ce travail de thèse nous étudions les transferts de chaleur à travers l'isolation électrique de câbles supraconducteurs refroidis par de l'hélium superfluide. L'isolation du câble constitue la plus importante barrière pour l'extraction de chaleur dans les aimants supraconducteurs du Grand collisionneur de hadrons (LHC) du CERN. Nous avons réalisé une étude expérimentale, une modélisation théorique et une recherche fondamentale pour caractériser l'isolation actuelle du LHC ainsi que pour développer de nouvelles idées d'isolation plus performante du point de vue thermique. Le résultat de ces études a permis de déterminer la stabilité thermique des aimants pour le LHC et pour ses futures améliorations.

Une technique de mesure innovatrice a été développée pour analyser expérimentalement l'échange de chaleur entre les câbles et le bain d'hélium superfluide. Cela a permis de décrire le comportement de la bobine du LHC en utilisant la réelle structure du câble et une thermométrie appropriée, tout en contrôlant la pression appliquée.

Nous avons développé un nouveau système d'isolation amélioré du point de vue thermique, basé sur une plus grande porosité à l'hélium superfluide. Cela a pour but de résister à de grandes charges thermiques, comme pour le projet d'amélioration du LHC à Haute Luminosité (HL-LHC). Les mesures expérimentales ont montré une amélioration importante de l'échange de chaleur par rapport à l'isolation *de pointe* utilisée dans le LHC.

Nous avons développé un modèle théorique d'échange de chaleur qui explique quantitativement les résultats expérimentaux des isolations du LHC et HL-LHC. Nous avons identifié les mécanismes d'extraction de chaleur, qui ont principalement lieu à travers des micro-canaux d'hélium. Nous avons estimé que leurs dimensions moyennes varient entre quelques μm et des dizaines de μm , selon le système d'isolation. Dans le modèle nous avons considéré les lois classiques qui régissent l'écoulement dynamique de l'hélium superfluide. Cependant la validité de ces lois dans de tels micro-canaux n'a jamais été démontrée.

Nous avons développé un nouveau système expérimental pour étudier l'échange de chaleur à travers des micro-canaux. Des techniques de micro-fabrication ont été employées pour graver les canaux jusqu'à des profondeurs de $16\ \mu\text{m}$. Nous avons mesuré les écoulements classiques laminaires et turbulents, en démontrant ainsi la validité de ces lois de transport de chaleur indépendamment de la géométrie et de la taille du canal jusqu'à ces dimensions.

Pour conclure, nous avons utilisé les résultats d'échange de chaleur expérimentaux et théoriques obtenus pour déterminer la stabilité des aimants pour le LHC et le HL-LHC. Nous avons estimé leur marge de quench et nous l'avons comparé au dépôt de chaleur induit par le faisceau de particules. La différence résultante permet l'opération des aimants en toute sécurité par rapport aux pertes du faisceau.

Mots-clés : aimants supraconducteurs d'accélérateur, micro-canaux, hélium superfluide, isolations de câbles, LHC, LHC à Haute Luminosité, marge de quench, transferts de chaleur.

Acknowledgments

When I started my Ph.D. it was not clear where this work was going to lead me. Today, after few years, I can see that it has been a hilly way that filled me with contrasting feelings: from deep discouragement to extreme joy and enthusiasm. Luckily in this journey I was not alone . . .

I would like to express my sincere gratitude to Davide Tommasini for supervising my work at CERN. For sharing with me his experience and know-how, as well as providing me with his invaluable and continuous inspiration and enthusiasm. Our collaboration and his constant support helped to turn my Ph.D. in a real life experience.

I am also very grateful to Lenny Rivkin for having directed my thesis within the Particle Accelerator Physics Laboratory at EPFL. He gave me the opportunity to do a Ph.D. in a privileged environment and his trust and support helped me to grow as a scientist and a person.

I am very thankful to Bertrand Baudouy, not only for opening the doors of CEA to me, but mostly for his time, careful advice and never ending support.

I am indebted to David Richter for sharing with me his experience on the experimental measurements, as well as for all the stimulating discussions we had during these years.

In addition I wish to thank:

- Luca Bottura and Lucio Rossi for believing in me and for their constant support.
- Rob van Weelden and Johan Bremer for their understanding. I greatly appreciated their trust and support. They provided me with the best possible conditions to complete my work.
- Stéphane Sanfilippo for accepting to review my thesis, for the great interest he showed towards my work and for his valuable comments.
- Prof. Tran for having accepted and taken the time to be president of my Ph.D. jury.

Thanks to the several colleagues I had the chance to collaborate with:

- Aurélien Four and Fernando Lentijo for the collaboration during the tests that we carried out together and for the fun moments we shared.
- From the Magnets group: Paolo Fessia, Ezio Todesco, Clément Lorin, Bernardo Bordini and Francesco Bertinelli, as well as Sébastien Luzieux, Roberto Lopez, Federico Regis, Aziz Zaghloul, Angelo Bonasia, Pierre Jacquot, Sébastien Clement, Remy Gauthier and Ahmed Benfkhi.

- From the Cryolab: Hervé Allain, Gerhard Burghart, Jean-Luc Carpano, Daniel Cochet, Bram Colijn, Hendrie Derking, Laetitia Dufay-Chanat, Lina Hincapie, Thomas Eisel, Jean-Louis Servais, Sébastien Prunet, as well as Jeroen van Nugteren.
- From the Materials group: Alexandre Gerardin, Michael Guinchard and Maud Scheubel.
- From the Detectors group: Alessandro Mapelli and Paolo Petagna, as well as Miranda van Stenis, Thomas Schneider and André Braem.
- From EPFL: Boris Lunardi, Aurélie Pezous and Dominique Solignac.
- From the FLUKA team: Francesco Cerutti and Luigi Esposito.
- From the University of Bologna: Marco Breschi, Marco Casali and Marco Bianchi for the huge work we did together on the bus bars interconnections. Although not included in this thesis, it will be a remarkable memory of this period.
- From INFN Genoa: Riccardo Musenich.
- From CEA-Saclay: Chantal Meuris, François-Paul Juster for the pleasant and instructive discussions.

To conclude I wish to show my gratitude to my family and friends:

- To Viola for her endless support and inspiration. Without it I am not sure I would have been able to complete my work. Thanks for always listening to me and for incessantly encouraging me.
- To my parents, for their trust and support.
- To Gian Piero and Marielisa, who were always there for me.
- To my friends, in particular to Rocco, Michele, Vito, Diego, Alessio, Giovanni and all those who listened patiently to the endless talks about my thesis . . .

Contents

1	Introduction	1
2	LHC, superconducting magnets and superfluid helium	3
2.1	Introduction	3
2.2	The Large Hadron Collider	4
2.3	Superconducting magnets	6
2.3.1	Superconductivity	6
2.3.2	The LHC main magnets	7
2.4	Generalities on electrical insulation of superconducting cables	11
2.5	Superfluid helium	12
2.5.1	Physical properties	12
2.5.2	Thermodynamic equations	15
2.5.3	Heat transport in superfluid helium	21
2.5.4	Kapitza resistance	23
3	Experimental characterization of the LHC-type cable electrical insulation of superconducting magnets	25
3.1	Introduction	25
3.2	The LHC insulation	26
3.3	Development of the experimental program	27
3.3.1	Background notions	27
3.3.2	Sample preparation and instrumentation	28
3.3.3	Heating configurations	32
3.3.4	Assessment of the applied pressure	34
3.3.5	Cryogenic system	35
3.3.6	Measurements	35
3.4	Heat transfer results	38
3.4.1	Effect of mechanical pressure	40
3.4.2	Localized vs. distributed heat deposition	42
3.4.3	Thermal coupling between cables	43
3.4.4	Phenomenological analysis	44
3.5	Electrical measurements	46
3.6	Mechanical measurements	47
3.6.1	Insulation thickness	47
3.6.2	Elastic modulus	50
3.6.3	Stress relaxation	51

3.7	Conclusion	53
4	Development and characterization of a thermally enhanced insulation for the High Luminosity (HL) - LHC	55
4.1	Introduction	55
4.2	Background notions	56
4.3	The HL-LHC insulation	56
4.4	Experimental program	58
4.5	Heat transfer results	59
4.5.1	Effect of mechanical pressure	60
4.5.2	Localized vs. distributed heat deposition	63
4.5.3	Thermal coupling between cables	66
4.5.4	Improved HL-LHC insulation	66
4.5.5	Phenomenological analysis	67
4.6	Electrical measurements	68
4.7	Mechanical measurements	69
4.7.1	Insulation thickness	69
4.7.2	Elastic modulus	71
4.7.3	Stress relaxation	72
4.8	Conclusion	74
5	Modeling of He II heat transfer through Nb-Ti cable insulation	77
5.1	Introduction	77
5.2	Background notions	78
5.3	Model description	78
5.4	LHC insulation	81
5.4.1	Model implementation	81
5.4.2	Results	85
5.4.3	Images of the slits on the cable small and large face	88
5.5	HL-LHC insulation	90
5.5.1	Model implementation	90
5.5.2	Results	92
5.5.3	Images of the micro-channels	94
5.6	Conclusion	95
6	Experimental and theoretical characterization of He II heat transfer in narrow channels	97
6.1	Introduction	97
6.2	Background notions	98
6.3	Development of the experimental program	98
6.3.1	Micro-channels fabrication	98
6.3.2	Sample preparation and instrumentation	101
6.3.3	Measurements	104
6.4	Samples and characterization	105
6.5	Results and analysis	107
6.5.1	Landau regime	108
6.5.2	Gorter-Mellink regime	110

6.5.3	Critical heat flux (end of Landau regime)	114
6.6	Conclusion	116
7	Estimation of the LHC and HL-LHC magnets quench margin	117
7.1	Introduction	117
7.2	Background notions	118
7.3	Beam loss heat deposit	118
7.4	LHC magnets	121
7.5	HL-LHC magnets	125
7.6	Conclusion	126
8	Conclusion	129
	List of publications	133
	List of presentations	135
	List of contributions to other topics	137
	Bibliography	138

Chapter 1

Introduction

The main superconducting magnets of the CERN Large Hadron Collider (LHC) particle accelerator operate in a helium cryogenic environment at a temperature of 1.9 K. During operation, the magnets experience heat generation or deposition due for instance to the ramping of the magnetic field, to beam loss or to the debris of collisions in magnets close to the interaction regions. An efficient heat extraction is essential to maintain the superconducting state of the conductors. The cooling of the coil is mainly determined by the cable electrical insulation, which constitutes the most severe barrier for heat extraction.

In the LHC Nb-Ti cables, the peculiar thermal properties of the superfluid helium coolant allow to overcome the thermal resistance associated to the cable insulation, thanks to the micro-channels network created by the insulation wrappings. The LHC magnets operation requires a good understanding of the heat transfer inside the coils. The relevant mechanisms determine the magnet thermal stability, which is crucial for the accelerator operation.

The next generation of superconducting magnets will be confronted with larger heat loads, as in case of the High Luminosity LHC upgrade (HL-LHC). This requires the development of new ideas of cable insulation systems that allow a further cooling improvement with respect to *the state-of-the-art* used in the LHC.

The actual operation of the LHC and its future upgrades require therefore a thorough knowledge of the thermal behavior of superconducting coils, with a particular attention to the cables electrical insulation. In this thesis work we systematically investigate the relevant heat transport mechanisms by performing experimental analyses, a theoretical modeling, as well as a fundamental research. The outcome of these studies is finally used to determine the stability of the LHC and HL-LHC superconducting magnets.

In chapter 2 we provide an overview of the Large Hadron Collider. The use of large scale superconducting magnets made of Nb-Ti alloy and the technology of cooling with superfluid helium are justified with respect to the specific requirements of the LHC machine. We introduce the phenomenon of superconductivity and the design of LHC superconducting magnets is discussed in terms of the aim of this work. We discuss the quench issue, i. e. the superconducting-to-resistive transition. Finally, we summarize the heat transport through superfluid helium in terms of the hydrodynamics of the two-fluid model.

In chapter 3 we present the experimental method that was developed to study the heat transfer through the electrical insulation of superconducting cables towards the superfluid helium bath. We conceived a program of experimental tests that required the

development of an innovative device based on the combination of the real cable structure, an appropriate thermometry and control of the applied pressure and of the heating configuration. The results of the experimental study prove that these features are essential to correctly characterize the thermal behavior of the complex helium porous insulation schemes. We quantify the heat extraction from the LHC main dipole coil, and provide a phenomenological explanation. At the end of the chapter we describe the electrical and mechanical characterization of the LHC insulation, as well as the experimental device developed to investigate the stress relaxation mechanisms.

Chapter 4 is devoted to a new concept of cable electrical insulation, referred to as HL-LHC, that is proposed to go beyond the current limits of the Nb-Ti technology and withstand high heat deposition. It aims at better exploiting the cooling potential of He II, while preserving electrical protection. We report the results of heat transfer measurements in superfluid helium bath performed with the experimental program described in the previous chapter. We compare them to those obtained with the LHC insulation, and we highlight the underlying thermal mechanisms. The results of the electrical and mechanical tests are reported as well. They complete the qualification of the HL-LHC insulation and are needed for the mechanical and magnetic design of future magnets.

In chapter 5 we present a theoretical heat transfer model to understand the thermal mechanisms occurring in the cable insulations. The model is focused on the superfluid helium region. The actual topology of the LHC and HL-LHC insulations are taken into account, and coupled He II and solid conduction heat transport mechanisms are implemented. It aims at explaining the experimental results reported in chapters 3 and 4, to determine the heat fluxes distribution and the unknown micro-channels dimensions. As for the latter item, the obtained results are compared to microscope imaging of the insulation tapes deformed under pressure. The model assumes that the mechanisms of heat transport follow the known laws of the superfluid dynamic regimes. However the validity of such laws was only demonstrated down to channels of $56\text{ }\mu\text{m}$ diameter, but not yet in channels as narrow as those created by the overlapping of the insulation tapes.

The open question of the previous chapter was the motivation for conceiving, developing and carrying out a new activity, both experimental and theoretical, to investigate the heat transport through micro-channels in the LHC cooling conditions. In chapter 6 we present this experimental program, that required the development of challenging samples and the exploitation of micro-fabrication techniques to etch channels down to a depth of $\sim 16\text{ }\mu\text{m}$. We report the results of heat transfer measurements. We propose an analysis based on the classical laminar and turbulent laws and on the critical heat flux separating these two dynamic regimes of superfluid helium.

In chapter 7 we use the results of the previous chapters to evaluate the stability of the LHC present and future Nb-Ti magnets, in terms of quench margin. Such results constitute the most advanced investigations performed so far on this topic, both from the experimental (chapters 3 and 4) and modeling (chapter 5) standpoint. The issue of the beam-induced quenches will become critical when the LHC will run at nominal beam energy, as well as after the luminosity upgrade. We estimate the quench margin of the LHC and HL-LHC magnets, and compare it to the beam induced heat deposition evaluated through particle shower simulations.

Chapter 8 contains conclusions and future perspectives of the work.

Chapter 2

LHC, superconducting magnets and superfluid helium

Contents

2.1	Introduction	3
2.2	The Large Hadron Collider	4
2.3	Superconducting magnets	6
2.3.1	Superconductivity	6
2.3.2	The LHC main magnets	7
2.4	Generalities on electrical insulation of superconducting cables	11
2.5	Superfluid helium	12
2.5.1	Physical properties	12
2.5.2	Thermodynamic equations	15
2.5.3	Heat transport in superfluid helium	21
2.5.4	Kapitza resistance	23

2.1 Introduction

In this chapter we provide an overview of the Large Hadron Collider project. The use of large scale superconducting magnets made of Nb-Ti alloy and the technology of cooling with superfluid helium are justified with respect to the specific requirement of the LHC machine. Its main parameters and layout are summarized.

The phenomenon of superconductivity is introduced, and the design of LHC superconducting magnets is discussed in terms of the aim of this work. The issue of irreversible resistive transitions (quench) is briefly discussed.

In the last part of the chapter, the heat transfer through superfluid helium is summarized in terms of the hydrodynamics of the two-fluid model. The heat transport regimes are described, depending on the development of vorticity in the superfluid component and of a classical turbulence in the normal component.

2.2 The Large Hadron Collider

The aim of the European Organization for Nuclear Research (CERN) is the physics fundamental research to improve our fundamental understanding of matter [1]. CERN's flagship project, the Large Hadron Collider (LHC) [2] is a circular particle accelerator designed to push the energy frontier in particle physics [3]. The goal of the LHC is to analyze the interaction of hadron constituents at energies that have never been reached before in particle accelerators [4], in order to provide experimental evidences for the Higgs boson, super-symmetric particles, CP violation, B-physics, etc. The LHC has a circumference of 26.7 Km and is installed in the underground tunnel that previously housed the Large Electron-Positron Collider (LEP), in the Franco-Swiss border on the outskirts of Geneva. An aerial view of CERN and the surrounding region is shown in Fig. 2.1.



Figure 2.1: Aerial view of CERN and surrounding region. Three rings are drawn to show the position of the accelerator complex situated underground. The small ring shows the position of the Proton Synchrotron with a circumference of 600 m, the middle ring is the Super Proton Synchrotron with a circumference of 7 Km and the largest ring is the LHC. The Geneva lake and airport can be seen on the right and the Jura mountains on the left.

Bunches of about 10^{11} particles are prepared by the various pre-accelerators (the injector chain): the LINear ACcelerator (LINAC), the Proton Synchrotron Booster (PSB), the Proton Synchrotron (PS) and the Super Proton Synchrotron (SPS). The beam is injected into the LHC at the insertion points at the energy of 450 GeV, accelerated to nominal energy and circulated (stored) for as long as possible thus making it available for physics experiments. Two counter-rotating proton beams traveling in a vacuum chamber collide at a nominal center-of-mass energy of 14 TeV. The achieved nominal luminosity, which is a measure of the potential number of particle interactions for a colliding beam, is $10^{34} \text{ cm}^{-2}\text{s}^{-1}$. The collider also allows experiments with lead nuclei reaching a collision energy of 1150 TeV and a luminosity of $10^{27} \text{ cm}^{-2}\text{s}^{-1}$.

The basic layout of the LHC is depicted in Figure 2.2. It has eight arcs and eight straight sections. Each straight section can serve as an experimental or utility insertion. The four massive particle detectors observing the phenomena induced by the hadron collisions are: ATLAS (point 1), CMS (point 5), ALICE (point 2) and LHC-b (point 8).

Point 2 and 8 also contain the injection systems for Beam 1 and Beam 2, respectively. The beams only cross from one magnet bore to the other in the four experimental (or interaction) regions. The remaining four straight sections do not have beam crossings. Insertion 3 and 7 contain two collimation systems each. Insertion 4 contains two Radio Frequency systems to independently accelerate the two beams. The straight section at point 6 contains the beam dump insertion where the two beams are vertically extracted from the machine.

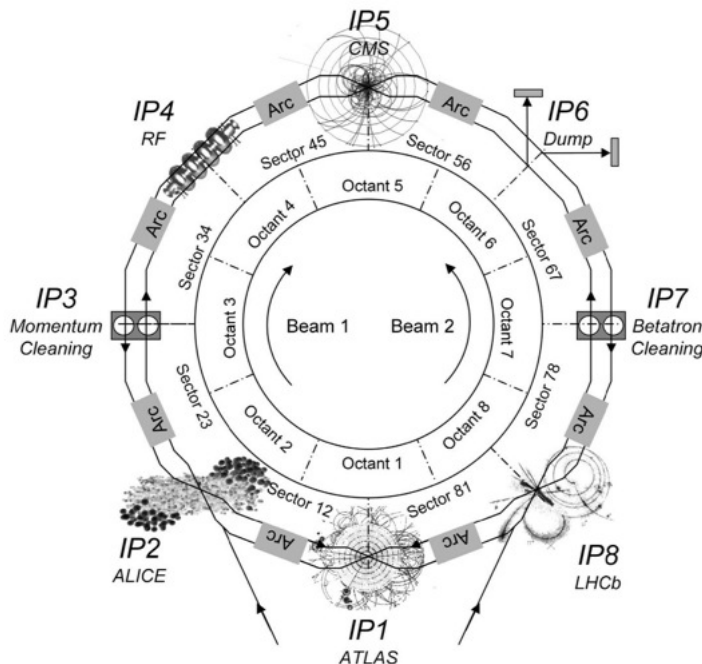


Figure 2.2: Schematic layout of the LHC.

Three fundamental elements are necessary in an accelerator to modify the particle trajectory and velocity, using electric and magnetic fields:

- Radio Frequency (RF) cavities increase the particle energy at every turn, based on an alternating electrical potential which acts on the particles as an accelerating field;
- dipole field magnets in the arcs bend the beam, thus guiding it on the reference “circular” trajectory;
- quadrupole magnets focus or defocus the particles onto the reference orbit, preventing them from diverging from the center of the beam pipe.

The bending dipole field intensity is imposed by the curvature of the orbit and by the particles energy. The equilibrium condition of the Lorentz and the centrifugal forces of the particle beam requires a magnetic field that changes with and respect to the particle energy and velocity for a designed circular orbit. Therefore the RF cavities and the superconducting magnets work in synchronization to ensure that the beam orbit remains the same throughout the beam injection, acceleration and storage. Accelerators functioning in this way are classified as synchrotrons. For the LHC the protons beam energy of 7 TeV on a circular trajectory with a curvature radius of 2803 m requires a nominal bending dipole field of 8.33 T. As for the LHC quadrupoles magnets, they are designed for a gradient of 223 T/m and a peak field of about 7 T.

At the moment of writing the thesis, the LHC operation is limited by the defective splices of the magnet interconnections [5]. After two years of exploitation at about half its design value, the operation beam energy was increased to 4 TeV. While the full energy will be attained after the splices consolidation in 2014, CERN is preparing a plan to upgrade the LHC complex, in order to fully exploit its capabilities and provide with the opportunity to discover new physics [6]. A Luminosity upgrade (High Luminosity LHC) is foreseen around 2020, and a pre-study started to explore the possibility of an Energy upgrade (High Energy LHC) around 2030. Both upgrades strongly rely on advanced accelerator magnet technology, requiring dipoles and quadrupoles of accelerator quality and operating fields in the 11-13 T range for the luminosity upgrade [7] and 16-20 T range for the energy upgrade [8].

2.3 Superconducting magnets

A high current density is needed to generate the required 8.33 T dipole magnetic field, and for this reason a superconducting magnet system was designed. The use of superconducting wires is the only solution to achieve the required field strength without losses, and keep the total cost reasonably low.

2.3.1 Superconductivity

Superconductivity is a remarkable phenomenon whereby certain metals, when cooled down to very low temperatures, become excellent conductors of electricity. It was discovered in 1911 by the dutch physicist H. Kamerlingh Onnes, only three years after he had succeeded in liquefying helium. Unlike the gradual change of the electrical resistance with temperature in common metals, the superconducting state appears quite abruptly at the critical temperature T_c which is a characteristic parameter of the specific metal. Below this temperature the resistance is not just very small; as far as it can be seen from the results of some very sensitive experiments, it is absolutely equal to zero. In addition to the critical temperature, superconductors also have a critical magnetic field, above which they revert from the superconducting state to the normal resistive state. To fully describe the electromagnetic behavior of this matter, it is necessary to introduce also a critical current density J_c to those of T_c and B_c . All these properties are related to each other by the critical surface in (T,B,J) space, which is characteristic of the material in question. Fig. 2.3 shows the critical surface of Nb-Ti and Nb₃Sn. Superconductivity prevails everywhere below this surface with normal resistivity everywhere above it. Among the large variety of metals and alloys that become superconductive at liquid helium temperature, Nb-Ti and Nb₃Sn are basically the only two materials that are commercially available for large scale magnet production [9].

Despite the fact that its upper critical field is only 10 T at 4.2 K, the large use of Nb-Ti is mainly due to its extreme ductility which permits effective and simple fabrication methods for wires and cables. For this reason it is widely used in magnets of moderate field strength (up to 6.5 T at 4.2 K). Cooling with superfluid helium at 2 K increases the field level to about 9 T, as needed in the LHC.

For higher fields Nb₃Sn or (Nb,Ta)₃Sn with upper critical fields of about 20 T at 4.2 K are used. Nb₃Sn is considered as an option for the LHC upgrades, although some

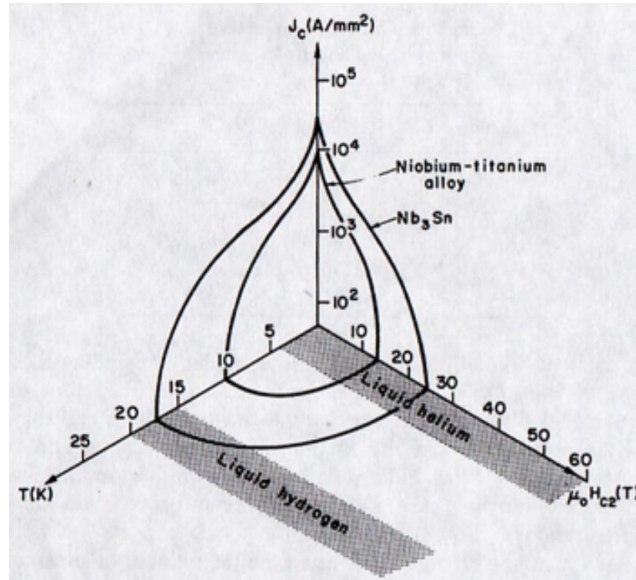


Figure 2.3: Critical surface of Nb-Ti and Nb₃Sn in (T,B,J) space (from [10]).

considerations need to be done. Because of its brittleness it cannot be drawn to thin filaments like Nb-Ti, but must be formed in the final geometry by high-temperature heat treatment. However, fully reacted multifilamentary Nb₃Sn strands are sensitive to mechanical stress, showing a reduction of their current-carrying capacity. Therefore accelerator magnets cannot be wound from the fully reacted cable, because a strong degradation would happen in the coil head region. The heat treatment must be performed after coil winding. Moreover, bare wires and cables with open voids are strongly affected by the transverse stress in the pre-compressed coil. A large improvement is gained when the voids in the cable are filled with epoxy or solder because then the applied pressure is evenly distributed and local stress enhancements are avoided. The drawback is the strong reduction of the heat extraction from the coil.

2.3.2 The LHC main magnets

There are three large operating accelerators built with superconducting magnets [2]: the Tevatron (Fermilab in Chicago, USA), HERA (Desy in Hamburg, Germany) and RHIC (BNL in New York, USA). All make use of classical Nb-Ti superconductors cooled with normal liquid helium at a temperature slightly above 4.2 K, and their operational fields are relatively low (4 T for the Tevatron, 4.7 T for HERA and 3.45 T for RHIC). The only way for obtaining fields of and above 8 T in accelerator magnets using Nb-Ti with sufficient margin is to cool the superconductors to temperature below 2 K. This technique was successfully applied at the French Tokamak Tore Supra magnet, in operation at Cadarache. Below 2.17 K, helium is in the so-called superfluid state, with much lower viscosity and much higher heat transfer capacity than that of liquid helium above 2.17 K. These properties determine the design of the cooling system and permit a drastic reduction of the helium flow through the magnets. On the other hand, between 4.2 K and 1.9 K the enthalpy of metals and in particular of the superconducting cables is reduced by almost an order of magnitude. As a consequence higher temperature appear for a given

deposit of energy. Such feature calls for particular care in limiting the heat loads like for instance those originating in conductor motions, which have their origin in the large electromagnetic forces exerted on the coil windings by the magnetic field. This calls for strong force-retaining structures.



Figure 2.4: The LHC tunnel.

Fig. 2.4 shows a picture of the 15 m long main dipoles installed in the LHC tunnel, whereas Fig. 2.5 shows the relevant cross-section. They feature a compact and cost-saving two-in-one design, where two beam channels with separate coil systems are incorporated within the same magnet. The coils are supported by laminated collars and by the iron yoke, which also increases the field by about 19% and shields it so that no magnetic field leaves the magnet. Located in grooves in the iron yoke, bus bars accommodate the cables to power the magnets of the arcs which are connected in series. The so-called *cold-mass* is the space delimited by the inner wall of the beam pipes on the beam side and by a cylinder on the outside. It is immersed in a bath of superfluid liquid helium that acts as a heat sink.

The helium in the *cold-mass* is slightly above the atmospheric pressure. Such cooling conditions brings several important technical advantages with respect to saturated He II [11]. The helium in the *cold-mass* is cooled down to 1.9 K by means of a heat exchanger tube, located in the upper part of the magnet cross-section, where two-phase saturated helium flows. Heat management is a fundamental aspect of superconducting magnet design in the presence of substantial heat loads. The coil temperature shall be kept below the transition value determined by operating field and current density, corresponding to transition of the superconductor to the resistive state (quench). Heat loads of accelerator superconducting magnets vary considerably depending on magnet type and function. Heat in the coil can be for instance deposited by beam particles, or generated inside the magnet as AC losses. The main barrier to heat extraction from the coil is represented by electric insulation wrapped around superconducting cables [12] [13]. The collars consist indeed of laminations that provide a very good thermal link to the cold source. The heat path from the cables towards the heat exchanger tube is schematically shown in Fig. 2.6 (left).

; Each coil consists of an upper and a lower pole made of superconducting cables packed

2.3. Superconducting magnets

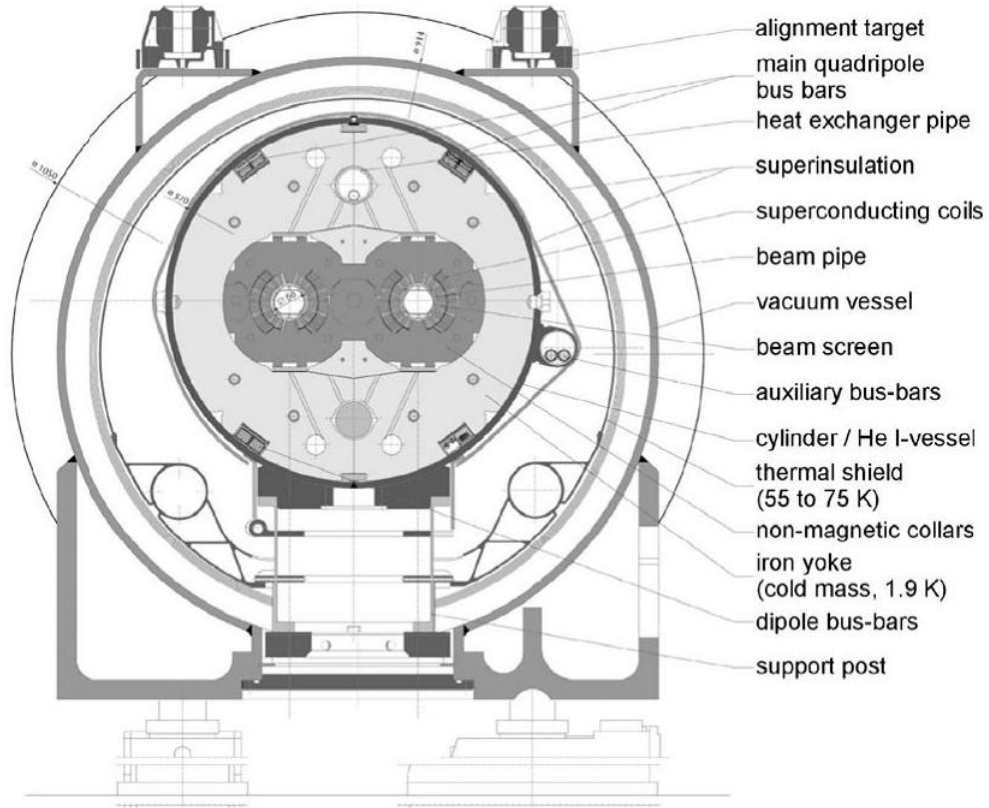


Figure 2.5: Cross-section of the LHC main dipole.

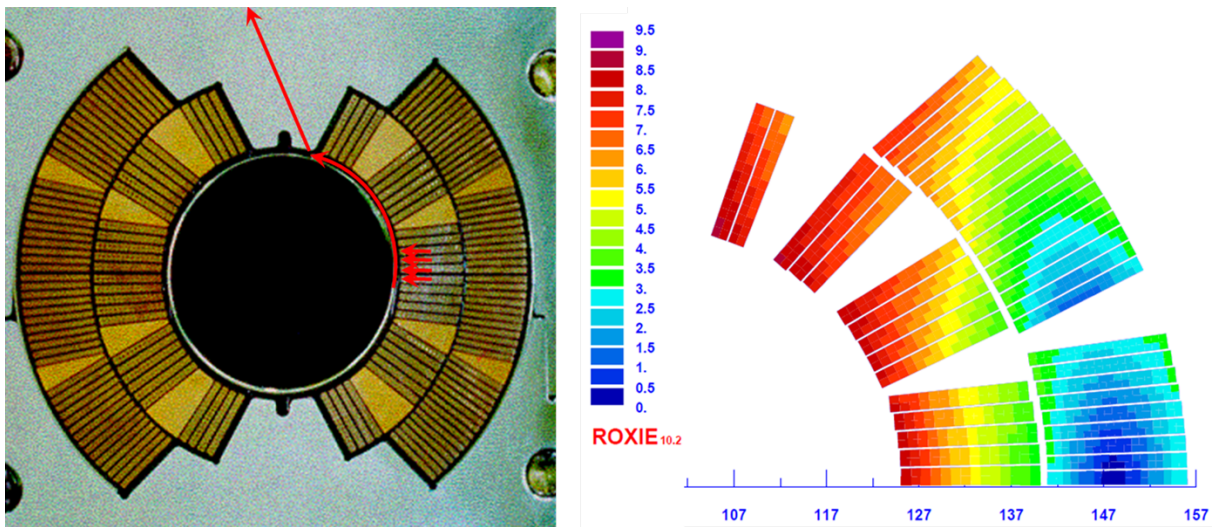


Figure 2.6: Left: sketch of the heat path from the cables towards the heat exchanger tube (red arrows). Right: six-block design of a quarter cross-section of the LHC main dipoles. The magnetic field map is reported as well [14].

into a six-block design: four in the inner layer and two in the outer layer, with graded current density. In Fig. 2.6 (right) a zoom of a quarter cross-section of a dipole coil is shown, as well as the relative magnetic field map for the nominal operating current of 11.85 kA. The coils approximate the ideal current distribution generating a “pure” dipolar

field in the beam pipe. Copper wedges are added (in the blank spaces between the blocks of conductors) to give to the coil a circular-like shape and to fine-tune the field quality in the apertures.

The superconducting cables are made of several strands (28 for the inner layer, 36 for outer layer), that are twisted to minimize the strength of eddy currents due to a changing magnetic field. The strands are compressed into a flat two layers structure with a (keystoned) trapezoidal shape, the so-called Rutherford cable (Fig. 2.7 (a) and (b)). The geometrical parameters of the mentioned cables will be reported in section 3.3.2 (Table 3.2). The strands are made of multi-filaments, as shown in Fig. 2.7 (c). The filaments are twisted to ensure equal current distribution and to reduce the strength of eddy currents, which can have an impact on the achievable field quality and on the quench process. The filament diameter must be in the range of some μm to avoid flux jumping. A large number of filaments are embedded in a copper matrix, as shown in Fig. 2.7 (c), that provide mechanical stability and at the same time serve as an electrical bypass of high conductivity and as a heat sink in case of quench.

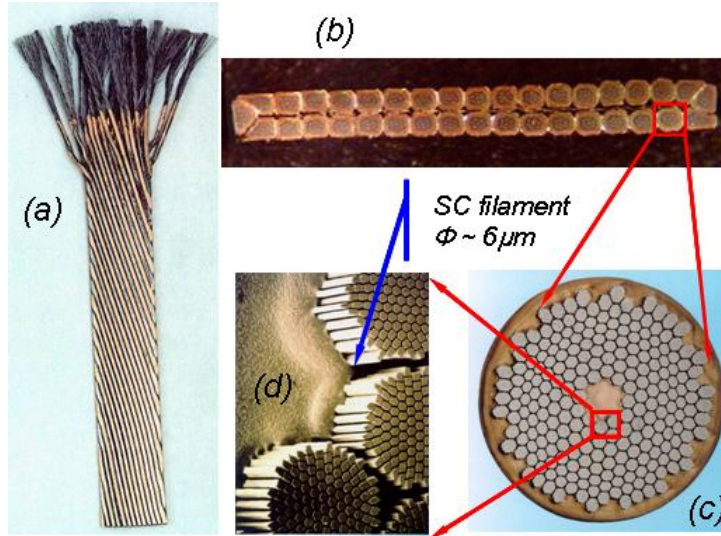


Figure 2.7: Top view (a) and cross-section (b) of a superconducting Rutherford cable. Cross-section of an individual strand of the cable, showing the Nb-Ti filaments embedded in the copper matrix (c). Close-up of the Nb-Ti filaments (d).

The magnets close to the interaction regions constitute the inner triplet, i.e. a string of three superconducting quadrupoles (Q1 - Q3) installed on both sides of every interaction point, aimed at the final squeeze of the beams before collision (Fig. 2.8). The LHC inner triplets are made of the MQXA [15] and MQXB [16] quadrupoles that were built by the US-Japan collaboration. The High Luminosity LHC (HL-LHC) upgrade project [17] will require the replacement of the existing inner triplets in the CMS and ATLAS experimental areas with more powerful ones. The new quadrupole magnets will be exposed to increased heat deposition [18], calling therefore for a stronger resistance to heat loads.

Two options exist for the new magnets, either the promising Nb_3Sn or the well-established Nb-Ti technology. Nb_3Sn has a fairly high critical temperature ($\sim 19\text{ K}$), hence a high temperature margin. This allows a good heat transfer rate despite the helium-tight typical insulation, which consists of a resin impregnation protecting the brittle

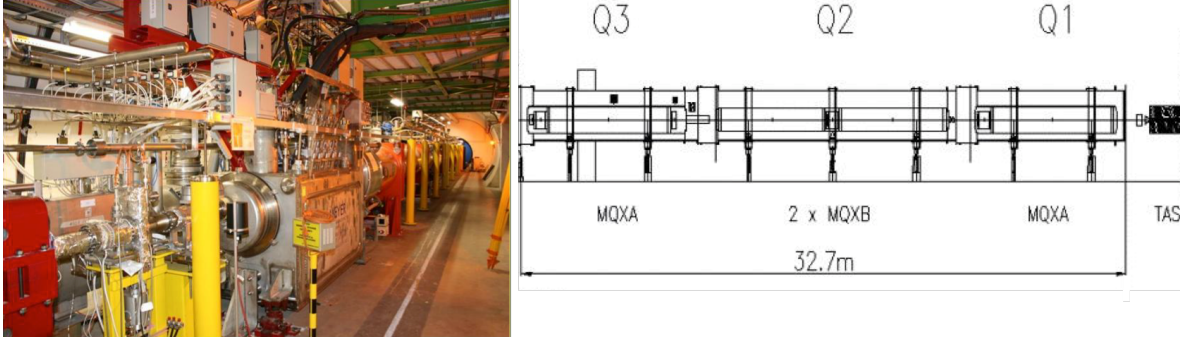


Figure 2.8: Picture and layout of the present LHC inner triplet. The interaction point is located on the right of both images, after the Target Absorber Secondaries (TAS).

superconducting cables but preventing a direct contact between cable and helium bath [19]. On the other hand Nb-Ti has a lower critical temperature (~ 9 K). The corresponding lower temperature margin limits the heat extraction capacity. However, the advantage of Nb₃Sn in terms of heat extraction can be considerably reduced if the heat transfer capability of Nb-Ti coils is improved by acting on the cable electrical insulation [20].

A large aperture Nb-Ti magnet was initially foreseen for the Phase I of the LHC luminosity upgrade [21] [22]. In view of the consolidation of the main bus bars interconnections following the 2008 incident [5], the LHC operational schedule was revised and the luminosity upgrade project was re-scoped in 2010. The baseline is now to concentrate on one single upgrade at a later stage around 2020, rather than on two phases, which will allow studying the potential of the Nb₃Sn superconductor technology. A choice will be made in the next years between the Nb-Ti and the Nb₃Sn options [23]. In this thesis we focus on the heat extraction issues related to the Nb-Ti option.

2.4 Generalities on electrical insulation of superconducting cables

The design of the electrical insulation of Nb-Ti superconducting magnets depends on several competing factors [20]. In addition to fulfilling dielectric requirements, the insulation must:

- possess mechanical strength to withstand the strong compression of the coil;
- preserve ductility at cryogenic temperature;
- provide cohesion between coils turns to allow coil handling during magnet assembly;
- be radiation resistant;
- be able to accommodate thickness variation of the various coil components to facilitate a constant coil size;
- present a moderate thermal shrinkage;
- feature an adequate heat conductivity.

All of the above tasks have to be accomplished with a minimum thickness (in the order of 0.1 - 0.2 mm) to maximize the bare / insulated conductor aspect ratio.

State-of-the-art Nb-Ti insulation, developed for the LHC magnets [2], is the result of a continuous evolution started in the early 1970s for the ISR [24], passing through SSC [25],

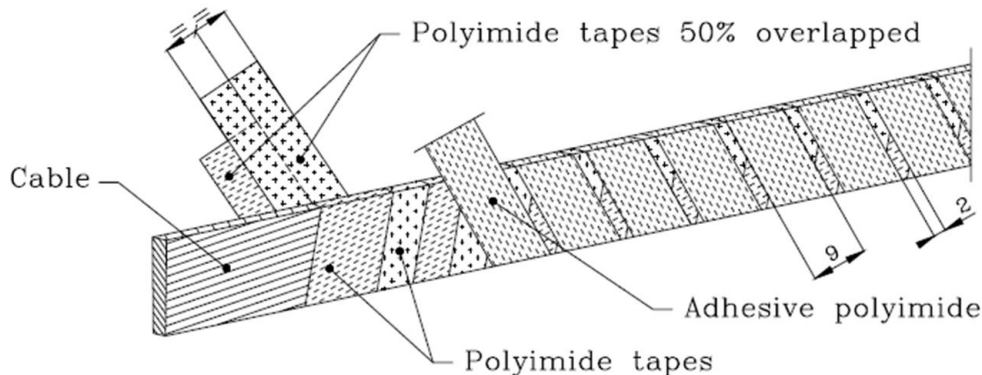


Figure 2.9: Rutherford cable wrapped with the LHC insulation (from [2].)

HERA [26] and RHIC [27]. This two layers solution is shown in Fig. 2.9. It consists of polyimide tapes arranged in layers helically wound around the cable. The first, inner, layer has the function to dielectrically insulate adjacent turns. The interturn voltage that arises in the case of a quench is around 100 V and the current can make its way across the insulation in correspondence of material defects (punch through), or along the insulation surface. To reduce the punch-through risk and to provide a sufficiently long surface path, the first layer is composed by two 50% overlapped tapes. The second, outer, layer is intended to protect the first layer during coil winding, magnet assembly and operation. It must also provide cohesion between coil turns and must create gaps for helium to reach the inner layer [28]. The second layer consists therefore of a single and thicker polyimide tape with, on the outer face, a thin coat of polyimide adhesive activated by heat treatment. The adhesive coating was specifically developed to avoid flowing [29] [30], necessary condition for the permeability of the analyzed insulations. The second layer is wound, with spacing, in the opposite direction with respect to the inner one.

2.5 Superfluid helium

2.5.1 Physical properties

Of all the cryogenic fluids, helium exhibits a behavior that most nearly approximates that of an ideal fluid. This is caused mostly by the weak intermolecular potential that helium enjoys. It further manifests itself in the fact that helium has the lowest critical point of all fluids ($T_{crit} = 5.2$ K, $p_{crit} = 2.26$ bar). As a result of this near ideality, much of the behavior of the gaseous and liquid helium above the superfluid transition can be treated in terms of classical models. On the contrary, certain characteristics of helium, in particular those of the liquid state below the superfluid transition and also the solid state, have properties which are determined by quantum mechanics [10]. In this section we briefly summarize some of its exceptional physical properties [31], which are very different from other cryogenic or non-cryogenic fluids.

Liquid helium features a small density compared to liquid nitrogen and liquid water, but higher in vapor phase at atmospheric pressure because it is closer to the critical point. Its viscosity is several orders of magnitude smaller than nitrogen and water. Latent vaporization heat of helium is ten times lower than nitrogen and a hundred times lower

than water, although the specific heat of liquid at atmospheric pressure is of the same order of magnitude.

Fig. 2.10 shows the helium phase diagram where, in addition to the conventional characteristics such as the critical point and two-phase coexistence, several unique features can be observed:

- unlike all other substances, the solid state is not obtainable in helium at any temperature unless an external pressure in excess of 2.5 MPa (25 bars) is applied;
- liquid helium is also exceptional in that it can exist in either of two very different states. He I is the normal liquid with characteristics that are typical of classic fluids. In these region, helium acts as a weakly interacting gas, which is at least in part due to its weak molecular interaction and low viscosity. The viscosity of He I is comparable to that of air at room temperature;
- the superfluid state (He II) has physical features that are truly exceptional. Most notable of these features are the transport properties, with a vanishingly small viscosity and an apparent thermal conductivity many orders of magnitude larger than liquids or even high-conductivity solids. This is the reason why no temperature gradients form in He II. The line that separates the two liquid states is called the λ -line, because the specific heat near the transition has the shape of the Greek letter λ (see Fig. 2.11 (right)). The λ -transition represents a second-order phase transition, which means it has a discontinuous slope in the temperature dependence of the entropy. There is no latent heat of formation of the He II state and the coexistence of He II and He I in equilibrium conditions is not possible. The λ -transition is 2.172 K at saturated vapor pressure and decreases gradually with increasing pressure, until it intersects the solid coexistence boundary;
- finally, the helium diagram is also unique because of the lack of a triple point of coexistence between liquid, vapour and solid, because the solid state can exist only under an external pressure.

A detailed description of the helium properties can be found in [10].

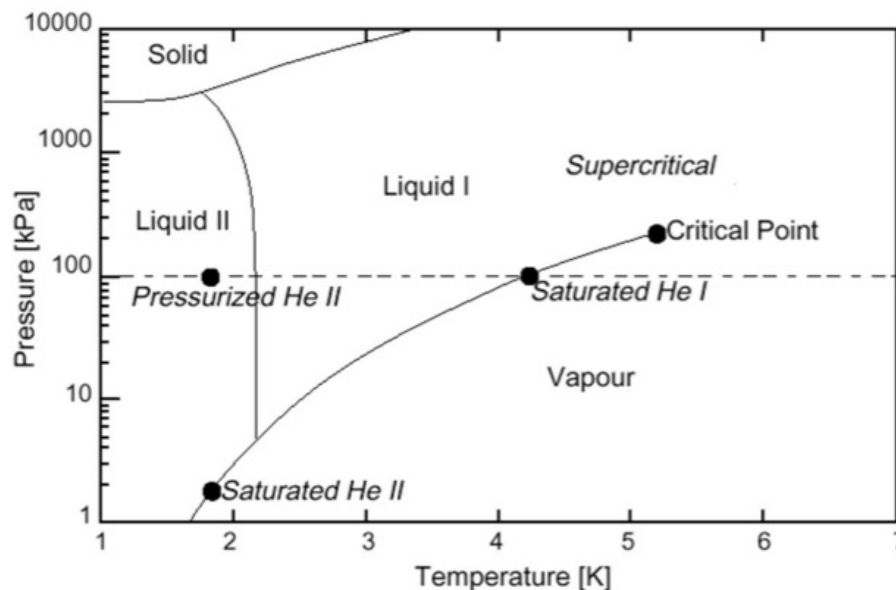


Figure 2.10: Phase diagram of helium (^4He).

The helium properties presented in Figs. 2.11 and 2.12 as a function of temperature at atmospheric pressure come from the HEPAK data base (Helium PAcKage) [32].

For normal helium ($T > T_\lambda$), the density decreases while increasing the temperature, which is the case for classical fluids. Nevertheless, for superfluid helium ($T < T_\lambda$) the density increases until reaching a maximum at T_λ (Fig. 2.11 (left)).

The He I specific heat c_p presented in Fig. 2.11 (right) varies between 2300 J/kg.K around T_λ and 5200 J/kg.K at $T = 4.2$ K. For a perfect gas c_p is equal to $(5/2) \cdot R$, where R is the perfect gas constant equal to 8.31 J/mol.K. Applying this to helium which has a molar mass of 4 g/mol, we obtain a c_p of 5190 J/kg.K which is a value near the He I c_p at 4.2 K. This is due to the fact that He I behaves like a perfect gas. In case of He II the temperature dependence is cubic below 0.6 K, whereas between 0.6 K and 1 K it follows a $T^{6.7}$ law. Between 1 K and T_λ , c_p follows a $T^{5.6}$ law. As already stated, the λ transition is a second-order transition without latent heat of formation between He I and He II.

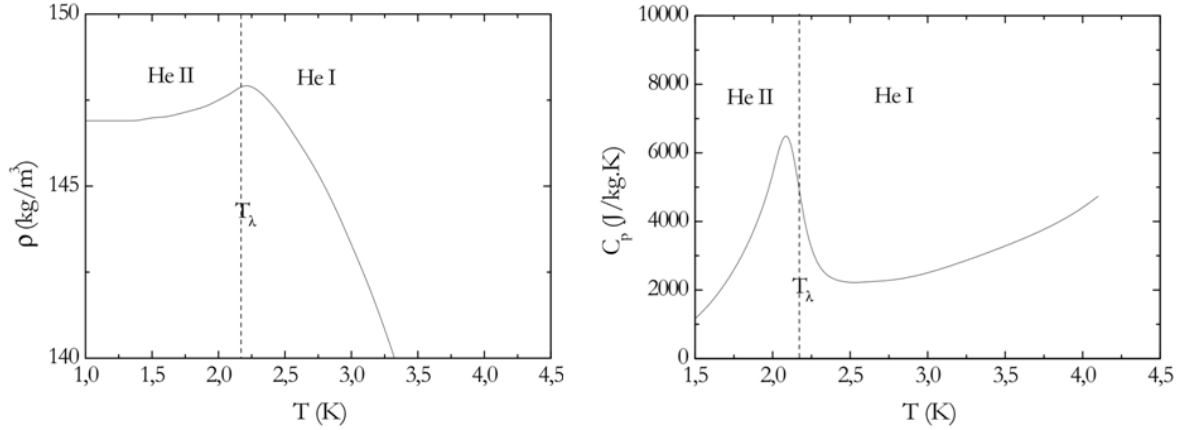


Figure 2.11: Evolution of density (left) and specific heat (right) as a function of temperature at 0.1 MPa.

The entropy function s shown in 2.12 (left) follows a cubic law until T_λ and a linear law above. It features the same temperature dependence as the specific heat, since s is linked to c_p through the integral $s = \int (c_p/T) dT$. The second-order transition can be observed at T_λ , where the entropy curve has a change in slope.

The dynamic viscosity in case of He I is of the same order of magnitude as the vapour phase of a classical fluid ($3 \cdot 10^{-6}$ Pa.s). In case of He II the viscosity can be measured by two methods. The first one uses a viscometer by pressure drop in the laminar regime through a micro-tube ($d \approx 1 \mu\text{m}$). The second method is based on the principle of amortization of oscillations of a disk in rotation. For a classical fluid the results are the same with both methods, whereas for He II different results are obtained.

The method of the laminar flow gives a zero viscosity whereas the method using the oscillator disk gives a viscosity of the order of 10^{-6} Pa.s. Fig. 2.12 (right) shows the evolution of the latter. This experimental difference is at the origin of the two fluids model. In such model He II is supposed to be composed of a normal component, which features the viscosity measured by the oscillator disk experiment, and of a superfluid component with a zero viscosity.

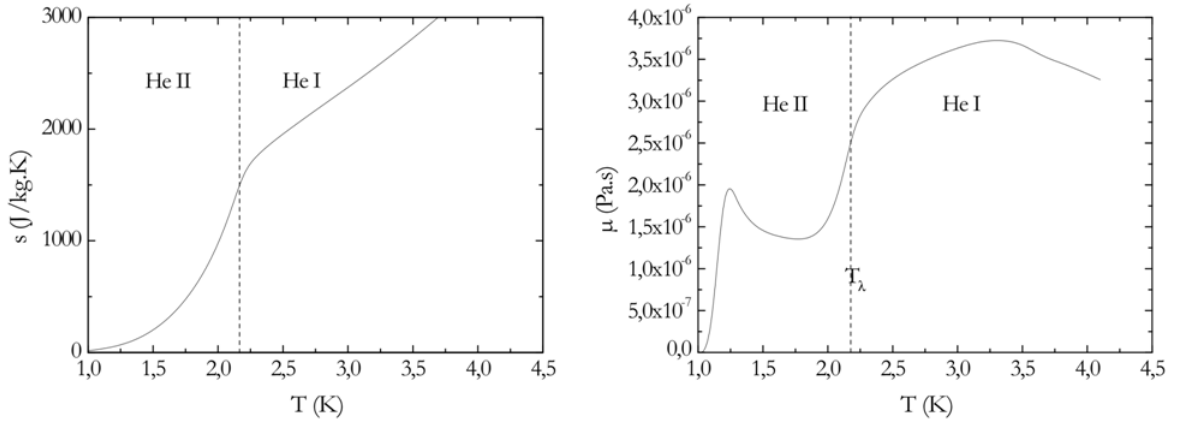


Figure 2.12: Evolution of entropy (left) and dynamic viscosity (right) as a function of temperature at 0.1 MPa.

2.5.2 Thermodynamic equations

Two fluid model equation

From the Landau theory, helium below T_λ is a mixture of a normal component (the normal fluid with density ρ_n and velocity field \mathbf{v}_n) and a superfluid component (the superfluid with density ρ_s and velocity field \mathbf{v}_s). The total density is denoted ρ and is the sum of the density of the two components :

$$\rho = \rho_n + \rho_s. \quad (2.1)$$

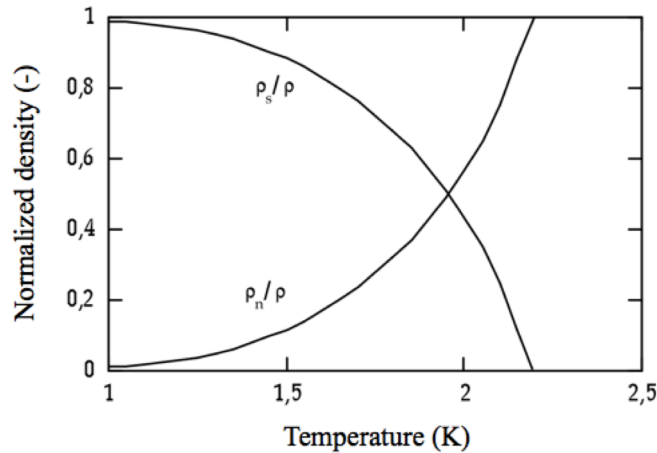


Figure 2.13: Evolution of the relative densities ρ_s/ρ and ρ_n/ρ as a function of temperature.

For a given temperature the ratio between normal fluid density and total density is unique, as shown in Fig. 2.13. This ratio strongly depends on temperature and for $T < T_\lambda$ we can write:

$$\rho_n/\rho = (T/T_\lambda)^{5.6}. \quad (2.2)$$

This graph shows explicitly that the superfluid component disappear for temperature above T_λ . To describe the thermodynamic state of He II, it is necessary to have more independent variables. A classical fluid has 5 independent variables but superfluid helium needs 8 independent variables: 2 thermodynamic variables and 2 velocity fields. Landau postulated that the velocity of the superfluid component \mathbf{v}_s is a new variable for the whole fluid, independent from the center of mass velocity and it is irrotational. This means that the superfluid velocity follows the following condition:

$$\nabla \times \mathbf{v}_s = \mathbf{0}, \quad (2.3)$$

hence the velocity field of the superfluid component derives from a potential Φ :

$$\mathbf{v}_s \propto \nabla \Phi. \quad (2.4)$$

For a temperature below T_λ the liquid is more ordered due to the fact that a big number of atoms have the same fundamental energy level. From a quantum mechanics point of view, the λ transition can be considered like a transition order-disorder and we can associate a wave function Ψ which plays the role of an order-parameter. This order parameter is a complex number. It gives the fundamental energy state. Its module corresponds to the number of atoms at the fundamental energy state. It describes in fact the superfluid density:

$$|\psi|^2 = \rho_s e^{2i\Phi}. \quad (2.5)$$

In agreement with Landau's assumption, this formalism due to Onsager [33] and Feynman [34] showed that the superfluid velocity field relates to the phase of the order-parameter Φ and comes from a potential, defined by:

$$\mathbf{v}_s = \frac{\hbar}{m} \nabla \Phi = \frac{h}{2\pi m} \nabla \Phi, \quad (2.6)$$

where h is Plank constant and m is helium atom mass. Following this model, the entropy is only transported by the normal fluid. We can then relate the entropy flux to the normal fluid component :

$$\mathbf{S} = \rho s \mathbf{v}_n - \kappa \frac{\nabla T}{T}, \quad (2.7)$$

with s the entropy mass and k the helium thermal conductivity. For most cases, the conductive term is negligible with respect to the convective term and we can define a heat flux carried by the normal fluid component:

$$\mathbf{q} = \rho s T \mathbf{v}_n. \quad (2.8)$$

The total fluid momentum equation is written:

$$\rho \mathbf{v} = \rho_n \mathbf{v}_n + \rho_s \mathbf{v}_s. \quad (2.9)$$

\mathbf{v} is the barycentric velocity of helium flow. The particular process of heat transport implies that all heat flux causes a normal fluid flow. Therefore all heat emission at a solid wall in contact with He II is communicated to the normal fluid and its movement

is followed by that of the superfluid, if we consider a mass flow null like $\rho_n \mathbf{v}_n + \rho_s \mathbf{v}_s = 0$ (counter-flow).

This intern convective character is at the origin of the remarkable properties of heat transport in He II. The study of He II dynamics can be associated with heat transport studies since the heat is transported by the normal fluid component. The dynamic regimes of the superfluid and of the normal component flows correspond to the thermal regimes of He II, which is the reason of our interest in the He II dynamics.

Dynamics of He II at low velocity: Landau regime

The He II dynamic equations are presented at the first order for the velocity fields \mathbf{v}_n and \mathbf{v}_s . This choice is justified by the weak importance that second order terms have in heat transport. Very good explanations of second order terms effects were presented by Khalanikov [35], Donnelly [36] and Putterman [37]. On the other hand for velocities higher than certain values we will introduce non linear terms of $\mathbf{v}_n - \mathbf{v}_s$, allowing to model the dynamic of what is called superfluid turbulence.

The equations presented below define the Landau regime where He II fluid has no vortex with quantified and constant circulation. In this case the velocity fields of the “two fluids” are weakly coupled via the mass conservation equation. The mass equation is written:

$$\frac{\partial \rho}{\partial t} + \nabla \cdot (\rho \mathbf{v}) = 0. \quad (2.10)$$

The momentum equation for the total fluid is written as for a classical incompressible fluid, noticing that only the normal fluid component is viscous and that the viscosity force is only function of its velocity field. We have:

$$\frac{d\rho \mathbf{v}}{dt} = -\nabla p + \eta \Delta \mathbf{v}_n + \rho \mathbf{g}, \quad (2.11)$$

where p is the pressure of the total fluid, η is the viscosity of the normal fluid component which is the only one to produce dissipative effects. The operator d/dt represents the total derivative.

The main issue of the behavior of this two fluids mixture concerns the evolution equation of the superfluid component. The hypothesis at low velocity is to consider that the superfluid flow is a potential flow and that it is possible to prove that this potential corresponds to the chemical potential [35]. Landau defines the dynamic equation of the superfluid velocity field based on the expression of the chemical potential gradient which is, under the previous hypothesis, expressed as:

$$\frac{d\mathbf{v}_s}{dt} = -\nabla \mu = s \nabla T - \frac{1}{\rho} \nabla p. \quad (2.12)$$

When the chemical potential is constant, the above equation can be written as:

$$\nabla p = \rho s \nabla T. \quad (2.13)$$

This is the well-known London equation in He II [38].

From the previous equations, we can deduce the evolution equations of the two velocity fields \mathbf{v}_n and \mathbf{v}_s as:

$$\frac{d(\rho_s \mathbf{v}_s)}{dt} = \rho_s s \nabla T - \frac{\rho_s}{\rho} \nabla p + \rho_s \mathbf{g} \quad (2.14)$$

and

$$\frac{d(\rho_n \mathbf{v}_n)}{dt} = -\rho_s s \nabla T - \frac{\rho_n}{\rho} \nabla p + \eta \Delta \mathbf{v}_n + \rho_n \mathbf{g}. \quad (2.15)$$

A last equation is necessary to entirely describe the system, as the entropy conservation equation, neglecting the dissipative effects. We saw that only the normal component transports the heat. The entropy equation (without interactions) is expressed as:

$$\frac{\partial(\rho s)}{\partial t} + \nabla \cdot (\rho s \mathbf{v}_n) = 0. \quad (2.16)$$

Dynamic of He II in the superfluid turbulence regime

When \mathbf{v}_s is greater than a critical velocity, there is a local destruction of superfluidity in He II. This corresponds to development of vortex in the superfluid flow. From the equation 2.6 the circulation of \mathbf{v}_s on a closed boundary, not reduced to a point, is quantified as:

$$\oint \mathbf{v}_s \cdot d\mathbf{l} = \frac{h}{2\pi m} \oint \nabla \Phi \cdot d\mathbf{l} = \frac{h}{2\pi m} \oint d\Phi = \frac{nh}{m}, \quad (2.17)$$

since $\oint d\Phi$ is the variation of the phase of the order-parameter for a complete turn along the boundary. h/m is the quantum of circulation. If we consider this boundary as a circle with radius r , the circulation is equal to:

$$\oint \mathbf{v}_s \cdot d\mathbf{l} = 2\pi r \mathbf{v}_s = \frac{nh}{m}. \quad (2.18)$$

The nucleation and development of vortex lines satisfying equation 2.18 still remains a not totally understood phenomenon, despite a lot of work was done since Vinen [39]. We can consider that, in dimensions greater than the micrometer, it exists a critical velocity below which vortex are in the state of germ and have no influence. We are referring to a superfluid environment (free vortex). In confined environments, this development is delayed by the interaction with the wall and the critical velocity can considerably increase.

The superfluid component always satisfies the irrotational criterion except in a finite number of points or singular lines that are the vortex cores. These vortex cores are not superfluid but made of predominantly normal helium. The superfluid bulk is then charged with foreign lines that can be seen by the normal component. In other words, a new interaction between the two components develops. The corresponding force called “mutual friction” must be considered in the previous equations.

The first phenomenological model of superfluid turbulence was proposed by Vinen. The superfluid vortex network is in this case linked to the thermodynamic variables [39]. This model is based on the determination of the forces applying on the vortex network. The growth of vortex is directly linked to the dynamic effect due to the relative velocity field of the two components $\mathbf{v}_n - \mathbf{v}_s$. In a He II flow a vortex line of unit length undergoes an interaction force from the normal fluid, called the mutual friction, whose module is:

$$|\mathbf{f}_{ns}| = \frac{B\rho_n\rho_s}{2\rho} \frac{h}{m} |\mathbf{v}_n - \mathbf{v}_s - \mathbf{v}_t|. \quad (2.19)$$

\mathbf{v}_t is the velocity field of the vortex line and B an adimensional coefficient experimentally determined and temperature dependent. This mutual force translates the internal coupling between the two components of the two fluids model.

The existence of this force was introduced the first time by Gorter and Mellink [40]. The theoretical justification of this expression still remains incomplete, especially for the introduction of the relative velocity field of the vortex network in the superfluid $\mathbf{v}_s - \mathbf{v}_t$. We can assume the hypothesis that the vortex network has the same velocity field of the superfluid, hence $\mathbf{v}_s - \mathbf{v}_t$ is replaced by \mathbf{v}_s . Some authors showed that this hypothesis is wrong and that \mathbf{v}_t is proportional to $\mathbf{v}_n - \mathbf{v}_s$, with a proportionality coefficient dependent on temperature [41]. For simplicity and because this point is not elucidated, we overcome this question by assuming that this effect is integrated in the temperature dependence of B [42].

In Vinen's model the turbulence is supposed fully developed. By analogy with classical turbulence, one condition of fully developed turbulence stipulates that the average distance between the vortex of the network must be smaller than the smallest dimension of the bulk [43]. The force generated on the vortex network per unit volume is linked to the force per unit vortex length, by introducing a vortex line density L_0 . At equilibrium this force is expressed as:

$$\mathbf{F}_{ns} = \frac{2}{3} \mathbf{f}_{ns} L_0. \quad (2.20)$$

This force is introduced in the momentum equation of the superfluid component \mathbf{v}_s . Vinen considers the volumetric vortex lines density distribution L homogeneous and isotropic. The increase of L is directly proportional to the interaction force between a vortex line and the normal fluid \mathbf{f}_{ns} . The increase of the vortex lines density is defined as:

$$\left(\frac{dL}{dt}\right)_p = \chi_1 \frac{|\mathbf{f}_{ns}|}{\rho_s h/m} L^{3/2}, \quad (2.21)$$

where χ_1 is an adjustable constant, close to 1, dependent on the geometric arrangement of the vortex lines. This representation of the vortex lines density production supposes that a vortex network already exists, because if $L = 0$ then $(dL/dt)_p = 0$. Vinen proposed an empirical expression of the decrease of turbulence analogous to classical fluids:

$$\left(\frac{dL}{dt}\right)_d = -\chi_2 \frac{h}{m} L^2, \quad (2.22)$$

where χ_2 is a constant whose value is close to 1. The value L_0 at equilibrium is given by $(dL/dt)_p = (dL/dt)_d$, so that:

$$L_0^{1/2} = \frac{\chi_1}{\chi_2} \frac{B}{2} \frac{\rho_n}{\rho} \frac{m}{h} |\mathbf{v}_n - \mathbf{v}_s|. \quad (2.23)$$

L_0 is about 1 m^{-2} per unit volume, for $|\mathbf{v}_n - \mathbf{v}_s| = 0.01 \text{ ms}^{-1}$ at 1.6 K.

This theory considers the turbulence as homogeneous and isotropic, so that L_0 does not depend of the geometry of the bulk, but only on the temperature or on an associated

variable. We can express the force \mathbf{F}_{ns} as a function of the relative velocity $\mathbf{v}_n - \mathbf{v}_s$, by replacing equation 2.23 in 2.20:

$$\mathbf{F}_{ns} = A\rho_n\rho_s|\mathbf{v}_n - \mathbf{v}_s|^2(\mathbf{v}_n - \mathbf{v}_s). \quad (2.24)$$

A is the temperature dependent Gorter-Mellink coefficient. It was measured by different authors. Fig. 2.14 reports the values measured by Vinen [39].

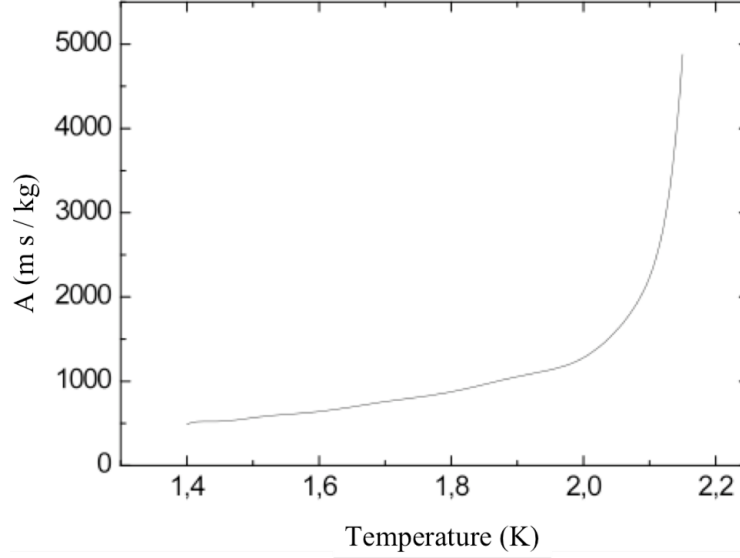


Figure 2.14: Gorter-Mellink coefficient A measured by Vinen [39].

The momentum equation is modified by the appearance of the interaction force between the normal fluid and the vortex. Equation 2.14 is then rewritten by introducing the mutual friction force:

$$\frac{d(\rho_s \mathbf{v}_s)}{dt} = \rho_s s \nabla T - \frac{\rho_s}{\rho} \nabla p + \rho_s \mathbf{g} + \mathbf{F}_{ns}. \quad (2.25)$$

Replacing \mathbf{F}_{ns} by its expression as function of $\mathbf{v}_n - \mathbf{v}_s$, the previous equation becomes:

$$\frac{d(\rho_s \mathbf{v}_s)}{dt} = \rho_s s \nabla T - \frac{\rho_s}{\rho} \nabla p + \rho_s \mathbf{g} + A\rho_n\rho_s|\mathbf{v}_n - \mathbf{v}_s|^2(\mathbf{v}_n - \mathbf{v}_s). \quad (2.26)$$

The interaction force is internal, therefore it only acts between the normal and the superfluid components and does not act on the whole fluid. To calculate the momentum equation of the normal fluid component, we use the momentum equation 2.11. We find an equation similar to equation 2.15, where the mutual friction is added:

$$\frac{d(\rho_n \mathbf{v}_n)}{dt} = -\rho_s s \nabla T - \frac{\rho_n}{\rho} \nabla p + \eta \Delta \mathbf{v}_n + \rho_n \mathbf{g} - A\rho_n\rho_s|\mathbf{v}_n - \mathbf{v}_s|^2(\mathbf{v}_n - \mathbf{v}_s). \quad (2.27)$$

As just noticed, the effects of superfluid turbulence are of internal nature. Therefore no effects on the pressure gradient are expected. Allen and Reekie confirmed experimentally that the pressure gradient is defined by the same equation in the superfluid turbulent regime and in the Landau regime [44]. It is this observation that allowed Gorter and

Mellink to base the approximation of the mutual friction term on the hypothesis of the average laminar flow of the normal component:

$$\nabla p = \eta \Delta \mathbf{v}_n \quad (2.28)$$

We will see that this hypothesis is not always valid. However, Vinen's model does not describe the transition between the two dynamic regimes: the regime without vortex and the turbulent regime. It is currently admitted that the mutual friction appears for a velocity \mathbf{v}_s greater than a critical value corresponding to the appearance of vortex.

The critical superfluid velocity $|\mathbf{v}_{sc}|$ is the velocity from which vortex develop in He II, corresponding to the superfluid turbulence regime. Different theories allowed establishing a theoretical expression of the critical superfluid velocity, based on the creation of a vortex at the outlet of a channel [34] or on the definition of the critical velocity by Landau [45] :

$$|\mathbf{v}_{sc}| = \frac{\hbar}{md} \left(\ln \frac{d}{a} \right). \quad (2.29)$$

a is the size of the vortex core ($\approx 10^{-8}m$) and d is the flow diameter. Other empirical expressions of the critical velocity were proposed, for instance by Van Alphen [46] :

$$|\mathbf{v}_{sc}| \approx d^{-1/4}. \quad (2.30)$$

From experimental results, Craig [47] showed that equation 2.30 is an approximation of the more general expression:

$$|\mathbf{v}_{sc}|^3 d \approx b \ln \left(1 + \frac{c}{|\mathbf{v}_{sc}|} \right), \quad (2.31)$$

where b and c are experimental adjustable constants. These expressions of $|\mathbf{v}_{sc}|$ depend on the geometrical dimensions but not on temperature. An empirical temperature dependent correlation was proposed by Ladner and Tough [48]. It will be recalled in chapters 5 and 6.

2.5.3 Heat transport in superfluid helium

In this section we consider the steady-state heat transport without fluid movement, i.e. with a zero mass flow $\rho \mathbf{v}$. At first we address the Landau regime, followed by the superfluid turbulent regime.

As already stated, only the normal fluid component carries the heat. The heat flux density is expressed as:

$$\mathbf{q} = \rho s T \mathbf{v}_n. \quad (2.32)$$

Every heat contribution leads to a normal fluid flow and a counter-flow of superfluid as consequence. This equation, combined with the momentum equations of the two components, permits to define the transport laws in He II. It is then possible to establish the correspondence between the critical velocity \mathbf{v}_{sc} and the critical heat flux $\mathbf{q}_c = -\rho \frac{\rho_s}{\rho_n} s T \mathbf{v}_{sc}$.

Landau regime

We consider here the total momentum equation 2.11 in steady-state which leads to the Poiseuille equation:

$$\nabla p = \eta \Delta \mathbf{v}_n. \quad (2.33)$$

Considering a channel with constant cross-section and the London equation (2.13), equation 2.33 can be solved. The normal component of the velocity is related to the pressure gradient and the temperature gradient:

$$\nabla p = \rho s \nabla T = \frac{\beta}{d^2} \eta \mathbf{v}_n, \quad (2.34)$$

where d is the characteristic length of the channel, and β is a constant determined by the geometric conditions.

Let us now consider the expression of the heat flux, equation 2.32. By eliminating the normal component of the velocity in equation 2.34, we can relate the heat flux and the temperature gradient as:

$$\mathbf{q} = \frac{d^2 (\rho s)^2 T}{\beta \eta} \nabla T. \quad (2.35)$$

This expression looks like a Fourier type pure conduction law, with an effective thermal conductivity $d^2 (\rho s)^2 T / (\beta \eta)$. For instance, if we consider a circular tube with a diameter of 10 μm filled with liquid He II at 1.9 K, the effective thermal conductivity is equal to 5.10^4 W/m.K , i.e. 100 times more than that of a very pure copper at the same temperature.

If equation 2.35 were the only expression limiting heat transport in He II, we could easily increase the effective thermal conductivity by increasing the diameter of the flow. However, there is a physical limit to that. It is the existence of a critical superfluid velocity. For velocity greater than the critical velocity, a second regime of heat transfer appears: the superfluid turbulence.

Gorter-Mellink regime

Following the same approach of the previous section, it is easy to show from equations 2.26 and 2.27 that the expression of the temperature gradient (equation 2.35) has an additional term corresponding to the mutual friction effects:

$$\nabla T = -\frac{\beta \eta}{\rho s d^2} \mathbf{v}_n - \frac{A \rho_n}{s} |\mathbf{v}_n - \mathbf{v}_s|^2 (\mathbf{v}_n - \mathbf{v}_s). \quad (2.36)$$

Using $\rho_n \mathbf{v}_n = -\rho_s \mathbf{v}_s$ and the equation 2.32 of the heat flux density, equation 2.36 can be rewritten as:

$$\nabla T = -\frac{\beta \eta}{(\rho s)^2 d^2 T} \mathbf{q} - \frac{A \rho_n}{\rho_s^3 s^4 T^3} |\mathbf{q}|^2 \mathbf{q}. \quad (2.37)$$

The first term on the right hand side is the one we have in the Landau regime. The second term on the right hand side is due to the mutual friction. It is not dependant on the diameter d and it features a cubic dependence on the heat flux. This term dominates

the temperature gradient at high heat fluxes and with sufficiently large diameters. As an example, for a temperature of 1.9 K and a diameter of 1 mm, the mutual friction term dominates for heat fluxes greater than 100 W/m². For practical applications of much higher He II heat fluxes, the first term on the right hand side can be ignored [10].

Fig. 2.15 graphically summarizes the whole He II heat flow regime, by assuming constant properties. Both the laminar (dashed lines) and turbulent (dashed - dotted lines) characteristics are shown for different diameter channels. Critical velocities evaluated through different models are reported. The dotted line shows the behavior of the transition region between the two main heat transport regimes, which is in general quite complex and of difficult interpretation.

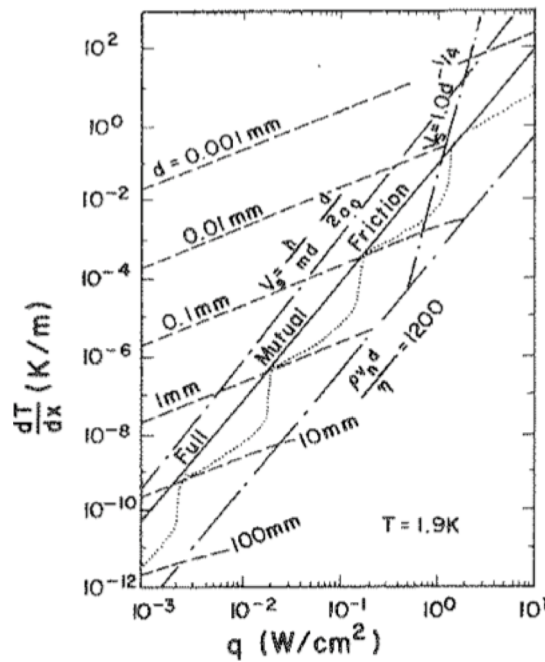


Figure 2.15: He II heat transport regimes at 1.9 K, from [49].

2.5.4 Kapitza resistance

In case of heat transfer from a solid wall to He II, the first thermal barrier is the interface solid-liquid associated to the Kapitza resistance, from the name of the physicist who identified the nature of the exchange liquid-wall in He II [50]. This thermal resistance causes a temperature difference through this interface which is predominant in front of the temperature difference that can exist in He II.

The temperature discontinuity is due to difference in acoustic properties between He II and solid. The thermal transmission coefficient of Kapitza h_{Kap} is defined as:

$$h_{Kap} \triangleq \lim_{\Delta T \rightarrow 0} \left(\frac{q}{\Delta T} \right) \quad (2.38)$$

$$\Delta T = T_p - T_f. \quad (2.39)$$

T_p is the temperature of the surface in contact with He II, and T_f is the He II temperature.

Two theories are available to explain the origin of Kapitza conductance: the theory of phonons radiation and the theory of acoustic mismatch. The results obtained with these two theories predict either too high (phonons radiation theory) or too low (acoustic mismatch theory) values. However, the theories write the phenomena of Kapitza conductance with the same heat transfer law:

$$q = \chi_{Kap}(T_p^4 - T_f^4), \quad (2.40)$$

where χ_{Kap} is the Kapitza coefficient.

When $\Delta T \ll T_f$, equation 2.40 can be simplified as:

$$q = 4\chi_{Kap}T_f^3(T_p - T_f) = h_{Kap}(T_p - T_f), \quad (2.41)$$

where $h_{Kap} = 4\chi_{Kap}T_f^3$.

From a practical point of view, the value of the Kapitza conductance is experimentally determined since theories do not succeed to predict them.

Furthermore, the Kapitza conductance is a function of different parameters linked to the material itself, its roughness and its shape. For copper with temperature between 1.8 K and 2 K, for instance, Van Sciver [10] compiled existing works and identified the Kapitza heat transfer coefficient h_{Kap} (W/(m².K)) to be in the range:

$$400T_f^3 \leq h_{Kap} \leq 1100T_f^3. \quad (2.42)$$

Chapter 3

Experimental characterization of the LHC-type cable electrical insulation of superconducting magnets

Contents

3.1	Introduction	25
3.2	The LHC insulation	26
3.3	Development of the experimental program	27
3.3.1	Background notions	27
3.3.2	Sample preparation and instrumentation	28
3.3.3	Heating configurations	32
3.3.4	Assessment of the applied pressure	34
3.3.5	Cryogenic system	35
3.3.6	Measurements	35
3.4	Heat transfer results	38
3.4.1	Effect of mechanical pressure	40
3.4.2	Localized vs. distributed heat deposition	42
3.4.3	Thermal coupling between cables	43
3.4.4	Phenomenological analysis	44
3.5	Electrical measurements	46
3.6	Mechanical measurements	47
3.6.1	Insulation thickness	47
3.6.2	Elastic modulus	50
3.6.3	Stress relaxation	51
3.7	Conclusion	53

3.1 Introduction

In this chapter we present the experimental method that was developed to qualitatively and quantitatively study the heat transfer through the electrical insulation of superconducting cables towards the cooling superfluid helium bath. We conceived a program of

experimental tests that required the development of an innovative device implementing new specificities with respect to the *stack method* originally developed at CEA Saclay, France and later in KEK, Japan. The improvements concern the combination of real cable structure, thermometry, control of applied pressure and of heating configuration. Such features proved to be essential to correctly characterize the thermal behavior of the complex helium porous insulation schemes.

The developed experimental program aims on the one hand at describing the thermal behavior of the LHC superconducting coils. This is the best means to evaluate the magnet stability, as it will be shown in chapter 7. On the other hand it provides indications for the elaboration of a thermal numerical model of the coil, that will be described in chapter 5.

The heat extraction from the LHC main dipole coil was quantified as a function of the steady-state cable temperature rise. Several mechanical and thermal conditions were tested, corresponding to different parts of the coil and to different heating patterns, respectively. A qualitative analysis of the results is provided, that will serve as a basic input for the quantitative analysis reported in chapter 5.

The chapter is concluded by the description of the electrical and mechanical characterizations of the LHC insulation, which provide a benchmark for the development of new insulation schemes. The development of a new experimental device to investigate the insulation stress relaxation mechanisms is presented.

3.2 The LHC insulation

The LHC insulation scheme used for the Main Bending (MB) dipole and Main Quadrupole (MQ) magnets is shown in Fig. 3.1. It is composed of three wrappings of polyimide tapes, whose geometric parameters are listed in Table 3.1 [2].

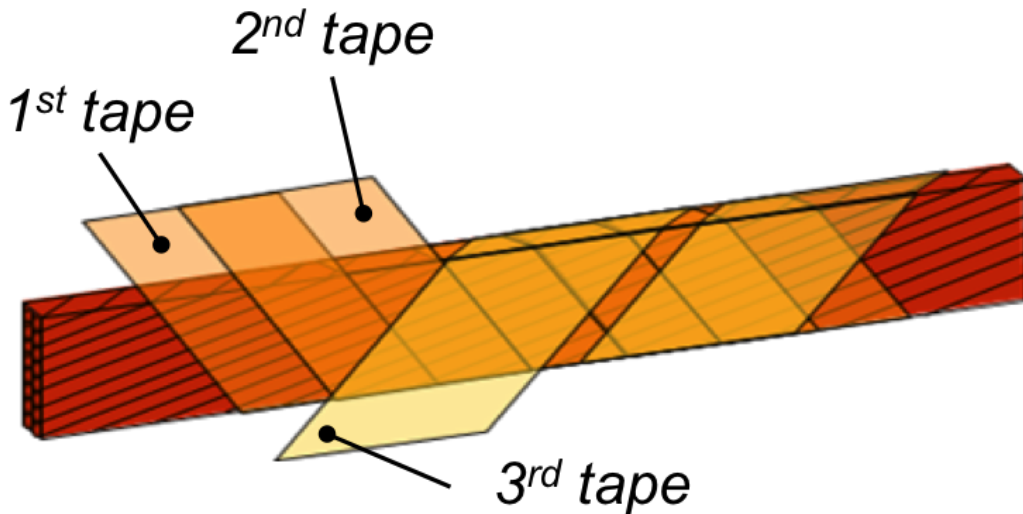


Figure 3.1: LHC insulation scheme.

The requirements of the electrical insulation of superconducting cables and the evolution that led to the LHC scheme were recalled in section 2.4. The first two tapes are 50% overlapped. They ensure the electrical insulation by providing a sufficiently long surface

3.3. Development of the experimental program

LHC insulation scheme	1 st tape	2 nd tape	3 rd tape
MB	11 mm wide	11 mm wide	9 mm wide
	no spacing	no spacing	2 mm spacing
	50 μm thick	50 μm thick	69 μm thick
		50% overlap 1 st tape	cross wrapped
MQ	11 mm wide	11 mm wide	9 mm wide
	no spacing	no spacing	2 mm spacing
	50 μm thick	37.5 μm thick	55 μm thick
		50% overlap 1 st tape	cross wrapped

Table 3.1: Geometric parameters of the LHC insulation schemes.

path for electrical discharge. The third tape is intended to protect them and to provide cohesion between adjacent coil turns, thanks to a 5 μm thick coat of polyimide based adhesive on the outer surface (included in the third tape thickness). This glue is activated by thermal treatment during the curing cycle. The third tape is cross-wrapped with respect to the first two tapes, with a spacing of 2 mm to create channels for the He II coolant between the coil turns.

3.3 Development of the experimental program

3.3.1 Background notions

The *stack method* was first used at CEA-Saclay, France, during the R&D phase of the LHC main magnets [28][51][52]. The presence of a direct link between cables and He II bath was assessed. Several insulating materials and technologies were tested, investigating their impact on the cooling capability of the superfluid helium coolant. The main limitation of these tests was the use of solid conductors (stainless steel plates) instead of real cables, which were heated by Joule heating. Although the conductor surface was machined to reproduce the external cable surface, this setup did not allow to have helium inside the conductor. Therefore the cable cross-section below T_λ was not isothermal.

Similar measurements on stack samples were later carried out in KEK, Japan, in order to qualify the LHC MQXA interaction region quadrupole [53] [54] [55]. Resistive cables with the same geometry of the superconducting ones were used, allowing superfluid helium to fill the interstices among strands. Isothermal conditions on the cable cross-sections could therefore be obtained. The impact of the cable structure (solid conductor vs. actual porous conductor) was clearly shown [53]. The cable ends were sealed to prevent heat leaks. However these tests only focused on the insulation of the mentioned magnet. They had mainly to deal with flowing issues of the epoxy resin film resulting in sealing of the insulation porous structure.

Heat transfer studies carried out at CERN [56] concerned in a first stage the analysis of high ramp rate quench data of 1 m long LHC model dipoles. The developed technique is a unique method providing heat transfer data of a real magnet in close-to real heating

conditions. Nevertheless it is difficult to obtain results for low heat fluxes below T_λ .

In a second stage, tests were carried out on a smaller scale setup, closer to the CEA and KEK mentioned ones. The sample was in this case a segment from a (superconducting) LHC production dipole coil. The sample was instrumented and heat was generated in a way inspired by the DC method for the inter-strand contact resistance measurement [57]: current was injected into a few strands generating heat in the contacts between all strands. Heat generation in this case was not completely uniform over the sample cross-section and length, although one can consider so in a first approximation because of the large number of strands contact. The importance of this test is that for the first time a real piece of coil was measured. However this new measuring technique featured some limitations, mainly associated to the manipulation of the sample and altering of its properties. The temperature sensors were not placed on the hottest strands where the current was injected, but on others which followed passively in the wake of the injecting pair. This feature of the superconducting sample allows to catch less details of the heat transfer curves with respect to the samples prepared for our study [58]. Finally, in its first version [56] the sample suffered heat leaks from its extremities which were not properly sealed.

3.3.2 Sample preparation and instrumentation

The test samples were prepared from a resistive Cu-Ni (Cu-10wt%Ni) cable with the same geometry of the LHC Rutherford cable type 01, i.e. the inner layer cable of the main dipoles [2] (Table 3.2). The cable was insulated according to the scheme described in section 3.2. Six cable pieces were alternately stacked to compensate for the keystone angle, thus forming a rectangular stack.

		cable 01	cable 02
		inner layer MB	outer layer MB
			both layers MQ
strand diameter	(mm)	1.065 ± 0.0025	0.825 ± 0.0025
number of strands	(-)	28	36
cable mid thickness (50 MPa)	(mm)	1.900 ± 0.006	1.480 ± 0.006
cable thin edge	(mm)	1.736	1.362
cable thick edge	(mm)	2.064	1.598
width	(mm)	$15.10 +0/-0.02$	$15.10 +0/-0.02$
keystone angle	(degree)	1.25 ± 0.05	0.90 ± 0.05
transposition pitch	(mm)	115 ± 5	100 ± 5

Table 3.2: Strands and cables geometric characteristics of the LHC main dipoles (MB) and main quadrupoles (MQ).

The stack was cured over 170 mm according to one of the two bonding cycles shown in Fig. 3.2. They differ because of the pressure of either 80 or 130 MPa applied perpendicularly to the cables flat face. These values were taken as minimum and maximum possible magnet curing pressure. The other features are common to the two cycles, namely:

- a 60 minutes long pre-heating phase up to 135 °C. A firm contact (10 MPa) is guaranteed from the very beginning of the curing cycle;

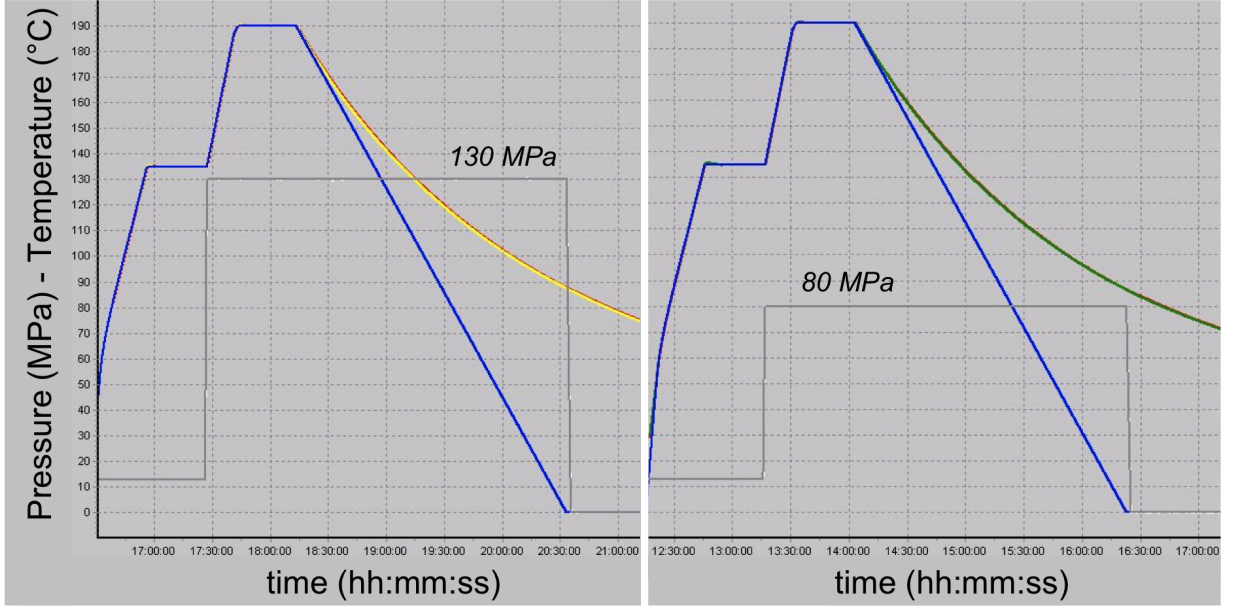


Figure 3.2: Curing cycle at 130 MPa (left) and 80 MPa (right).

- the mould is closed at a temperature of 135 °C. The pressure of 80 or 130 MPa is applied during 3 hours (grey line);
- the temperature of 190 °C is reached and kept for 30 minutes, in order to thermally activate the glue on the outer surface of the third insulation tape;
- the pressure is released when the imposed temperature has dropped to 0 °C (blue line). As shown in Fig. 3.2, the corresponding actual stack temperature is between 80 and 90 °C (overlapping yellow, green and red lines).

The importance of implementing all these features was demonstrated in [29]. They allow to improve the bonding quality by exploiting the whole potential of the used polyimide glue.

The samples prepared for the thermal and electrical tests were cured at 130 MPa. This choice is conservative, because the LHC reference cycle is at 80 MPa. The samples prepared for the mechanical tests underwent either the 80 or 130 MPa curing cycle, as defined in the relevant sections. A comparison of the mechanical properties of samples prepared with the two cycles will be shown in sections 3.6 and 4.7. Fig. 3.3 shows the curing mould (left) and a top and side view of a cured LHC (MB) six-units stack.

One of the two central cables was instrumented with an array of nine Au-Fe (Au-0.07at%Fe) vs. Chromel thermocouple junctions (TCJs). Thanks to their small dimensions, the TCJs could be installed inside the cable strands. In order to avoid short-circuits under the high compression loads acting on the sample, grooves were machined along some selected strands before insulating the cable, to host the TCJs and their wires. The grooves are 0.5 mm wide and 0.6 mm deep. They are shown in Fig. 3.4, as well as the position of the TCJs. TCJ no. 2 and 6 are located close to the cable small faces, whereas all the others are in the middle of the cable. TCJ 2 through 6 are located in the central part of the cable, whereas TCJ 1 and 7 through 9 are closer to the sample extremities.

After the curing cycle of the sample, the third insulation tape of the cable adjacent to the one to instrument was cut along the cables small face. This cable was temporarily

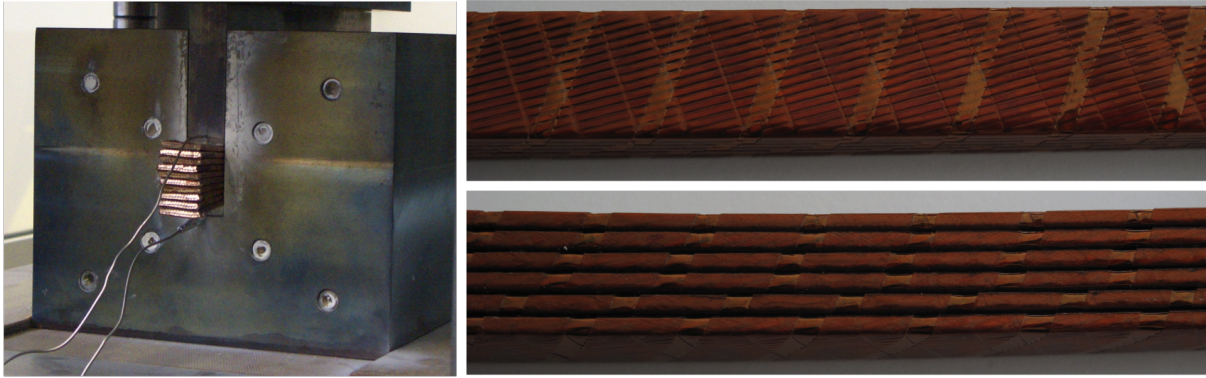


Figure 3.3: Curing mould (left). Top and side view of a cured LHC (MB) six-units stack (right).

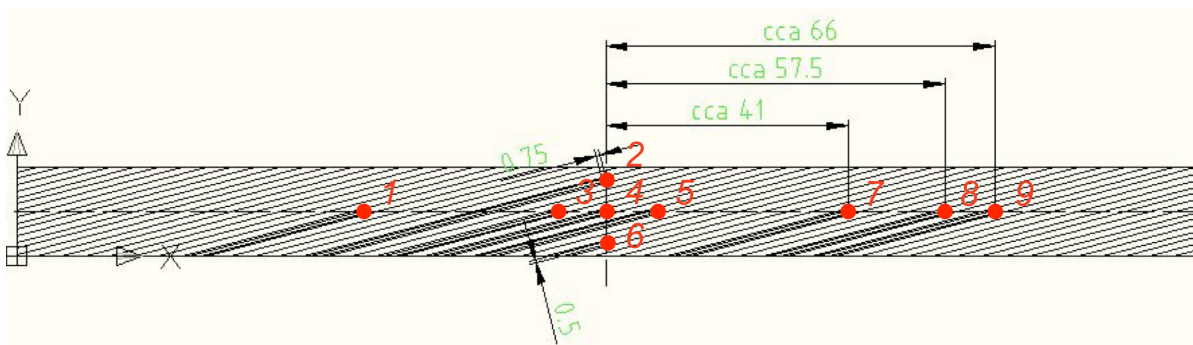


Figure 3.4: Location of the nine thermocouple junctions and of the corresponding grooves.

taken out from the stack, as shown in Fig. 3.5, while its first and second tape remained intact. Small squares of insulation were removed from the large face of the central cable at the end of each groove, allowing the TCJs to be installed. The TCJs wires were drawn along the groove towards the thick edge of the cable and through the insulation outwards (Fig. 3.6). The holes drilled in the polyimide tapes were then sealed using epoxy resin, both on the flat and on small face, as shown in Fig. 3.7 (left).



Figure 3.5: Sample being instrumented.

The thermocouples were made by soldering the Au-Fe and the Chromel wires. The junction was varnish insulated, as shown in Fig. 3.7 (middle). The thermocouple wires were extended by copper lead wires up to the readout instrument [59]. In order to avoid the

3.3. Development of the experimental program

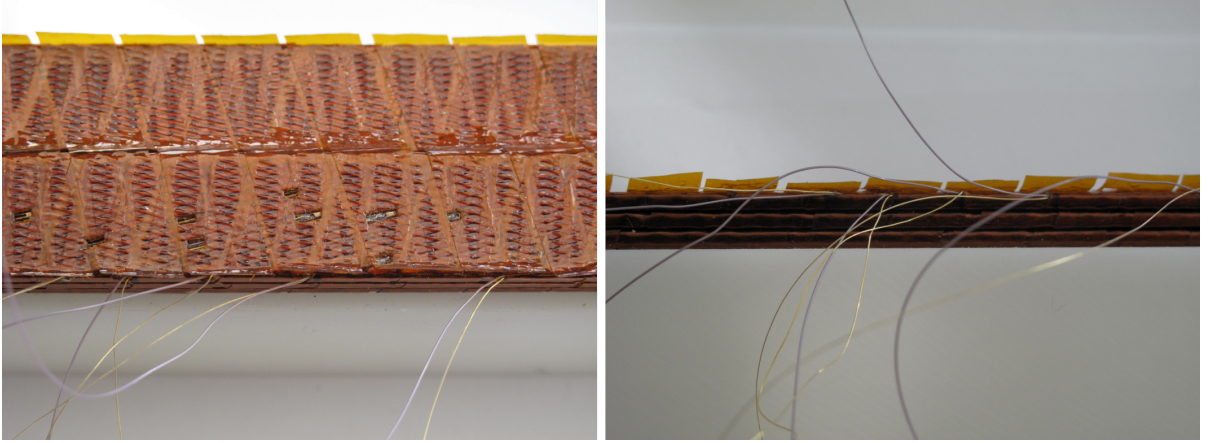


Figure 3.6: Details of the sample instrumentation. Top and side view (left and right, respectively).

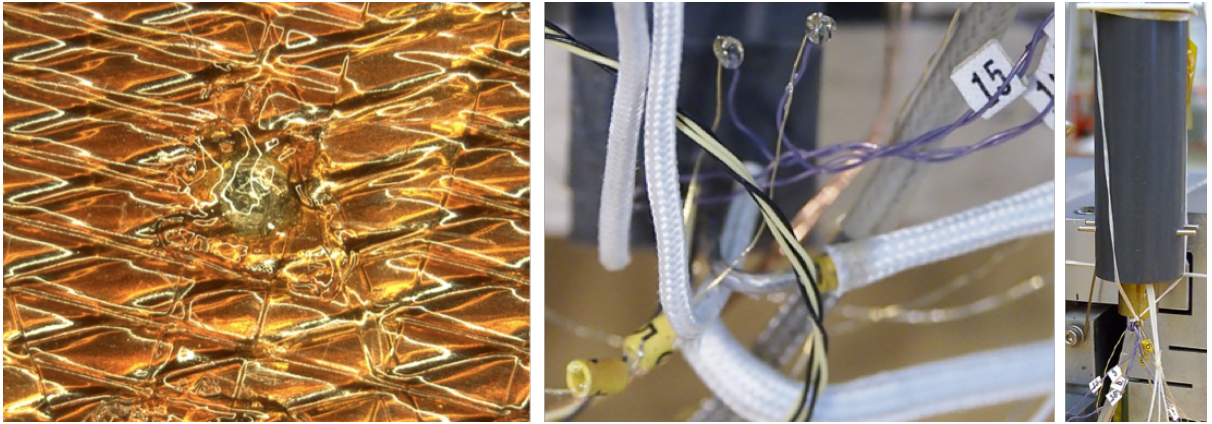


Figure 3.7: Detail of an installed TCJ (left), of the thermocouple-to-lead junctions (middle), and of the OFHC copper tube (right).

use of connectors along them, a feed-through was realized in the cryostat top plate. All thermocouple-to-lead junctions were placed together inside a OFHC copper tube in the He bath (Fig. 3.7 (right)), instrumented with a germanium temperature sensor.

The sample preparation was completed by adding 3 mm thick fiberglass plates on top and bottom of the stack. They served as thermal separator and as a mechanical structure element. Epoxy resin plugs on the sample extremities were also added, sealing together stack and fiberglass plates, to prevent longitudinal parasitic cooling. Fig. 3.8 shows a picture of the instrumented sample.

The sample was installed in an aluminum-alloy spring-like holder (Fig. 3.9), allowing to apply a compressive pressure on the cables large face over the central 150 mm. The pressure ranging between 5 and 100 MPa is applied at room temperature and held during the test. The spring shape allows to compensate for the differential thermal contractions of the different components, in order to avoid pressure reduction when cooling down. Both cables small faces are in direct contact with the He II bath over the central 156 mm. Fig. 3.10 shows the sample installed for testing.

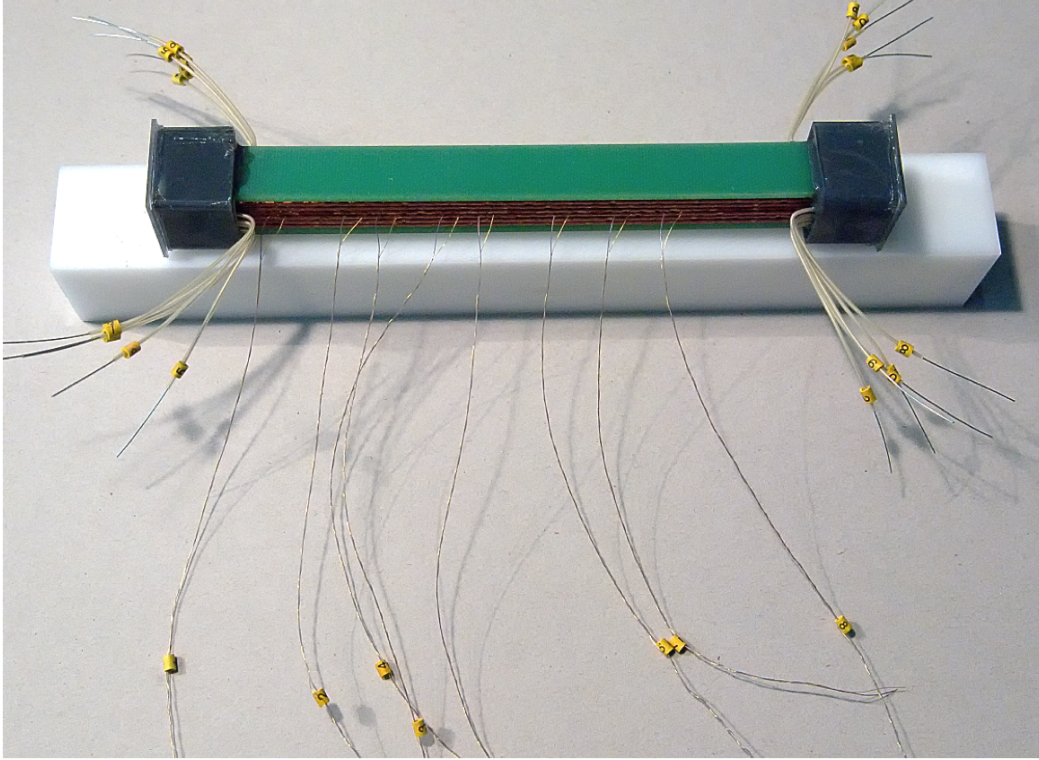


Figure 3.8: Instrumented sample, ready to be installed in the sample-holder.

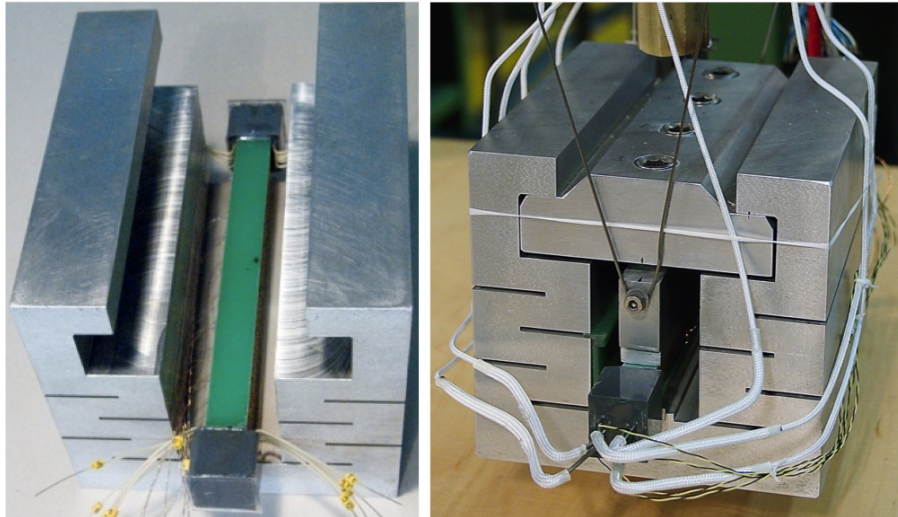


Figure 3.9: Sample installed in its holder (left) and under compression (right).

3.3.3 Heating configurations

Heat in the cables was uniformly generated by supplying DC current to the resistive strands. Five adjacent cables were connected at their extremities to the current supply, as it can be seen in Fig. 3.5. The sixth cable is necessary only for geometrical reasons. Up to 30 A current was fed either into one single cable or into several cables, through He gas cooled current leads. The heat generated was calculated using the measurement of the voltage at the cable extremities and of the injected current. The estimation of the error in

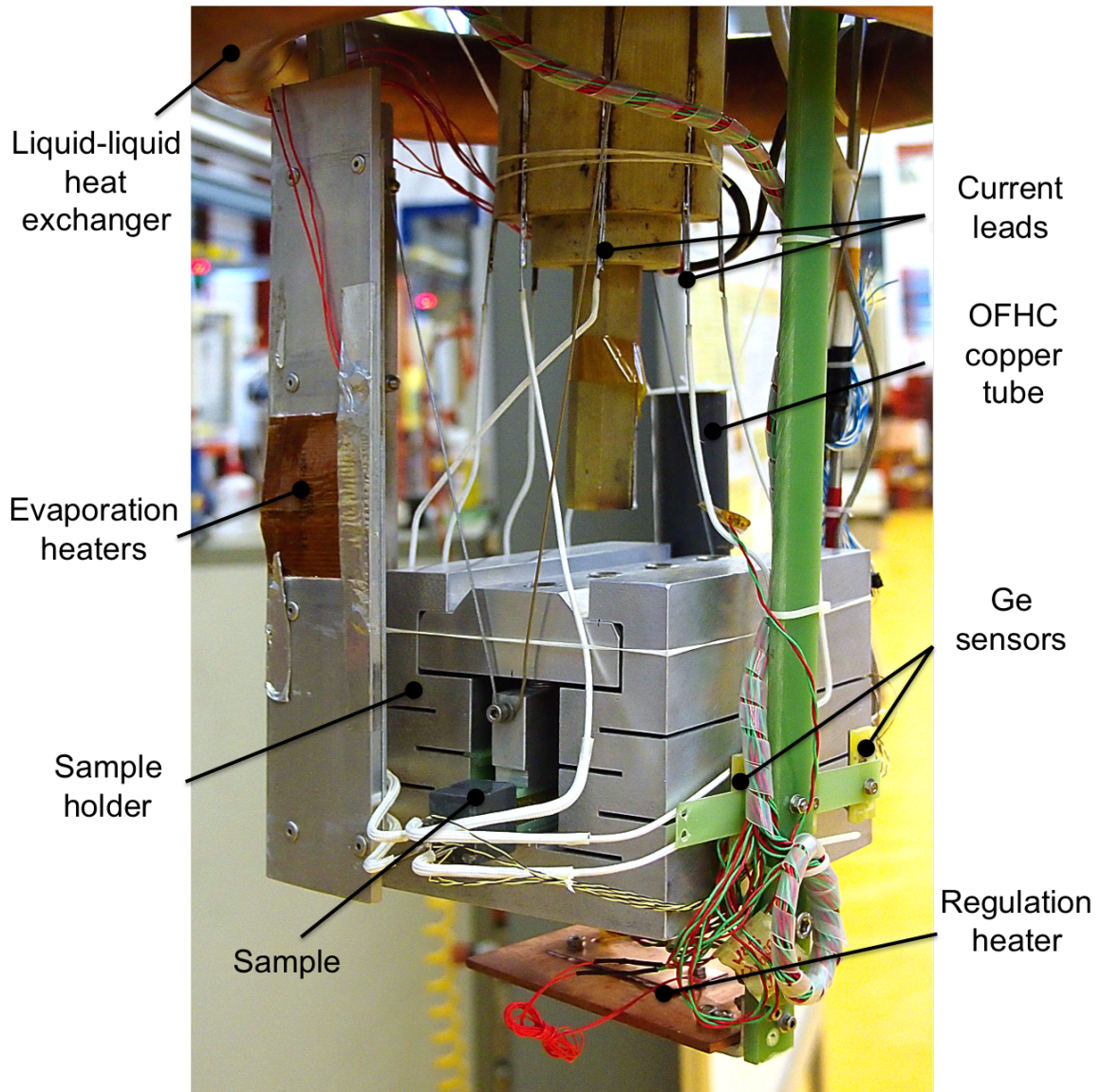


Figure 3.10: Sample installed for testing.

this calculation was done through the law of propagation of uncertainty. The overall error was evaluated to be smaller than 0.1% of the measured value.

We can distinguish the following possible heating configurations of the sample:

- symmetric heating, i.e. heating of one or three central cables, or of all the five cables. This allows to study the impact of a localized heat deposition versus a distributed one;
- asymmetric heating, i.e. when the instrumented cable does not coincide with the central heated cable. This permits to address in a different way the thermal coupling between cables.

An example is shown in Fig. 3.11. The scheme of a symmetric configuration is shown on the left, where the only central cable is heated. The scheme on the right represents an asymmetric configuration where the heated cable is adjacent to the central instrumented one. This simulates in a first approximation the presence of another instrumented cable,

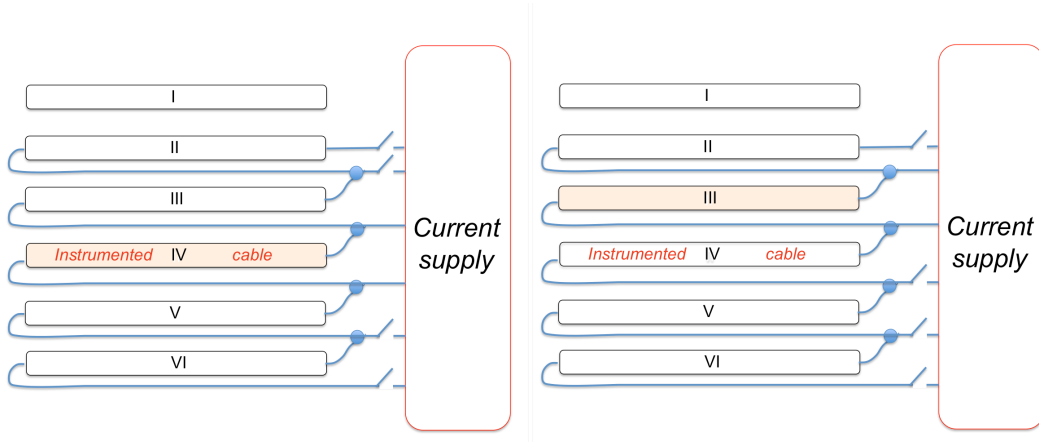


Figure 3.11: Symmetric heating configuration where the heated cable is the instrumented one (left). Asymmetric heating configuration where the heated cable is adjacent to the instrumented one (right).

as if in the left picture we were simultaneously monitoring the temperature of cable IV and III / V.

3.3.4 Assessment of the applied pressure

The pressure applied on the cable large faces at room temperature corresponds to a different pressure at low temperature because of the differential thermal contraction, of the variation of elastic moduli of all the components and of the forces due to the sample-holder spring shape.

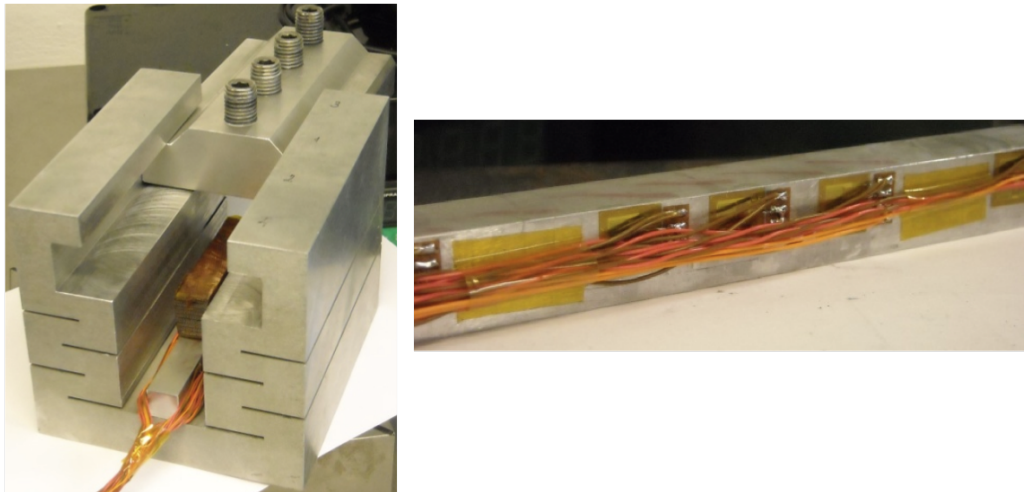


Figure 3.12: Bar instrumented with strain gauges (right) placed under the sample (left) to measure the pressure applied on the sample.

The actual pressure applied on the sample at cryogenic temperature was verified through a dedicated measurement. An aluminum-alloy bar was instrumented with strain gauges and placed under the sample, as shown in Fig. 3.12. The sample holder was closed at a defined pressure and cooled down to liquid nitrogen temperature. The measurements were performed at two pressure levels. The results, expressed as average of ten strain

3.3. Development of the experimental program

Pressure applied at 300 K (MPa)	Pressure measured at 77 K (MPa)
27	26
77	85

Table 3.3: Average pressure applied at ambient temperature vs. average pressure measured at liquid nitrogen temperature.

gauges, are reported in Table 3.3. No pressure reduction was found for low pressure levels, whereas a slight increase was observed for higher pressure levels. The values indicated in the following sections and chapters refer to the pressure applied at room temperature.

3.3.5 Cryogenic system

The heat transfer measurements were performed in cooling conditions similar to those of the LHC magnets, i.e. in a 0.1 MPa pressurized bath regulated to the temperature of 1.9 K. The used cryostat is a double bath (or Claudet-bath) cryostat [60] previously used for critical current measurements on LHC superconducting cable strands [61]. Its inner diameter is 425 mm and its height is 1.5 m. It is thermally insulated from the environment by a vacuum vessel. Two conduction-cooled copper insulation screens and super-insulation layers provide a further protection against the radiation heat source.

The interior of the cryostat is schematically depicted in Fig. 3.13. A plate made of insulating material (λ -plate) divides it in two parts. The liquid helium in the upper bath is always at ~ 4.2 K whereas the lower bath can be cooled down to 1.9 K at atmospheric pressure by pumping on a toroidal heat exchanger. The cold source is produced by a heat exchanger coupled with a Joule-Thomson valve. A counterflow heat exchanger fed by liquid helium is cooled by low-pressure gaseous helium. The fluid expansion is performed by an isenthalpic process in a throttle valve to feed the cold source with a liquid-gas mixture [60].

The lower bath hosts the sample-holder. The λ -plate features feed-throughs for the measurement wires. The solenoid shown in Fig. 3.13 is not present in the current setup. For 1.9 K tests, the lower bath temperature is stabilized within 0.2 mK and regulated by means of a regulation heater. The temperature is controlled by means of two germanium probes, known for their long-term stability [62], with an absolute precision of 10 mK. Automatic ABB software fully monitors all the cryogenic operations.

3.3.6 Measurements

Among the thermocouples, the Au-0.07at%Fe vs. Chromel one exhibits a large sensitivity of more than $8 \mu\text{V/K}$ down to 1.5 K [63]. Therefore it is particularly well suited to measure small temperature differences in the temperature range of liquid and superfluid helium. It measures directly the voltage between the junction and the bath, which is produced along the portions of the thermocouple wires that experience temperature differences.

The small voltage signals were measured by a nano-voltmeter (Keithley 2182) connected

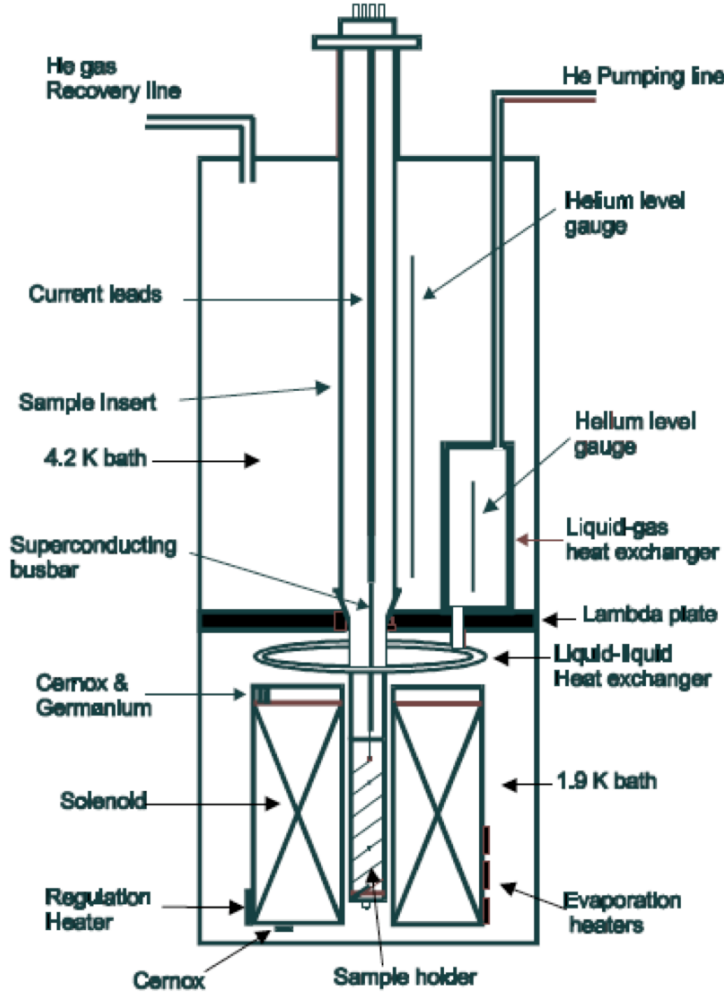


Figure 3.13: Schematic description of the cryostat.

to a scanner card (Keithley 7168) via a switch mainframe (Keithley 7001) to scan eight channels. The measured voltage was correlated to the temperature difference between the junction and the bath through the data table provided by Lake Shore Cryotronics [64]. A correction was applied according to the performed *in-situ* calibration: the thermocouple-to-lead junctions were heated by a heater wound around the OFHC copper tube, thermally insulated from the bath by a plastic tube as shown in Fig. 3.7 (right); the Ge temperature sensor measured the actual temperature inside the tube, while the bath was kept at 2.16 K, just below T_λ . The signal of the Ge sensor was read by a multi-meter (Keithley 2001), as well as the voltage across the cables and the current flowing through them (Keithley 2001 and 2000, respectively).

The thermocouple junctions aimed at measuring the strands temperature must be electrically insulated from the strands themselves. The measured temperature lies therefore in between the strands temperature and that of the helium inside the cable. A compromise between good electrical insulation and as high as possible thermal conductivity was found to be a varnish insulation (Fig. 3.7 (middle)).

The heat loss through the instrumentation wires is negligible with respect to the heat generated in the cable.

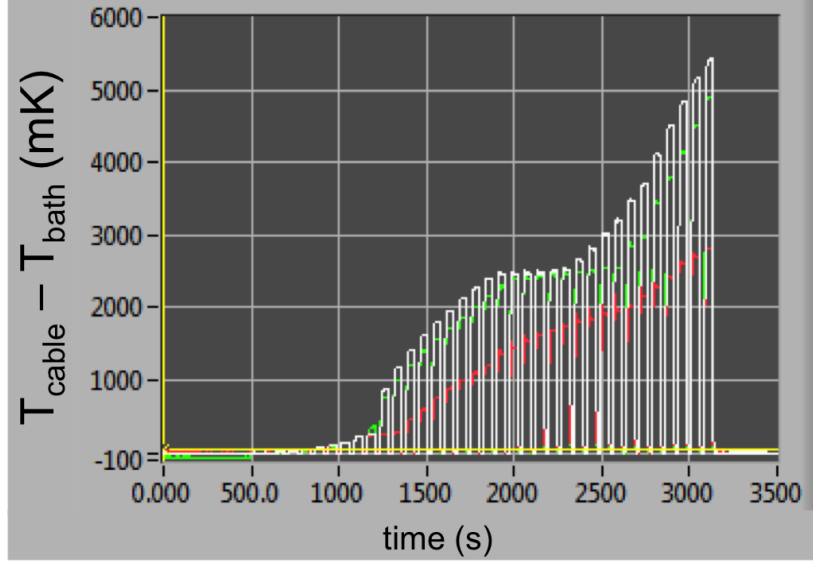


Figure 3.14: Time evolution of the temperature sensors, as shown by the LabVIEWTM program used for the data acquisition.

Fig. 3.14 reports the time evolution of the measured temperature difference between cable and bath, as shown by the LabVIEWTM program used for the data acquisition. The steady-state temperature levels were evaluated by averaging the signals in the last 75 s of 90 s long heat pulses, separated by 60 s of no heating time. It was experimentally verified that this time delay is sufficiently long to reach the steady-state.

This is confirmed by the calculation of the system time constants. The response time of the He II volume inside the cable can be estimated by writing the 1-D time-dependent heat diffusion equation in Gorter-Mellink regime as: $\partial T / \partial t = (f / 3\rho c_p q^2) \partial^2 T / \partial x^2$ [52]. T is the temperature, t the time, f the superfluid equivalent thermal conductivity, c_p the specific heat, ρ the density, q the heat flux density and x the space coordinate. An equivalent of the system diffusivity can be written as $D = f / (3\rho c_p q^2)$. It is dependent on the heat flux and can be calculated for small heat flux changes by assuming constant thermal properties in the considered temperature range. The diffusion time associated to it is $\tau_{diff} = 3\rho c_p q^2 l^2 / f$, where l is the characteristic dimension of the system. τ_{diff} is always smaller than 0.2 ms. In case the cable temperature exceeds T_λ , the time constant associated to diffusion in the strands cross-section is smaller than 1 s in the considered temperature range. In order to estimate the thermal inertia of the cable components (strands and helium among them), we can write the equation $\rho c_p dT / dt = -hA(T - T_{bath}) = -(T - T_{bath}) / R$, where V is the volume, h the heat transfer coefficient through the insulation, A the heat exchange surface, T_{bath} the bath temperature and R the thermal resistance of the sample. We can build the time constant $\tau_{inertia} = \rho c_p V R$. In the worst case of an insulation featuring a high thermal resistance, its value is of 1 s for both the helium and the strands. Finally, the characteristic time of heat extraction through the insulation is estimated considering the same case of high thermal resistance insulation. In the most unfavorable case of a cable temperature of 10 K, this time does not exceed 10 ms.

In case of thermocouples with short circuits to the cable, reversing the transport current in the cable can allow to correct the sensor signal. When the current is reversed, the

voltage due to the short circuit reverses sign whereas the thermocouple voltage does not. By averaging the forward and reverse current voltage measurements, the error due to the presence of short circuits was eliminated.

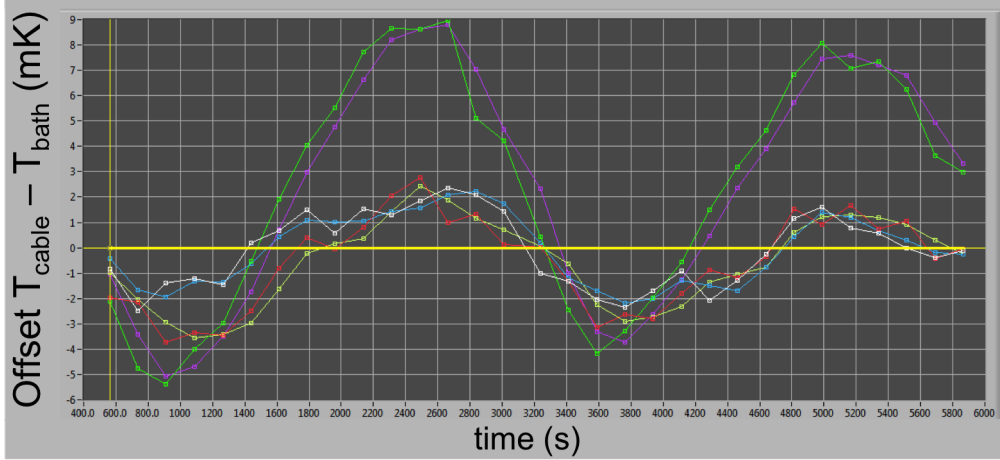


Figure 3.15: Evolution of the zero offset during a test.

The uncertainty on the recorded temperature is due to the calibration of the TCJs and to the measurement itself. The calibration error was calculated as the error of the reference sensor plus the error due to the fitting curve. The measurement uncertainty is due to the uncertainty of the nano-voltmeter plus the electromagnetic noise on the TCJs. The latter was estimated to be the principal source of error in our temperature measurement. It was evaluated to be less than 3 mK or 3% of the measured value, whichever is bigger.

Furthermore the instrumentation can show a zero offset, that is a signal value measured with no heat deposit, hence without input to the measuring instrument. Fig. 3.15 shows the evolution of this offset during a test, where it did not overcome 9 mK. In the post-processing the zero offset was subtracted from the measured signal.

3.4 Heat transfer results

The efficiency of the heat transfer from the cable to the cooling bath is described by their steady-state temperature difference as a function of the heating power in the instrumented cable. The measurements were performed under different conditions of applied pressure and heating configuration. Only the most significant results are reported in the following.

Three out of the nine installed thermocouples (no. 5, 6 and 7) survived up to a pressure of 50 MPa, whereas only TCJ no. 5 and 6 could withstand larger compressive loads. As long as the temperature of the helium inside the cable was below T_λ , all of them measured the same temperature. This can be seen in Fig. 3.16 and is a consequence of the real shape of the cable. The superfluid helium fills indeed the interstices among the strands, thus allowing to obtain an uniform temperature in the cable. The good reproducibility of the results for these temperature levels also gives confidence in the sensor mounting and installation.

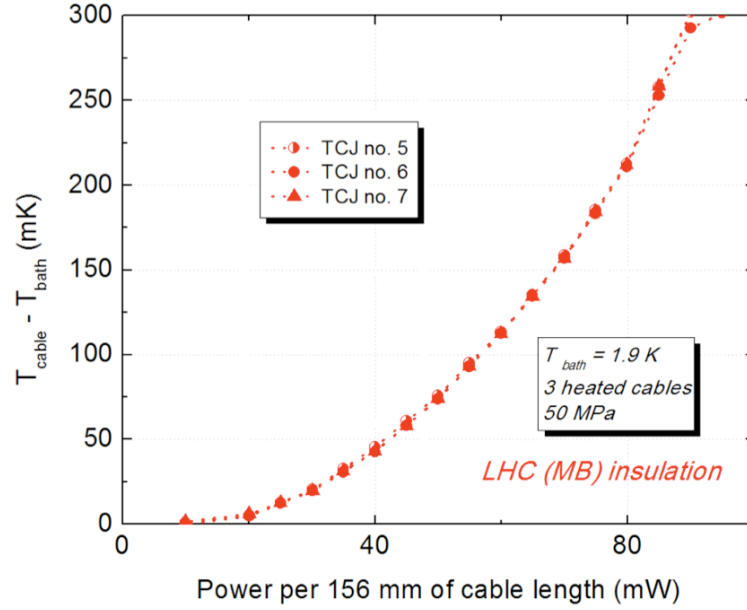


Figure 3.16: Temperature rise of central cable vs. heat load for the LHC (MB) insulation in 1.9 K He II bath. Comparison of the measured thermocouples below a temperature rise of 300 mK. The lines are a guide to the eye.

The non linear shape of the heat transfer curves is the signature of heat extraction occurring non only through solid conduction across the insulation tapes, but also through He II paths. These paths can be identified as micro-channels connecting the helium inside the conductor to the helium bath. This issue will be qualitatively addressed in section 3.4.4, whereas a quantitative analysis will be provided in chapter 6.

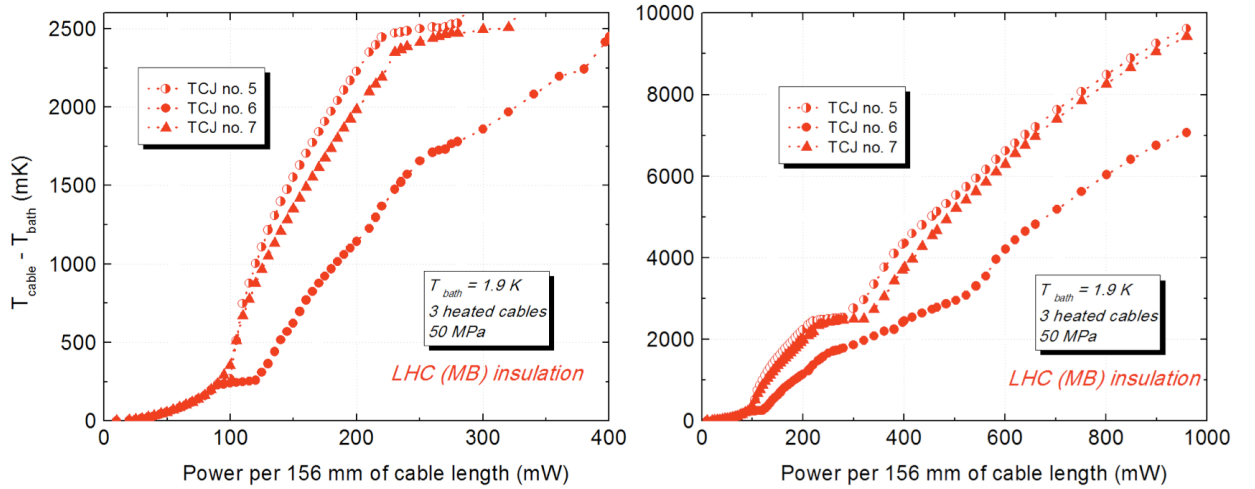


Figure 3.17: Temperature rise of central cable vs. heat load for the LHC (MB) insulation in 1.9 K He II bath. Comparison of the thermocouples signal in the whole measured temperature range. The lines are a guide to the eye.

The helium and polyimide heat extraction mechanisms can be considered in parallel as a first approximation. Polyimide solid conduction is always present, whereas the helium

contribution is strongly affected by the temperatures and heat fluxes. Depending on the helium phase, the helium heat transfer can feature degradation in certain temperature (or heat flux) ranges. In such situations the polyimide conduction mechanism becomes predominant.

As soon as the temperature of the helium inside the cable overcomes T_λ , temperature gradients develop in the cable. This is shown in Fig. 3.17, on the left up to a temperature difference of 2.6 K and on the right for the whole measured temperature range. The change of heat transfer regime can be observed in the reported plots at a temperature difference slightly above 300 mK, because the measured temperature is higher than that of helium.

TCJs no. 5 and 7, both located in the middle of the cable, show a similar behavior. Above the λ transition their recorded temperature suddenly increases, as expected, because of the worsened heat transfer properties of normal liquid helium. The heat transfer mechanism is now dominated by solid conduction rather than helium. This is confirmed by the almost linear curve behavior, typical of the Fourier law. At a temperature difference of around 4.3 K TCJs no. 5 and 7 show a plateau due to the increased heat removal in the nucleate boiling regime. Their subsequent temperature increase is due to film boiling formation on the heated surface, corresponding to a large thermal resistance.

The behavior of TCJ no. 6 differs from the others. It is located close to the cable edge, thus featuring a better cooling. When the helium in the middle of the cable undergoes the λ transition, the cooling of the cable edges is still important and the heat flux extracted from there has not yet reached the critical heat flux. The helium in the cable edges is still superfluid even for the higher heat flux due to the developed temperature gradient between middle and edge of the cable. This results in a plateau of TCJ no. 6, as long as the critical heat flux is not exceeded. Once that happens, we can observe a sudden temperature increase also in TCJ no. 6. For a higher heat flux of around 250 mW, TCJ no. 6 is influenced by the nucleate boiling phenomenon occurring in the middle of the cable. That makes reducing the slope of its curve. Finally it can be observed that no plateau is associated to the nucleate boiling transition, and the worsening of heat transfer due to film boiling occurs at a higher temperature with respect to the other sensors. The reason could be a small quantity of helium in the cable edge, and a larger thermal resistance of the TCJ no. 6 varnish insulation.

In the following sections we will refer to TCJ no. 5, unless specified otherwise.

3.4.1 Effect of mechanical pressure

Fig. 3.18 and 3.19 report the measured heat transfer curves for several applied pressure levels, up to a of temperature rise of 300 mK and 3 K, respectively. The power indicated on the x-axis refers to the central cable, while three central cables were heated up simultaneously.

The applied pressure affects the heat transfer occurring in the cable large faces. The higher the applied pressure is, the lower is the heat transfer. This proves that the helium penetrating the void spaces between adjacent cables plays a role in the cable cooling, and that the cable large face does not only provide solid conduction towards adjacent cables. Such effect is more evident at low pressures. As it will be clear from the mechanical results (section 3.6), the cable is softer in these conditions, hence its porous structure undergoes a large size reduction. The specific heat transfer mechanisms will be identified through

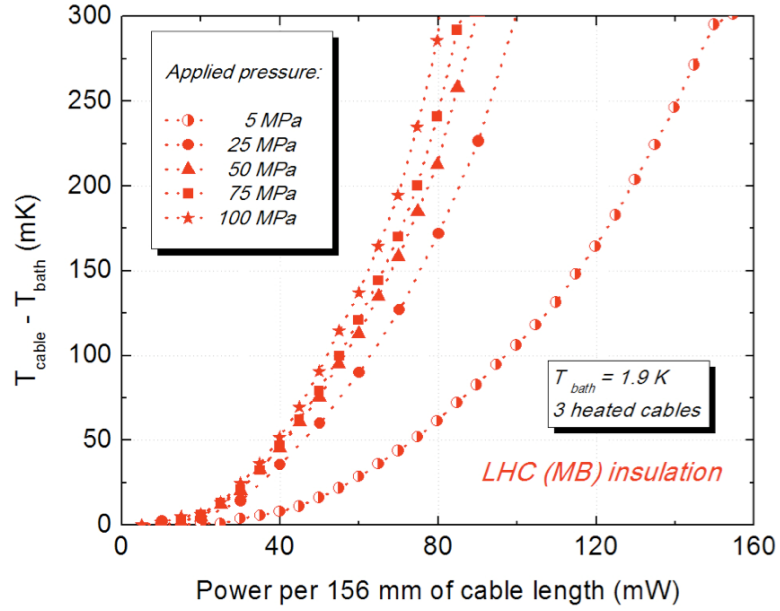


Figure 3.18: Temperature rise of central cable vs. heat load for the LHC (MB) insulation in 1.9 K He II bath. Comparison of different applied pressures below a temperature rise of 300 mK. The lines are a guide to the eye.

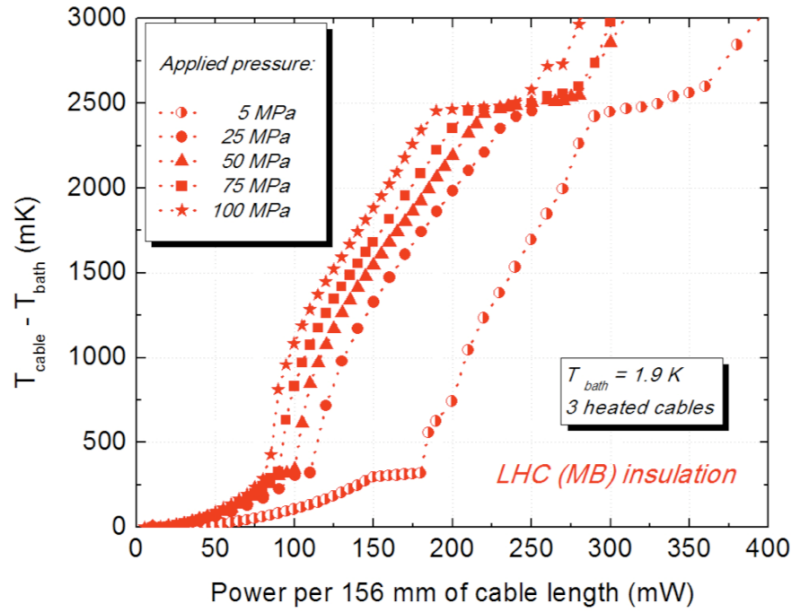


Figure 3.19: Temperature rise of central cable vs. heat load for the LHC (MB) insulation in 1.9 K He II bath. Comparison of different applied pressures below a temperature rise of 3 K. The lines are a guide to the eye.

modeling of the experimental system, as described in chapter 5.

The same effect of the applied pressure was not appreciated in previous stack measurements. A small impact was observed in [52], but the tested cable insulation was not comparable with the LHC type, since it featured fiberglass tapes pre-impregnated with epoxy resin. The insulation tested in [54] was instead similar to the LHC one, but no

impact of the applied pressure was found. The reason was the considerable epoxy flow during curing which blocked the void spaces between the insulation tapes, thus preventing superfluid helium from filling them. This was confirmed by the larger cooling potential of insulations with a reduced amount of epoxy. An analogous problem of blocking of insulation cooling channels was observed at FNAL, US, during the thermal qualification of the LHC MQXB interaction region quadrupole [65].

It can be concluded that the LHC (MB) insulation takes advantage of the research work done by CERN and Kaneka High-Tech Materials on the coating glue [29]. The drastic reduction of glue flowing mentioned in section 2.4 is a necessary condition for the permeability to helium, especially on the cable large faces.

In fig. 3.19 a plateau around T_λ can be noticed. It is more evident for the 5 MPa curve. Such behavior was already observed in [54]. It is probably due to a cooling path between TCJ and bath, more open in case of small pressure level. In our measurements these plateaux often end when boiling phenomena happen in other cable locations, making somehow easier to reach the critical heat flux. This thesis mainly deals with the He II heat transfer and underlying thermal mechanisms, whereas phenomena occurring in the vicinity and above T_λ would require further investigations.

The effect of the applied pressure on the heat extraction from the cable is important in view of the magnet operation. Depending on its position in the coil cross-section, each cable will be subjected to a different level of applied pressure after current powering. However the applied pressure is not the only mechanical phenomenon influencing the heat exchange in the coil. Other examples are the plastic deformation due to the peak pressure and to creep (reported in section 4.5.1), as well as the curing cycle. These aspects will be addressed in section 3.6 from the mechanical standpoint.

3.4.2 Localized vs. distributed heat deposition

Measurements carried out in symmetric heating configuration with one heated cable showed a more efficient heat extraction than for three or five heated cables. They represent a localized vs. a distributed heat deposition, respectively. The results are shown in Figs. 3.20 and 3.21.

Below a temperature rise of 300 mK (Fig. 3.20), the heat extraction in case of one heated cable is significantly larger than for three or five heated cables, whereas the curves for three and five heated cables are very close to each other. When the adjacent cables are not heated, the heat transfer in the cable large faces increases both through polyimide solid conduction and through the helium micro-channels. At a fixed temperature rise, this increased heat extraction is larger than 50%. Therefore the channels formed by the 2 mm space in the third insulation layer do not constitute a thermal short circuit to the bath.

Adjacent cables are instead thermally coupled, as shown also in the next section. These results constitute an essential input for modeling (chapter 5).

Above a temperature rise of 300 mK, the three curves feature different slopes related to the different amount of polyimide heat conduction (Fig. 3.21). In particular in the one heated cable case the heated cable can fully exploit its large faces to transfer heat to its adjacent cables, which explains the larger slope of the corresponding curve.

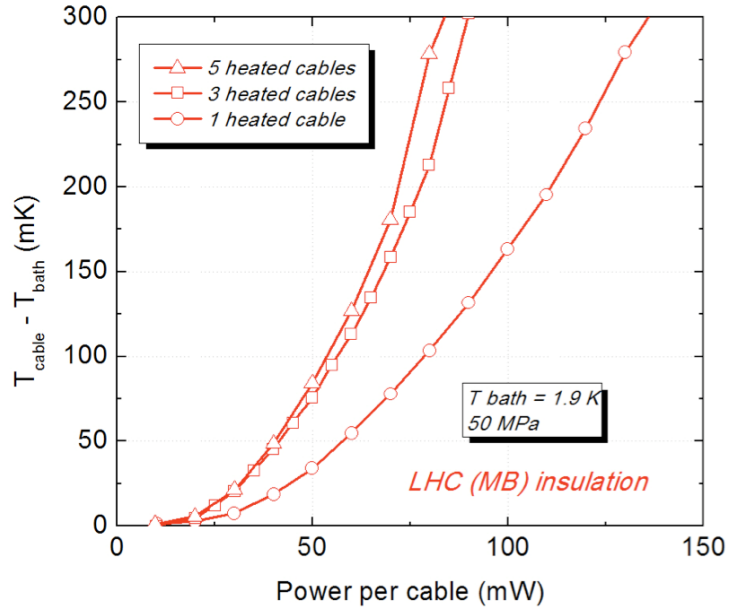


Figure 3.20: Temperature rise of central cable vs. heat load for the LHC (MB) insulation in 1.9 K He II bath. Comparison of different symmetric heating configurations below a temperature rise of 300 mK. The lines are a guide to the eye.

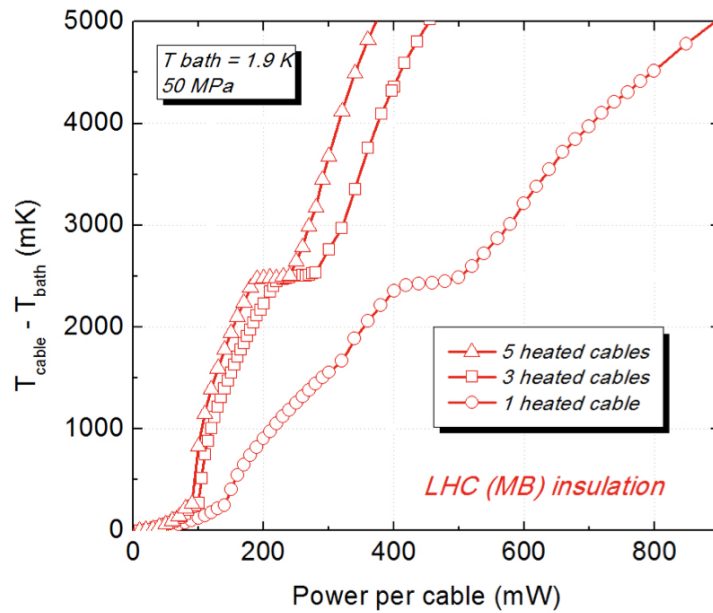


Figure 3.21: Temperature rise of central cable vs. heat load for the LHC (MB) insulation in 1.9 K He II bath. Comparison of different symmetric heating configurations below a temperature rise of 5 K. The lines are a guide to the eye.

3.4.3 Thermal coupling between cables

The measurement of the two heating configurations shown in Fig. 3.11 provides further information on the thermal coupling between adjacent cables. In the symmetric configuration the only instrumented cable is heated, whereas in the asymmetric one the

heated cable is adjacent to the instrumented one. As it can be observed in Fig. 3.22, the temperature rise of the heated cable at which the adjacent (not heated) cable starts to increase its temperature is around 235 mK. This is due to the heat removed by the large faces of the heated cable that is partly transmitted to the adjacent cables.

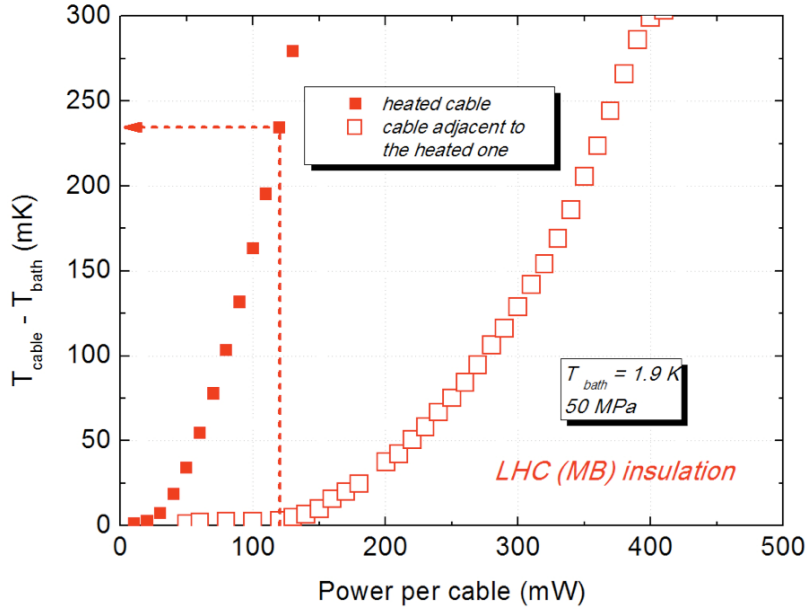


Figure 3.22: Temperature rise of the heated cable and of the adjacent one vs. heat load for the LHC (MB) insulation in 1.9 K He II bath.

3.4.4 Phenomenological analysis

In a two-dimensional simplification, heat is extracted from each cable through either the small or the large faces, as depicted in Fig. 3.23. The insulation is the same in the two cases but the mechanical conditions are different. No pressure is applied on the small faces, and the heat transfer in this direction (thermal resistance R_{sf}) occurs through He II paths and through polyimide solid conduction directly to the external helium bath. As far as the large faces are concerned, they are subjected to the pressure applied on the stack and are responsible for the coupling between adjacent cables. The He II and polyimide heat transfers cross in this case the cable insulation until the region between two insulated cables (R_{lf}). Part of the heat is evacuated towards the bath through the channels created by the spacing of the last insulation layer (R_{ic}), and part is evacuated towards the adjacent cable (R_{lf}). The anisotropy of the experimental system is evident. The details of the different heat transfer paths will be addressed in section 5.4.

The phenomenological analysis of the experimental results takes advantage of the He II heat transport laws presented in section 2.5, which are easily identifiable. In a temperature rise vs. heat load diagram, they are linear for small heat fluxes where the solid conduction is typically negligible (Landau regime). They are cubic elsewhere (Gorter-Mellink regime), recognizable from the linear solid conduction contribution [52].

Fig. 3.24 shows the experimental results of the LHC (MB) insulation in case of one heated cable, at an applied pressure of 50 MPa in 1.9 K bath. A logarithmic scale is

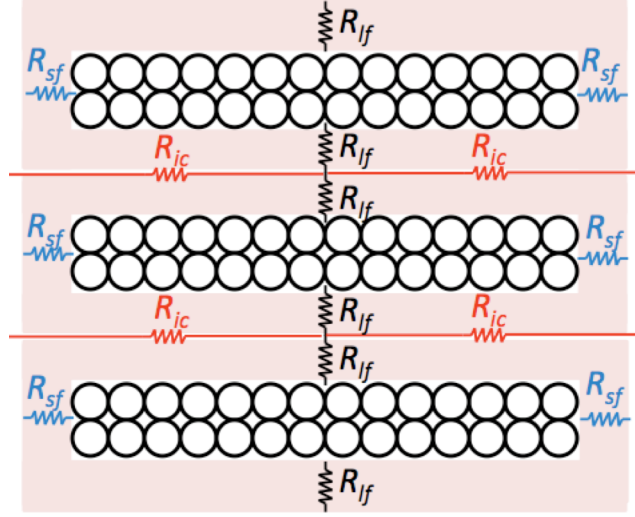


Figure 3.23: Simplified sketch of the stack thermal resistances.

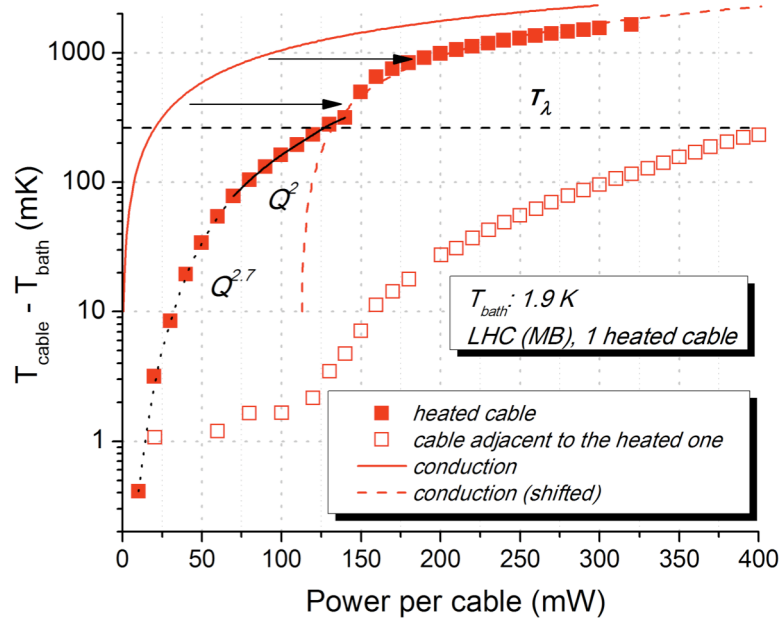


Figure 3.24: Temperature rise of central cable vs. heat load for the LHC (MB) insulation in 1.9 K He II bath. The corresponding temperature rise of the adjacent cable is also reported. The calculated conduction curve is shown, as well as the power laws fitting the measurements below 300 mK.

chosen to highlight the features of the heat transfer laws below and above the λ transition. Below T_{λ} the measurements can be reproduced by power laws whose exponent is related to the impact of mechanisms described by linear laws (polyimide conduction or He II laminar regime) on the overall heat transfer. The higher the exponent is, the more the measurements approach the He II Gorter-Mellink law. The effect of linear laws mechanisms is never negligible, because the exponent is always lower than 3. Furthermore, a sudden change of the exponent is identified, at around 65 mW. We believe that this is associated to the reduction of the relative weight of the Gorter-Mellink heat transfer, because of the decrease of the superfluid equivalent thermal conductivity above 1.95 K.

The (polyimide) conduction curve is also reported in Fig. 3.24, considered decoupled from the He II mechanisms. It is estimated in a simplified way, by neglecting R_{ic} and by assuming an uniform temperature in the cable cross-section also above T_λ . It is calculated as the sum of the contribution of the cable small faces towards the 1.9 K bath and of the cable large faces towards the adjacent cables, whose temperature is reported as well. The second contribution is more important because of the larger heat transfer surface. If shifted to the point where the abrupt rise in temperature associated to the λ transition occurs, the conduction curve reproduces fairly well the experimental data after this point. The solid conduction mechanism becomes dominant, that is confirmed by the corresponding temperature rise of the adjacent cable. However the He II mechanism is still present above T_λ , maybe because the only helium undergoing the λ transition is that close to the cable [66], or because of temperature inhomogeneity in the cable cross-section.

3.5 Electrical measurements

The electrical tests were performed in air on two-units stacks made of the superconducting inner layer cable of the LHC main dipoles. The stacks were cured according to the 130 MPa curing cycle (Fig. 3.2 (left)). As shown in Fig. 3.25 (left), a compressive pressure was applied in the middle of the sample, over 113 mm. During the tests the relative humidity was between 23 and 30%, at a temperature between 24.4 and 26.1 °C.

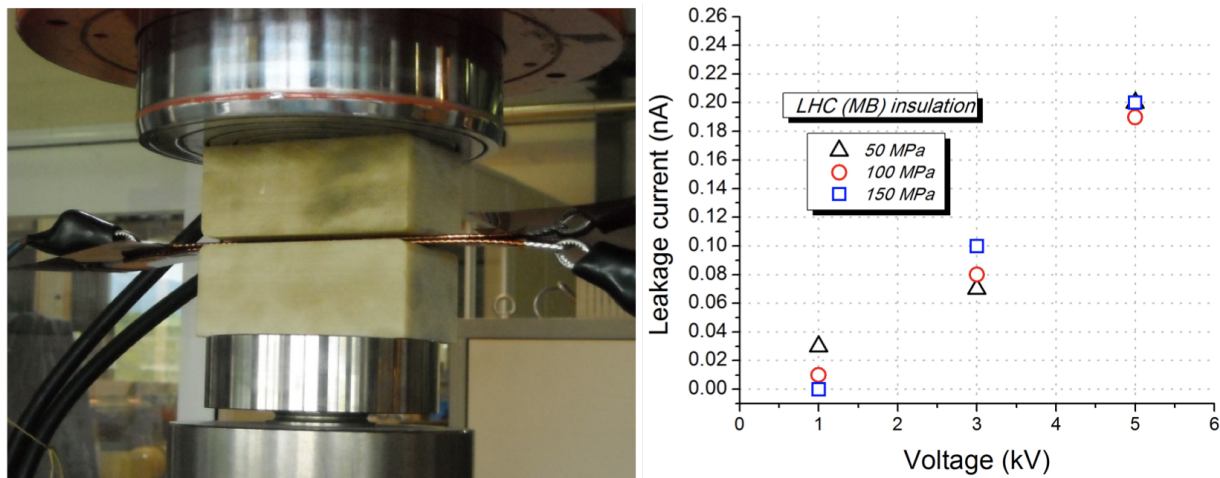


Figure 3.25: Experimental setup for dielectric measurements (left). Leakage current for the LHC (MB) insulation, at applied pressures of 50, 100 and 150 MPa (right).

Measurements of dielectric strength were performed under a compression of 80 MPa. The tests were repeated three times. Only for one sample the discharge occurred in the compressed zone, at 18 KV. For the other samples it took place outside the compressed area, in a region of mechanical discontinuity, despite the cables at the sample extremities had been separated by an insulated foil. The dielectric strength was in these cases 22 KV, but this must be considered a conservative minimum. These results are in agreement with previous tests [67].

Measurements of the inter-turn leakage current were also performed, at different compressive pressures of 50, 100 and 150 MPa. The leakage current was recorded two

minutes after the application of voltages of 1, 3 and 5 KV. Its value was found to be always extremely small, as shown in Fig. 3.25 (right), one or two orders of magnitude lower than 1 nA in all cases.

3.6 Mechanical measurements

The mechanical characterization of the cable insulation is needed for the mechanical and magnetic design of the magnet. Tests were performed to investigate the insulation thickness under load, the stack elastic modulus and the stress relaxation at ambient temperature. The experimental setups and the representative results are discussed in the following sections.

The first two information were obtained by stress-displacement measurements, which establish the azimuthal oversize of each coil layer under a chosen pressure. They help to optimize the size of the compacted coil during curing, in order to make sure that the cable insulation thickness will be nominal under operational conditions of the magnet.

The stress relaxation test is realized to evaluate the stress loss due to insulation creep mechanism. Such information is needed to set the coil pre-stress at the end of the collaring process, that is applied in order to mitigate the impact of the electro-magnetic forces on the coil. These forces are directed towards the mid-plane and outwardly. They tend to separate the coil from the pole and compress the mid-plane region. The application of a pre-stress minimizes then the cable motion during excitation.

The samples used were ten-units stacks. They were made of either the inner or the outer layer cable of the LHC main dipoles, called cable 01 or 02 respectively [2]. Their geometric parameters are recalled in Table 3.2. Cable 02 is more compacted than cable 01 and the two cables constitute different substrate to the insulation, affecting its behavior. The cables were insulated according to the LHC MB and MQ schemes, whose parameters are reported in Table 3.1. The stacks were cured according to one of the two bonding cycles described in section 3.3.2 (Fig. 3.2), to a pressure of either 80 MPa or 130 MPa. The two curing pressures were used in order to identify possible effects of this parameter on the final characteristics of the cured stack and they represent a lower and upper limit, respectively. Therefore four stacks were prepared for each insulation scheme. Four more stacks made of bare cables were prepared, made as well of type 01 and 02 cables and cured according to each of the two bonding cycles.

3.6.1 Insulation thickness

The used experimental apparatus allows to compress a stack of cables with a manual press and to measure the pressure and displacements at ambient temperature. The stack was held in the groove of a steel mold and loaded in compression along the vertical direction through a 120 mm long steel upper bar (Fig. 3.26 (left)). The vertical direction is perpendicular to the cables large face and corresponds to the azimuthal direction in the coil. No loads or constraints were applied in the horizontal direction (the lateral spacers shown in the picture were used to position the sample, then removed not to prevent its lateral expansion). The pressure was measured with a sensitivity of 1 MPa. The displacement was measured and averaged through four displacement indicators, with a sensitivity of 1 μm , between the upper surface of the mold and a surface tied to the upper bar. During

the measurements the pressure was increased until a peak value of 100 MPa, then reduced to zero.

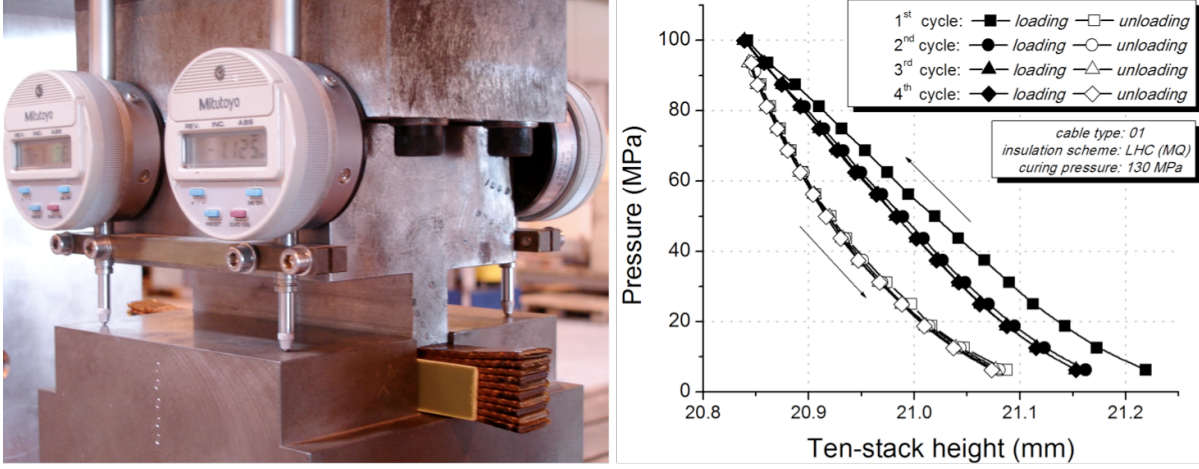


Figure 3.26: A cable-stack being compressed in the measuring device (left). Pressure as a function of the stack height, monitored during four successive cycles (right). The considered stack is made of type 01 cables wrapped with LHC MQ insulation, cured at 130 MPa.

Fig. 3.26 (right) shows the evolution of the stack height versus the applied pressure for successive compression cycles, showing that the first loading on a virgin stack is very different from the subsequent ones. The hysteresis that the curve exhibits between loading and unloading evolves from cycle to cycle, stabilizing after three cycle. The results reported in the following refer to at least the last of three cycles performed up to the same peak pressure. Furthermore, at the end of the unloading part of each cycle the contact between the stack and the steel bar used to compress it was lost, in order to allow a complete relaxation of the stack. This is needed to obtain a good reproducibility of the loading curve, as proven in [68]. The raw measurements were corrected taking into account the mold deformation, measured compressing a reference steel bar of known Young modulus.

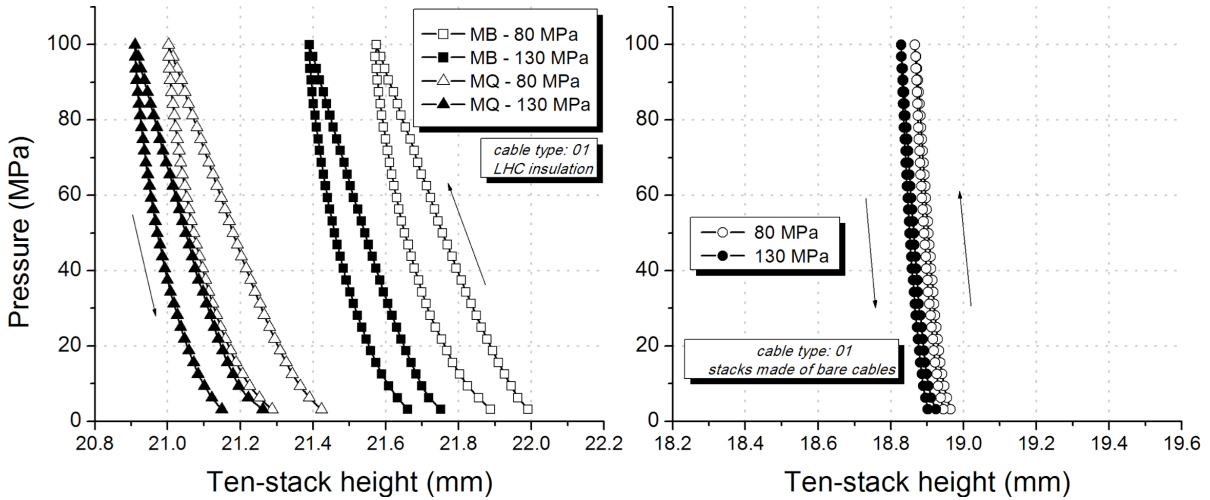


Figure 3.27: Applied pressure vs. height of stacks made with the LHC insulations (left), and of stacks made of bare cables (right). The considered stacks are prepared using cable 01 and both curing cycles.

Fig. 3.27 (left) shows the applied pressure vs. height of stacks prepared with the MB and MQ insulation schemes, using cable 01 and both curing cycles. The results present the same nonlinear hysteretic behavior observed in previous works [68] [69]. The behavior is different in the loading and in the unloading branches. The loading phase features a smaller slope, and the stack rigidity increases with stress. The hysteresis depends on the peak pressure reached during the compressive phase, as it will be shown in section 3.6.3. The effect of a larger curing pressure (130 MPa) with respect to a smaller one (80 MPa), which is obviously to reduce the stack height, is here quantified.

The measurement of stacks made of bare cables, shown in Fig. 3.27 (right), allowed to determine the insulation thickness on the cable large face. This was obtained subtracting the height of the bare cables stacks from that of the corresponding insulated cables stacks, then dividing by 20. Fig. 3.28 shows the pressure vs. insulation thickness curves for MB and MQ, for different curing cycle (left) and different cable (right). A common feature of all the tested samples is the thickness reduction mainly occurring at low pressures. This is in agreement with the observation of a larger worsening of the heat transfer through the cable insulation between 0 and 50 MPa than between 50 and 100 MPa (section 3.4.1). The curing pressure has the already mentioned effect. As for the impact of the cable type, the insulation is thicker if wrapped around cable 02 with respect to cable 01. This is due to the different strands number and dimensions (Table 3.2), which affect the void spaces in the cable and make cable 02 more compacted than cable 01.

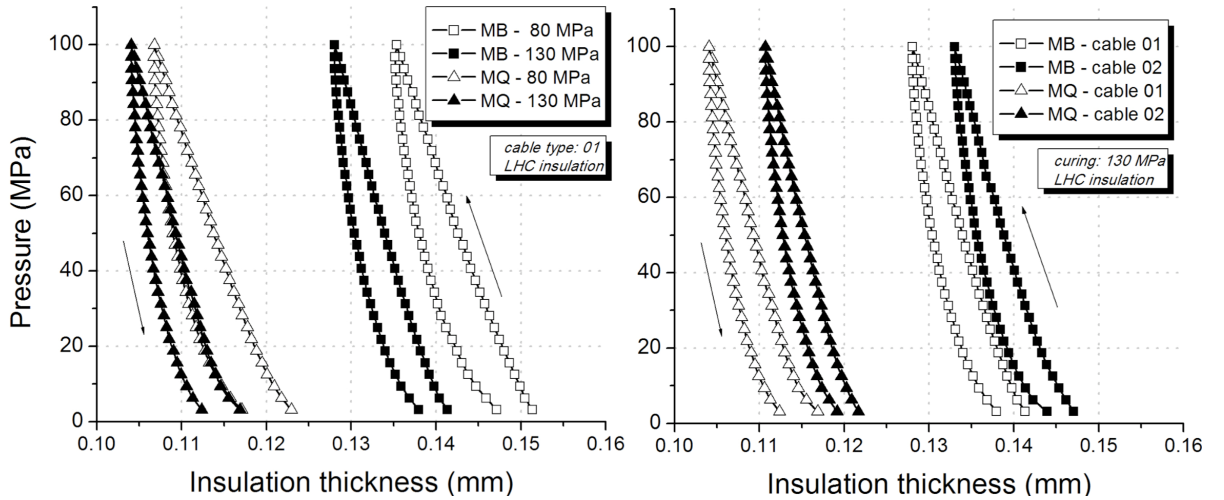


Figure 3.28: Applied pressure vs. thickness of the LHC insulations, for different curing cycles (left) and different cables (right).

The thickness values at the reference pressure of 50 MPa on the unloading branch are summarized in Table 3.4. It is worth reminding that these values were obtained in case of a peak pressure seen by the stacks of 100 MPa. They are compared to the geometrical thickness, i.e. the sum of the thickness of the insulation tapes. It can be remarked that:

- the loss in thickness (between geometrical and measured one) is higher for samples cured at 130 MPa vs. samples cured at 80 MPa, by about 2-4 μm ;
- the loss in thickness is higher for cable 01 than for cable 02, by about 5-10 μm , due to the higher compaction of cable 02.

Insulation scheme	Cable type	Curing pressure (MPa)	Geometrical thickness (μm)	Measured thickness (μm)
MB	01	80	169	138
MB	01	130	169	130
MB	02	80	169	140
MB	02	130	169	136
MQ	01	80	142.5	109
MQ	01	130	142.5	105
MQ	02	80	142.5	115
MQ	02	130	142.5	113

Table 3.4: Measured insulation thickness of the LHC insulation schemes, at 50 MPa compression during the unloading phase. The peak pressure of the cycle is 100 MPa.

3.6.2 Elastic modulus

The elastic modulus at room temperature E of the different stacks was calculated from the stress-displacement curves reported in the previous section. It is computed as $E = d\sigma/d\epsilon = (d\sigma/dl)l_0$, where σ is the applied pressure, ϵ the strain, l the stack height under pressure and l_0 the unloaded stack height. In agreement with [70] and [71], l_0 is defined as the stack height at a small pressure on the loading curve (0.6 MPa in our case).

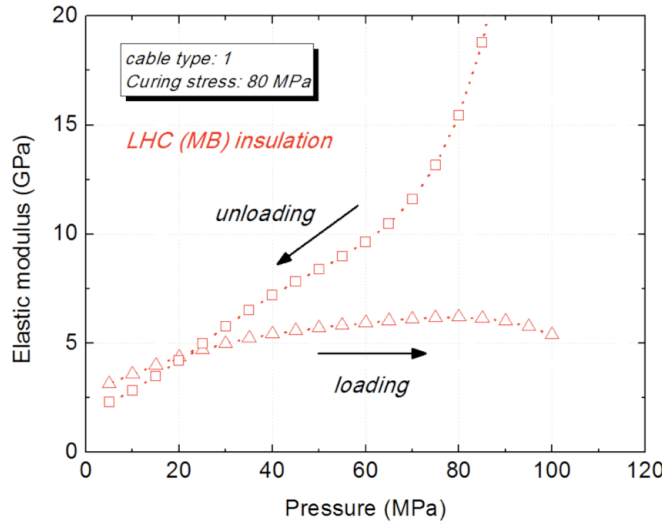


Figure 3.29: Stack elastic modulus vs. pressure for the loading and unloading branches of the LHC (MB) insulation scheme.

Fig. 3.29 shows the elastic modulus during the loading and unloading curves of the stack made of cable 01, LHC (MB) insulation, cured at 80 MPa. As observed in section 3.6.1, the stack is softer at low pressures during loading, where small pressure changes cause large displacements. An increase of the elastic modulus until 6.2 GPa can be indeed observed during the loading phase, up to a pressure of 80 MPa. It slightly reduces for higher pressures. The elastic modulus during the unloading phase is much larger than

during the loading phase. It reaches values of the order of 15 GPa at a pressure of 80 MPa. These results are in agreement with previous works [68]. It should be noticed that the elastic modulus during the unloading phase depends on the peak pressure. For the same load, at higher peak pressure of the cycle corresponds a smaller elastic modulus [68]. The curves reported here refer to a peak pressure of 100 MPa.

3.6.3 Stress relaxation

The aim of this campaign is to compare the profile of pressure losses on the cable stacks due to the polyimide creep. The knowledge of this pressure loss, together with those due to collar elastic stretching and to differential thermal shrinkage between coil and collars during cool down, is needed to set the collaring load in order to obtain the desired pre-stress.

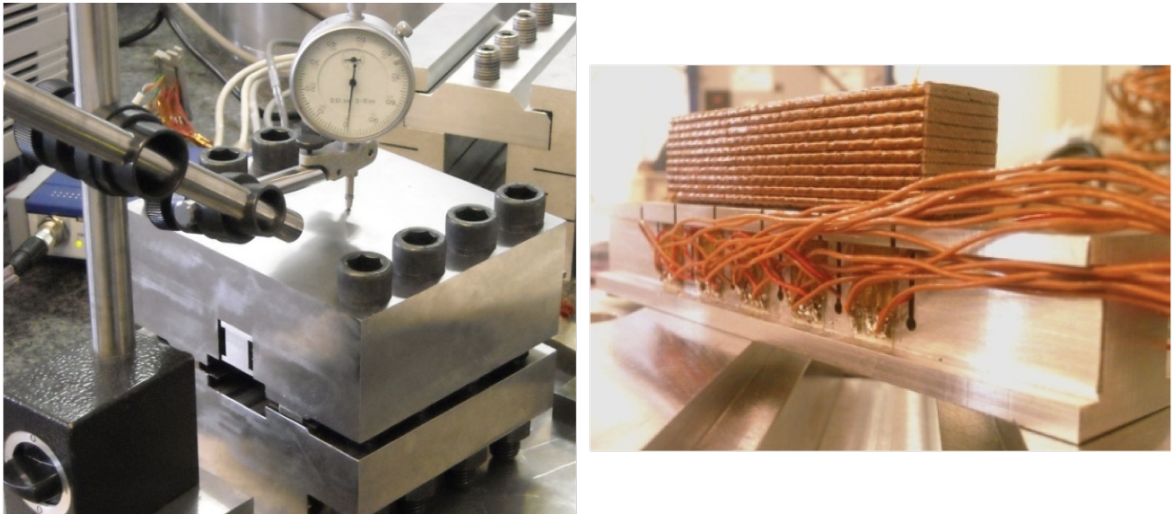


Figure 3.30: Experimental setup for stress relaxation measurements (left). Detail of the instrumented bar (right).

A test set up was designed and built as shown in Fig. 3.30. The force was applied on two series of four bolts and the pressure was measured via five pairs of mechanically independent strain gauges over a length of 80 mm. Continuous data acquisition of the five pairs was performed. Fig. 3.31 shows a typical curve of stress measurement as a function of time. The largest loss (90% of the total) takes place during the initial ten days after the application of the force (70% after the first day). Further 3% of the initial pressure is lost in the following five weeks, and further 3% would be lost for week 10. We can conclude that measurements up to ten days duration provide good indication of the global stress relaxation behavior, allowing a comparison among different insulation schemes.

Table 3.5 provides the percentage losses for the MB insulation for three different initial peak pressures p_{max} . Measurements refer to cable type 01. The percentage losses after one, five and ten days are quite constant with respect to the initial peak pressure. This important feature allows scaling the losses to the same peak pressure for tests that did not undergo the same initial pressure. Scaling was performed among measurements that took place in a range of maximum 20 MPa.

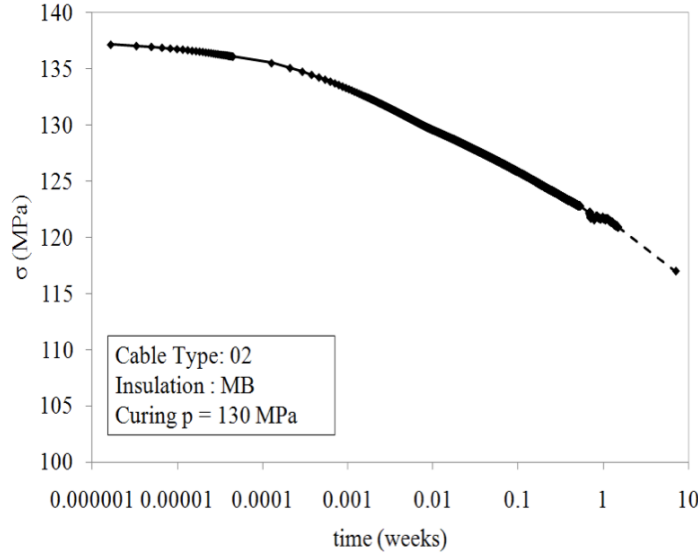


Figure 3.31: Time evolution of the stress relaxation.

p_{max} (MPa)	$\Delta p/p_{max}$ 1 day (%)	$\Delta p/p_{max}$ 5 days (%)	$\Delta p/p_{max}$ 10 days (%)
96	21	24	25
118	23	27	28
130	22	25	27

Table 3.5: Stress relaxation as a function of the initial peak pressure p_{max} for the LHC MB insulation wrapped around cable 01.

The pressure loss for the MB insulation scheme features significant differences whether wrapped around cable 01 or 02. In case of cable 01, the loss after 10 days is 33 MPa. This value is considerable, if compared to other insulation schemes. The experiment was repeated using a completely new sample stack and the results of the second experiment confirmed the first ones. A much smaller loss of 13 MPa is observed in case of cable 02, which is probably linked to the larger compactness of cable 02. We will recall these results in section 4.7.3, in comparison with the behavior of other insulation schemes. The influence of the curing pressure on the stress relaxation will be described there as well.

The use of a collar structure makes it very probable that coils will be submitted to higher pre-stress during the collaring process with respect to that at which they will be stored and from which the stress relaxation will start. We wanted therefore to investigate the effect of this kind of cycle from the stress relaxation point of view. The following testing sequence was adopted to simulate the coil life (Fig. 3.32):

- (a) three cycles up to 100 MPa, the last of which is reported ($\sigma_{max} : 100 \text{ MPa}$);
- (b) three cycles up to 120 MPa, the last of which is reported ($\sigma_{max} : 120 \text{ MPa}$);
- (c) one cycle up to 110 MPa and one cycle up to 100 MPa, both reported in the figure ($\sigma_{max} : 120 \text{ MPa}$);

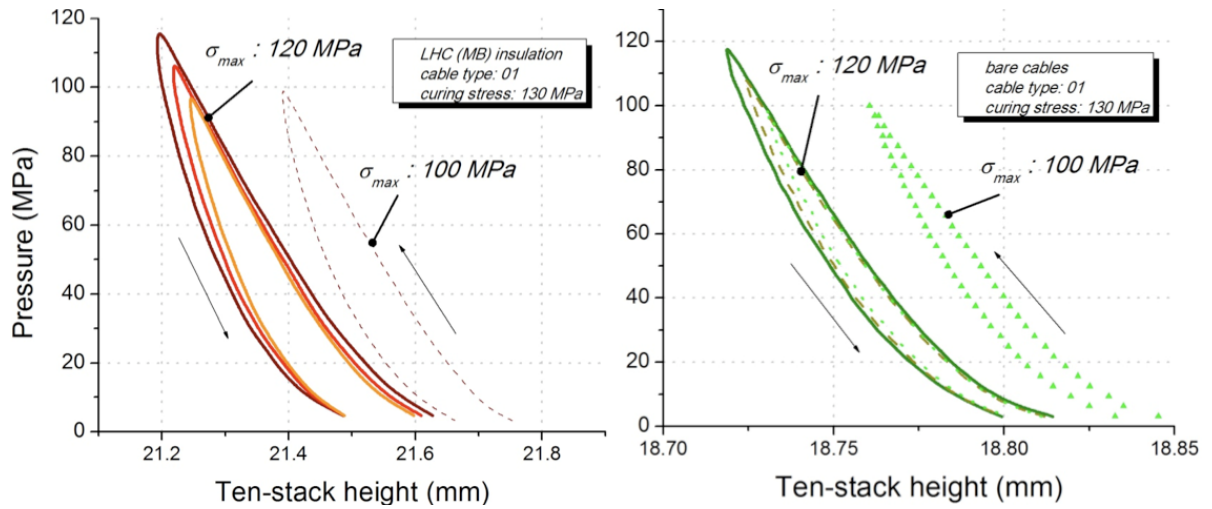


Figure 3.32: Pressure vs. height for different values of the maximum pressure σ_{max} seen by the samples. The LHC MB insulation is considered on the left, whereas a stack made of bare cables is considered on the right.

Two preliminary cycles were performed every time the peak pressure was exceeded. They are needed for the mechanical training of the sample, as shown in Fig. 3.26 (right). Fig. 3.32 (left) reports the results for the MB insulation. We can remark that the pressure - height curve is stable (after at least two training cycles) if the peak pressure is not exceeded. If this happens a plastic shift takes place. If the cycle is performed up to a maximum pressure that does not exceed the peak pressure, the loading branches of the different cycles nearly superpose (as in all the cycles performed up to a σ_{max} of 120 MPa).

The same cycle was applied to a stack made of bare cables. The results are reported in Fig. 3.32 (right). All the features shown in Fig. 3.32 (left) are present, including the shift between the first and the other cycles. On the other hand the shift is smaller. The amplitude of the hysteresis cycle, which is a measurement of the power dissipation, is also smaller. It can be concluded that the friction among strands plays an important role in the stack behavior, amplified by the presence of insulation.

3.7 Conclusion

The developed experimental program that was described in this chapter allowed to understand and quantify a number of thermal features of the LHC cable insulation. The results of the tests highlighted the important role of superfluid helium. It penetrates inside the cable through the insulation porous structure, making the cable temperature uniform below T_λ . This constitutes an input for the model of the insulation that will be described in chapter 5. The superfluid helium heat transfer constitutes a significant mechanism for heat extraction. Such mechanism can be further exploited, as it will be shown in the next chapter. Thermal gradients develop in the cable cross-section above T_λ , where the middle and edge of the cable show different cooling characteristics. These characteristics will be used in chapter 7 to identify the most thermally unstable regions of the magnet. The mechanical pressure applied on the sample affects the heat transfer mechanisms in the cable large faces and can considerably reduce the heat extraction. This

observation proves the non negligible role of the cable large faces. The measurement of different heating configurations allowed to quantify the existence of a good thermal coupling between adjacent cables.

The electrical and mechanical characterizations presented at the end of the chapter constitute a benchmark for the development of new insulation schemes, as shown in the next chapter. The setup developed to measure the stress relaxation allowed to observe that the largest pressure losses take place during the first days after the application of the initial force, and that the relative losses can be considered independent with respect to the initial peak pressure. A different behavior was observed depending on the compactness of the superconducting cable around which the LHC insulation was wrapped. It was also shown that the peak stress seen by the coil during its life is an important parameter to be taken into account in setting its working point.

Chapter 4

Development and characterization of a thermally enhanced insulation for the High Luminosity (HL) - LHC

Contents

4.1	Introduction	55
4.2	Background notions	56
4.3	The HL-LHC insulation	56
4.4	Experimental program	58
4.5	Heat transfer results	59
4.5.1	Effect of mechanical pressure	60
4.5.2	Localized vs. distributed heat deposition	63
4.5.3	Thermal coupling between cables	66
4.5.4	Improved HL-LHC insulation	66
4.5.5	Phenomenological analysis	67
4.6	Electrical measurements	68
4.7	Mechanical measurements	69
4.7.1	Insulation thickness	69
4.7.2	Elastic modulus	71
4.7.3	Stress relaxation	72
4.8	Conclusion	74

4.1 Introduction

Superconducting magnets having to withstand larger heat loads than in the current LHC operation need more efficient heat extraction from the coil. This is the case of the inner triplets of the High Luminosity LHC (HL-LHC) upgrade project [18][72], which will replace the existing low- β quadrupole magnets in the ATLAS and CMS insertion regions [7] [17].

This chapter is devoted to an innovative concept of cable electrical insulation, hereafter referred to as HL-LHC, that is proposed to improve the thermal performance of Nb-Ti

coils. It aims at better exploiting the cooling potential of He II, while preserving electrical protection.

We describe the HL-LHC features and the systematic investigations performed with the experimental program described in the previous chapter. The results of heat transfer measurements in superfluid helium bath of different variants of HL-LHC insulations are presented and compared to those obtained on the LHC insulation, as reference. Several mechanical conditions and heating configurations are considered, and the underlying thermal mechanisms are highlighted.

The results of the electrical and mechanical tests are reported as well. They complete the qualification of the HL-LHC insulation and are needed for the mechanical and magnetic design of future magnets.

4.2 Background notions

The existence of a margin to increase the heat transfer with respect to the LHC insulation had been already shown in the past. Wrapping all the insulation tapes in the same direction allows to reduce the average length of the helium slits, providing twice the heat extraction of the LHC insulation [28]. Another possibility is drilling holes in the cable small faces, as proposed in [52] and [73]. Although this insulation scheme would not fit the LHC electrical requirements, measurements in He II bath demonstrated that an important increase of the heat transfer can be obtained through the holes, especially for small temperature rise [52].

The HL-LHC concept differs from the mentioned attempts. The layout of the scheme and the role of the insulation tapes are radically changed with respect to standard insulations. In particular the overlapped wrapping of the first two tapes is eliminated, since it constitutes the main thermal resistance. The idea is to create bare regions of cable thanks to a specific tapes overlap, while providing dielectric insulation. These bare regions are located on the four cable faces. They are coupled to large channels, aimed at efficiently cooling the strands. More details are provided in the next section.

4.3 The HL-LHC insulation

The HL-LHC insulation scheme, also referred to as Enhanced Insulation (EI), is shown in Fig. 4.1. As the LHC insulation it is made of three wrapped polyimide tapes, but with different function as explained below. The geometric parameters of four variants of HL-LHC schemes (EI4, EI3, EI5, EI6) are listed in Table 4.1. The standard HL-LHC scheme is the EI4 one. Two more versions (EI1 and EI2) were mechanically characterized at the beginning of the experimental campaign [74], but not retained after the first screening. They featured the same geometric parameters as EI3 and EI4, except for the thinner third tape (55 μm).

All the three polyimide layers are wound with spacing. The electrical insulation is provided by the combined effect of the first and third tape, which are wrapped in the same direction. The second tape is cross-wrapped in the opposite direction with respect to the others. Its role is to avoid a direct overlap between them, thus providing cooling channels

HL-LHC insulation scheme	1 st tape	2 nd tape	3 rd tape
EI4	9 mm wide 1 mm spacing 50 μm thick	3 mm wide 1.5 mm spacing 75 μm thick 50% cross wrapped	9 mm wide 1 mm spacing 69 μm thick 50% overlap 1 st tape
EI3	9 mm wide 1 mm spacing 50 μm thick	3 mm wide 1.5 mm spacing 50 μm thick 50% cross wrapped	9 mm wide 1 mm spacing 69 μm thick 50% overlap 1 st tape
EI5	9 mm wide 1 mm spacing 50 μm thick	3 mm wide 0.5 mm spacing 75 μm thick 50% cross wrapped	9 mm wide 1 mm spacing 69 μm thick 50% overlap 1 st tape
EI6	4.5 mm wide 1 mm spacing 50 μm thick	3 mm wide 1.5 mm spacing 75 μm thick 50% cross wrapped	4.5 mm wide 1 mm spacing 69 μm thick 50% overlap 1 st tape

Table 4.1: Geometric parameters of the HL-LHC insulation schemes.

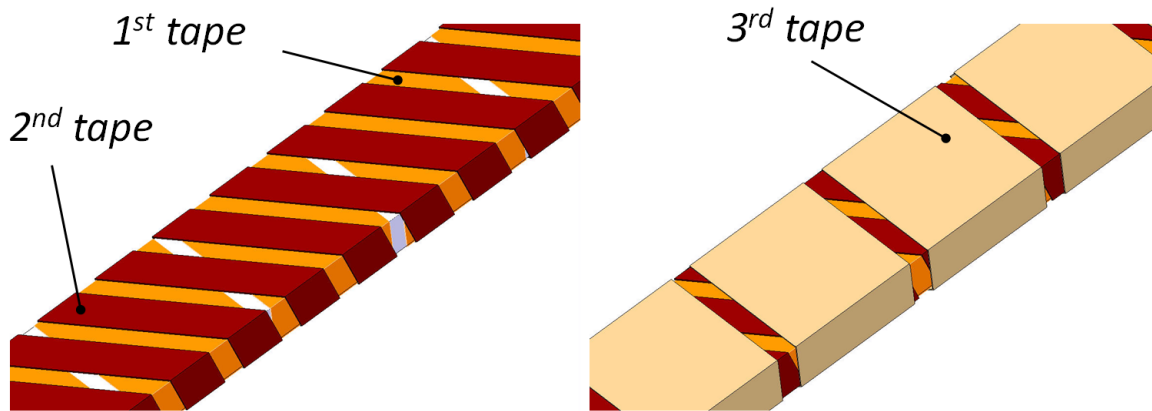


Figure 4.1: HL-LHC insulation scheme.

and dielectric insulation. As for the LHC insulation, the third tape features a thermally activated adhesive film on its external part, to provide mechanical stability to the coil.

The scheme evolved from the initial version [75] [76], to enable the automatic wrapping of commercially available tapes in a semi-industrial environment (Fig. 4.2 (left)). Fig. 4.2 (right) shows pictures of two insulation stages after wrapping of the second (top) and of the third tape (bottom).

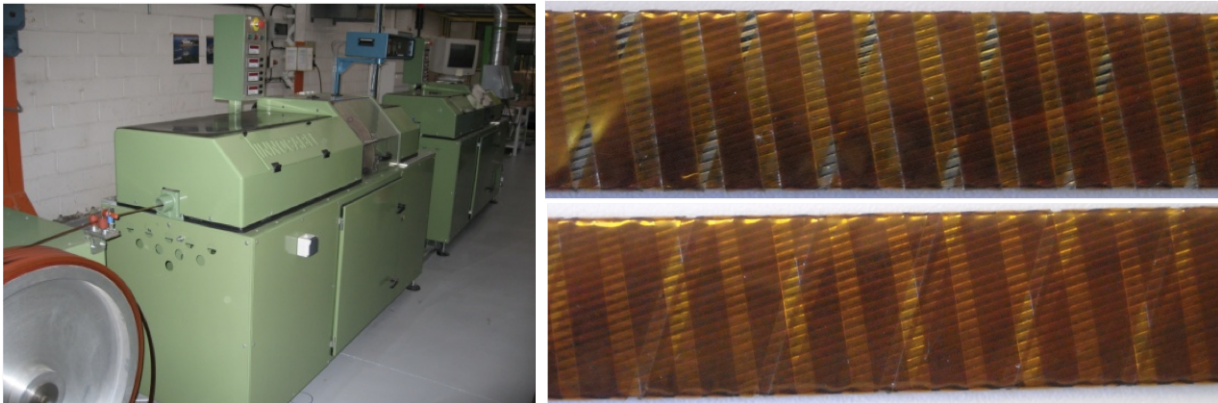


Figure 4.2: CERN insulating machine (left). Picture of a cable after wrapping the HL-LHC first two tapes (top right) and all the three tapes (bottom right).

4.4 Experimental program

The experimental program is the same as described in section 3.3. The samples were also prepared in the same way, except for the insulation schemes which are the HL-LHC ones described in the previous section. The top and side view of a cured HL-LHC (EI4) six-units stack are presented in Fig. 4.3.



Figure 4.3: Top and side view of a cured HL-LHC (EI4) six-units stack.

4.5 Heat transfer results

We report in this section the most significant results of the heat transfer tests performed on the HL-LHC insulation. All the eight thermocouple junctions (TCJs) installed in the EI4 sample could withstand the applied pressure. Their behavior is shown in Fig. 4.4 up to a temperature rise of 300 mK. As already observed for the LHC (MB) insulation, the temperatures measured by the different sensors coincide as long as the helium inside the cable is superfluid. The heat transfer curve behaves strongly non linearly, because of the presence of He II paths that will be discussed in section 4.5.5 and chapter 5.

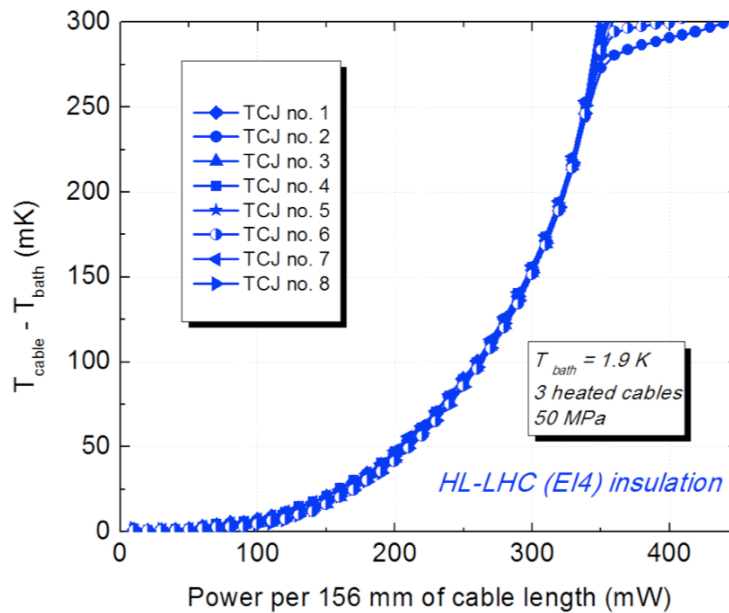


Figure 4.4: Temperature rise of central cable vs. heat load for the HL-LHC (EI4) insulation in 1.9 K He II bath. Comparison of the measured thermocouples below a temperature rise of 300 mK. The lines are a guide to the eye.

The temperature uniformity of the cable is lost as soon as the helium inside it undergoes

the λ transition. This can be observed in Fig. 4.5, on the left up to a temperature difference of 2.6 K and on the right for the whole measured temperature range.

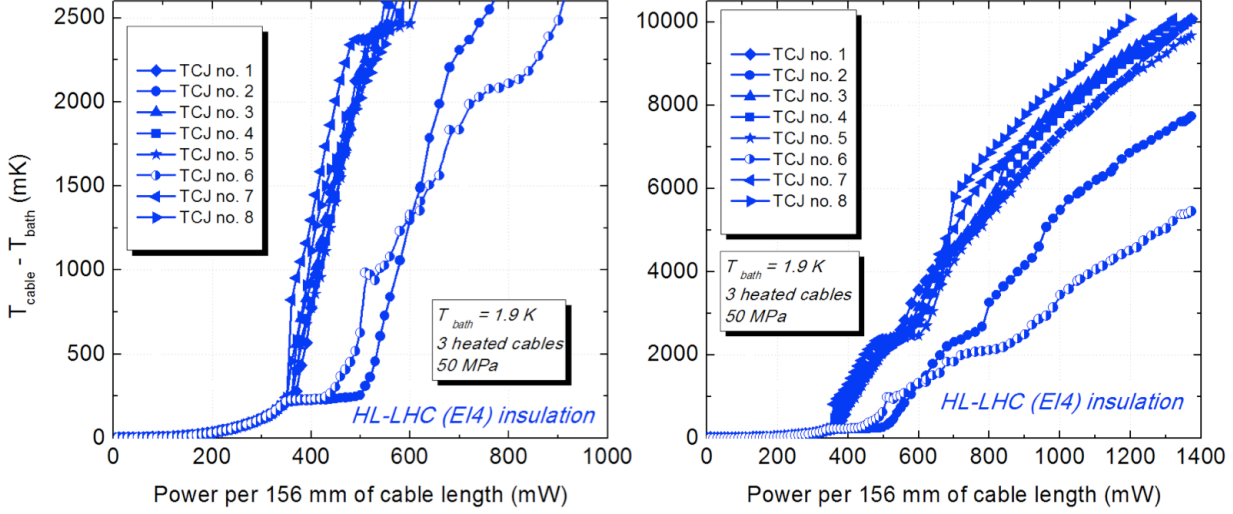


Figure 4.5: Temperature rise of central cable vs. heat load for the HL-LHC (EI4) insulation in 1.9 K He II bath. Comparison of the thermocouples signal in the whole measured temperature range. The lines are a guide to the eye.

The middle part of the cable features a different behavior than the edges. This was the case also for the LHC MB insulation, and many of the features described in section 3.4 can be observed here as well. All the TCJs located at an equal distance from the cable small faces behave similarly. After the sudden temperature increase following the He II to He I transition their heat transfer curve is governed by the solid conduction law, except for the plateau due to the boiling phenomena. The TCJs located in the cable edges (no. 2 and 6) are better cooled. They feature the already observed plateau around 300 mK. The following take off occurs at the same heat flux that induces nucleate boiling in the middle of the cable, which apparently contributes in “breaking” superfluidity. The behavior of TCJ no. 6 for higher heat fluxes is less regular. That might be due to alteration of the sample during sensor installation.

In the following we will refer to TCJ no. 5, unless specified otherwise, to allow a direct comparison to LHC insulation.

4.5.1 Effect of mechanical pressure

Fig. 4.6 shows the measured heat transfer curves of a sample insulated with the HL-LHC (EI4) insulation, up to a temperature rise of 300 mK. Several levels of applied pressure are considered, and the corresponding results of the LHC (MB) insulation are reported. The power indicated on the x-axis refers to the central cable, while three central cables were heated up simultaneously.

The heat extraction through the HL-LHC insulation at a fixed temperature proved to be at least four times more efficient than through the LHC standard insulation. Such improvement is of great importance for future Nb-Ti superconducting magnets, that will be able to withstand larger heat deposition. This can be achieved thanks to the large

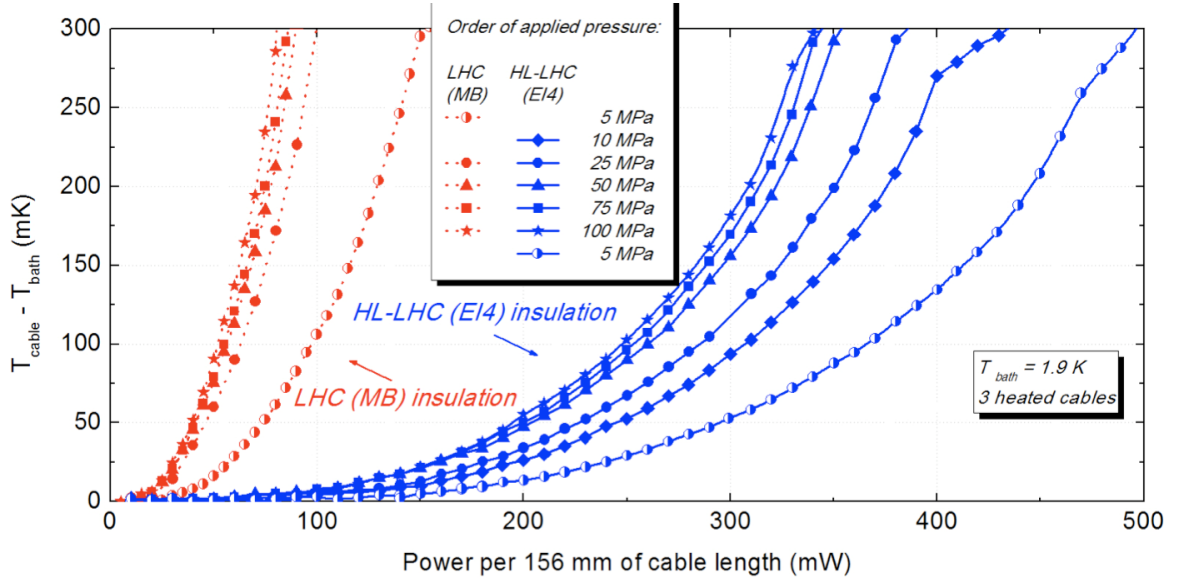


Figure 4.6: Temperature rise of central cable vs. heat load for the HL-LHC (EI4) and LHC (MB) insulations in 1.9 K He II bath. Comparison of different applied pressures below a temperature rise of 300 mK. The lines are a guide to the eye.

amount of He II made available by the channels directly linking the strands to the external bath, where a fully developed turbulent regime is established (sections 4.5.5 and chapter 5). It is worth noticing that such good thermal performances of the HL-LHC could not have been obtained without the development work done to avoid flowing of the polyimide glue (section 2.4).

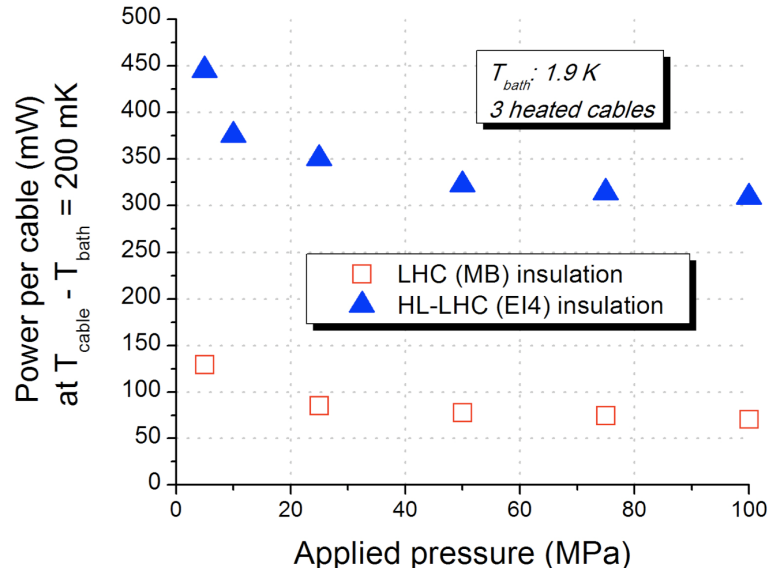


Figure 4.7: Power dissipated in the HL-LHC (EI4) and LHC (MB) samples as a function of the applied pressure, for a constant temperature increase of 200 mK.

The improvement of heat transfer holds at the highest applied pressure, despite the reduction of the channels size. This feature is clearly shown in Fig. 4.7, reporting the power extraction in HL-LHC vs. LHC insulation as a function of the applied pressure,

for a constant temperature rise of 200 mK. The decrease of power extraction is more significant at low pressures, since the sample is softer (section 4.7) and the micro-channels undergo a large size reduction, whereas it tends to an asymptotic value for high pressures. The pressure of 100 MPa that we applied at room temperature corresponds to about the maximum pressure of 118 MPa expected on the coil mid-plane during powering of the MQXC magnets for the HL-LHC upgrade [77].

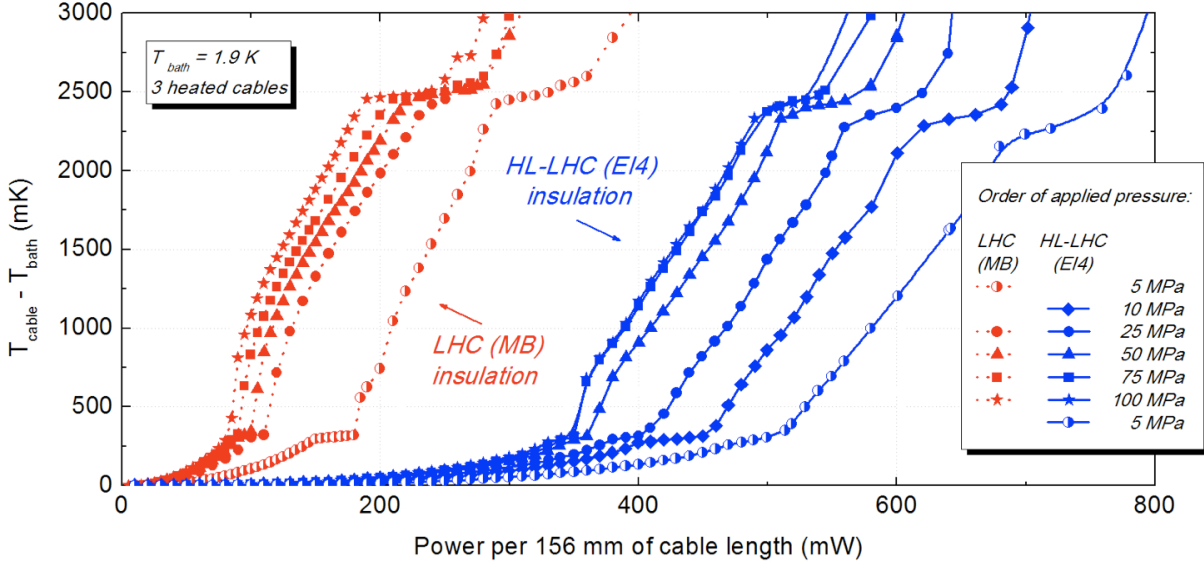


Figure 4.8: Temperature rise of central cable vs. heat load for the HL-LHC (EI4) and LHC (MB) insulation in 1.9 K He II bath. Comparison of different applied pressures below a temperature rise of 3 K. The lines are a guide to the eye.

Fig. 4.8 reports the heat transfer curves up to a temperature rise of 3 K. These results will serve as a basis for the estimation of the magnets quench margin in chapter 7.

The measurement at 100 MPa on the EI4 sample was repeated after 20 days, keeping in the meantime the sample under a 100 MPa pressure. The difference with the previous measurement was not significant, meaning that the creep effect in this time scale does not have an impact on the heat transfer. This is probably due to the fact that the creep effect is more evident during the first days, as shown in section 4.7.3, which is the time the sample usually remains under pressure before being measured. It would be anyhow difficult to assess the almost certain influence of the creep mechanism on the heat extraction because of the time needed to cool down the sample, where the creep effect is by far more important.

There are also other mechanical effects influencing the channels size. For the EI4 sample analyzed so far, the maximum pressure applied after the curing cycle was 100 MPa. Fig. 4.9 shows the comparison of the EI4 and MB curves to another variant of HL-LHC (EI3) that was cycled up to only 50 MPa. Despite the smaller thickness of the EI3 second insulation tape (50 instead of 75 μm), resulting in a smaller channels cross-section, the heat extraction is larger than in EI4. This result can be explained because of the smaller plastic deformation, which will be addressed from the mechanical point of view in section 4.7.3. The maximum pressure in all the other reported measurements is 100 MPa.

The effect of the curing was not investigated but might be not negligible. The curing

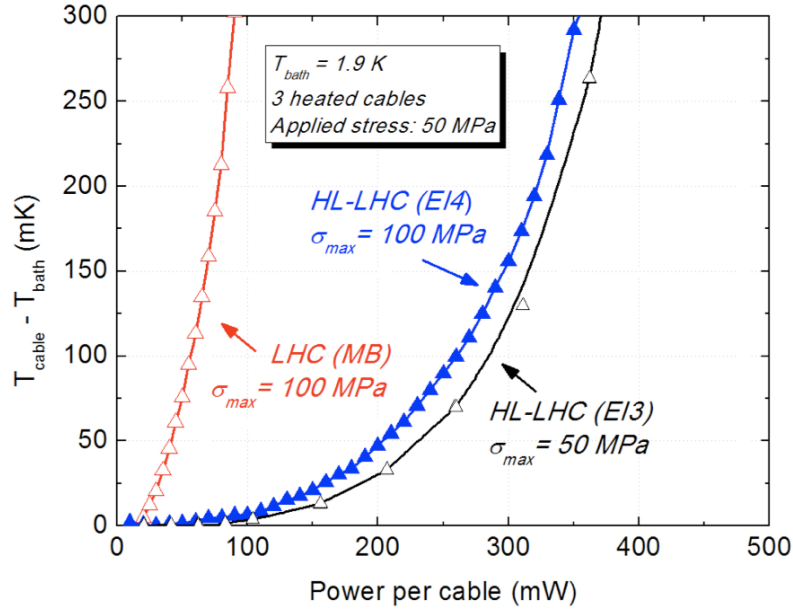


Figure 4.9: Temperature rise of central cable vs. heat load in 1.9 K He II bath. The HL-LHC EI3 and EI4 insulations are compared to the LHC MB one, for different maximum pressure seen by the samples.

cycle at 130 MPa used to prepare our samples is conservative with respect to the expected curing pressure ranging between 50 [77] and 80 MPa [68]. Evaluating the impact of this parameter would require an experimental verification.

4.5.2 Localized vs. distributed heat deposition

Fig. 4.10 shows the results of measurements performed in symmetric configuration while heating one, three or five cables, below a temperature rise of 300 mK. The HL-LHC curves for three and five heated cables cases overlap, whereas the one heated cable curve only provides a slight improvement of heat extraction. The comparison of these curves provides information on the coupling between adjacent cables, in comparison to the LHC insulation. These data are used to build Fig. 4.11, which provides an explanation of these results with respect to the LHC insulation.

Fig. 4.11 shows the increase in terms of extracted power, if passing from three to one heated cable configuration. In case of the LHC (MB) sample, the central cable can transfer more heat to the adjacent cables than in the HL-LHC (EI4) sample. Therefore the HL-LHC insulation allows adjacent cables to be more thermally decoupled than the LHC insulation does, thanks to an efficient heat transfer between the cable and the bath.

The results of measurements in the mentioned heating configurations up to a temperature rise of 10 K are presented in Fig. 4.12. More pronounced differences between the different heating configurations arise, also in the case of HL-LHC three and five heated cables (overlapping below 300 mK). This is a direct consequence of the saturation of the micro-channels among the insulation tapes. Above T_λ they no longer provide a thermal short circuit between cable and bath. The slope of the curves depends on the solid conduction heat transfer, as already observed. A larger heat transfer, as in the case of one heated cable, corresponds to a smaller slope.

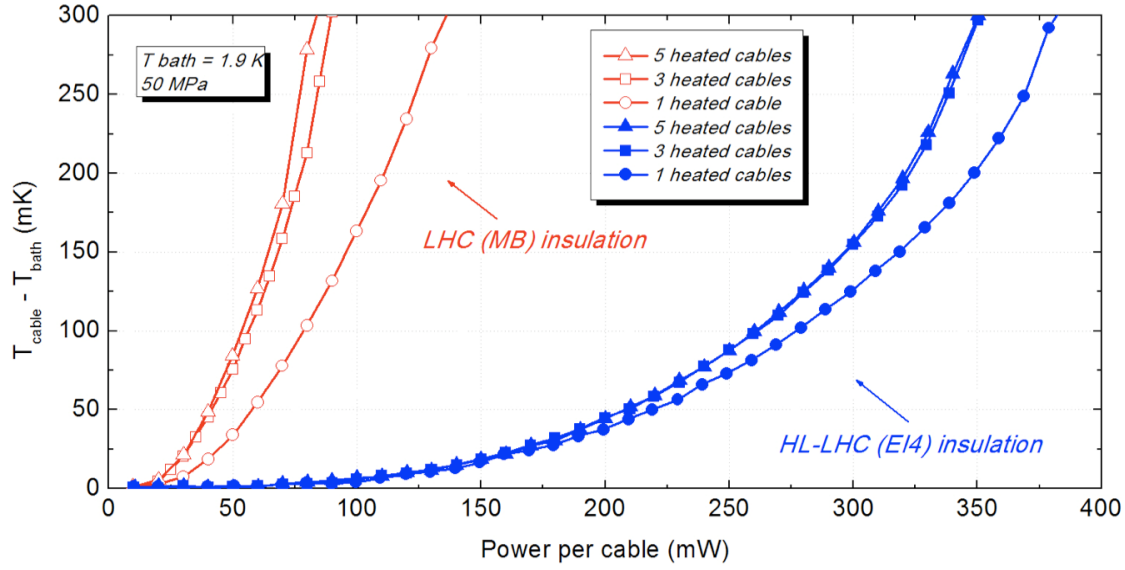


Figure 4.10: Temperature rise of central cable vs. heat load for the HL-LHC (EI4) and LHC (MB) insulations in 1.9 K He II bath. Comparison of different symmetric heating configurations below a temperature rise of 300 mK. The lines are a guide to the eye.

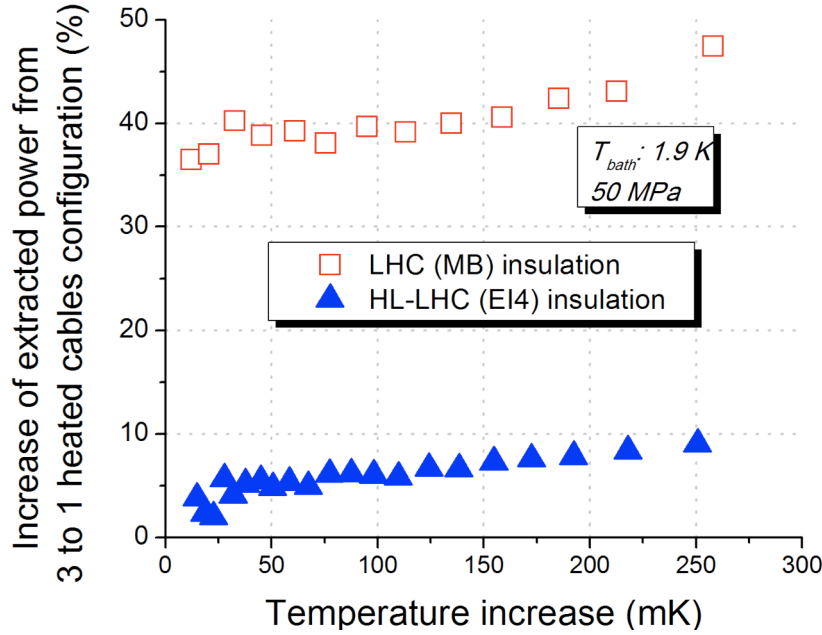


Figure 4.11: Increase of extracted power as a function of the temperature rise when passing from 3 to 1 heated cables configuration. The HL-LHC (EI4) and LHC (MB) samples are considered, at an applied pressure of 50 MPa.

Fig. 4.13 shows heat transfer curves of the HL-LHC (EI3) insulation, for one and three heated cables, both at an applied pressure of 10 and 50 MPa. The relative increase of heat transfer when going from three to one heated cable is larger at 10 MPa than at 50 MPa. This means that, if no other cables are heated, the central one can transfer more heat to the bath through the He II channels located between itself and the adjacent cables (that are indeed larger at 10 MPa), rather than by solid conduction to its adjacent cables. Such

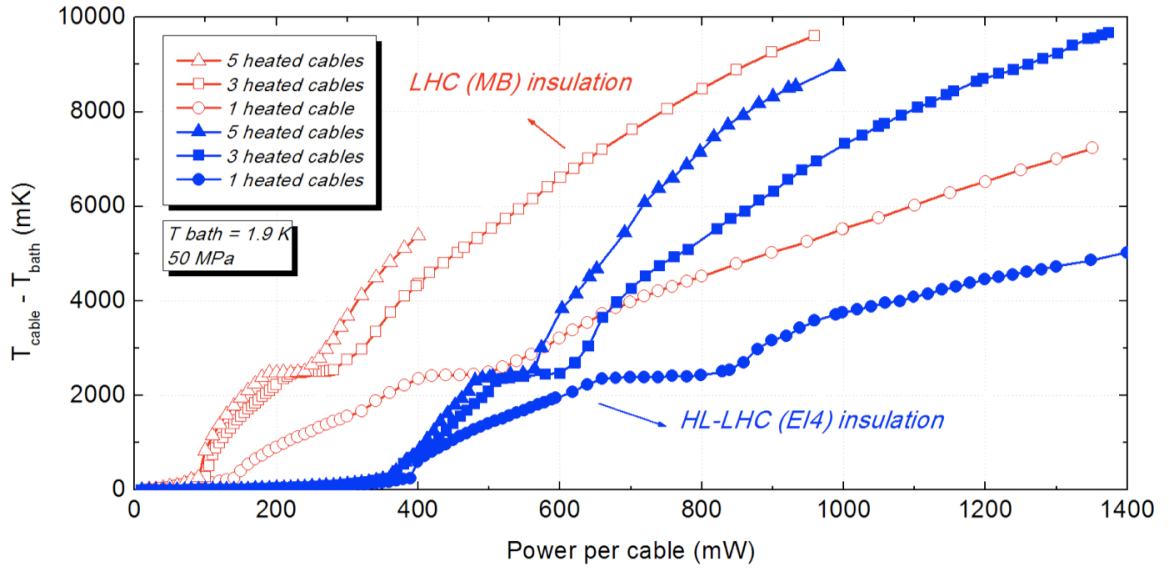


Figure 4.12: Temperature rise of central cable vs. heat load for the HL-LHC (EI4) and LHC (MB) insulations in 1.9 K He II bath. Comparison of different symmetric heating configurations below a temperature rise of 10 K. The lines are a guide to the eye.

qualitative observation will be confirmed by the calculations presented in section 5.5.2.

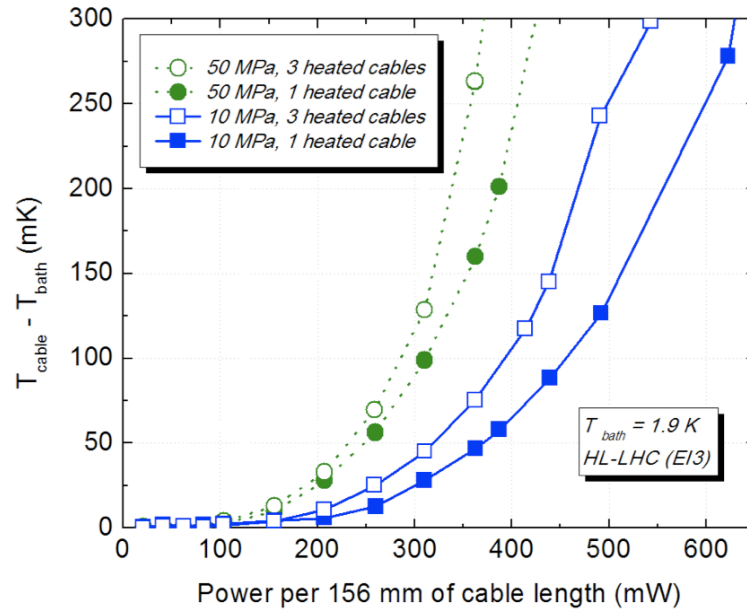


Figure 4.13: Temperature rise of central cable vs. heat load for the HL-LHC (EI3) insulation in 1.9 K He II bath. Two applied pressures (10 and 50 MPa) and two heating configurations (one and three heated cables) are considered. The lines are a guide to the eye.

4.5.3 Thermal coupling between cables

A further confirmation of the weak thermal coupling between adjacent cables insulated with the HL-LHC scheme is provided in Fig. 4.14. The considered heating configurations were described in sections 3.3.3 and 3.4.3. For the HL-LHC (EI4) insulation, the temperature rise of the heated cable at which the adjacent (not heated) cable starts to increase its temperature is 2100 mK. We remind and show in the figure that the corresponding value for the LHC (MB) insulation is 235 mK. The HL-LHC scheme allows a better access of He II to the strands through the micro-channels network, thus explaining the weaker thermal coupling.

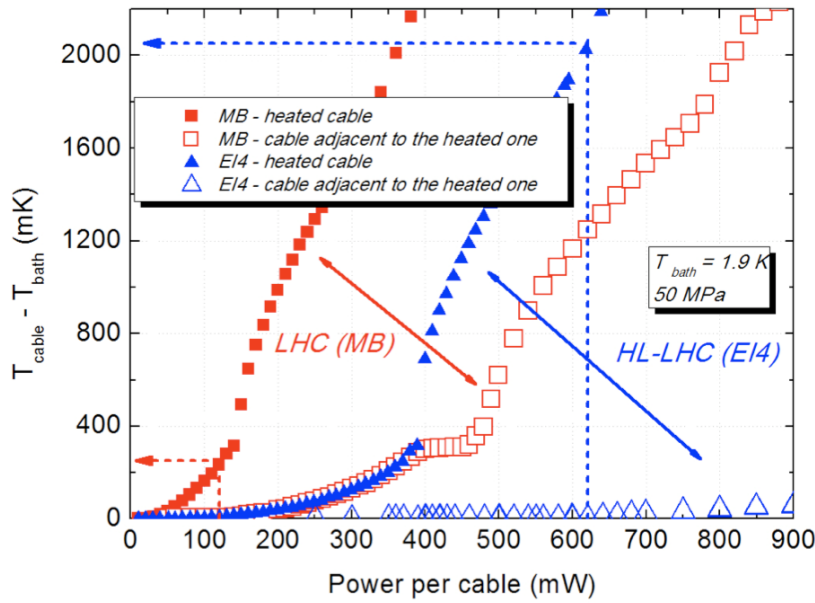


Figure 4.14: Temperature rise of the heated cable and of the adjacent one as a function of the power dissipated in the heated cable. The HL-LHC (EI4) and LHC (MB) samples are considered, at an applied pressure of 50 MPa.

4.5.4 Improved HL-LHC insulation

Besides the presented EI3 and EI4, two other variants of the HL-LHC insulation were studied to provide indications on the most significant parameters for the heat extraction. Their geometric parameters are reported in Table 4.1. Each of them features one different geometric parameter with respect to EI4. In particular, in EI5 the second tape is wound with 0.5 mm spacing (instead of 1.5 mm). In EI6 the first and third tapes are 4.5 mm wide (instead of 9 mm). Fig. 4.15 presents the comparison among EI4, EI5 and EI6, in case of one heated cable at an applied pressure of 50 MPa. The LHC (MB) insulation curve is reported as well.

The EI5 insulation shows intermediate thermal performances between LHC (MB) and EI4. The EI6 one features a more efficient heat transfer than the standard HL-LHC (EI4) insulation. The heat extraction of EI6 at fixed temperature is almost twice that of EI4, therefore around eight times better than the LHC (MB) insulation.

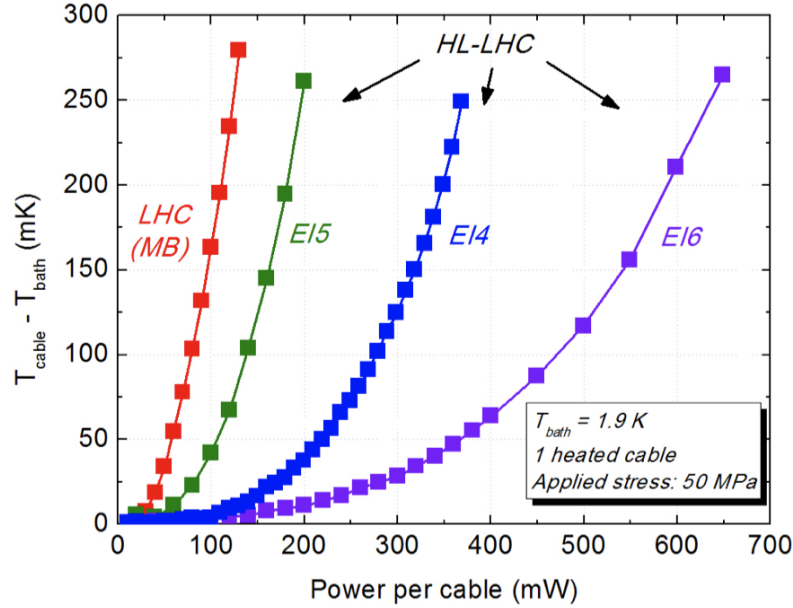


Figure 4.15: Temperature rise of the heated central cable vs. heat load for three variants of HL-LHC insulations (EI4, EI5 and EI6) in 1.9 K He II bath. The LHC insulation heat transfer curve is reported for comparison. The lines are a guide to the eye.

The main geometric parameters affecting the heat transfer in the HL-LHC insulations are the channels length and cross-section, as well as the number of openings between the second and the first / third insulation tape. Although EI5 and EI6 samples feature 60 openings per cable compared to 50 for EI4, the minimum channels length is 6 mm for EI6 and 10 mm for the others. The number of openings and the spacing between adjacent turns of the second tape (and the thickness of the second tape) determine the total geometrical surface of the channels. EI6 has the largest value between the three, whereas EI5 has the smallest. The actual channels cross-section is an unknown parameter featuring a non linear dependence on the applied pressure, on the maximum pressure seen by the sample, on the curing cycle and on creep mechanisms. More details on the heat extraction mechanisms in the HL-LHC insulations will be provided in section 5.5.

The results presented in this section show that there is potential for further improving the heat transfer through the HL-LHC insulation. However the thermal behavior is not the only requirement of a cable insulation for superconducting magnets. The electrical robustness and mechanical stability must be ensured as well. Such investigations were carried out for the EI4 insulation and are reported in sections 4.6 and 4.7, but not for the EI6 insulation.

4.5.5 Phenomenological analysis

Fig. 4.16 shows the results of the HL-LHC (EI3) insulation in logarithmic scale, in case of one heated cable. As long as the helium in the cable does not overcome the λ transition, the temperature rise is proportional to $Q^{3.2}$ or $Q^{3.1}$. The He II Gorter-Mellink heat transfer is predominant, thus making the solid conduction effect negligible. We remind that the solid conduction cannot be neglected for the LHC scheme, because of the

less effective micro-channels (section 3.4.4). These observations and the geometry of the insulation wrappings seem to confirm the existence of a micro-channels network among the different cable faces, that would explain the larger heat extraction. Each face would not be independent on the others as it is the case in the LHC insulation. This would also suggest that the cable large faces give an important contribution to cooling, in contrast to the LHC insulation behavior. We will deal with these issues in section 5.5.

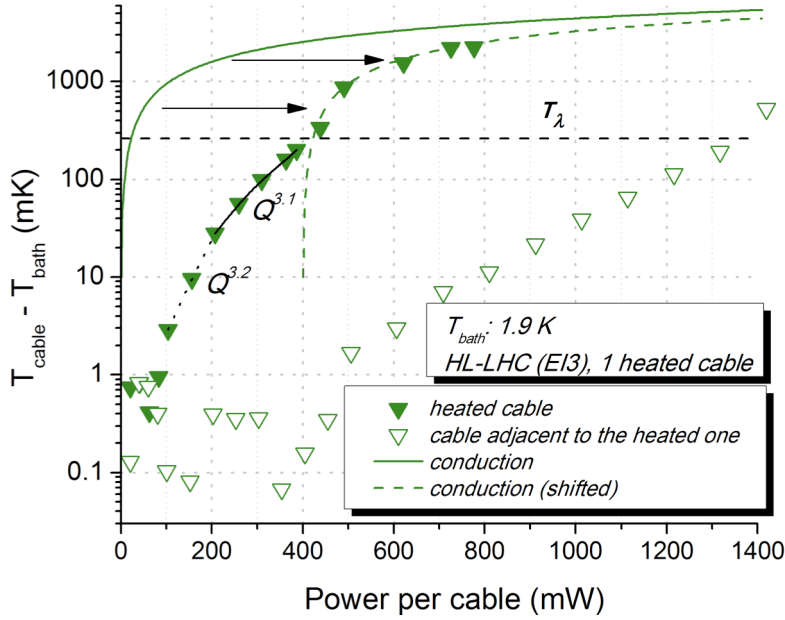


Figure 4.16: Temperature rise of central cable vs. heat load for the HL-LHC (EI3) insulation in 1.9 K He II bath. The corresponding temperature rise of the adjacent cable is also reported. The calculated conduction curve is shown, as well as the power laws fitting the measurements below 300 mK.

The conduction curve is also reported in Fig. 4.16. It is considered decoupled from the He II mechanism and calculated as described in section 3.4.4. It becomes dominant above T_λ , when the adjacent cable starts to increase its temperature. The shifted conduction curve shown in the figure appears in good agreement with the measured data. The shift might be explained because of the He II still present at the micro-channels exit into the bath, or because the edges of the cable are colder than its central region.

4.6 Electrical measurements

The setup described in section 3.5 was used to electrically characterize the HL-LHC EI3 and EI4 insulation schemes. The results are reported in Table 4.2. Though smaller than that of the LHC (MB) insulation, the measured breakdown voltage of the standard HL-LHC insulation (EI4) is larger than 11 KV. It is orders of magnitude higher than the inter-turn voltage arising in case of a quench (100 V). The results of previous tests carried out on different EI schemes [67][76] confirm these values. The robustness of the electrical protection provided by the overlapped first and third layer is then validated on cables samples. As already mentioned, these values must be taken as a conservative minimum, since except in one case the discharge did not occur in the compressed area.

Insulation type	1 st sample	2 nd sample	3 rd sample
LHC (MB)	>22-23	18	>22
HL-LHC (EI3)	>9	>12	>8
HL-LHC (EI4)	>14	>12	>11

Table 4.2: Dielectric strength test (kV).

Measurements of the inter-turn leakage current did not show striking differences among the three types of insulation, and no significant dependence on the applied pressure (Fig. 4.17).

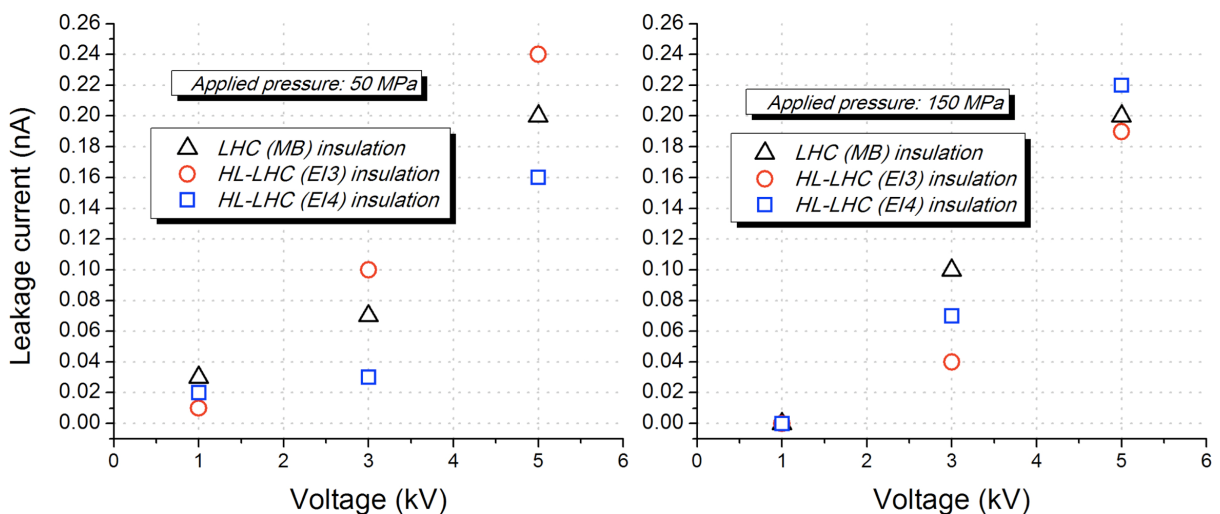


Figure 4.17: Leakage current for the LHC (MB) and HL-LHC (EI3 and EI4) insulations, at applied pressures of 50 MPa (left) and 150 MPa (right).

4.7 Mechanical measurements

The experimental setups described in section 3.6 were used to mechanically characterize the HL-LHC EI3 and EI4 insulation schemes. EI1 and EI2 were also tested, though the results are not reported here.

4.7.1 Insulation thickness

The pressure-displacement measurements of the HL-LHC insulations showed that the height of the EI4 stacks is always larger than all the other insulation schemes due to the thicker insulation tapes constituting it. On the contrary, the height of the EI3 stacks is included between that of LHC MQ and MB. Our measurements performed on cables stacks were compared to arch measurements, by normalizing to the number of cables in the arch. Fig. 4.18 from [77] shows a very good agreement for the EI4 insulation (here called MQXC, from the name of the relevant magnet) in the unloading phase. In the loading phase a difference can be observed at low pressure, which vanishes at high pressure.

Furthermore, it is shown that the same pressure leads to a larger displacement on the HL-LHC insulation than on the LHC one, because of the more porous structure.

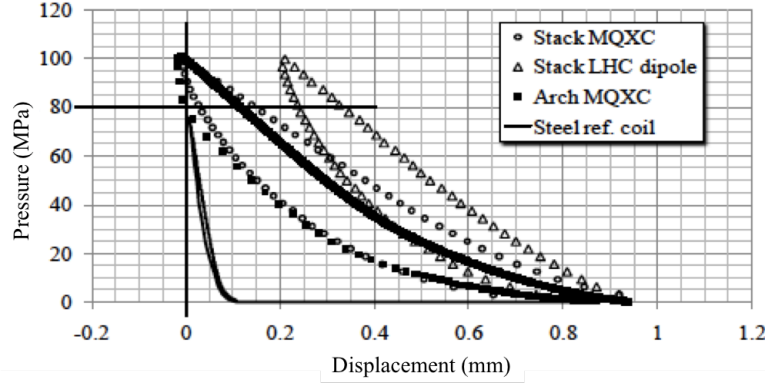


Figure 4.18: Coil pressure vs. azimuthal displacement for a steel reference coil, ten stacks from LHC dipole and MQXC, scaled to be compared with MQXC coil arch (from [77]). The zero on the x-axis represents the coil nominal size.

Fig. 4.19 reports the pressure vs. insulation thickness curves for EI3 and EI4, for different curing cycle (left) and different cable (right). Table 4.3 summarizes the values measured at 50 MPa compression on the relevant unloading branch. The features observed in section 3.6.1 for the LHC insulations can also be observed for the HL-LHC ones.

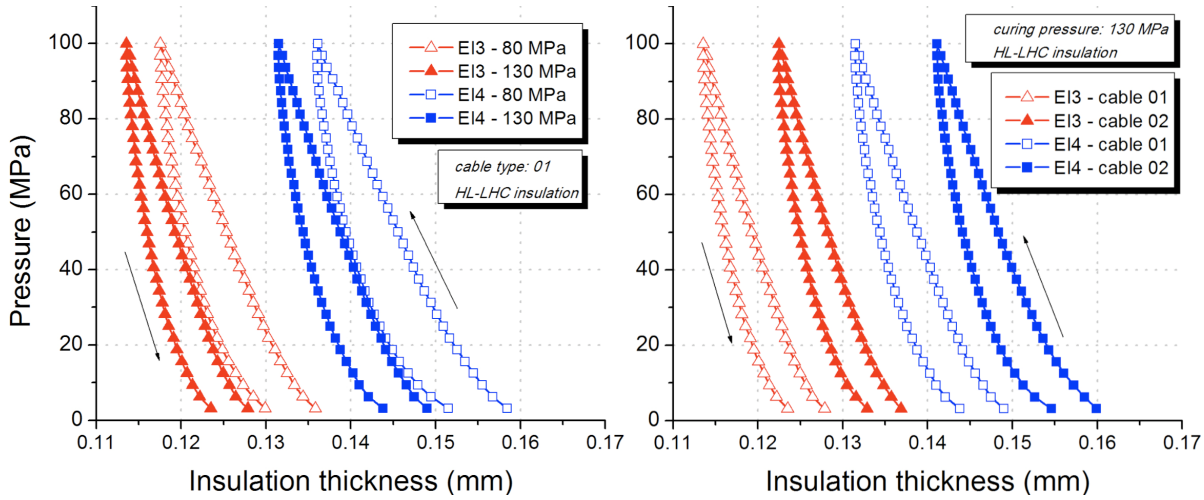


Figure 4.19: Applied pressure vs. thickness of the HL-LHC insulations, for different curing cycles (left) and different cables (right).

Fig. 4.20 compares the values of Tables 3.4 and 4.3, in terms of loss between the geometrical and the measured thickness. All the combinations of insulation scheme, curing pressure and cable type are taken into account. The higher loss in thickness for samples cured at higher pressure and for the less compacted cable 01 are evident. Furthermore, the loss in thickness for the HL-LHC insulation is higher than for the LHC one. This is linked to the presence of a higher void fraction and to the higher localized peak stresses originated at the crossing of the different tapes.

Insulation scheme	Cable type	Curing pressure (MPa)	Geometrical thickness (μm)	Measured thickness (μm)
EI3	01	80	169	120
EI3	01	130	169	116
EI3	02	80	169	129
EI3	02	130	169	125
EI4	01	80	194	139
EI4	01	130	194	134
EI4	02	80	194	147
EI4	02	130	194	144

Table 4.3: Measured insulation thickness of the HL-LHC insulation schemes, at 50 MPa compression during the unloading phase. The peak pressure of the cycle is 100 MPa.

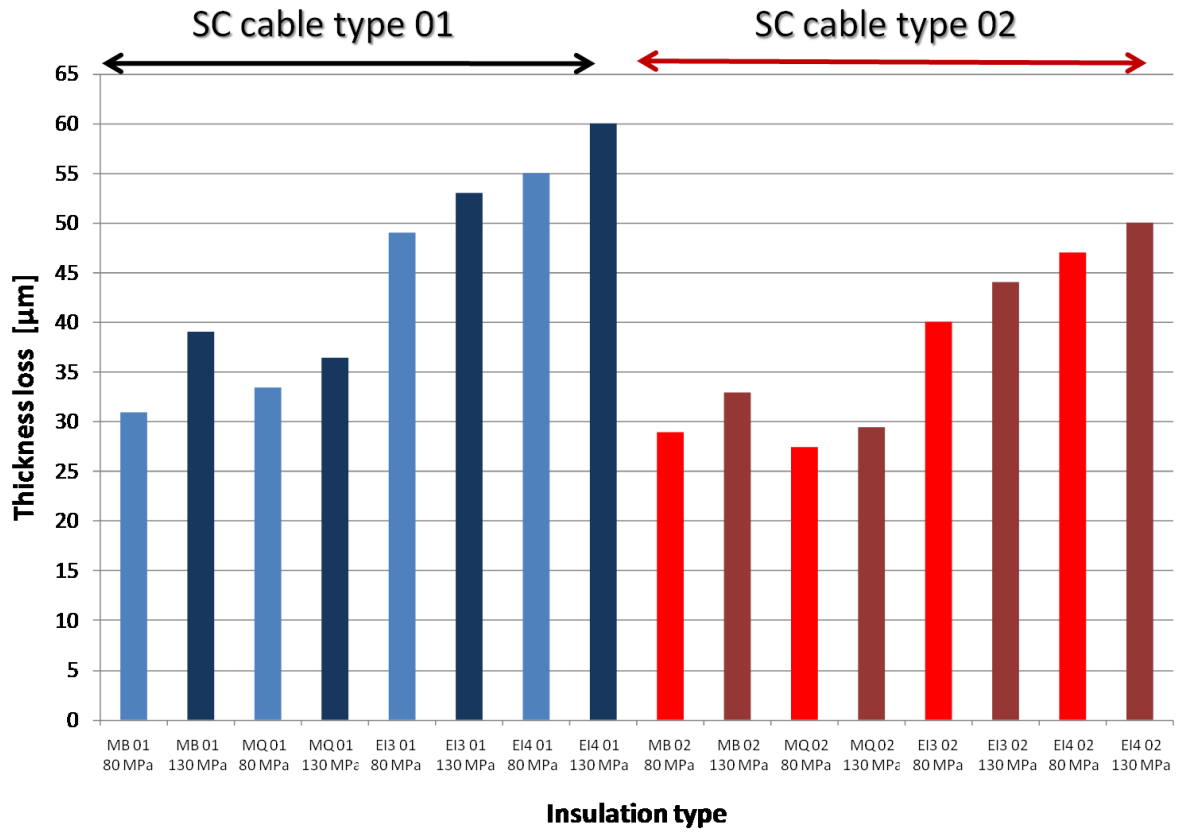


Figure 4.20: Thickness loss between the theoretical and the measured one for the LHC (MB, MQ) vs. the HL-LHC (EI3, EI4) insulation schemes. All the different combinations of curing cycle and cable type are considered.

4.7.2 Elastic modulus

Fig. 4.21 reports the elastic modulus as a function of the applied pressure during loading and unloading. The HL-LHC (EI4) insulation is confronted with the LHC (MB) one, in

p_{max} (MPa)	$\Delta p/p_{max}$ 1 day (%)	$\Delta p/p_{max}$ 5 days (%)	$\Delta p/p_{max}$ 10 days (%)
96	19	22	25
121	23	26	26
130	20	23	24

Table 4.4: Stress relaxation as a function of the initial peak pressure p_{max} for the HL-LHC EI4 insulation.

case of the inner layer cable of the LHC main dipoles, for a curing pressure of 80 MPa. The same features described in section 3.6.2 can be observed: a significant increase during loading at small pressures, and the unloading phase characterized by larger values. The HL-LHC insulation shows a softer behavior than the LHC insulation because of the more porous structure. However this only corresponds to an approximately 10% reduction of the elastic modulus.

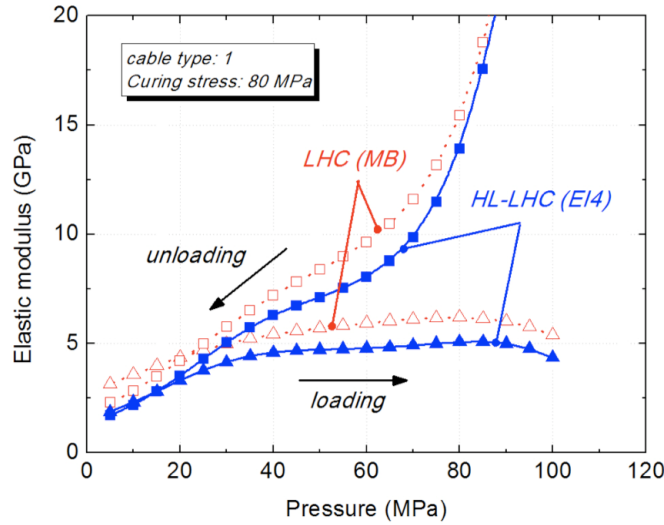


Figure 4.21: Stack elastic modulus vs. pressure for the loading and unloading branches of the HL-LHC (EI4) and LHC (MB) insulation schemes.

4.7.3 Stress relaxation

The test setup introduced in section 3.6.3 was used to study also stacks wrapped with HL-LHC insulations.

Table 4.4 reports the percentage losses for the EI4 insulation after one, five and ten days from the application of the force. The losses do not substantially change for different initial peak pressures. This confirms what already observed for the LHC MB insulation (Table 3.5) and allows scaling the losses to the same initial pressure for tests starting from different initial pressures. This was applied in a range of maximum 20 MPa.

In Fig. 4.22 (left) we compare the losses for the LHC (MB) and HL-LHC (EI3 and EI4) insulation schemes for cable type 01, normalized to an initial pressure $p_{s,max}$ of 120 MPa.

It is possible to observe that the maximum losses after ten days vary between 24 MPa and 33 MPa, therefore in a quite narrow band. The EI3, which uses a thinner intermediate polyimide layer to create helium channels, presents smaller losses than the EI4 that has a larger void fraction. The MB insulation presents larger losses than all the other schemes even if it is more compact. The experiment was repeated using a completely new sample stack and the results of the second experiment confirmed the preliminary ones.

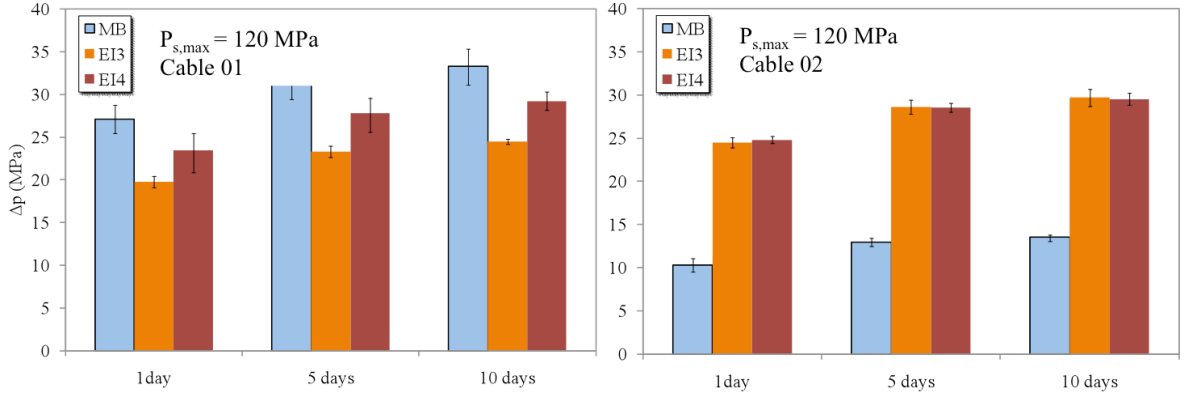


Figure 4.22: Stress losses for the LHC (MB) and HL-LHC (EI3 and EI4) insulation schemes. Data are scaled to an initial peak pressure of 120 MPa. cable 01 is considered on the left (original initial peak pressure: 122 MPa for MB, 120 MPa for EI4, 107 MPa for EI3), and cable 02 on the right (MB and EI3 scaled from 140 MPa).

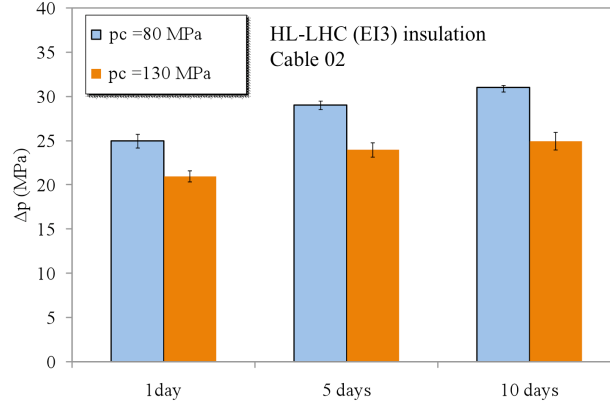
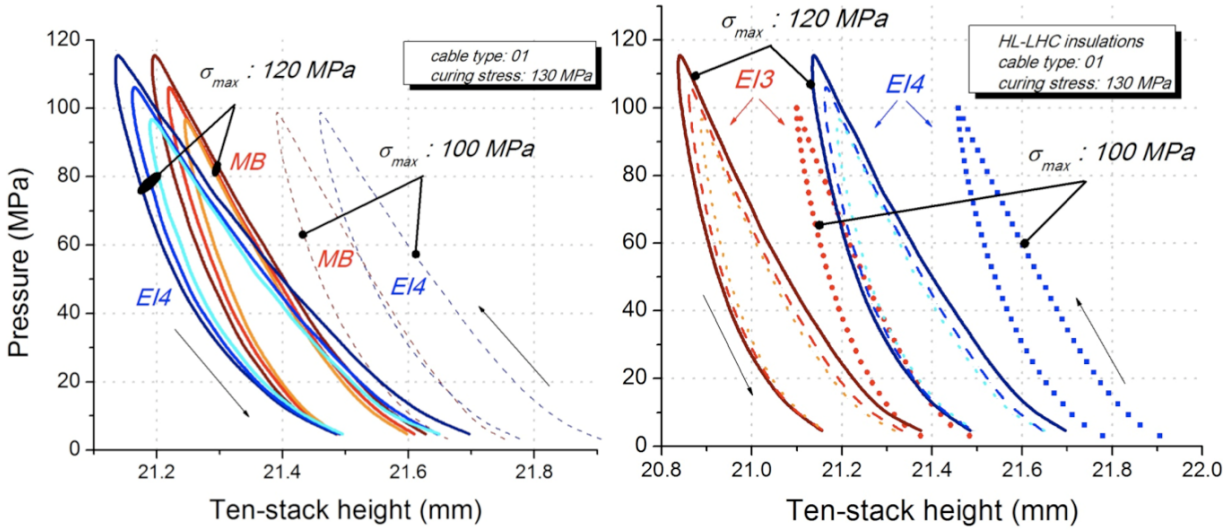
In Fig. 4.22 (right) we report the losses for the cable 02. While the losses for the HL-LHC insulations are very similar to the ones recorded for cable 01, for the MB the situation is drastically different showing much smaller values. This behavior could be explained if we consider two different dominant mechanisms of stress relaxation:

- the first takes place at the interface between the superconducting cable and the first tape of insulation and is linked to the viscoplastic deformation of the material among the cable strands. This phenomenon seems to be dominant for the MB insulation: placed on a more compact substrate (cable 02) it shows lower pressure losses;
- the second takes place between layers and is linked to the pressure concentration on the edges of the insulation tape. This is characteristic of the interfaces and contacts around the discontinuous intermediate layer of the HL-LHC insulations and it seems to be dominant for these schemes. This is also confirmed by the fact that the change of the void fraction in the insulation by only changing the thickness of the second tape does not strongly modify the stress relaxation behavior (EI3 vs. EI4).

Note that for measurements on cable 02 the peak pressure for MB and EI3 was 140 MPa. The data were scaled down to be coherent with the measurements shown for cable 01.

The influence of the curing pressure (p_c) on the stress relaxation was investigated for the EI3 scheme wrapped on cable 02. It can be observed in Fig. 4.23 that a higher curing pressure helps to stabilize the cable, limiting (by 20%) the stress losses after assembly. The stack undergoes a sort of “pre-creep” during curing. This could bring to prefer a higher curing pressure in order to stabilize the coils.

The effect of the peak pressure σ_{max} seen by the samples is investigated following the same procedure described in section 3.6.3. Fig. 4.24 reports the results for the EI4 insulation, compared to the LHC MB insulation (left) and to the EI3 one (right). The

Figure 4.23: Influence of the curing pressure (p_c) on the relaxation pressure loss.Figure 4.24: Pressure vs. height for different values of the maximum pressure σ_{max} seen by the samples. The HL-LHC EI4 insulation is compared to the LHC MB one on the left, and to the HL-LHC EI3 on the right.

features that were observed on MB can be observed also on EI3 and EI4. The loss in thickness when exceeding the peak pressure is more pronounced for the HL-LHC insulations, and mainly for EI4, because of the larger void fraction. These results are in agreement with the heat transfer reduction observed in section 4.5.1, whether the stack undergoes a higher peak pressure.

4.8 Conclusion

The better thermal performance of the HL-LHC (EI4) insulation with respect to the LHC one was demonstrated by a spectacular increased heat transfer capacity of at least a factor of four. The performed experiments proved that this improvement does not reduce with the applied pressure, up to the levels typical of magnet operation. Therefore the proposed insulation is a suitable candidate for future superconducting magnets that will deal with large heat loads. This is the case of the inner triplets quadrupoles of the HL-LHC

upgrade project, for which it was developed. In this frame the new insulation is currently being used for the prototype of the so-called MQXC magnet [77]. The possible use of the HL-LHC insulation is also being considered for other projects, such as the separation dipole (D1) [78] for the HL-LHC project, and fast ramped magnets for the SIS300 synchrotron of FAIR, GSI (CRISP project [79]).

The measurement of different heating configurations highlighted the thermal decoupling of adjacent cables wrapped with this new insulation. A helium micro-channels network exists indeed between the insulation tapes, thus allowing an efficient heat transfer between cables and bath. The presented phenomenological analysis suggests that the dominant heat transport mode is a helium fully developed turbulent regime. In the next chapter we will deal with the details of the micro-channels network and with the relevant heat transfer mechanisms. Furthermore, the tests of variants of the standard HL-LHC scheme demonstrated that there is potential for further improving the heat extraction. This can be useful in view of future developments, provided that the electrical robustness is ensured.

The electrical robustness of the HL-LHC (EI4) insulation proved to be satisfactory. As far as the mechanical tests are concerned, they showed a larger thickness loss and a 10% reduction of the elastic modulus with respect to the LHC insulations. From the stress relaxation point of view, the behavior of the HL-LHC insulation is similar to the LHC (MB) one for the type 01 cable, whereas it presents larger relaxation when applied on the type 02 cable. It was shown that a higher curing pressure helps to limit the stress losses after assembly, by roughly 20%. The effect of the peak stress during cycling was pointed out, which is associated to a reduction of the heat extraction.

Chapter 5

Modeling of He II heat transfer through Nb-Ti cable insulation

Contents

5.1	Introduction	77
5.2	Background notions	78
5.3	Model description	78
5.4	LHC insulation	81
5.4.1	Model implementation	81
5.4.2	Results	85
5.4.3	Images of the slits on the cable small and large face	88
5.5	HL-LHC insulation	90
5.5.1	Model implementation	90
5.5.2	Results	92
5.5.3	Images of the micro-channels	94
5.6	Conclusion	95

5.1 Introduction

In order to understand the mechanisms of heat transport occurring in the cable insulations, we developed a theoretical heat transfer model. The actual topology of the LHC (MB) and HL-LHC (EI4) insulations is taken into account, and coupled He II and solid conduction heat transport mechanisms are implemented. The model is focused on the superfluid helium region, where the strands temperature is below T_λ , and on the relevant thermal mechanisms. It aims at reproducing the experimental results reported in chapters 3 and 4, to determine the heat fluxes distribution and the unknown micro-channels dimensions. As for the latter item, the obtained results are compared to microscope imaging of the insulation tapes deformed under pressure.

The model assumes that the mechanisms of heat transport follow the known laws of the superfluid dynamic regimes. However the typical dimensions of the micro-channels created by the overlapping of the insulation tapes are typically smaller than those for

which the validity of such laws was demonstrated. This specific aspect is addressed by a dedicated experimental program that will be described in chapter 6.

In chapter 7 the developed model will be applied to the actual geometry of the LHC and HL-LHC magnets, in order to predict the magnet response to a beam induced heat deposit.

5.2 Background notions

Previous modeling attempts of He II stack measurements either addressed the only superfluid contribution in terms of uni-dimensional equivalent channels [55], or qualitatively identified the different heat transfer paths [28]. The different experimental setup used in [66] and [80], rather than considering the entire heat transfer in a stack, focused on a simplified one-dimensional heat transfer. This allowed a first decoupled modeling of the polyimide and helium heat transfer contributions. The work presented in this chapter aims at extending the latter quantitative method to the case of anisotropic three-dimensional coupled heat transfer mechanisms, in order to describe the thermal behavior of Nb-Ti coils.

5.3 Model description

The experimental setup is simulated by a network model where steady-state heat transfer balance equations are solved at the nodes. The model is two-dimensional and describes the cables cross-section. Indeed the Joule heating dissipated in the cable is uniform in the longitudinal direction and the epoxy plugs at the sample extremities prevent from parasitic cooling in that direction, so that heat is transversally extracted from the cable. Furthermore it was shown in the previous chapters that all the thermo-couple junctions located in different cable cross-sections measure the same temperature below T_λ , due to the superfluid helium filling the interstices among the strands. Therefore every sample cross-section features the same temperature, which justifies the two-dimensional hypothesis.

However the temperature gradients between the outer strands surface and the external bath develop in the three spatial directions. The model is developed to take into account the three-dimensional shape of the helium channels and their thermal coupling to the insulation tapes, through the definition of nodes in the cable insulation.

The mentioned experimental evidence of equal temperature measured in the different thermo-couple locations below T_λ also means a uniform temperature over the cable cross-section. This allows describing each cable by a single node. The heat transfer between adjacent nodes can occur through polyimide solid conduction, superfluid (He II) conduction or both contributions in parallel. The simplified implementation of the coupling between these thermal mechanisms, as well as the location of the nodes in the insulation, depend on the insulation scheme and will be specifically addressed in sections 5.4.1 and 5.5.1. In this section we define how every contribution is calculated and we discuss the model hypotheses and limits.

The polyimide conduction is calculated using the Fourier law. The linearity of the polyimide thermal conductivity in the considered temperature range allows to approximate

its integral with an average value:

$$Q_{pol.} = \sum_{i=1}^P \frac{A_{pol.i}}{\delta_{pol.i}} \int_{T_j}^{T_k} k_{pol.}(T) dT \approx \sum_{i=1}^P \frac{A_{pol.i}}{\delta_{pol.i}} \cdot \bar{k}_{pol.av}(T_j, T_k) \cdot (T_k - T_j). \quad (5.1)$$

T_j and T_k are the temperatures of two adjacent nodes, $k_{pol.}$ is the temperature dependent polyimide thermal conductivity and $\bar{k}_{pol.av}(T_j, T_k)$ is the average value between T_j and T_k . P is the number of insulation portions between nodes j and k having surface $A_{pol.i}$ and thickness $\delta_{pol.i}$.

The polyimide thermal conductivity at low temperature was investigated by several authors, as summarized in Fig. 5.1. Data from Baudouy [81] in the superfluid region agree with those from Lawrence [82] that are taken over a larger temperature range. Furthermore data from Lawrence and from NIST [83], which refer to two different temperature ranges, are in agreement in the overlap of the two ranges. In the following we will retain values from Baudouy rather than from Cryocomp [84] or Barucci [85]. The latter differ by a factor of two below T_λ and to our knowledge there are not other experimental values confirming them. The sensitivity of the model to the polyimide thermal conductivity was assessed. Assuming different values than those from [81], the results of the computations do not change by more than 10%.

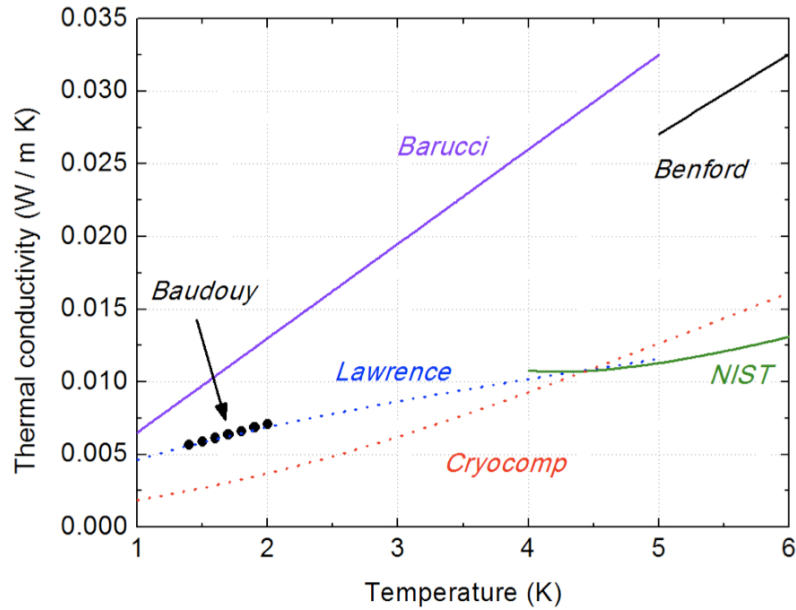


Figure 5.1: Polyimide thermal conductivity at low temperature, compiled from different sources [81]–[86].

As for the heat transport through the micro-channels located between the insulation tapes, we assume that it follows the laws of laminar and turbulent regimes of superfluid helium. However a fundamental study investigating whether these macro-scale laws are valid in such narrow channels and slits is missing. We developed for this reason a dedicated experimental setup and performed He II heat transfer measurements through micro-channels. This issue will be addressed in chapter 6. The validation of the mentioned laws to small dimensions is mainly of concern for the LHC insulation, since as it will be shown the average size of the channels in the HL-LHC insulation is typically larger.

The integral expressions of equations 2.35 and 2.37 are implemented in the numerical model. In particular the Landau heat flux Q_{Lan} is calculated as:

$$Q_{Lan} = \sum_{i=1}^N \frac{A_{ch,i} \cdot d_{ch,i}^2}{l_{ch,i}} \int_{T_j}^{T_k} \frac{[\rho(T) \cdot s(T)]^2 \cdot T}{\beta \cdot \eta(T)} dT, \quad (5.2)$$

where ρ is the density of the bulk helium, s the entropy, T the temperature, η the viscosity and β is a coefficient depending on the channel cross-section. N is the number of channels between nodes j and k featuring surface $A_{ch,i}$, length $l_{ch,i}$ and diameter $d_{ch,i}$ (if circular). In the considered case of channels rectangular cross-section with sides $a_{ch,i}$ and $b_{ch,i}$, the relation between normal fluid velocity, pressure and temperature gradient [87]–[10] yields a β of 12 and a $d_{ch,i}$ expressed as a combination of $a_{ch,i}$ and $b_{ch,i}$:

$$d_{ch,i} = \sqrt{\frac{a_{ch,i} \cdot b_{ch,i}}{b_{ch,i}/a_{ch,i} + a_{ch,i}/b_{ch,i}}}. \quad (5.3)$$

The Gorter-Mellink heat flux Q_{G-M} is calculated as:

$$Q_{GM} = \sum_{i=1}^N \frac{A_{ch,i}}{l_{ch,i}^{1/3}} \left[\int_{T_j}^{T_k} \frac{\rho_s(T)^3 \cdot s(T)^4 \cdot T^3}{A_{GM}(T) \cdot \rho_n(T)} dT \right]^{1/3} = \sum_{i=1}^N \frac{A_{ch,i}}{l_{ch,i}^{1/3}} \left[\int_{T_j}^{T_k} f(T) dT \right]^{1/3}, \quad (5.4)$$

where ρ_s and ρ_n are the density of the superfluid and of the normal components respectively, f is the He II equivalent thermal conductivity and A_{GM} is the Gorter-Mellink coefficient.

The variables ρ , s , η , ρ_s , ρ_n , f and A are temperature dependent. Their values come from the HEPAK database [32] with an error typically smaller than 1%. They all refer to a helium pressure of 0.1 MPa.

The transition between the two dynamic regimes of superfluid helium is related to the onset of vorticity in the superfluid and in the normal components. It occurs at a critical heat flux density that depends on the channel dimension. Also in this case, a fundamental study in pressurized He II in narrow channels is needed, to experimentally determine the critical heat flux density in such small dimensions. Chapter 6 will deal with this topic as well. In the following we will use the critical heat flux density Q_{c1} predicted by Ladner and Tough [48], which is temperature dependent unlike the other expressions that can be found in literature (section 2.5). This critical heat flux is associated to the critical velocity of the superfluid component and is expressed as:

$$Q_{c1} = \frac{4 \cdot \alpha}{\gamma_0(T_{bath}) \cdot D} \cdot \rho_s(T_{bath}) \cdot s(T_{bath}) \cdot T_{bath}. \quad (5.5)$$

α is an experimentally determined constant value depending on dimension and shape of the tested channels, that is approximately equal to 1. D is the hydraulic diameter and γ_0 is a temperature and geometry dependent parameter, equal to 102 s/cm² for a bath temperature T_{bath} of 1.9 K. The other functions ρ_s and s are also evaluated at the same T_{bath} . It is worth noticing that equation 5.5 was determined in saturated He II for particular channel geometries, by making use of empirical coefficients.

The Kapitza resistance between strands and helium is neglected. This choice is due to the uncertainty associated to the the measured cable temperature, which lies between the temperature of the strands and that of the helium inside the cable because of the electrical insulation of the temperature sensors (section 3.3.2). The polyimide-helium Kapitza resistance is neglected as well, because more than one order of magnitude smaller than the thermal resistance of the polyimide bulk material [81]. The strands-polyimide contact resistance is not considered because of the large associated uncertainty [88].

Although the geometry of the insulation scheme is considered in the model, a fundamental uncertainty remains on some parameters, mainly the channels cross-section and the presence of possible restrictions along the channels length. We have shown in the previous chapters that besides the effect of the pressure applied during the test, several other mechanisms can influence the micro-channels topology and dimensions, e.g. the curing cycle, the plastic deformation due to the applied pressure and to the creep effect, the stress induced by the differential thermal contractions of the coil components. All these mechanisms affect the micro-channels among the insulation tapes, thus making hard to precisely determine their shape and dimension from a mechanical standpoint. In the following, we will determine the channels average dimensions from a thermal point of view, assuming that they do not vary along the channels length. Because of the mentioned uncertainties, we preferred not to over complicate the modeling.

The steady-state hypothesis allows to assume in each node that the algebraic sum of the heat fluxes exchanged with the other nodes and of the heat sources is zero. All the heat balance equations are written in the form of a matrix system: $H \cdot T = Q$. Each term of the matrix H is the sum of the heat transfer coefficient associated to the heat flux entering or exiting a node. Each row contains all the contributions relative to a single node. T is the vector of the temperatures at the nodes. Q is the vector of the heat sources, where the only terms different from zero are those corresponding to the nodes representing the cables, whether heated.

All the heat flux contributions except the heat sources are temperature dependent, as from equations 5.1, 5.2 and 5.4. Therefore the matrix system is solved by subsequent iterations, as long as the elements of the vector T feature a percentage relative variation smaller than 0.01%. Another iteration loop is present, external to the previous one. It is performed to determine the free parameters of the model that allow reproducing experimental measurements carried out with different heating configurations and different applied pressures. These parameters are the unknown channels dimensions and will be detailed in section 5.4.1 for the LHC insulation and in section 5.5.1 for the HL-LHC insulation.

5.4 LHC insulation

5.4.1 Model implementation

This section analyzes the LHC main bending (MB) dipole insulation scheme shown in Fig. 5.2, where some helium heat transfer paths are also highlighted. They will be discussed in this section. The geometric parameters of the three wrapped polyimide tapes are listed in Table 3.1.

The first two tapes create large aspect ratio micro-channels featuring different thickness

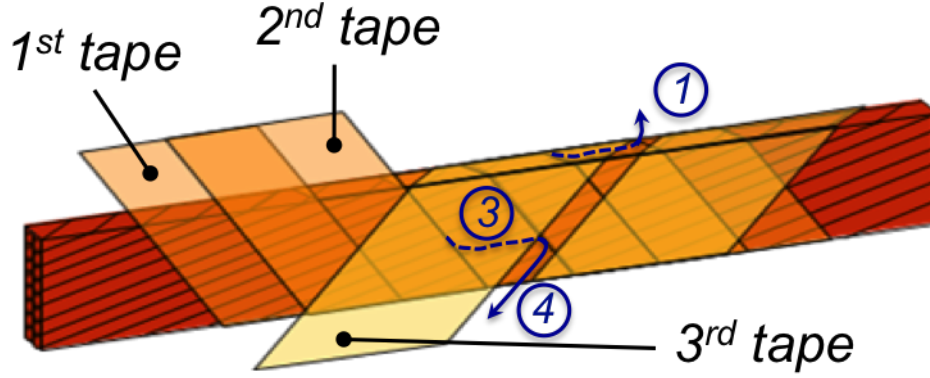


Figure 5.2: LHC insulation scheme. Two helium heat transfer path are also shown (see text for description).

whether located on the compressed or on the not compressed cable face, as shown in Fig. 5.3. Therefore we distinguish the behavior of the cable large face from that of the cable small face. In the following we will refer to these micro-channels as slits in the cable longitudinal direction having the width of the relevant cable face.

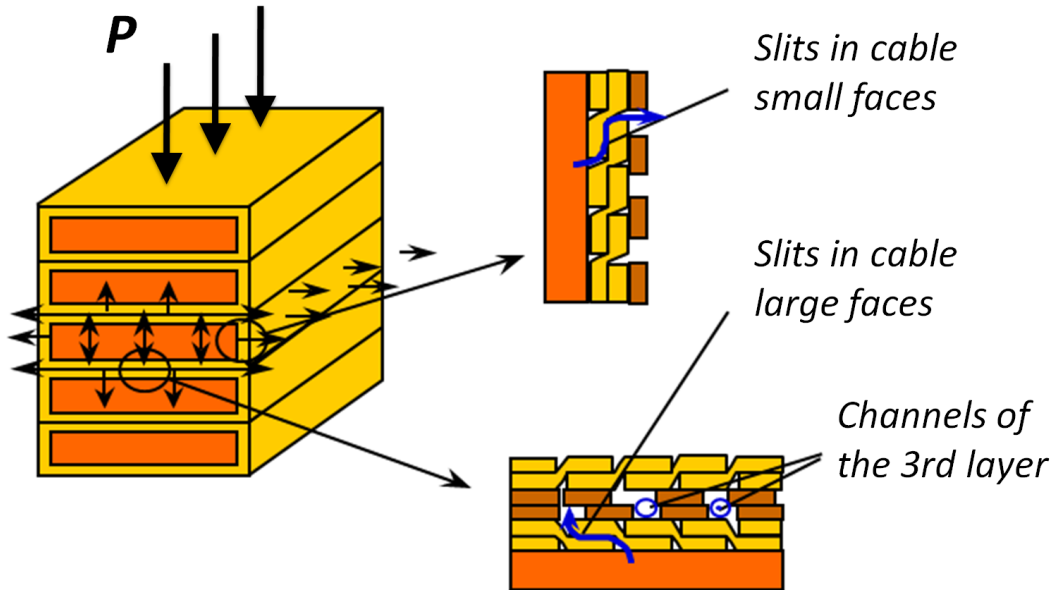


Figure 5.3: Sketch of the LHC insulation slits on the cable small and large faces, in the stack setup (from [52]).

Fig. 5.4 shows a detailed sketch of the insulation and of the heat transfer paths implemented in the model. The top and bottom pictures refer to the cable small and large face, respectively.

The slits on the cable small face provide the same heat extraction for every pressure applied on the stack, because they are not affected by the pressure applied by the sample-holder. Furthermore they are open to the bath. Their length depends on the tapes overlap, varying between a minimum of 6 mm if they exit on the spacing of the third tape, thus in

the external bath (path 1), and a maximum of 11 mm if they exit in the middle of the third tape (path 2). We calculate the total number of slits from the sample length and the width of the first two tapes. 18% of them are 6 mm long slits. For the remaining longer slits an average length is assumed.

The heat extraction through the cable small face is completed by solid conduction through polyimide, which does not feature any dependence on the applied pressure either. It is the sum of two contributions: conduction through the only first two tapes where the spacing of the third tape is (path 5), and through all the three tapes elsewhere (path 6). According to [52], we assume the polyimide conduction surface equal to the total surface with two polyimide tapes for the heat path 5, and with three tapes for the heat path 6. The considered thickness is $100\text{ }\mu\text{m}$ for heat path 5 and $169\text{ }\mu\text{m}$ for heat path 6.

The cable small face is the only one for which it is assumed that He II and polyimide conduction heat transfer are decoupled. This hypothesis was demonstrated to be consistent in [66].

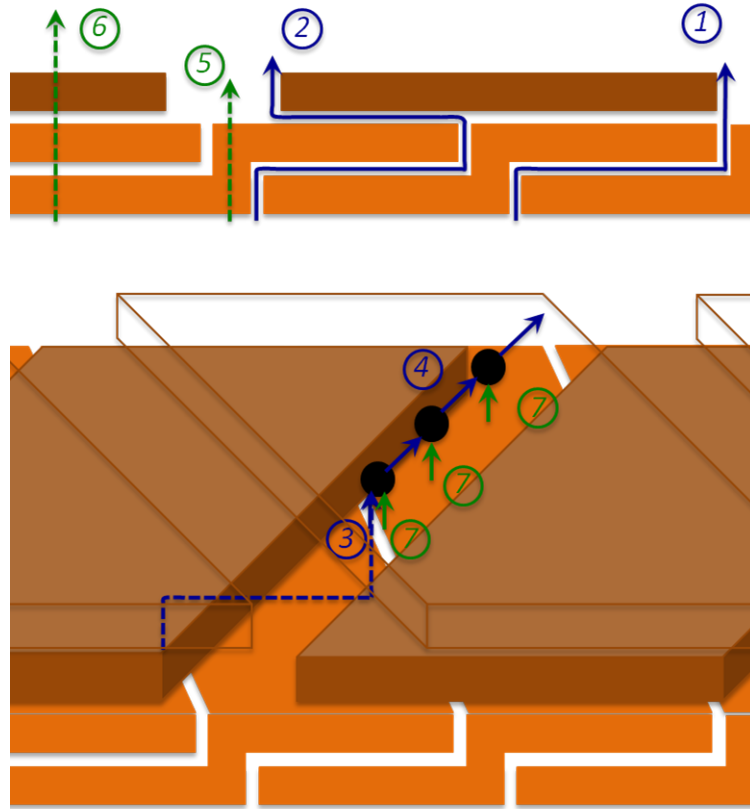


Figure 5.4: Sketch of the heat transfer paths implemented in the model, where the black balls represent the nodes. The top picture refers to the cable small face, whereas the bottom picture refers to the cable large face.

The description of the cable large face is more elaborate. The length of the slits is the same as before, whereas their thickness depends on the applied pressure. The slits (heat path 3) are not directly open to the bath, but to the channels located in the 2 mm spacing of the third layer. These third layer channels are in contact with the bath at their

extremities, through the heat paths 4. Polyimide heat transfer between the cables and the third layer channels along their length is also taken into account, through the first two insulation tapes (heat paths 7). The above mentioned hypotheses on the polyimide conduction surface and thickness are made here as well. As depicted in Fig. 5.4 (below), several nodes are defined to describe the link between slits and third layer channels, as well as the coupling between He II and polyimide heat transfer. The model accounts for the possibility that the He II link between slits and third layer channels might occur in each of the 3 nodes shown (for each half cable width), calculating the corresponding surface.

The polyimide heat path 8 allows a direct coupling of adjacent cables through the contact surface between their third tapes, as well as a link between one cable and the third layer channels of its adjacent cable, through their relevant surfaces. The compressed insulation thickness on the large cable face is derived from the mechanical measurements reported in section 3.6.

Several other nodes are defined: they correspond to the cables where the heat can be deposited, and to the bath that is kept at a constant temperature of 1.9 K.

Fig. 5.5 shows the simplified sketch of the model cross-section, where all the six cables of the measured stack are described. It is worth underlining that, although the sketch refers to the cables-stack cross-section, the third spatial direction is taken into account:

- to describe the slits in the cable longitudinal direction and the third layer channels, as explained;
- to consider all the slits, channels and polyimide surfaces along the sample length, which are lumped in one single cross-section.

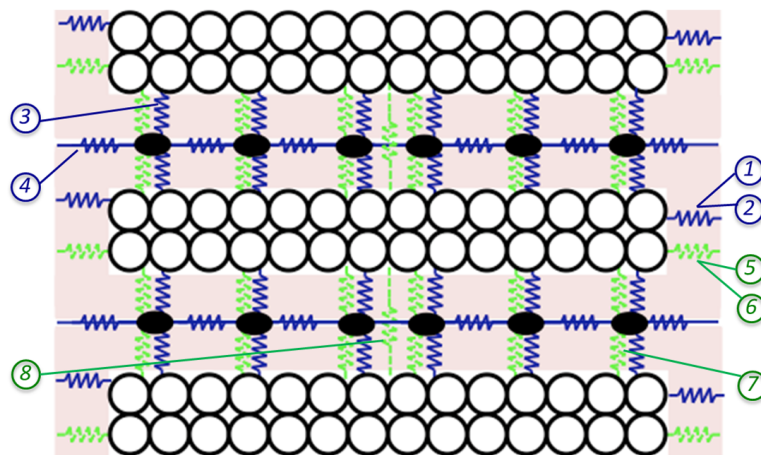


Figure 5.5: Sketch of the model developed for the LHC insulation. The black ovals are the nodes. The dark blue resistances represent the helium heat paths, whereas the light green resistances represent the polyimide heat paths.

The unknown dimensions, which constitute free parameters of the model, are:

- a. the thickness of the slits in the cable small faces: th_{small} ;
- b. the cross-section of each slit in the cable large faces: A_{large} ;
- c. the cross-section of the third layer channels. This parameter $A_{channel}$ will be expressed in terms of percentage of the non-pressed channels cross-section, i.e. 2 mm x 69 μm .

5.4.2 Results

The results are presented in terms of temperature increase as a function of the power dissipated in the 156 mm long central conductor, in a pressurized He bath at 1.9 K. The first results shown in Fig. 5.6 are obtained with a simplified model not considering the slits in the cable large faces. Calculations are compared to measurements in case of two heating configurations: one heated cable (the central one) and five heated cables. The choice of the same optimized values for th_{small} and $A_{channel}$ does not allow reproducing both measurements: if the calculation is in good agreement with the measurement for the five heated cables case, some heat removal is missing in the one heated cable case. Adding the slits in the cable large faces provides a solution to this problem, since the corresponding heat extraction is larger if the cables adjacent to the central one are not heated. It is worth reminding that heat transfer measurements from a stack sample already provided qualitative information on the mechanisms occurring in the cable large face (section 3.4.1). They proved that the helium penetrating the void spaces between adjacent cables plays a role in the cable cooling.

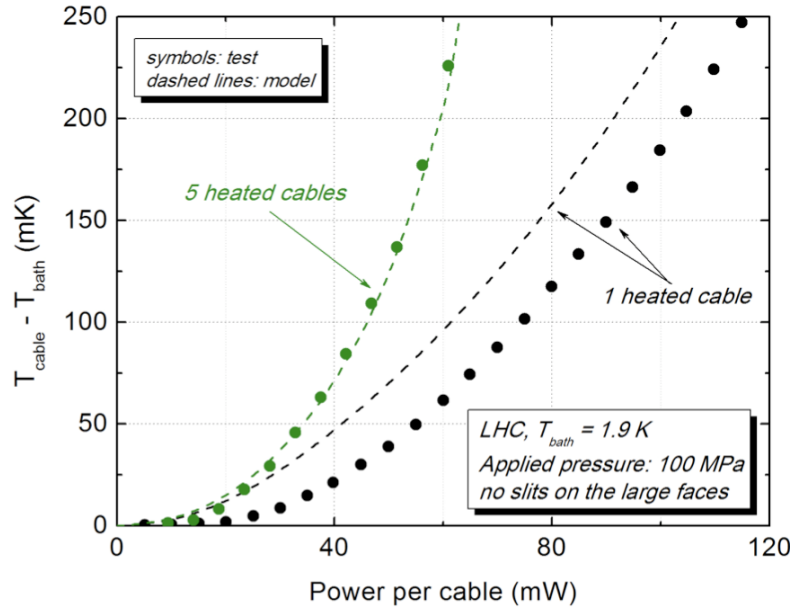


Figure 5.6: Heat transfer curves through the LHC insulation for different heating configurations, simplified model without channels in the cable large faces (curves) vs. measurements (markers).

Fig. 5.7 reports the results obtained with the full model described in the previous section, compared to the measurements performed at an applied pressure of 50 MPa. Good agreement is found for the different heating configurations, with the following choice of the unknown parameters:

- $th_{small} = 6.64 \mu\text{m}$;
- $A_{large} = 1.69 \mu\text{m}^2$;
- $A_{channel} > 10\%$.

The small value of A_{large} is associated to a regime of pure superfluidity, as it will be shown, that allows an extremely larger heat transfer than in other regimes. It is useful to remind that such values are obtained in the assumption of a constant cross-section

along the channel length. In case of the large (pressed) cable face this hypothesis is not as reliable as for the small (non pressed) face, because the channels will feature several and important restrictions. A_{large} has to be considered as the equivalent cross-section under the mentioned assumptions. It is worth noting that larger values of $A_{channel}$ do not substantially modify the results of the calculation, since the bottleneck of the heat extraction through the cable large faces is represented by the He II and polyimide heat transport towards the channels of the third layer.

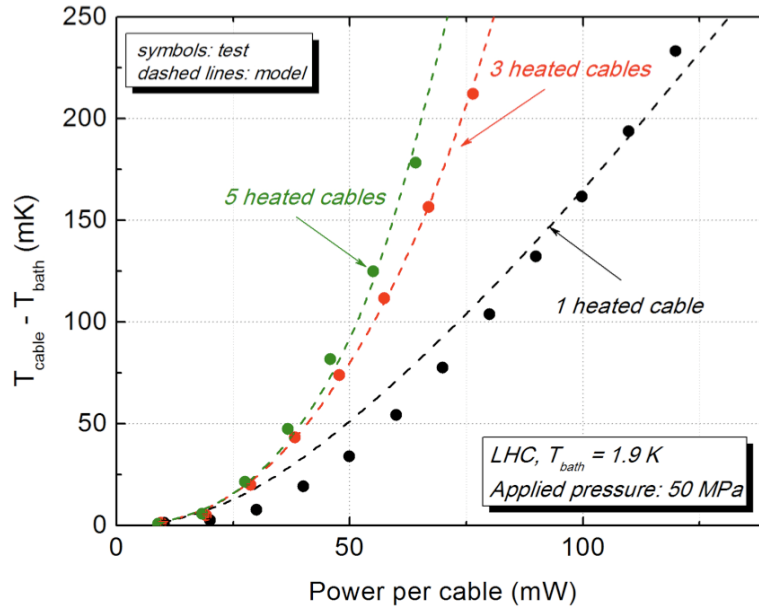


Figure 5.7: Heat transfer curves through the LHC insulation for different heating configurations, model (curves) vs. measurements (markers).

The heat fluxes exiting the cable can be grouped into the following contributions:

- He II through the cable small faces (heat paths 1 and 2);
- Polyimide conduction through the cable small faces (heat paths 5 and 6);
- He II through the cable large faces towards the third layer channels (heat path 3);
- Polyimide conduction through the cable large faces towards the third layer channels (heat path 7);
- Polyimide conduction between adjacent cables (heat path 8).

Fig. 5.8 reports such contributions, in case of 3 heated cables at an applied pressure of 50 MPa. The He II heat flux through the cable small faces is the largest contribution. It represents more than 60% of the total heat extraction for small temperature increase. It tends towards a vertical asymptote while approaching T_λ , and its relative contribution decreases to 50%. The polyimide conduction through the cable small faces and between adjacent cables is small, whereas the two mechanisms of heat transfer to the channels of the third layer in the cable large faces play a non negligible role. In particular, the polyimide contribution through the cable large faces represents 20% of the total heat extraction. The critical heat flux delimiting the Landau from the Gorter-Mellink region is estimated to be 16 mW for the slits of the cable small faces and 100 mW for those of the cable large faces.

This means that the He II heat transfer is always described by equation 5.4 for the slits of the cable small faces and by equation 5.2 for the slits of the cable large faces.

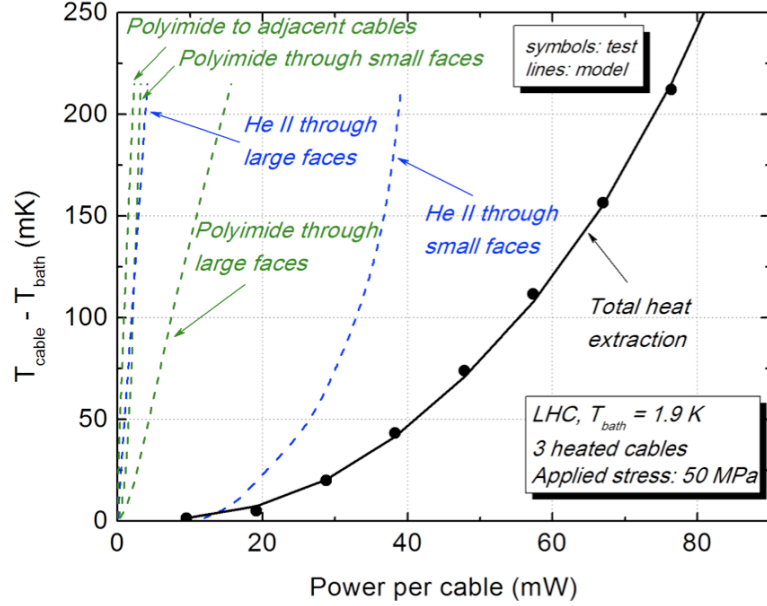


Figure 5.8: Contributions to the heat extraction through the LHC insulation.

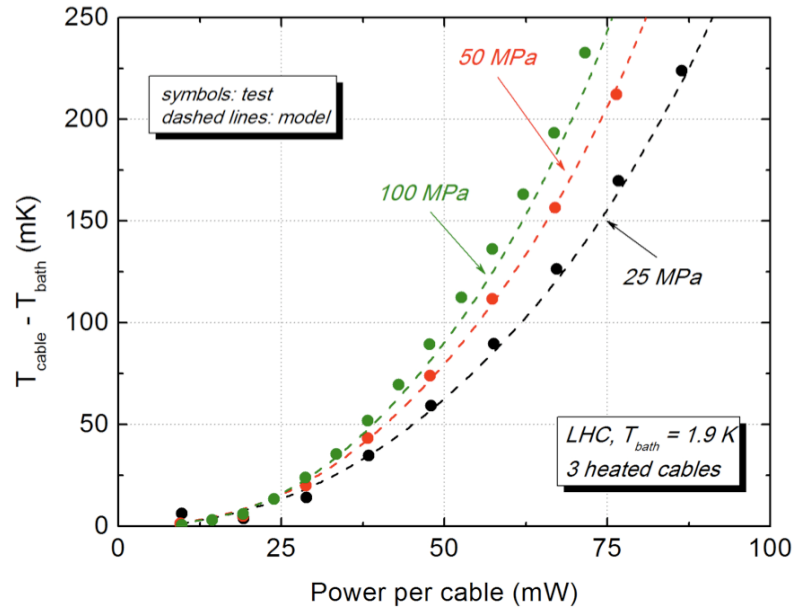


Figure 5.9: Heat transfer curves through the LHC insulation for different applied pressures, model (curves) vs. measurements (markers).

Fig. 5.9 presents the case of 3 heated cables for different applied pressures. The same th_{small} of $6.64 \mu\text{m}$ is used in all cases, because it does not depend on the pressure. The other parameters decrease while increasing the pressure, as reported in Table 5.1. In general the agreement between the LHC model and the relevant measurements is within

Insulation scheme	slits/channels	25 MPa	50 MPa	100 MPa
LHC (MB)	th_{small}	6.64 μm	6.64 μm	6.64 μm
	A_{large}	1.72 μm^2	1.69 μm^2	1.63 μm^2
	$A_{channel}$	>20%	>10%	>5%

Table 5.1: Summary of the average slits and micro-channels dimensions for the LHC insulation. They were determined with the developed model as a function of the applied pressure.

7%, except for the one heated cable configuration where the error can be larger below a temperature increase of 100 mK.

5.4.3 Images of the slits on the cable small and large face

Stacks made of two insulated cables were prepared in order to visualize their electrical insulation under the microscope. The 2-units stacks were cured according to the 80 MPa cycle mentioned in section 3.3.2. Two different methods were employed to prepare the samples:

1. the stack is inserted in a small sample holder which applies the required pressure. A cut of sample and sample holder can be realized in the cable transversal direction or with a small angle with respect to it, while always compressing the sample;
2. the stack is vacuum impregnated, while compressing it with the required pressure. The impregnation resin allows freezing the insulation tapes, although the pressure is released after removal of the sample from the mould. In this case the absence of the sample holder allows cutting the sample along the preferred direction.

In both cases the sample preparation was completed by polishing the cross-section. Both methods were used to take micro-scope images of the LHC (MB) and HL-LHC (EI4) insulation schemes. For each insulation, the images obtained with the two methods are in agreement. However, for the LHC insulation it is more interesting to look at the cable cross-section. Therefore in this section we will address the first method, and the pictures here shown were obtained with it. The second method is more useful for the HL-LHC insulation since it allows obtaining images of the micro-channels cross-section, where the predominant heat transfer occurs (see section 5.5). Hence it will be addressed in section 5.5.3.

Fig. 5.10 shows the sample holder applying an average pressure of 57 MPa at room temperature on the 2-units stacks (left). The middle picture is the polished cross-section of the sample, whereas the picture on the right shows a micro-scope image obtained with a small enlargement.

The pictures reported in Fig. 5.11 are details of the cable small faces, where the strands and the slits between the tapes can be clearly identified. They feature a non-constant thickness ranging approximately from 3 to 18 μm , which is in agreement with the theoretical thickness of around 7 μm determined through the modeling.

Fig. 5.12 shows two details of the insulation on the pressed cable large faces. It is possible to distinguish some slits between the tapes, as those assumed in the model.

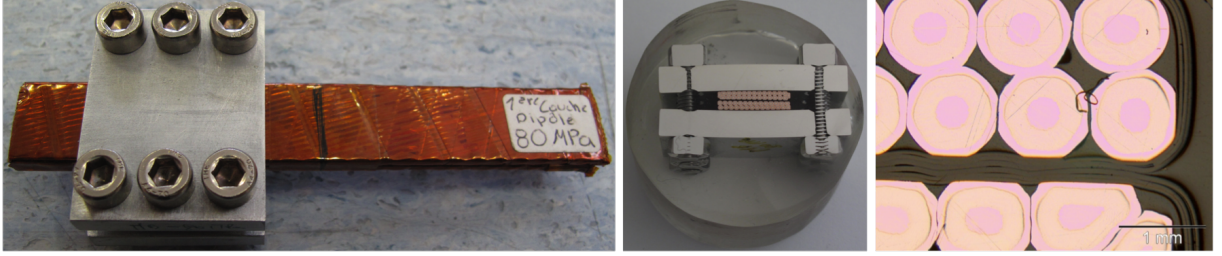


Figure 5.10: Sample holder and 2-units stacks (left). Polished sample cross-section (middle). Micro-scope image obtained with a small enlargement (right).

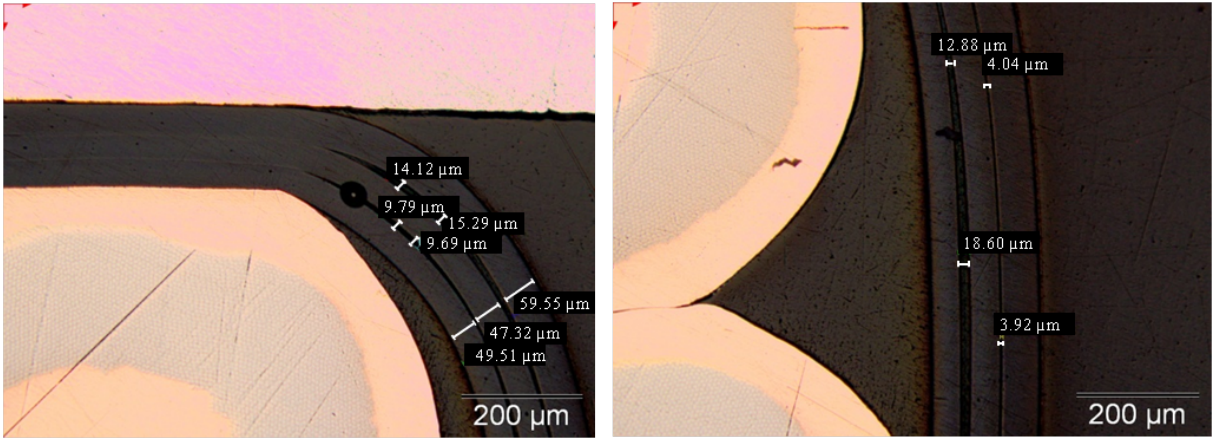


Figure 5.11: Slits in the LHC insulation scheme located on the cable small faces. Left: insulation around a strand located between the cable small and large face. Right: insulation close to strands in the cable small face.

However, they are far from featuring a constant shape and thickness. This observation confirms hypotheses and results of the model developed for the LHC insulation.

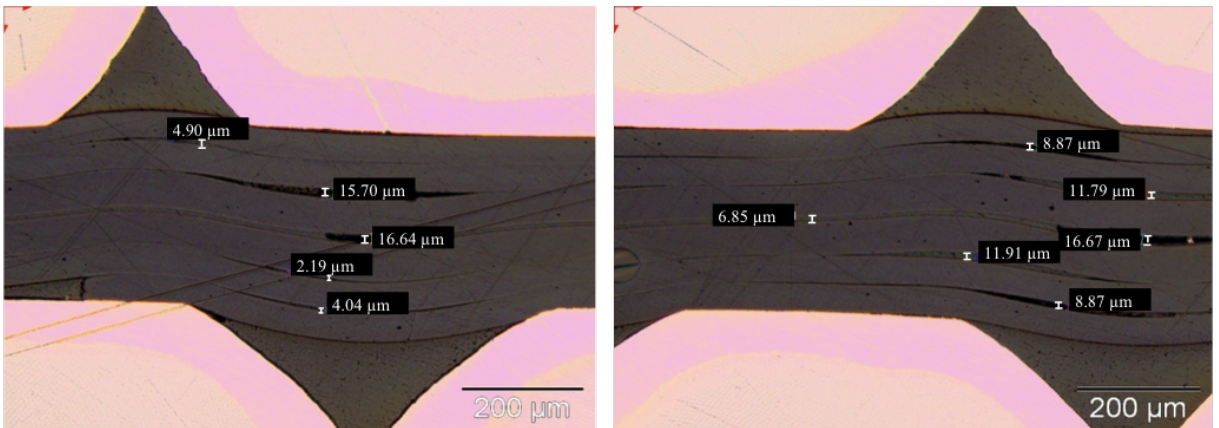


Figure 5.12: Slits in the LHC insulation scheme located on the cable large faces.

5.5 HL-LHC insulation

5.5.1 Model implementation

This section analyzes the HL-LHC (EI4) insulation scheme shown in Fig. 5.13. The geometric parameters of the three wrapped polyimide tapes are listed in Table 4.1.

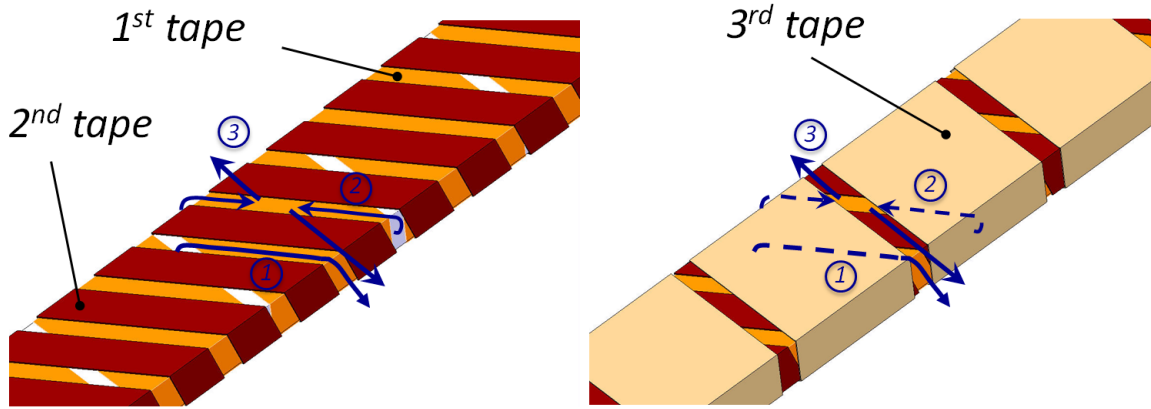


Figure 5.13: HL-LHC insulation scheme. The main helium heat transfer path are also shown (see text for description).

The main innovations of the HL-LHC scheme are the channels created along the second tape, as well as the openings between first and second tape and between second and third one. This provides a large direct path from the strands to the bath.

The mentioned channels, hereafter referred to as second layer channels, are 9.5 mm long. They can either come out in the cable small face (heat path 1), hence directly to the bath, or in the cable large face (heat path 2). In the latter case a supplementary channel length has to be considered before reaching the bath, along the edges of the third tape (heat path 3). We will refer to this supplementary length as to third layer channels. The total length between strands and bath through second and third layer channels can reach a maximum of 17.4 mm. These He II heat paths are presented in Fig. 5.13.

Every second layer channel lies on the cable large faces for most of its length. In this zone it is submitted to the pressure applied on the stack, hence all the channels feature the same minimum cross-section. For this reason, unlike what we did for the LHC insulation, the heat transfer contribution of the large face will not be differentiated from that of the small face.

The choice of not separating the thermal behavior of small and large cable faces has also a physical meaning. The described helium heat transfer paths run indeed around the cable, concerning at the same time its small and large faces. This is confirmed by the results of the heat transfer tests performed in [89], through a setup aimed at reproducing the behavior of the only compressed large face. The measurements performed in such conditions show a small improvement of heat transfer through the HL-LHC insulations (EI4, EI3) with respect to the LHC (MB) one, of around 25%. This is much smaller than the major improvement measured in our tests (section 4.5). Small and large cable faces must therefore work together to exploit the He II open structure of the HL-LHC insulation.

Fig. 5.14 shows a detailed sketch of the insulation and of the heat transfer paths implemented in the model. Both the second layer channels (helium heat path 1 or 2)

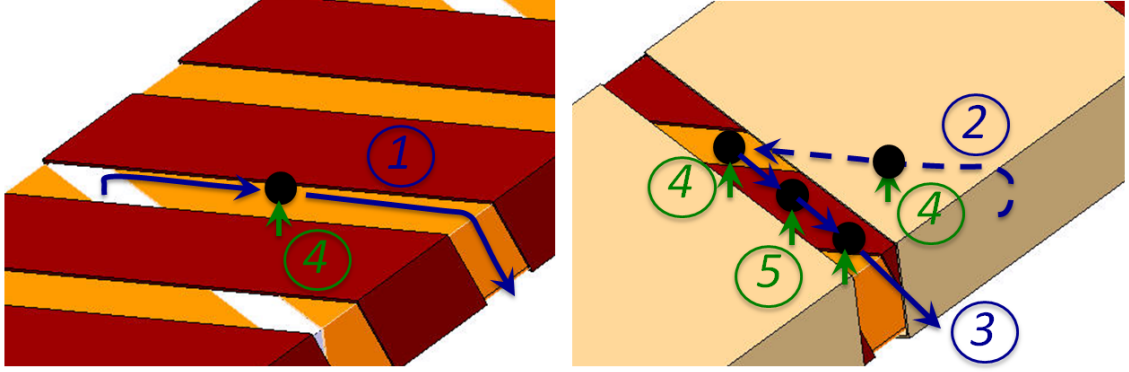


Figure 5.14: Sketch of the heat transfer paths implemented in the HL-LHC model. The black nodes represent the nodes.

and the third layer channels (helium heat path 3) are described. 12% of the second layer channels exit directly in the bath. The remaining ones are coupled to the third layer channels.

A node is defined in the middle of the second layer channels, to consider the coupling with the polyimide heat transfer occurring through the first insulation tape (heat path 4). Other nodes are defined along the third layer channels. They account for heat deposit along their length due to:

- helium second layer channels (heat paths 1 and 2);
- polyimide conduction through the first insulation tape (heat path 4);
- polyimide conduction through the first and second insulation tapes (heat path 5).

The model accounts for the possibility that the He II link between second and third layer channels might occur in each of the 3 nodes shown in Fig. 5.14 (for each half cable width), calculating the corresponding surface. The remaining nodes concern the link between polyimide conduction and third layer channels. This feature of the model is schematically shown in Fig. 5.15, in the heat transfer paths shown above and below the strands.

Two more nodes are defined, corresponding to the cable strands and to the 1.9 K external bath. The polyimide solid conduction contributions through the cable small face, as well as towards the adjacent cables, are implemented. The geometrical insulation thickness (of either two or three tapes) is considered for the small face. The average compressed insulation thickness, derived from the measurements reported in section 4.7, is used for the large face.

The slits in the cable longitudinal direction, that were considered for the LHC insulation, are neglected in this case because noticeably smaller than the second layer channels.

It was shown in section 4.5.3 that adjacent cables insulated with the HL-LHC scheme are thermally decoupled to each other well above T_λ . A model focusing on one single cable could therefore be developed, assuming the adjacent cables to be at the bath temperature. Its simplified sketch is reported in Fig. 5.15. As for the LHC model, besides the cable cross-section we also take into account the third spatial direction to describe all the helium channels along their whole length, as well as the coupling with the polyimide conduction mechanism.

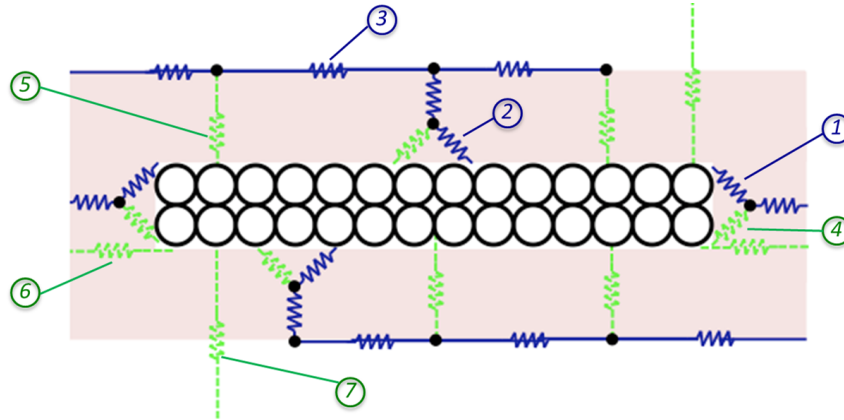


Figure 5.15: Sketch of the model developed for the HL-LHC insulation. The black circles are the nodes. The dark blue resistances represent the helium heat paths, whereas the light green resistances represent the polyimide heat paths.

The unknown dimension constituting the only free parameters of the model is the cross-section of the second layer channels. The cross-section of the third layer channels is considered to scale accordingly. This parameter $A_{channel}$ is expressed in terms of percentage of the non-pressed channels cross-section, i.e. $1.5 \text{ mm} \times 75 \text{ }\mu\text{m}$.

5.5.2 Results

Fig. 5.16 reports the results obtained in case of one and five heated cables, compared to measurements performed at an applied pressure of 50 MPa. A good agreement is found with an $A_{channel}$ of 39% in the five heated cables case and of 44% in the one heated cable case. This difference is due to the fact that, in the one heated cable case, the central conductor can profit of the channels network of its cold adjacent cables. Therefore the actual channels cross-section should be estimated in the five heated cables case.

The heat fluxes exiting the cable can be grouped into the following contributions:

- He II through the second layer channels (heat paths 1 and 2);
- Polyimide conduction through the first tape to the middle of the second layer channels (heat path 4);
- Polyimide conduction through first and second tape to the third layer channels (heat path 5);
- Polyimide conduction through cable small faces (heat path 6);
- Polyimide conduction between adjacent cables (heat path 7).

Fig. 5.17 reports such contributions in case of five heated cables compressed at 50 MPa. The He II heat flux through the second layer channels is by far the largest contribution, representing 90% of the total heat extraction. The critical heat flux delimiting the Landau from the Gorter-Mellink regime is estimated to be 36 mW through equation 5.5, thus confirming the establishment of a fully developed turbulent regime. The polyimide heat fluxes have a minor impact. Among them, the most significant one is that through the first tape to the middle of the second layer channels. It represents less than 10% of the total heat extraction.

Fig. 5.18 presents the case of five heated cables for different applied pressures. The

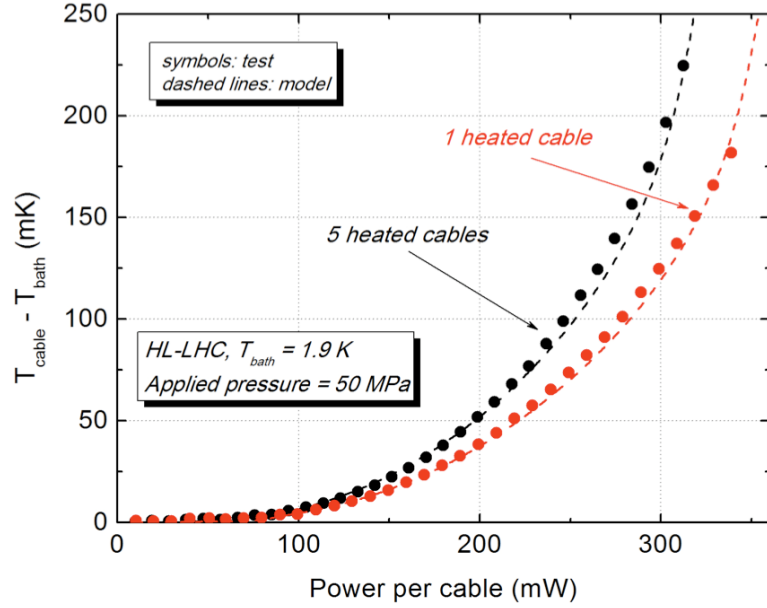


Figure 5.16: Heat transfer curves through the HL-LHC insulation for different heating configurations, model (curves) vs. measurements (markers).

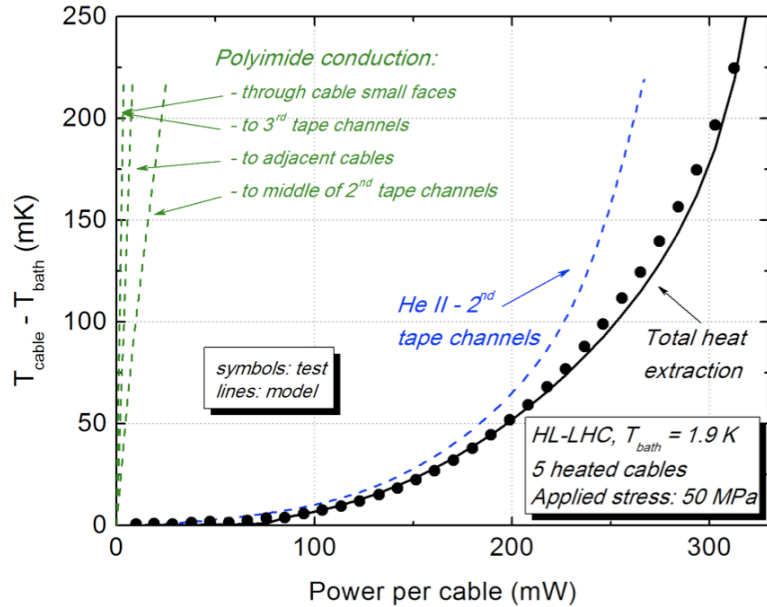


Figure 5.17: Contributions to the heat extraction through the HL-LHC insulation.

$A_{channel}$ values that better fit the experimental data are reported in Table 5.2. $A_{channel}$ decreases while increasing the pressure, and is sufficiently large even at the highest pressures required for magnet operation. In general the agreement between the HL-LHC model and the relevant measurements is within 6%.

The average channels cross-section obtained with the presented thermal model is comparable to that obtained with similar models on other variants of HL-LHC insulations [90][91], albeit not validated for the different mechanical and heating configurations tested. A

Insulation scheme	channels	25 MPa	50 MPa	100 MPa
HL-LHC (EI4)	$A_{channel}$	41%	39%	35%

Table 5.2: Summary of the average micro-channels dimensions, for the HL-LHC insulation. They were determined with the developed model as a function of the applied pressure.

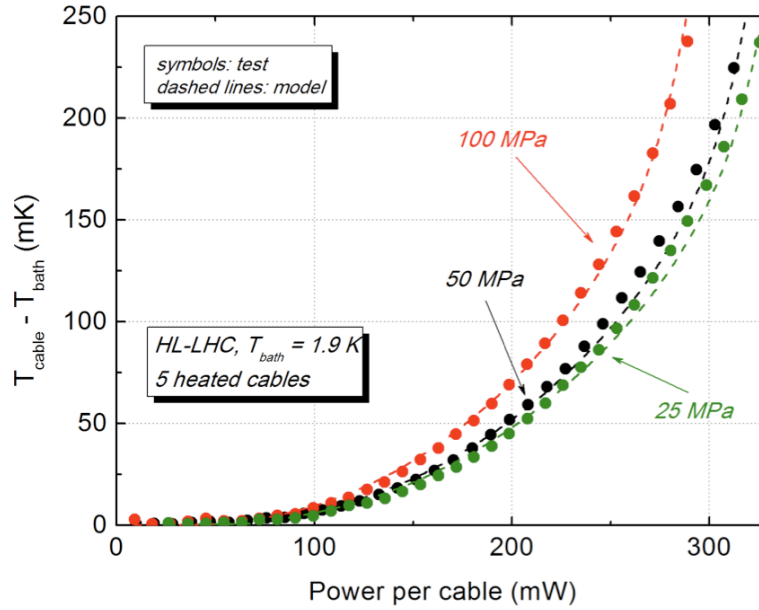


Figure 5.18: Heat transfer curves through the HL-LHC insulation for different applied pressures, model (curves) vs. measurements (markers).

finite elements model was also developed to investigate the channel deformation in the HL-LHC (EI4) scheme from the mechanical point of view [92]. The main approximation of our thermal model is to consider average dimensions for the channels, uniform along their length. As far as the mechanical model is concerned, it does not take into account plastic deformations due for instance to the curing cycle and to creep mechanisms, as well as the stress induced by the differential thermal contractions of the coil components. Despite that, the values of minimum $A_{channel}$ predicted by the mechanical model at 50 and 100 MPa (48 and 39%, respectively) are not far from those determined in this section.

5.5.3 Images of the micro-channels

The images presented in this section were obtained on samples made of impregnated cables, as explained in section 5.4.3. The impregnation resin injected in the vacuum mould is the CTD-101, which features a very low viscosity and is for this reason used for impregnating Nb₃Sn cables [93]. During the impregnation an average pressure of 49 MPa at room temperature was applied on the 2-units stacks. The pressure was released after removal of the sample from the mould. However, the low-viscosity resin penetrated in the void spaced between the insulation tapes allowed freezing them. Fig. 5.19 shows the

vacuum impregnation mould on the left, and polished sample cross-sections on the right.

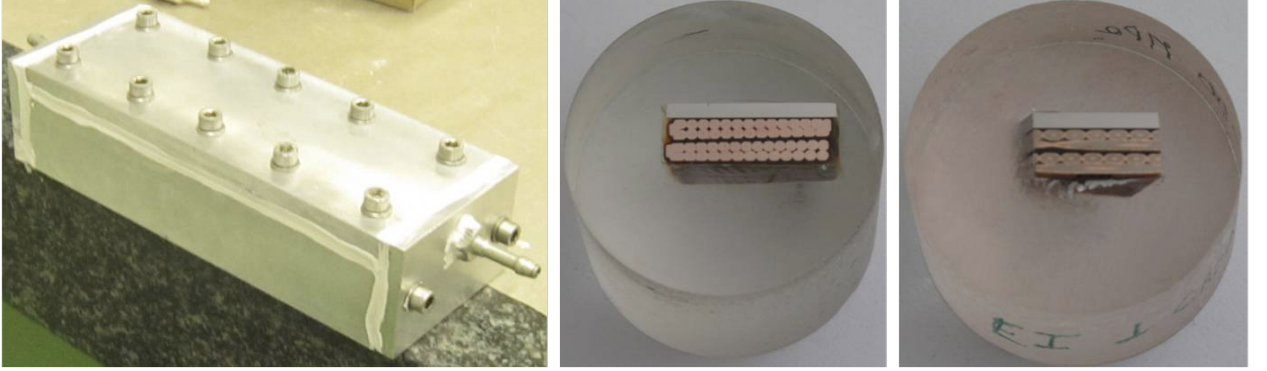


Figure 5.19: Mould for vacuum resin impregnation (left). Polished sample cross-sections: perpendicular to the cable longitudinal direction (middle) and to the second layer channels (right).

The pictures in Fig. 5.20 show details of the insulation in the compressed cable large face (between adjacent cables). The cut direction is perpendicular to the second layer channels of one of the two cables. It is observed that the second and third layers channels are open in the majority of the cases, though they feature drastic cross-section reduction in few other cases (bottom right picture). In general, the microscopic visualization of the HL-LHC insulation confirms the presence of an extremely open structure, even at high applied pressures. This observation agrees with the large measured and modeled heat extraction. The insulation structure is far from regular, therefore it is worth stressing once more that the channels dimension determined through the thermal model has to be considered as an average cross-section.

We also took images of the cable small face, where we could observe similar slits as in the LHC insulation scheme (Fig. 5.11). These slits featured a non-constant thickness between approximately 0 and 25 μm . Such dimensions cannot provide an explanation for the large heat transfer capacity of the HL-LHC insulation, as the thermal model also confirmed.

5.6 Conclusion

The developed model allowed to quantitatively explain the results of the experimental heat transfer tests reported in the two previous chapters. By comparison to measurements performed in different heating configurations and at different applied pressures, the model allowed identifying the main mechanisms for heat extraction in the LHC and HL-LHC schemes. The He II micro-channels were recognized to be responsible for the most significant heat transfer. Their unknown dimensions were identified from the thermal analysis, and confirmed by microscope images.

In the LHC insulation, the micro-channels consist of slits created by the tapes overlap. They feature an average thickness of about 7 μm in the non-pressed (small) cable face, permitting the establishment of a turbulent regime. In the pressed (large) cable face the equivalent cross-section of each slit is instead smaller than 2 μm^2 , resulting in a laminar regime. In the HL-LHC insulation, the micro-channels are located between the wrappings of the intermediate tape. In the mechanical conditions typical of magnet operation they

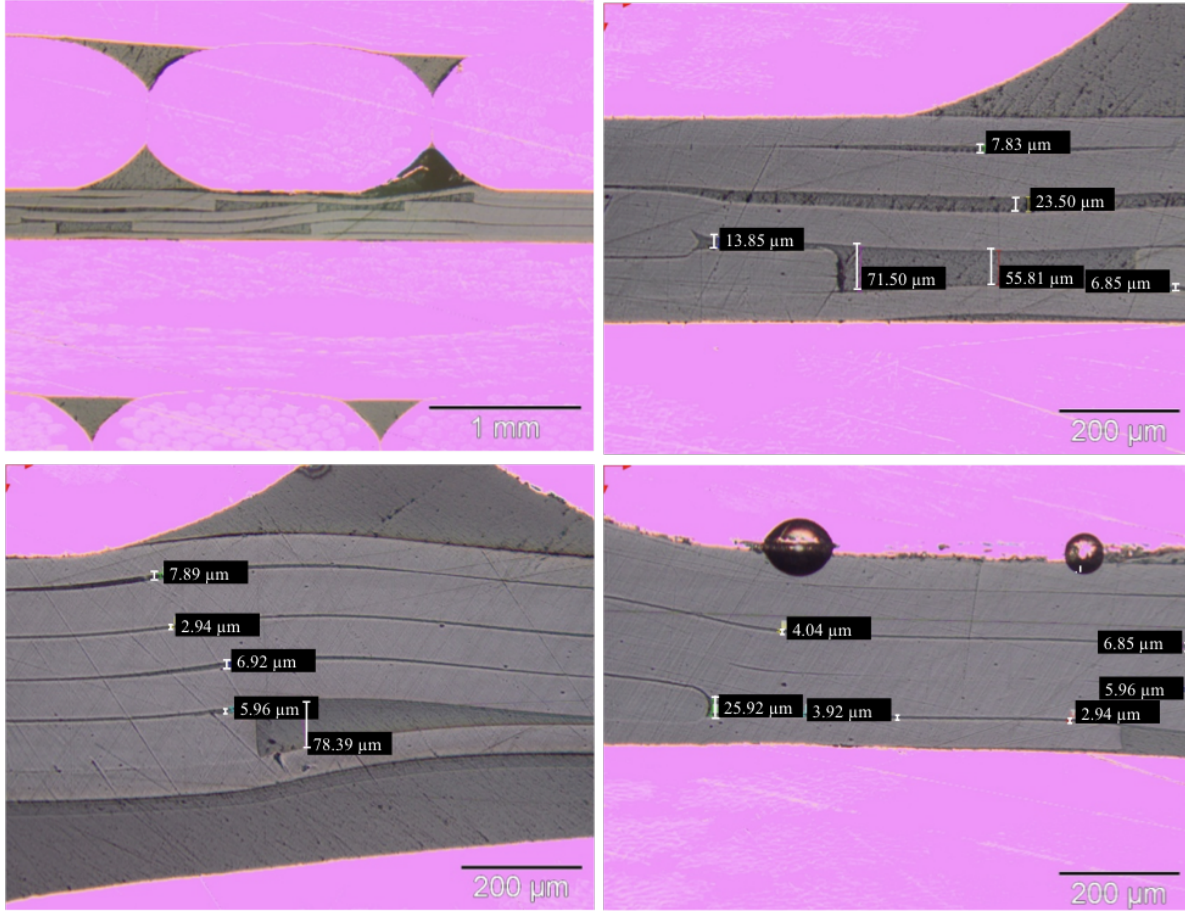


Figure 5.20: Micro-channels in the HL-LHC insulation scheme on the cable large faces (between adjacent cables). The top left picture is obtained with a small zoom, whereas a larger enlargement is used for the others.

feature an average cross-section of about 40% of their non-pressed geometrical size, which allows the establishment of a fully developed Gorter-Mellink regime.

Chapter 6

Experimental and theoretical characterization of He II heat transfer in narrow channels

Contents

6.1	Introduction	97
6.2	Background notions	98
6.3	Development of the experimental program	98
6.3.1	Micro-channels fabrication	98
6.3.2	Sample preparation and instrumentation	101
6.3.3	Measurements	104
6.4	Samples and characterization	105
6.5	Results and analysis	107
6.5.1	Landau regime	108
6.5.2	Gorter-Mellink regime	110
6.5.3	Critical heat flux (end of Landau regime)	114
6.6	Conclusion	116

6.1 Introduction

In the modeling presented in the previous chapter we assumed that the classical helium heat transport laws are valid for narrow channels with typical dimension often smaller than 10 μm . However the available literature shows that this was only confirmed down to channels of 56 μm diameter [94]. This was the motivation for conceiving, developing and carrying out a new activity both experimental and theoretical, to investigate the heat transport through micro-channels in pressurized superfluid helium.

This activity required the development of challenging samples. Micro-fabrication techniques were employed, in collaboration with the EPFL Center of MicroNanoTechnology and the CERN Physics department, to etch channels down to a depth of $\sim 16 \mu\text{m}$. Heat transfer measurements were performed in collaboration with the CEA-Saclay institute.

Steady-state conditions in static pressurized He II were addressed at different bath temperatures. The laminar and turbulent regimes were identified and the Gorter-Mellink parameter was determined as a function of temperature. The critical heat flux separating these two dynamic regimes of superfluid helium was also identified.

6.2 Background notions

The heat transport through micro-channels in the LHC conditions of pressurized He II (He IIp) was not much investigated. Few papers report results for cooling channels with dimensions of several mm, typically used for nuclear fusion and energy storage [95][96]. To our knowledge the only work recently investigating channels of hydraulic diameter smaller than 1 mm was [94], down to 56 μm .

On the other hand, extensive studies can be found in literature on micro-channels in saturated He II (He IIs) [49][97][98][99][100], with significant differences with respect to the LHC relevant cooling. For instance, the Gorter-Mellink coefficient in He IIs features a geometrical dependence whereas it does not in He IIp, at least down to 56 μm [94]. A different behavior was also observed in stack measurements [53].

6.3 Development of the experimental program

The developed experimental apparatus consists of micro-channels that connect an isothermal heated He II volume to the He II external bath. Two types of setup were developed, based on the same concept. In this section we describe the micro-channels fabrication techniques, the sample instrumentation and assembling, as well as the measurement technique.

6.3.1 Micro-channels fabrication

The part of the setup containing the micro-channels was prepared in a class 100 clean room [101]. It was made of two 525 μm thick Pyrex[®] wafers [102] with a diameter of 100 mm. An array of 158 to 1000 parallel micro-channels covering an area of 45 mm x 55 mm was etched in one of the wafers. The number of channels depends on their width and on the width of the walls separating them. These dimensions vary from one sample to another. Their length was kept constant at 55 mm and the micro-channels were connected via a single inlet distribution manifold and a single outlet. The second wafer served as cover.

During tests the samples were immersed in a helium bath. The choice of maximizing the number of channels was done to increase as much as possible the helium heat transfer, scope of the test. A low thermal conducting material was selected to reduce as much as possible the parasitic heat (Pyrex[®] solid conduction) towards the bath.

Three different etching techniques were adopted depending on the required depth of the micro-channels. They are all based on a photolithographic patterning process [103][104][105], that is schematically shown in Fig. 6.1. A photoresist film is applied on the wafer. It is a polymer which is sensitive to ultraviolet (UV) light. The original pattern to be transferred is printed in a photomask (corresponding to the negative in photography),

which is impenetrable for the UV light. The photomask is set in a mask-aligner/exposure tool, aligned to the photoresist-coated wafer and exposed to UV radiation. Exposure changes photoresist solubility, which enables selective removal of the resist film. The areas where the photoresist film are exposed are defined by the photomask, thus developing the desired pattern. The photoresist film resists etching, hence it acts as a mask for the subsequent etching of the underlying material. After etching, the wafer is cleaned to remove the etchant and the photoresist film.

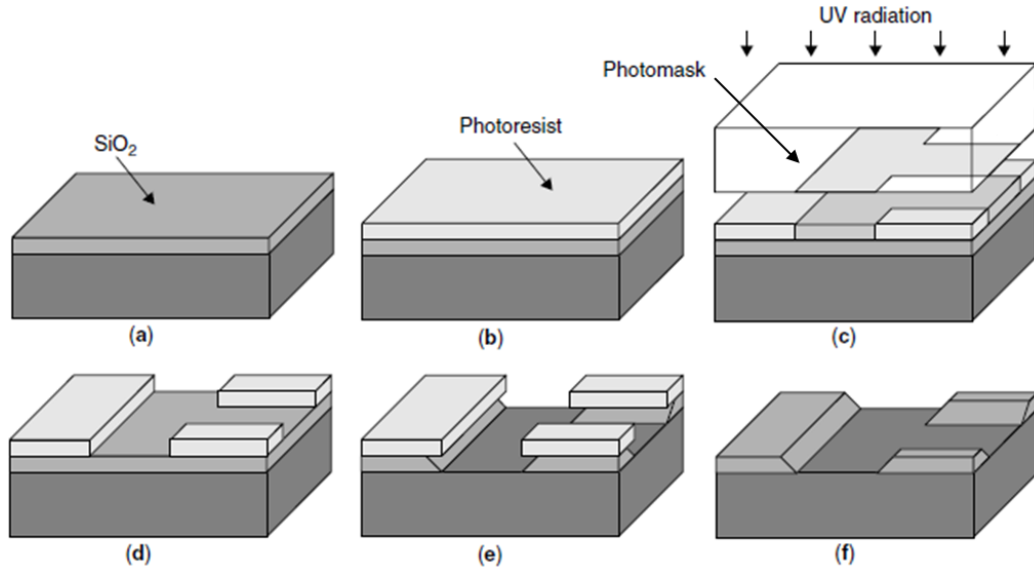


Figure 6.1: Lithographic patterning process (from [103]): oxide-film deposition (a); photoresist application (b); UV exposure through a photomask (c); development of resist image (d); etching of oxide (e) and photoresist removal (f).

For this project, channels deeper than 20 μm were realized by sandblasting (abrasive etching technique or powder blasting) [106]. A high-pressure mixture of air and powder ceramic particles are accelerated through a nozzle towards the wafer. Once the particles hit the wafer, they erode the surface at a rate of around 30 $\mu\text{m}/\text{s}\cdot\text{cm}^2$.

Channels with a thickness smaller than 20 μm were etched either by wet isotropic chemical etching or deep reactive ion etching (DRIE). In the wet etching case the wafers are immersed in a Buffered Hydrofluoric Acid (BHF) solution. This etchant chemically reacts with the wafer surface dissolving the wafer material, whereas the resist layer used as a hard mask (Cr-Au-Cr-Au) is immune to the etchant. The etch rate of Pyrex[®] in BHF (7:1) is of the 30 nm/min at 20 °C. DRIE etching is done in a vacuum chamber by reactive gases excited by RF-fields, and is a combination of chemical (reactive) and physical (bombardment) processes. In this case a layer of amorphous silicon (aSi) was used as a mask. Typical etch rates of Pyrex[®] are of the order of 450 nm/min with a mask selectivity of 10:1, meaning that for 10 μm of Pyrex[®] etched the thickness of aSi being etched is of about 1 μm . Both in wet etching and DRIE, one has to take into account the under-etching mechanism while designing the initial mask (Fig. 6.1 (e)). In the first case the isotropic etching front usually proceeds as a spherical wave from all points open to the etchant, whereas in the latter case the side walls are nearly vertical.

The micro-fabrication process-flow of the wafers for our two setups is illustrated in

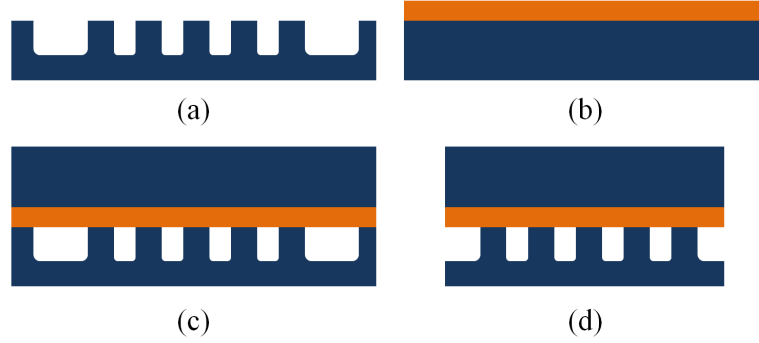


Figure 6.2: Fabrication process-flow of the first setup. The channels are etched in the lower Pyrex[®] wafer (a). A 50 nm aSi layer is deposited on the cover Pyrex[®] wafer (b) to anodically bond it to the structured wafer (c). The assembly is diced to open the manifolds to the heated volume and to the bath (d).

Figs. 6.2 and 6.3, respectively [107]. In both cases it starts with the etching of the channels in one wafer (Figs. 6.2(a) and 6.3(a)), and deposition by sputtering of a 50 nm layer of aSi on the surface of the second wafer (Figs. 6.2(b) and 6.3(b)).

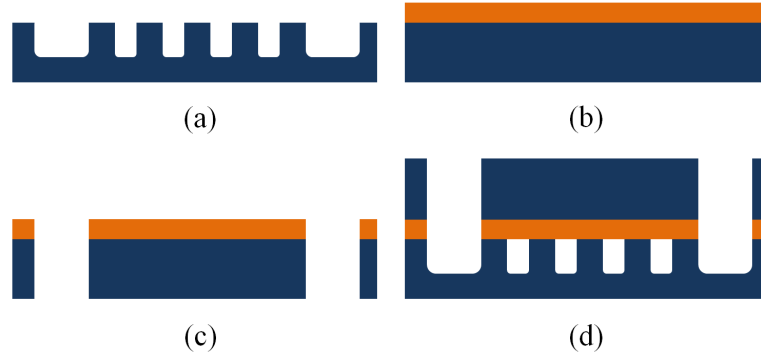


Figure 6.3: Fabrication process-flow of the second setup. The channels are etched in the lower Pyrex[®] wafer (a). A 50 nm aSi layer is deposited on the cover Pyrex[®] wafer (b). The latter is sandblasted to open through holes to link the channels to the heated volume and to the bath (c), once anodically bonded to the structured wafer (d).

In the first setup the cover wafer was left unstructured, whereas in the second setup it contained sandblasted through holes matching the dimensions of the inlet and outlet distribution manifolds (Fig. 6.3(c)). The two wafers were then anodically bonded to close the micro-channels (Figs. 6.2(c) and 6.3(d)). Anodic bonding, also known as electrostatic bonding, provides strong, hermetic and permanent chemical bonds across the interface [108]. It is realized between an electrically conducting material (e.g. silicon) and an ion conducting material (e.g. Pyrex[®]). In order to bond two Pyrex[®] wafers to each other we used an aSi intermediate layer. The two wafers were placed on top of one another and a high voltage of 1200 V was applied across them. A pressure of 1.5 bar was applied at a temperature of 350 °C. Since bonding entails elevated temperatures and our application is cryogenic, it is crucial that the thermal expansion of Pyrex[®] and aSi are similar in the whole temperature range to prevent stress development. Their thermal expansion coefficient features small

difference between room temperature and 600 °C (from 2.5 to $4 \times 10^{-6}/^{\circ}\text{C}$), whereas a small deviation exists below -50 °C. Repeated cooling tests to liquid nitrogen temperature (77 K) were carried out to verify the assembly mechanical resistance. No damage was observed by visual and microscopic inspection, thus confirming the results of [109].

In case of the second setup the fabrication is finished. A picture of the bonded wafers is shown in Fig. 6.4 (right). For the first setup, since there are no through holes, the assembly had to be diced in order to open the manifolds to the heated volume and to the bath (Figs. 6.2(d) and 6.4 (left)).

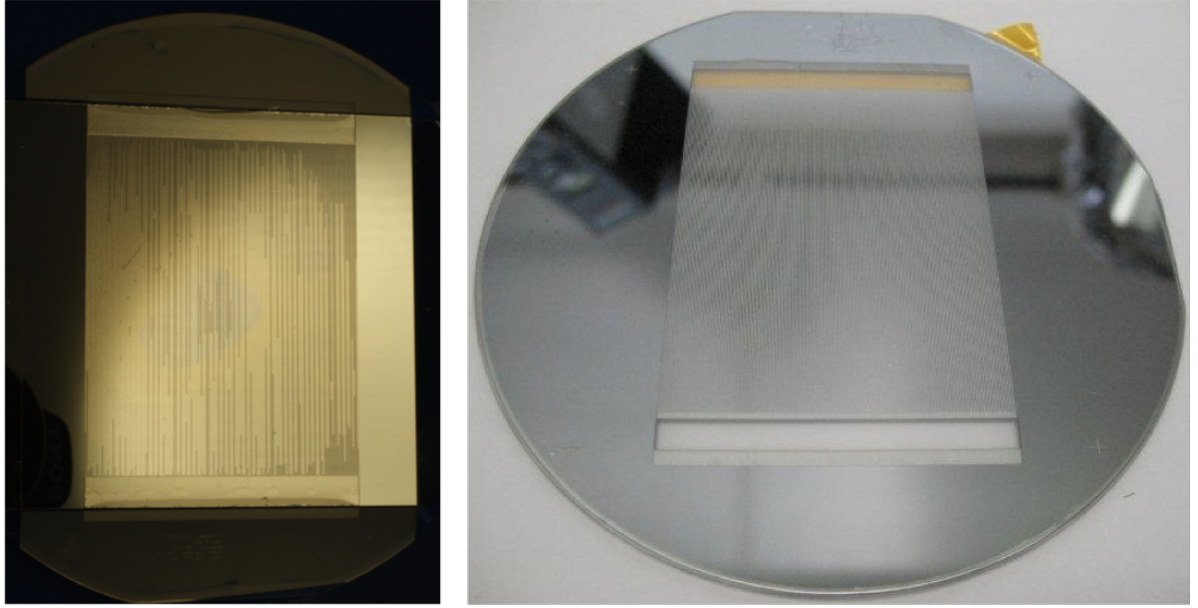


Figure 6.4: Bonded wafers realized for the first (left) and the second setup (right).

6.3.2 Sample preparation and instrumentation

In the first experimental apparatus the diced wafers were inserted on one extremity into other Pyrex[®] pieces, as shown in Fig. 6.5, thus creating an inner volume.

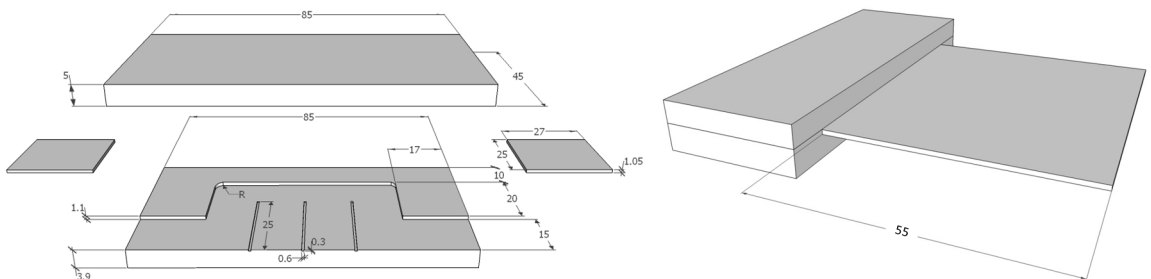


Figure 6.5: Three dimensional sketch of the Pyrex[®] pieces that were glued to the wafers (left), and of the assembled pieces (right) in the first setup.

Fig. 6.6 and 6.7 show a sketch and a picture of the instrumented samples prepared with the first setup, respectively. The inner volume is instrumented with two (redundant)

bare chip Cernox temperature sensors (CX-1050) and a manganin wire heater. The chosen sensors are among the smallest available, though very fragile. However the protected environment in which they were installed allows to safely use them.

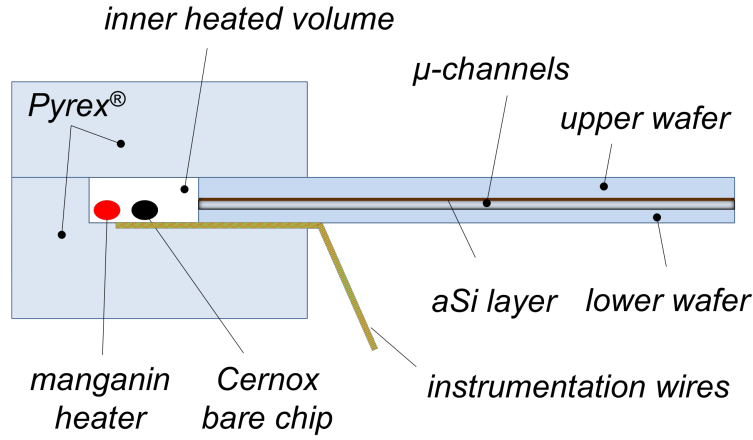


Figure 6.6: Sketch of the first experimental setup. Not to scale.

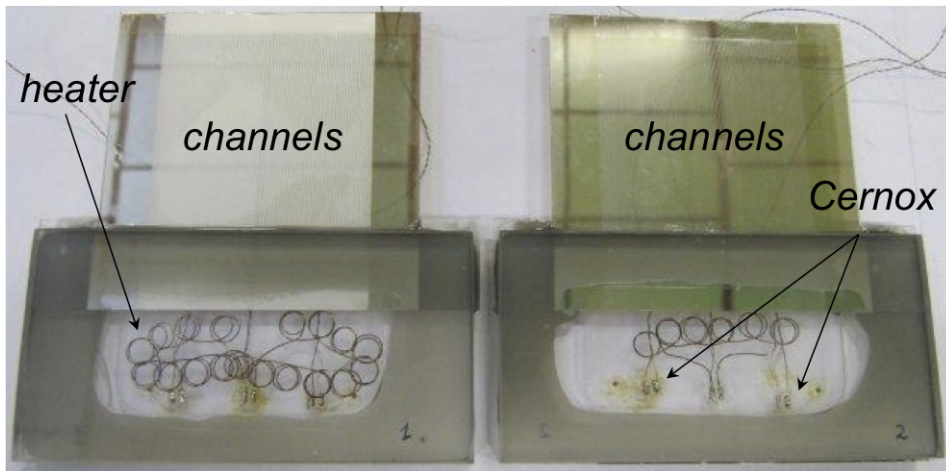


Figure 6.7: Picture of sample 1 and sample 2 (left and right respectively), prepared with the first setup.

The bonded wafers were glued to the other Pyrex[®] pieces using the 3M[®] DP190 epoxy resin charged with SiO₂. The much larger thermal contraction of any glue with respect to Pyrex[®] can easily be a source of cracks in the sample. If we consider the case of epoxy, the ratio of the relevant thermal contractions between room and He II temperature is roughly 25. We thermally cycled samples made of glued Pyrex[®] wafers and pieces, between room and liquid nitrogen temperature. These tests were carried out using several glues: epoxy resin (DP190), stycast (2850FT) with different catalysts (9, 24LV), Ecobond (286), araldite (F and MY750) with hardeners (HY905 and Jeffamine D400, respectively), polyurethane (Axson 11820 Iso1020). Some of them were also tried with different charges of SiO₂, or in combination with flexibilisators.

Though not all the glues behaved in the same way, the most important parameter proved to be the thickness of glue in contact with Pyrex[®]. A thin film of few hundred μm allows obtaining a resistant gluing without risk of cracks. We chose to use the 3M[®] DP190

epoxy resin, because it had already proven to be leak-tight to superfluid helium [66]. Helium leak-tightness measurements on mock-ups at room temperature preliminarily confirmed that, with extremely small leak rates between 10^{-9} and 10^{-10} mbar·l/s. A 10% SiO₂ charge was added to slightly reduce the thermal contraction, while maintaining the viscosity needed for gluing.

The phosphor bronze instrumentation wires were drawn through small grooves in one of the Pyrex[®] pieces (visible in Fig. 6.5 (left)) and sealed with the same resin (Fig. 6.10 (left)). After gluing, the samples were kept under pressure for 24 hours until the epoxy became dry.

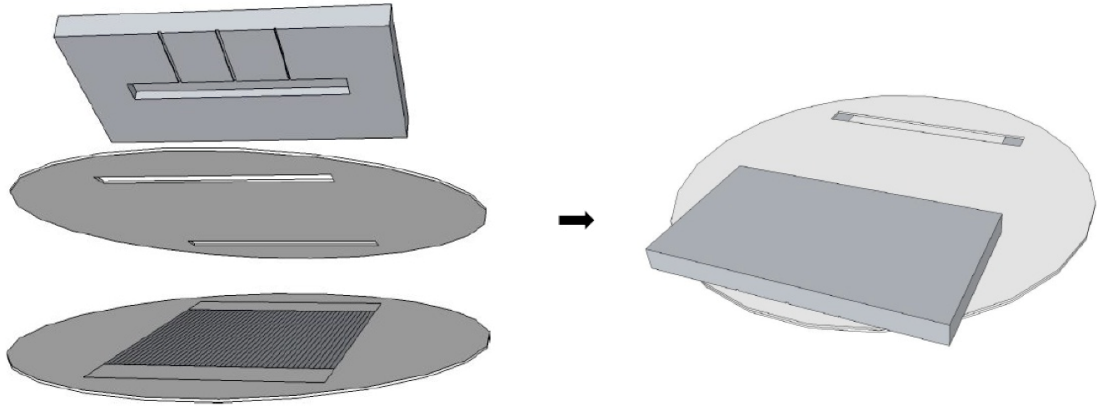


Figure 6.8: Three dimensional sketch of the Pyrex[®] piece that was glued to the wafers (left), and of the assembled pieces (right) in the second setup.

The first setup featured some problems because of the dicing that often broke the wafers. A second setup aimed at avoiding dicing and reducing the number of pieces to be glued was developed (Fig. 6.8). One single Pyrex[®] piece was used to host the heater and the sensors. The through holes in the upper wafer allow a direct contact of the inner volume to one extremity of the channels, and of the external bath to the other extremity.

Fig. 6.9 and 6.10 show a sketch and a picture of the instrumented samples prepared with the second setup, respectively. The instrumentation of the inner heated volume and the gluing were done in the same way as for the first setup. The second setup was simpler and avoiding the dicing operation made it less prone to cracks. This will constitute the baseline for future studies.

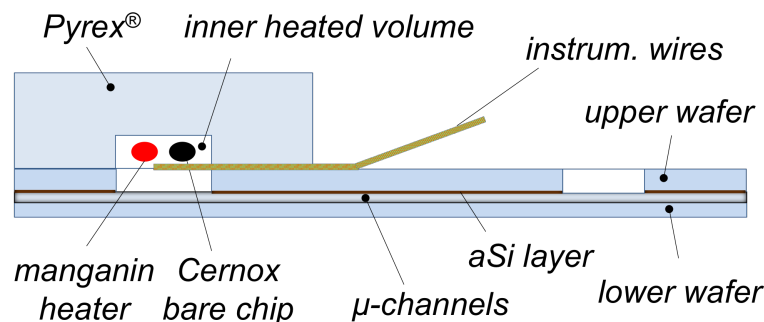


Figure 6.9: Sketch of the second experimental setup. Not to scale.

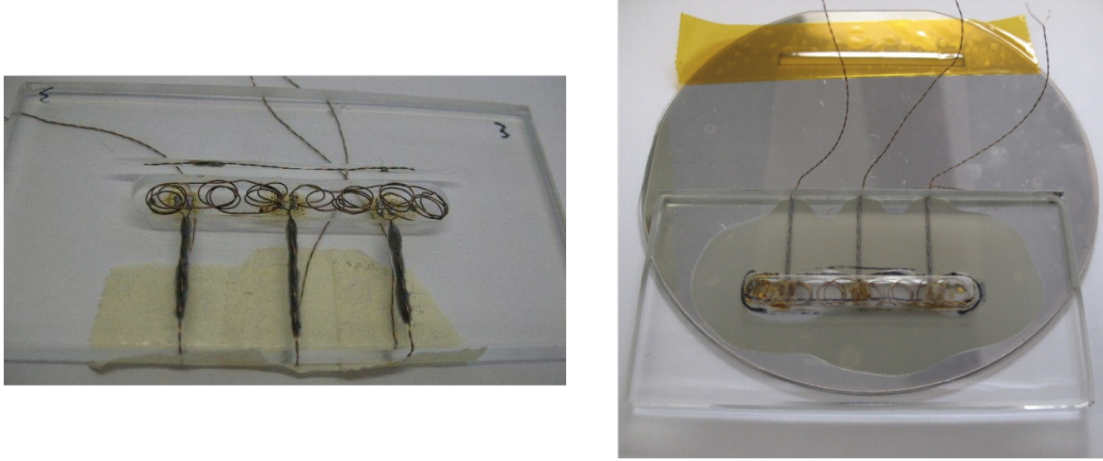


Figure 6.10: Picture of the instrumented Pyrex[®] piece in the second setup (left). Picture of sample 3 (right).

6.3.3 Measurements

The steady-state temperature rise of the isothermal inner bath was measured and correlated with the dissipated power, thus describing the heat transport through the channels. As previously stated, it is pivotal to have a large number of parallel channels between the same hot and cold sources to increase as much as possible the total channels cross-section. Since the sample is immersed in the bath, this reduces the ratio of (parasitic) Pyrex[®] solid conduction with respect to the heat transfer through the channels.

The temperature measurement was done using a lock-in amplifier (SR-850). The temperature sensors were calibrated *in situ* (in He II), with an absolute precision of about 1 mK and a sensitivity of 0.3 mK. The uncertainty in the temperature measurement was estimated as in section 3.3.6. It mainly comes from the error of the reference sensor during the calibration, which is by far more significant than the errors due to the fitting curve and to the instrument.

The heat generated by the manganin heater was determined through the measured voltage and the injected current. The error on the heat flux was mainly due to the measuring instrument, the source meter Keithley 2400. It was evaluated through the law of propagation of uncertainty to be lower than 0.5% of the measured value.

The heat loss through all the instrumentation wires is negligible with respect to the heat generated in the inner volume. Their percentage ratio was calculated to be lower than 0.005%.

The samples were installed in a Claudet-bath cryostat [110] similar to the one described in section 3.3.5. They were placed in horizontal position to eliminate gravitational effects. Measurements were performed in He IIp kept at a constant temperature in the range 1.7 - 2.0 K at a constant pressure around 1 bar. The cryostat bath temperature was regulated and held constant (± 1 mK) for the whole test over the range of dissipated power.

Prior to the measurement of the samples described in the next section, we verified the He II leak-tightness of the setup, and in particular of the glued and bonded pieces. We tested in superfluid helium bath a sample featuring no channels (sample 0), i.e. made of two bonded cover wafers. This resulted in a linear curve of temperature rise vs. power, starting in the origin of the axis. Therefore no He II leaks were present, but all the heat

was transferred from the inner volume to the bath through Pyrex[®] solid conduction.

6.4 Samples and characterization

Except sample 0 that did not undergo any etching (previous section), the other samples were realized using the mentioned techniques of sandblasting (sample 1), wet etching (sample 2) or DRIE etching (sample 3). Samples 1 and 2 were prepared with the first setup, whereas sample 3 was prepared with the second setup described in the previous section. After the first series of measurements, sample 3 was modified into sample 3*, as explained in the next section. The geometrical features of all the samples are summarized in Table 6.1. We refer to the equivalent diameter in terms of cross-section for sample 1, or to the equivalent rectangular cross-section for the others. The length of the channels is 55 mm in all cases.

Sample	MEMS technique	Setup	Channels	Characteristic dimensions (μm)	Channels total area (mm^2)
0	No etching	1 st	0	-	0
1	Sandblasting	1 st	158	$\Phi_{\text{equivalent}} = 100.4$	1.25
2	Wet etching	1 st	172	17.15 x 75.1	0.22
3	DRIE etching	2 nd	1000	$\sim 15.8 \times 24$	0.38
3*	DRIE etching	2 ^{nd*}	1000	$\sim 15.8 \times 24$	0.38

Table 6.1: Samples geometrical parameters.

Sample 1 is intended to validate the experimental setup. We checked the agreement with the fully developed turbulence theory, that has been so far studied only by Kimura *et al.* [94] in such narrow channels. Samples 2 and 3 aim at investigating for the first time the He II_p heat transport properties in channels with a thickness smaller than 20 μm .

The characteristic dimensions reported in Table 6.1 were obtained through characterization of the micro-channels performed using different techniques. We employed an optical microscope, an optical profiler and a Scanning Electron Microscope (SEM).

The channels realized by sandblasting feature a large wall roughness, as it can be observed in the pictures obtained with the three characterization techniques. Fig. 6.11 (left) was obtained with the optical microscope, where the dark regions correspond to the channels. Fig. 6.11 (right) is a three-dimensional image of the lower wafer, obtained with the optical profiler before bonding it to the upper cover wafer. Fig. 6.12 was obtained with the SEM. They show the typical cross-section of the sandblasted channels. Thanks to the observation of several channels, we could conclude that those etched with the sandblasting technique are a bit irregular: 20% of the sample 1 channels show a deviation from the average cross-section of the order of $\pm 7.5\%$.

The wall roughness is considerably decreased in sample 2, as it can be observed in Figs. 6.13 (left) and 6.14. Fig. 6.13 (right) shows the transversal cuts of the micro-channels, necessary for the SEM characterization. The shape of the wet etched channels is trapezoidal. The channels regularity is significantly improved with respect to sandblasted channels. A

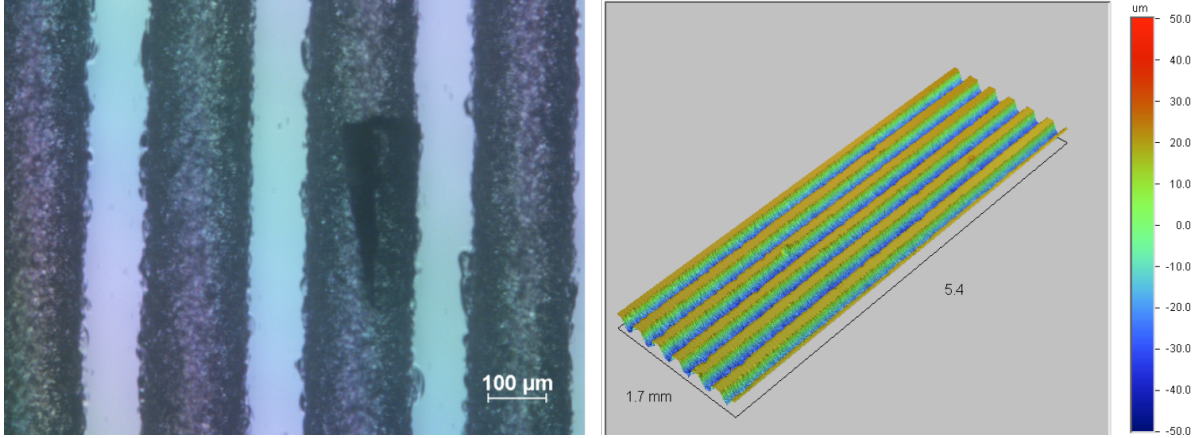


Figure 6.11: Characterization of sample 1 using the optical micro-scope (left) and the optical profiler (right).

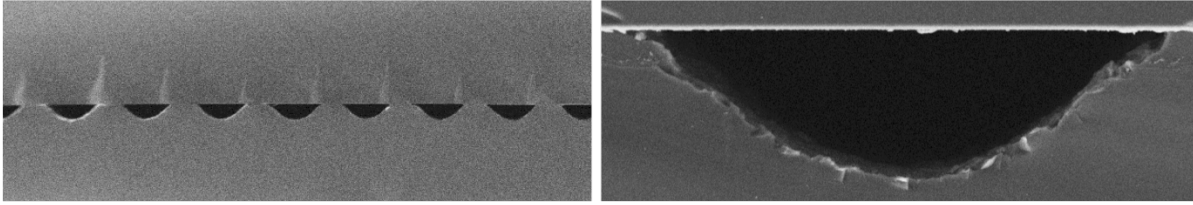


Figure 6.12: SEM characterization of sample 1.

maximum deviation from the average cross-section of $\pm 3.5\%$ is observed in 20% of the sample 2 channels.

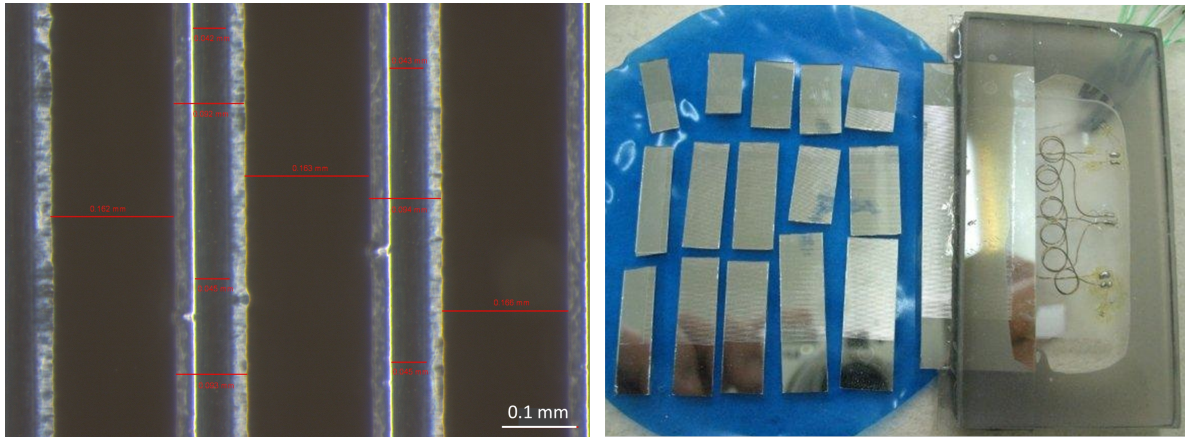


Figure 6.13: Sample 2: optical microscope characterization (left), and transversal cuts of the micro-channels for the SEM characterization (right).

Since the SEM characterization is destructive and future measurements are foreseen on sample 3, its channels were only characterized with the optical microscope (Fig. 6.15). We determined an average channels width of $24 \mu\text{m}$. The thickness of $15.8 \mu\text{m}$ reported in Table 6.1 was deduced from heat transfer considerations, as reported in the next sections.

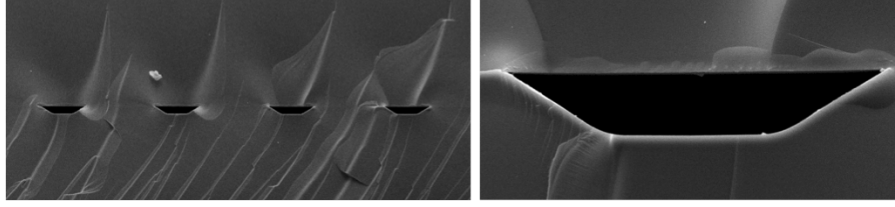


Figure 6.14: SEM characterization of sample 2.

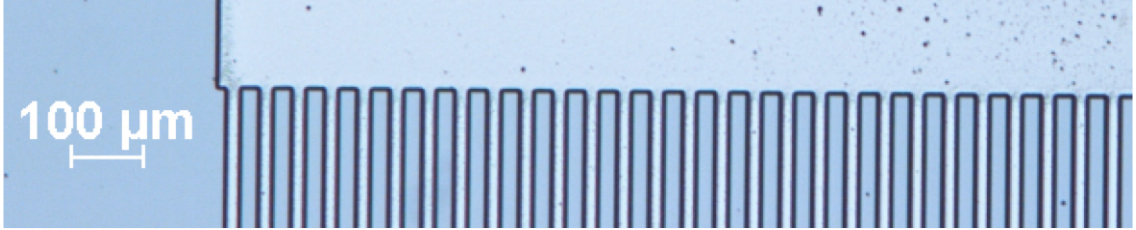


Figure 6.15: Optical microscope characterization of sample 3 / 3*.

6.5 Results and analysis

In the experimental tests we investigated a large range of heat flux, from 0.2 to 60 mW. We could observe the different thermodynamic regimes of superfluid helium: the Landau regime, the transition region and the Gorter-Mellink regime (section 2.5). The He II heat transfer is present at the same time as solid conduction through Pyrex[®] towards the external He II bath. For large heat fluxes the Pyrex[®] contribution can become no longer negligible with respect to the He II heat transfer, depending on the Pyrex[®] thermal properties as well as on the micro-channels dimension.

The measurements results are expressed in terms of steady-state temperature rise until 450 mK, as a function of the generated power. For sample 1, the only regime that could be identified was the turbulent one. Neither the laminar regime nor the transition region were observed. This is due to the large dimension of the channels, thus the turbulent regime begins at a small heat flux, and to our instrumentation that was not sensible enough. The Pyrex[®] solid conduction (computed from [111]) is not negligible for large heat fluxes, i.e. above 30 mW in case of 1.9 K external bath.

The laminar regime and the transition region were clearly identified for sample 2, as detailed in the following subsections. On the other hand the Gorter-Mellink regime could not be observed alone, that is to say without a significant contribution of the Pyrex[®] conduction. The latter term becomes dominant as soon as turbulence develops in the normal and superfluid components. This occurs because of the small number of channels (172) and of their small dimension, as well as because of the lack of an important thermal insulation with respect to the external bath. Thus for this sample we could only analyze the Landau regime and the transition region.

Sample 3 offers the most complete and significant results. At first we tested it in the usual setup (Fig. 6.9). The Landau regime and the transition region could be very well distinguished. At the beginning of the Gorter-Mellink regime the Pyrex[®] conduction was not negligible, despite the large number of channels (1000) providing a total cross-section larger than in sample 2. We hence decided to further insulate the channels from the

external bath. We glued other Pyrex[®] pieces, as shown in Fig. 6.16. In the measurements performed using this modified experimental setup (sample 3*), no differences were observed in the Landau regime, because of the extremely efficient He II heat transfer which makes the Pyrex[®] conduction anyhow negligible. On the other hand we could distinctly identify and analyze the Gorter-Mellink regime. The results of sample 3* reported in the next subsections refer to the modified setup.

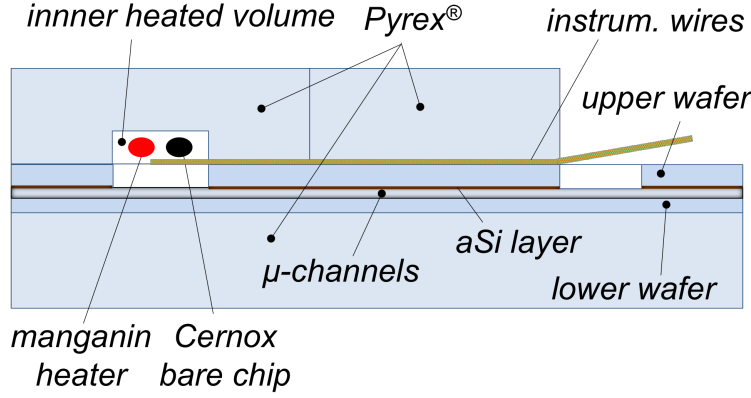


Figure 6.16: Sketch of the modified experimental setup of sample 3*. Not to scale.

In the performed analyses, we identified the heat flux range where the mentioned regimes are present. In case of the Gorter-Mellink regime, our analyses could be affected by other mechanisms than the He II heat transfer. To avoid that, the Pyrex[®] solid conduction was subtracted from the measured heat flux. It was calculated from the known geometrical dimensions and the material thermal properties [111]. Such simplified approach was confirmed by a detailed finite elements analysis of the experimental system [112], where the coupling between the thermal mechanisms and the actual temperature profile in the channels were taken into account.

However, all the reported analyses were performed in a range of heat flux where the Pyrex[®] conduction was negligible, i.e. below 10% of the measured heat flux, in order to reduce any error potentially coming from the evaluation of the heat losses.

6.5.1 Landau regime

The Landau regime was studied in samples 2 and 3 / 3*. The used relevant equation is :

$$Q_{Lan} = N \cdot \frac{A_{ch} \cdot d_{ch}^2}{l_{ch}} \int_{T_{bath}}^{T_i} \frac{[\rho(T) \cdot s(T)]^2 \cdot T}{\beta \cdot \eta(T)} dT, \quad (6.1)$$

where N is the number of channels with surface A_{ch} and length l_{ch} . The geometrical parameter d_{ch} is calculated from the channels dimensions a_{ch} and b_{ch} , in the approximation of a rectangular cross-section, according to equation 5.3: $d_{ch} = \sqrt{a_{ch} \cdot b_{ch} / (b_{ch}/a_{ch} + a_{ch}/b_{ch})}$. In this approximation the β coefficient is equal to 12. The helium temperature dependent properties ρ , s and η are the density of the bulk helium, the entropy and the viscosity, respectively. They were computer through the HEPAK database [32] at a pressure of

0.1 MPa. The integral on the temperature T is done between the bath temperature T_{bath} and the inner volume temperature T_i .

Fig. 6.17 reports the results of the experimental tests of sample 2, performed at several bath temperatures. The laminar regime at small heat fluxes can be clearly distinguished from a different regime taking place at high heat fluxes, as well as the transition between them. The laminar part of the measured curves was reproduced by varying the channels thickness, which determines (together with the width) the d_{ch} parameter of the above equation. We aim at obtaining for all the bath temperatures a d_{ch} equal or close to the theoretical d_{ch} obtained from the average channels dimensions 17.15 μm and 75.1 μm , that is 16.719 μm .

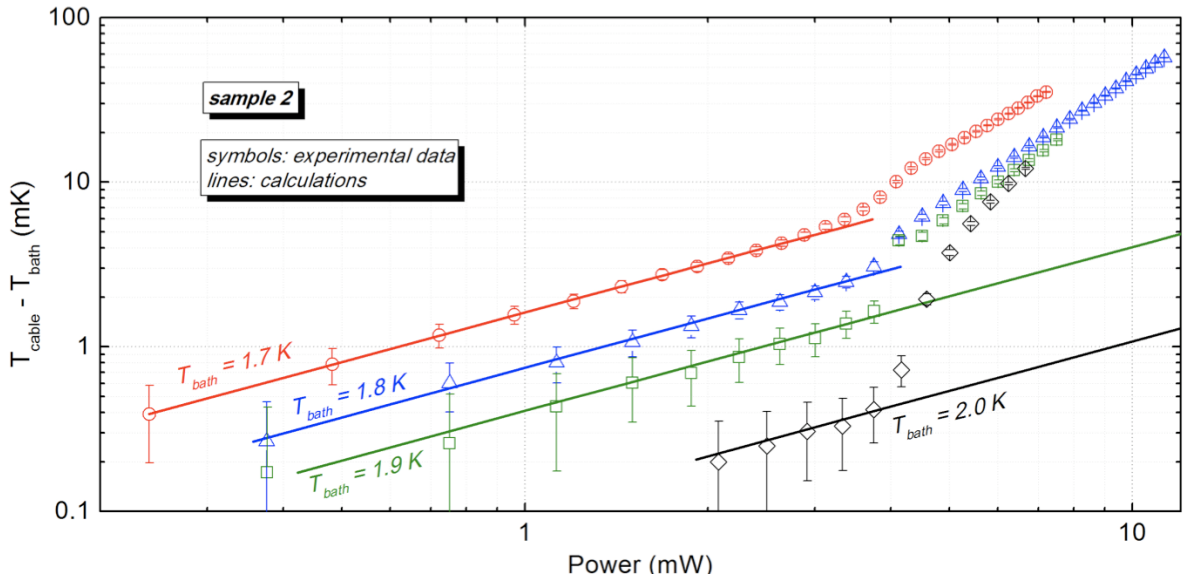


Figure 6.17: Temperature rise of the inner volume vs. heat generation in sample 2, for different temperatures of the external bath. Measurements (markers) vs. calculations (curves).

T_{bath} (K)	d_{ch} (μm)
1.7	16.94 ± 0.27
1.8	16.82 ± 0.35
1.9	16.79 ± 0.47
2.0	16.79 ± 0.42

Table 6.2: d_{ch} parameter evaluated for the sample 2 channels, from the experimental results at different bath temperatures.

The calculated curves were obtained using the d_{ch} parameter listed in Table 6.2 for each bath temperature. The d_{ch} values obtained from the experimental results are very close to the theoretical one. The total uncertainty on these values are between 1.5 and 2.8%. The maximum percentage difference with respect to the theoretical value of 16.719 μm is 1.4%.

Fig. 6.18 reports the tests results of sample 3* at various bath temperatures. Also in this case the different regimes can be easily identified. We followed the same approach above described to reproduce the laminar part of the measured curves, i.e. by varying the

channels thickness. In this case we do not know the exact thickness of the channels, but we determined the average channels width of $24 \mu\text{m}$ from optical microscope characterization. The channels thickness was estimated through this analysis of the Landau regime, and confirmed by the analysis of the Gorter-Mellink regime (next section).

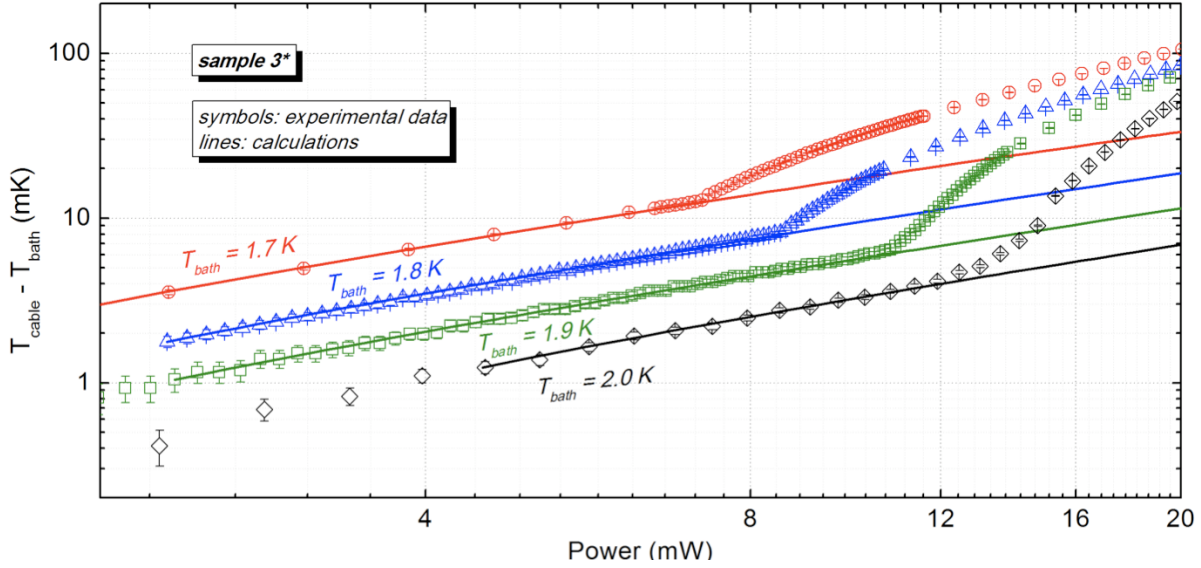


Figure 6.18: Temperature rise of the inner volume vs. heat generation in sample 3*, for different temperatures of the external bath. Measurements (markers) vs. calculations (curves).

The calculated curves were obtained using the channels thickness listed in Table 6.3 for each bath temperature. These values obtained from the experimental results are very close to each other, with a total uncertainty between 0.8 and 3%. The maximum percentage difference with respect to the average thickness of $15.8 \mu\text{m}$ is 1%.

T_{bath} (K)	Channels thickness (μm)
1.7	15.79 ± 0.29
1.8	15.95 ± 0.49
1.9	15.64 ± 0.33
2.0	15.83 ± 0.13

Table 6.3: Channels thickness evaluated for the sample 3* channels, from the experimental results at different bath temperatures.

6.5.2 Gorter-Mellink regime

The Gorter-Mellink regime was studied in sample 1 and sample 3*. The used equation is :

$$Q_{GM} = N \cdot \frac{A_{ch}}{l_{ch}^{1/3}} \left[\int_{T_{bath}}^{T_i} \frac{\rho_s(T)^3 \cdot s(T)^4 \cdot T^3}{A_{GM}(T) \cdot \rho_n(T)} dT \right]^{1/3}, \quad (6.2)$$

where N is the number of channels with surface A_{ch} and length l_{ch} . The helium temperature dependent properties ρ_s , ρ_n , s and A_{GM} are the density of the superfluid and of the normal components, the entropy and the Gorter-Mellink coefficient, respectively. They were computed through the HEPAK database [32] at a pressure of 0.1 MPa. The integral on the temperature T is done between the bath temperature T_{bath} and the inner volume temperature T_i .

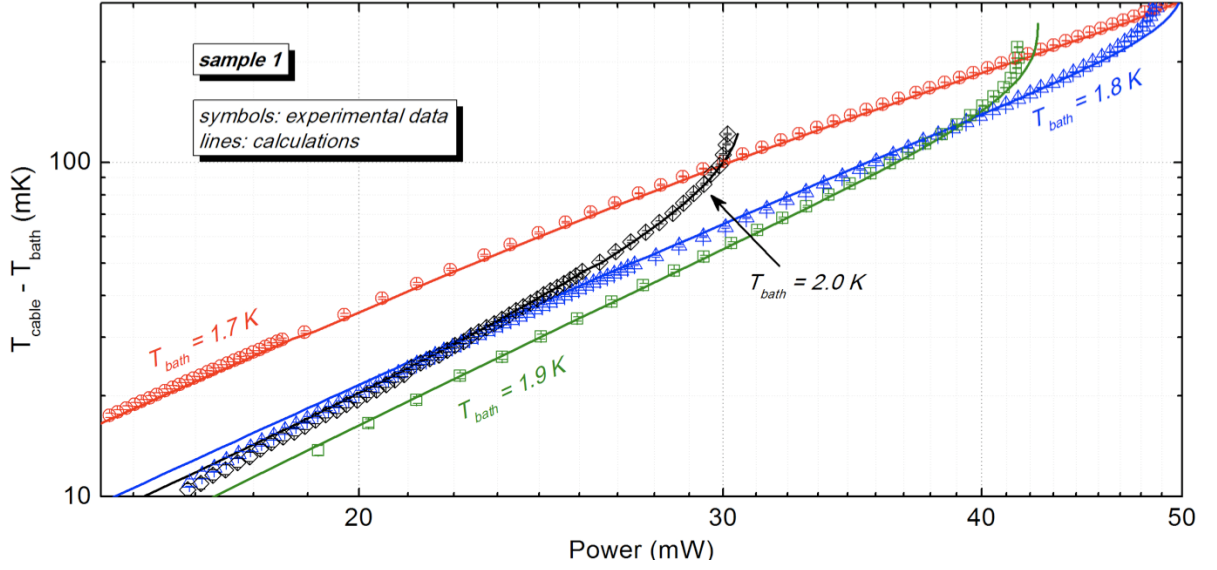


Figure 6.19: Temperature rise of the inner volume vs. heat generation in sample 1, for different temperatures of the external bath. Measurements (markers) vs. calculations (curves).

Fig. 6.19 reports the experimental results of sample 1, performed at several bath temperatures, where the only regime that could be observed is the Gorter-Mellink one. As explained at the beginning of the section, the Pyrex[®] solid conduction was subtracted from the measured heat flux, for both samples considered in this section. The curves calculated with equation 6.2 are reported as well, using the channels average equivalent diameter of 100.4 μm , determined in section 6.4. The agreement between measurements and calculation is good for all the bath temperatures. Some differences can be observed at small heat fluxes for a T_{bath} of 1.8 and 2 K, and at high heat fluxes for a T_{bath} of 1.8 and 1.9 K. However the maximum percentage difference is 1.9%.

In order to determine the Gorter-Mellink coefficient A_{GM} for different temperatures and compare it to the macro-scale theory, we considered the local equation:

$$\nabla T = - \frac{A_{GM} \cdot \rho_n}{\rho_s^3 \cdot s^4 \cdot T^3} \cdot q^3. \quad (6.3)$$

Some approximations were required. In particular the temperature gradient is not an accessible physical quantity in our tests. We considered $\Delta T/L$ instead, where L is the channels length. We took into account a temperature range small enough to have negligible variation of the fluid properties with respect to temperature. In such small range the coefficient $\frac{A_{GM} \cdot \rho_n}{\rho_s^3 \cdot s^4 \cdot T^3}$ can be taken as constant. The Pyrex[®] conduction was negligible in the considered range, as stated at the beginning of the section.

We reported ΔT as a function of $\frac{\rho_n \cdot L}{\rho_s^3 \cdot s^4 \cdot T^3} \cdot q^3$, as shown in Fig. 6.20 in the case of 1.9 K

bath temperature. The error bars are computed taking into account the uncertainty on the temperature rise, on the channels length and on the helium thermodynamic properties.

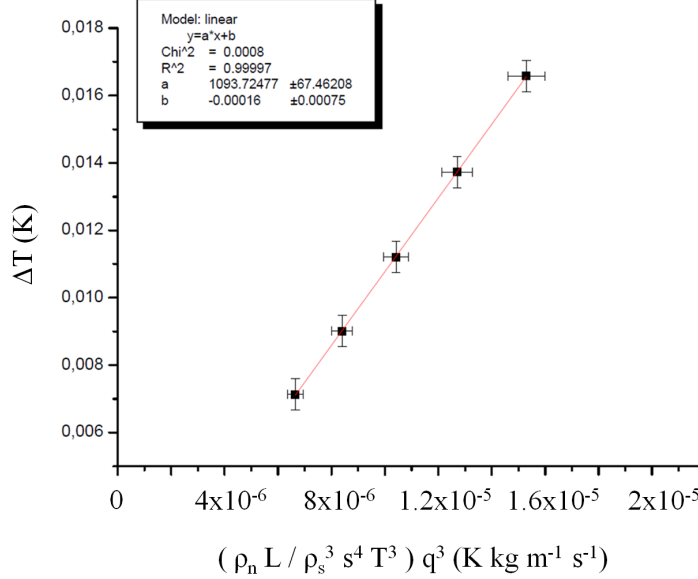


Figure 6.20: Evaluation of the Gorter-Mellink coefficient for sample 1, at a bath temperature of 1.9 K.

The slope of the curve interpolating these experimental data provides A_{GM} . In principle we should have interpolated using an equation $y = A_{GM} \cdot x$, according to equation 6.3. However, the presence of the Landau regime for small heat fluxes adds a y-intercept. Fig. 6.21 shows the Gorter-Mellink coefficient derived from the experimental data, compared to the theoretical value that can be found in literature [32], relative to the macro-scale case. The error bars take into account the confidence interval due to the described interpolation, as well as the uncertainty due to the non uniformity of the channels cross-section. They range between 5 and 7.3%, except at 2.015 K where they reach 11.8%.

The experimentally determined coefficient is very close to the theoretical one. The maximum percentage difference is 9.3% at 2.015 K, and is lower than 4.3% at the other temperatures. The theoretical coefficient is anyhow included in the uncertainty range, even at 2.015 K.

This result confirms the only study carried out so far in channels featuring dimensions of the order of 50 μm [94]. Furthermore, it provides a validation of the developed experimental set-up.

The same approach was used to analyze sample 3*, investigating for the first time the Gorter-Mellink regime in He IIp in dimensions smaller than 20 μm . The further insulation of the channels from the external bath (sample 3* instead of sample 3), described at the beginning of the section, was particularly important to avoid that the Pyrex[®] conduction affects the results. Fig. 6.22 reports the results of the tests performed at different bath temperatures. Unlike sample 1, other regimes than the turbulent one can be observed for smaller heat fluxes, namely the laminar regime (analyzed in the previous section) and the transition region. This is due to the smaller channels dimensions, therefore the turbulence develops at higher heat fluxes. The calculated curves were obtained using the dimensions

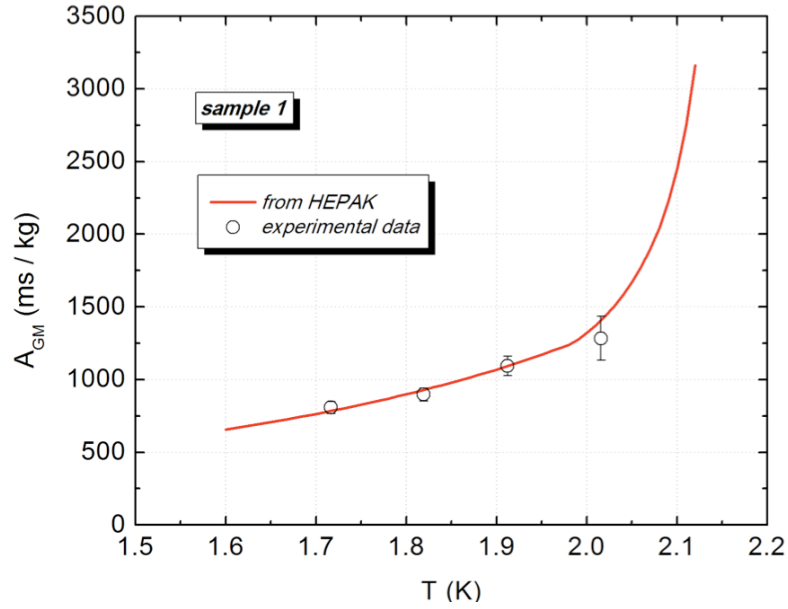


Figure 6.21: Gorter-Mellink coefficient as a function of temperature for sample 1. Derived from experimental data (markers) vs. from literature [32] (curve).

determined in the analysis of the Landau regime, i.e. $15.8 \mu\text{m} \times 24 \mu\text{m}$. They reproduce well the measured curves, from the beginning of the fully developed turbulence, for all the bath temperatures. The largest differences can be observed around T_λ . It is worth noticing that the temperature range of agreement between experimental and theoretical data decreases while increasing the bath temperature. This is mainly due to the proximity to T_λ , hence to the smaller number of measured points.

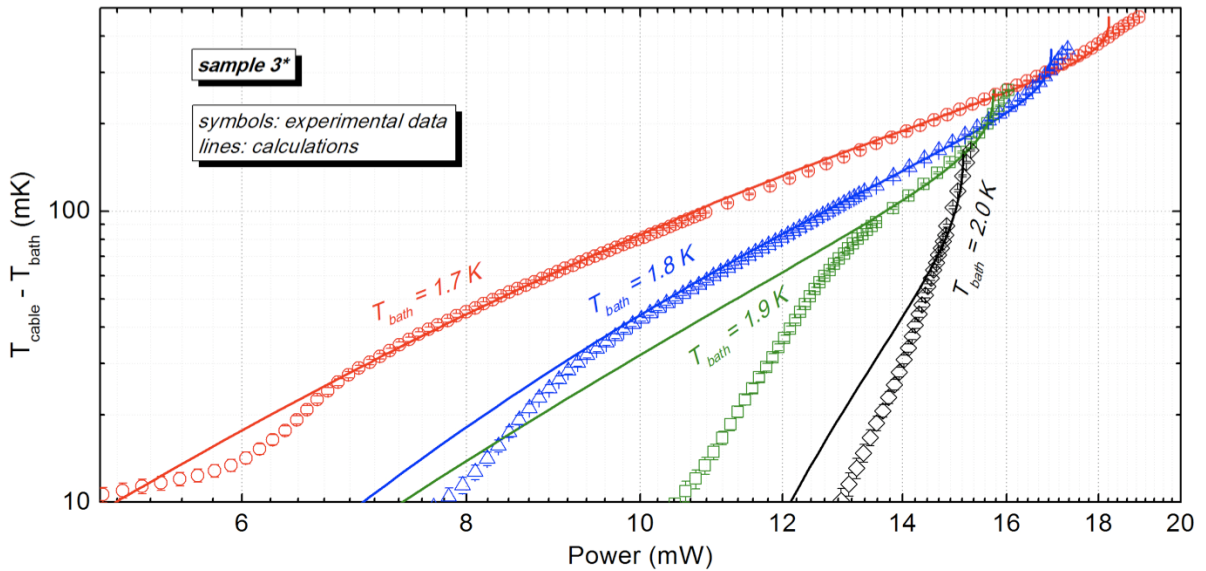


Figure 6.22: Temperature rise of the inner volume vs. heat generation in sample 3*, for different temperatures of the external bath. Measurements (markers) vs. calculations (curves).

Fig. 6.23 reports the obtained A_{GM} versus the theoretical one [32]. The total uncertainty is below 8.7%, except at 2.02 K where it is of 18.8%. The reason of such large error bar

for this temperature is the small validation interval of the Gorter-Mellink law, where the Pyrex[®] conduction is negligible. For the other temperatures the theoretical A_{GM} is very close to the experimental one, with a maximum difference of 3.35%, and anyhow inside the uncertainty range.

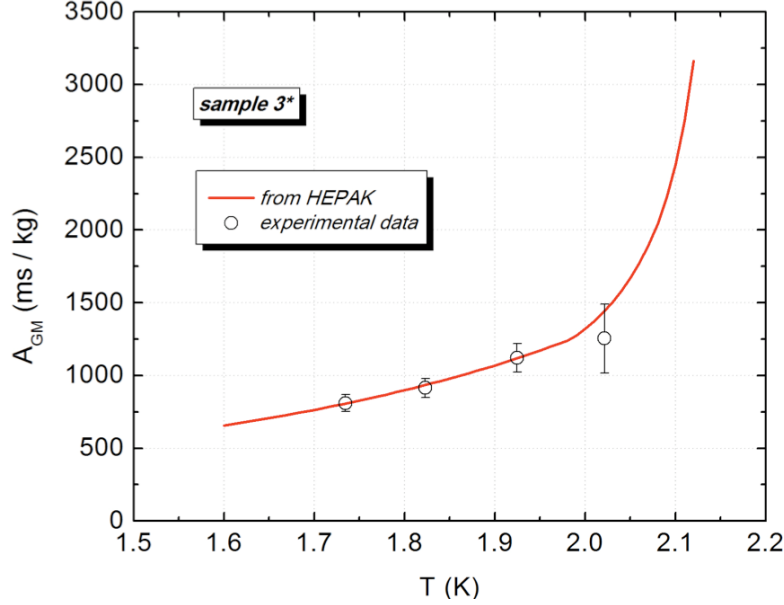


Figure 6.23: Gorter-Mellink coefficient as a function of temperature for sample 3*. Derived from experimental data (markers) vs. from literature (macro-scale) [32] (curve).

The presented results prove that the superfluid turbulence theory is valid at a level of confinement of the order of 16 μm . The Gorter-Mellink coefficient does not depend on the geometrical shape and size down to these small dimensions.

This behavior seems to be associated to the distribution of the vortex lines, which according to Vinen [43] are spaced by 1.1 μm at 1.9 K, with a core size of 0.3 nm. The dimension of the channels that we investigated is sufficiently larger, allowing the vortex lines to be uniformly and isotropically distributed. This would explain why the superfluid turbulence heat transfer characteristics in He IIp are not influenced by such channel size, whereas they would be in case of channel dimension of the order of the μm .

6.5.3 Critical heat flux (end of Landau regime)

The transition between He II laminar and turbulent regime does not occur all at once but through an intermediate region delimited by the critical heat fluxes Q_{c1} and Q_{c2} [49]. Q_{c1} corresponds to the onset of vorticity in the superfluid component, whereas Q_{c2} to the development of normal component turbulence. Q_{c1} can be identified in our measurements for samples 2 and 3*, and is shown in Fig. 6.24 as a function of the bath temperature T_{bath} . At a T_{bath} of 2 K the transition between laminar and turbulent regime is not as sharp as for lower bath temperatures. This was also observed by other authors [113], thus making difficult to estimate Q_{c1} . We focused therefore on the measurements at T_{bath} of 1.7, 1.8 and 1.9 K.

Fig. 6.24 also reports the Q_{c1} values predicted by Ladner and Tough (equation 5.5) [48],

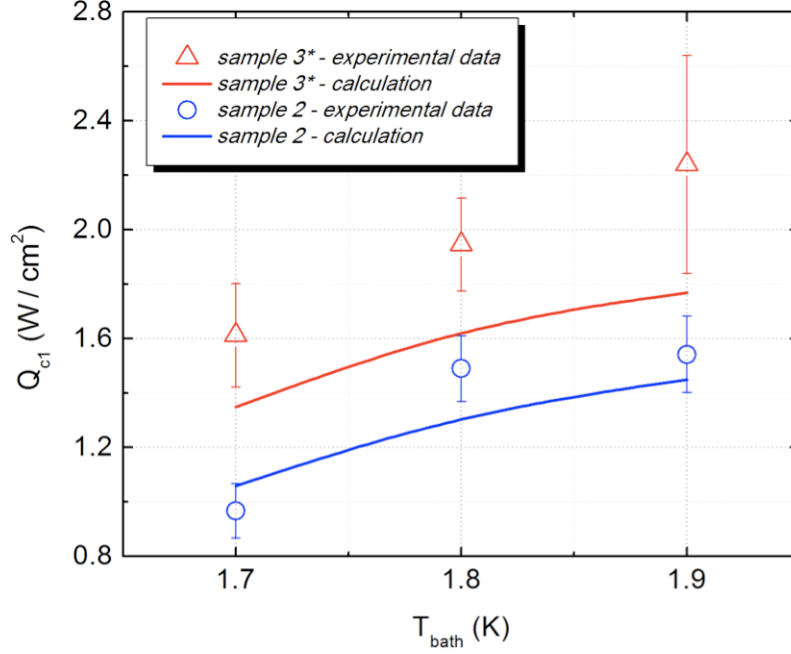


Figure 6.24: Measured critical heat flux Q_{c1} for samples 2 and 3* as a function of the bath temperature. The calculation according to Ladner-Tough criterion [48] is also reported.

in case of He IIs for rectangular geometries. The relevant equation is reported here for simplicity:

$$Q_{c1} = \frac{4 \cdot \alpha}{\gamma_0(T_{bath}) \cdot D} \cdot \rho_s(T_{bath}) \cdot s(T_{bath}) \cdot T_{bath}. \quad (6.4)$$

The empirical coefficients α and γ_0 depend on the channels geometry, which is not exactly the same of our setup. α is an experimentally determined constant value depending on dimension and shape of the tested channels. It is approximately equal to 1. γ_0 is a temperature and geometry dependent parameter. It is equal to 92, 94 and 102 s/cm² for a bath temperature T_{bath} of 1.7, 1.8 and 1.9 K, respectively. D is the hydraulic diameter. Despite the different helium conditions and the different geometry of our samples with respect to those analyzed in [48] (having an impact on the mentioned fitting parameters), a rather good agreement is found between measurements and calculations for sample 2. The differences are more important for sample 3*. However channels dimensions and shape are not completely known in this case, hence the considered cross-section is the rectangular one estimated from the previously reported analyses.

Although not reported in Fig. 6.24 because of the large error bars, for higher bath temperatures we observed a slight decrease of Q_{c1} . Such behavior agrees with the He II cooled channels network of superconducting cables electrical insulation studied in [52]. In that case the critical heat flux featured a peak between 1.9 and 2.1 K before decreasing while approaching T_λ .

In terms of the superfluid critical velocity v_{sc} , that is proportional to Q_{c1} , different and sometimes contradictory observations were made in the past in He IIs. Keller and Hammel showed a v_{sc} independent of temperature in slits of 200 μ m and 30 μ m thickness, except for temperatures near T_λ where the critical velocity became zero [114]. Griffiths [115] showed

an increase of v_{sc} up to 1.9 K, whereas Jones described a dependence on the superfluid density, thus decreasing as the temperature approaches T_λ [116].

6.6 Conclusion

The developed experimental program allowed to obtain a deeper insight of the thermal phenomena occurring in superconducting magnets cooled by pressurized superfluid helium. The hypotheses assumed in the previous chapter were confirmed in channels featuring a thickness of 16 μm .

The first main result of this study was the observation of the Gorter-Mellink regime in channels with equivalent diameter of $\sim 100 \mu\text{m}$, which confirmed the only study so far carried out in these conditions [94]. In different channels of thickness smaller than 20 μm we could clearly identify the laminar regime of pure superfluidity, or Landau. The critical heat flux Q_{c1} corresponding to its end featured an increase until around 1.9 K followed by a decrease towards T_λ , in agreement with some previous works.

The most significant result was the observation of a fully developed turbulent regime in channels featuring a thickness of $\sim 16 \mu\text{m}$. This regime is indeed the most interesting for superconducting magnets applications, as demonstrated in chapter 5. The Gorter-Mellink coefficient characterizing the regime was found to be in agreement with the theoretical one, confirming the independence of the relevant law from the channel geometrical shape and size down to these dimensions.

Chapter 7

Estimation of the LHC and HL-LHC magnets quench margin

Contents

7.1	Introduction	117
7.2	Background notions	118
7.3	Beam loss heat deposit	118
7.4	LHC magnets	121
7.5	HL-LHC magnets	125
7.6	Conclusion	126

7.1 Introduction

The results of the previous chapters allow to evaluate the stability of the LHC present and future Nb-Ti magnets, in terms of quench margin, which depends on the capability of the relevant insulations to withstand heat deposit. Such results constitute the most advanced investigations performed so far on this topic, both from the experimental (chapters 3 and 4) and modeling (chapter 5) point of view. The quench margin is compared to the beam induced heat deposition evaluated through particle shower simulations.

Until the 2011 operation, the LHC almost did not suffer from beam-induced quenches [117] [118]. The operation at half of the nominal beam energy provided indeed a large quench margin. However, the situation will drastically change when the nominal beam energy will be approached, after the first long shutdown to consolidate the main bus bars interconnections. At 6.5 - 7 TeV the superconducting magnets will run much closer to the critical surface, while being exposed to higher beam losses. The operating conditions will become more critical after the luminosity upgrade (HL-LHC), where the magnets close to the interaction points will have to deal with much larger heat loads. A detailed knowledge of the quench margin will therefore become crucial for the LHC operation, as well as for the conception of new superconducting magnets and for sizing the relevant cryogenic system.

7.2 Background notions

The amount of energy deposition that the magnets can withstand depends on the beam loss duration. For very fast losses of the order of 1-10 μs the magnets can only rely on the strands enthalpy reserve [119]. For slower losses the heat transfer to the helium contained inside the cable starts playing a role [120]. The coil stability is significantly improved thanks to the helium large specific heat, featuring a dependence on the superfluid, liquid and boiling phases [121]. For losses of few seconds duration or slower, the mechanisms of steady-state heat transfer through the cable insulation to the cryogenic system become dominant. The latter case is addressed in this chapter.

The coil stability is expressed in terms of quench margin, or quench limit. It represents the maximum amount of power per unit volume of cable that can be deposited in it without leading to a resistive transition (quench). The steady-state quench margin depends on several parameters as the insulation scheme and the relevant mechanical conditions (applied pressure, etc...), the magnet current (beam energy), the helium bath temperature and the beam loss profile.

Magnets quenches must be reduced as much as possible to optimize the beam time, as well as to reduce the risk of magnets failure. A control system was developed to predict an imminent beam-induced quench and dump the beam before quenching the magnet. The system is based on detectors, the Beam Loss Monitors (BLMs), which monitor the radiation field around the accelerator. They measure the flux of secondary particles (hadronic shower) produced during the collision of protons with the beam screen, the cold bore and the superconducting coils [122]. Reaction thresholds for the BLMs are set comparing the heat deposition due to the hadronic shower (computed with specific codes [123]) to the expected quench margin of the coil. A precise estimation of the quench margins allows a more efficient operation of the LHC, saving operation time and consequently increasing the integrated luminosity. Moreover, it provides an important input in the design of new superconducting magnets.

7.3 Beam loss heat deposit

The expected heat deposit in the superconducting coils due to beam losses is obtained through simulations performed with the FLUKA Monte Carlo code [124][125]. It is calculated in terms of energy or power density per primary event, which can be a single proton-proton collision in the interaction points or the loss of a single proton. We report in this section the results that are of relevance for our investigation.

Two main sources of beam loss are considered, due to primary collimators or to the debris of collisions from the Interaction Regions (IR). The first is important for the arc main dipole and quadrupole magnets, whereas the second concerns the inner triplet magnets (section 2.3.2). Other sources as the particle showers generated by the interaction of the beam with the residual gas or in the tertiary collimators protecting the inner triplet are expected to induce a negligible effect [126].

The power density distribution in the coils is estimated with a scoring mesh in cylindrical coordinates. The chosen bins (dimensions of the mesh elements) in the radial (r), azimuthal (Φ) and longitudinal (z) direction are respectively 2.5 mm, 2° and 10 cm.

Fig. 7.1 from [127] reports the longitudinal profile of the peak power (both over r and Φ) deposited in the arc MB and MQ magnets. The analyzed magnets are in cell 8-9 close to the IR7, and are the most exposed to beam losses. This study was done to investigate the impact of the Dispersion Suppressor (DS) collimator, in the frame of the Machine Development (MD) done in May 2011 [128] [129]. The case of 7 TeV beam energy refers to a 0.2 h beam lifetime, which was the original LHC scenario. The 3.5 TeV case refers to the actual loss rate during the MD, which was higher than in the LHC operation. The power is averaged over 15 mm in the radial direction, which is nearly equal to the cable width. These simulations depend on the impact maps on the primary collimators.

According to Fig. 7.1, the peak power on the MB and MQ magnets is of the order of 3-4 mW/cm³ at 7 TeV, and 11 mW/cm³ at 3.5 TeV when the collimators are more open. However, in case of 7 TeV this power must be reduced by five times because the actual LHC nominal scenario is of 1h beam lifetime [130]. This leads to a peak power from 0.6 to 0.85 mW/cm³.

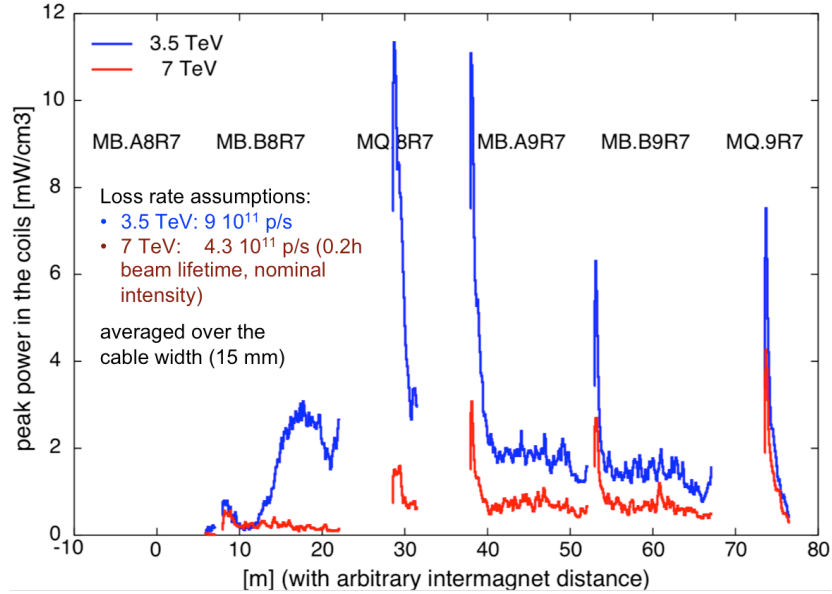


Figure 7.1: Longitudinal profile of the peak power in the MB and MQ magnets of cell 8-9 in sector 7, from [127]. A 0.2 h beam lifetime is considered at 7 TeV, whereas the May 2011 MD loss rate is considered at 3.5 TeV.

Fig. 7.2 from [131] reports the expected heat deposit in the IR1 inner triplet. Due to its proximity to the collision points and its strong magnetic field, the inner triplet is particularly exposed to the proton-proton collision debris and the risk of quench is consequently higher than for other magnets. Therefore its stability needs to be carefully investigated and suitable protection solutions must be implemented [132]. Fig. 7.2 (left) shows a 2-D map of the specific energy deposit in the coils region overlapped to the cross-section of the Q1 magnet (see section 2.3.2), at the longitudinal position of the peak power. It is expressed in MGray, for an integrated luminosity of 100 fb⁻¹. As for all investigated losses, the power density decreases strongly with the distance from the cold bore. Therefore the part of the coil that is more prone to quench, thus determining the quench margin, is the innermost part of the inner layer cable. Fig. 7.2 (right) shows the longitudinal distribution of the peak power along the coils of the inner triplet quadrupoles

(Fig. 2.8). It refers to 7 TeV at the LHC nominal luminosity of $10^{34} \text{ cm}^{-2}\text{s}^{-1}$. The origin is in the center of the ATLAS detector, where collisions take place. The blue curve refers to the peak radial power deposited in the innermost radial bin. The red and green curves refer to the averaged power over four or five radial bins, respectively. In the following we refer to the average done over five bins, to be consistent with the other values mentioned in this section, as well as with chapters 3 through 5 where the heat deposit in the cable is uniform.

The peak power on the inner triplet magnets in the LHC nominal conditions (7 TeV, $10^{34} \text{ cm}^{-2}\text{s}^{-1}$) is about 3.5 mW/cm^3 . An analogous study performed at 3.5 TeV at the 2011 luminosity ($3.5 \cdot 10^{33} \text{ cm}^{-2}\text{s}^{-1}$) provides a value of 0.4 mW/cm^3 from [131]. If scaled to the nominal luminosity, this leads to about 1.2 mW/cm^3 .

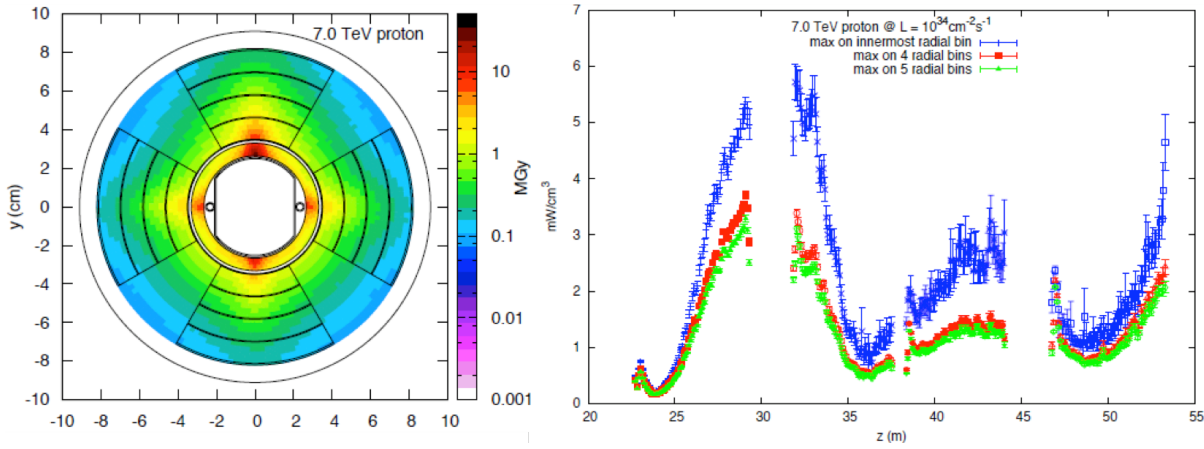


Figure 7.2: Heat deposit in the IR1 inner triplet due to the proton-proton collision debris, from [131]. Left: 2-D map of the specific energy deposit in the coils region, at the longitudinal position of the Q1 peak power, for an integrated luminosity of 100 fb^{-1} . Right: longitudinal profile of peak power density along the inner triplet coils. It refers to 7 TeV at the LHC nominal luminosity of $10^{34} \text{ cm}^{-2}\text{s}^{-1}$. Vertical bars indicate the statistical errors.

Fig. 7.3 from [131] concerns the longitudinal position of the peak power (Q1 magnet), in the same conditions of Fig. 7.2. Fig. 7.3 (left) reports the radial power deposition. The inner layer cable corresponds to about the first four radial bins on the left (the cable width of the MXQA magnet is 11 mm [2]). With the used radial scoring, the maximum radial power density (in the innermost bin) is 5.3 mW/cm^3 , i.e. less than twice the average power density in the cable of 3.8 mW/cm^3 . The average power density in the second layer cable is 1.3 mW/cm^3 , therefore the average heat deposit in the inner layer cable is three times larger than in the second layer cable. Fig. 7.3 (right) reports the azimuthal power deposition on the innermost bin. The maximum is at 90° ($\frac{\pi}{2}$ in the x-axis unit), i.e. in the cables located in the middle of the upper pole. The azimuthal scoring is roughly equal to the cable thickness, hence each point corresponds to a cable. The two cables on the right (or left) of the one receiving the highest heat deposit receive 90% and 80% of its dose.

For the HL-LHC upgrade a luminosity of $5 \cdot 10^{34} \text{ cm}^{-2}\text{s}^{-1}$ is foreseen. According to studies performed for the Phase I luminosity upgrade [133], and scaling with respect to the mentioned luminosity, the expected peak power averaged over the five radial bins is 7.5 mW/cm^3 . This value is more than twice the expected power deposit in the LHC nominal conditions.

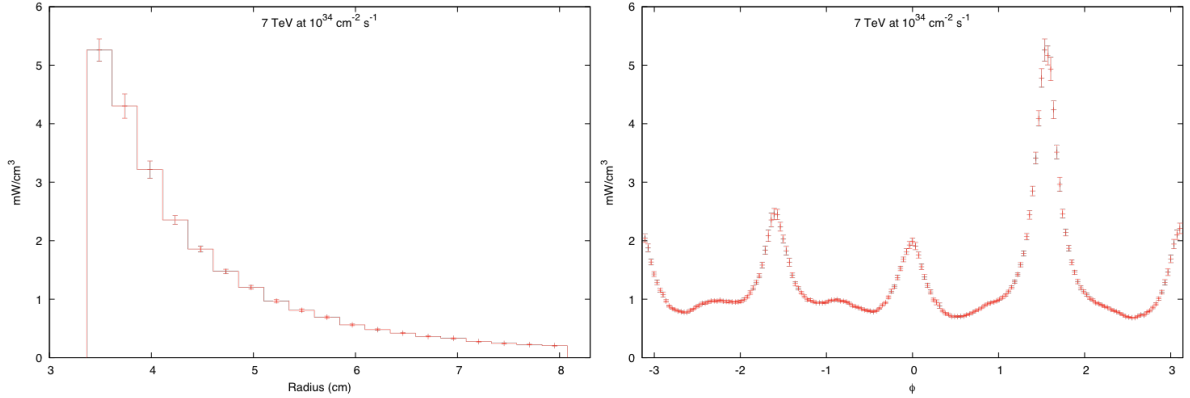


Figure 7.3: Heat deposit in the IR1 inner triplet due to the proton-proton collision debris, from [131], at 7 TeV and for the LHC nominal luminosity of $10^{34} \text{ cm}^{-2} \text{ s}^{-1}$. Vertical bars indicate the statistical errors. Left: radial power deposition at Q1 peak. Right: azimuthal power deposition on innermost bin at Q1 peak. The x-axis is expressed in radians, where 0 rad corresponds to the right hand side of the coil mid-plane.

The peak heat deposition identified by the presented studies is reported in the next sections, compared to the heat extraction in the relevant magnets. We refer to the power density averaged in the cable radial dimension.

7.4 LHC magnets

The quench margin is estimated looking at the most critical cables from the stability standpoint. The magnetic field is typically larger for cables far from the mid-plane, as shown in Fig. 2.6 (right). These cables feature therefore a lower critical temperature, resulting in a smaller quench margin. However, the losses impacting such cables are very unlikely, as shown in the previous section. The typical losses are concentrated in the horizontal and vertical planes, which constitute then the coil most critical regions. These are also the regions subjected to the maximum mechanical pressure, hence featuring the smallest heat extraction through the insulation as shown in chapters 3 through 5.

Two types of analyses were performed. In the first of them we used the model developed in chapter 5 to predict the thermal behavior of the most critical cables, as long as their temperature is below T_λ . This is representative of the magnet operation at the nominal beam energy of 7 TeV, where it would be suitable to maintain the superfluid regime. In the second analysis we used the experimental results presented in chapter 3 to determine the quench margin over the whole beam energy range.

The model of the cables in the coil configuration was built by modifying the stack model presented in chapter 5. In case of the inner layer cables, the largest of the small faces was considered adiabatic (unless specified otherwise), whereas the smallest face was in contact with the bath kept at a constant temperature. We considered the six cables located in the middle of the pole, where the maximum beam loss deposition occurs. The heat deposit in the cable was considered as uniform. For both the MB and MQ, we assumed the applied pressure of 50 MPa typical of the mid-plane [134].

Fig. 7.4 shows the results for the LHC MB inner layer. Different heating configurations are considered, namely a uniform heat deposit over all the cables and a localized heat deposit in one single cable. The improved heat extraction in the latter case is mainly

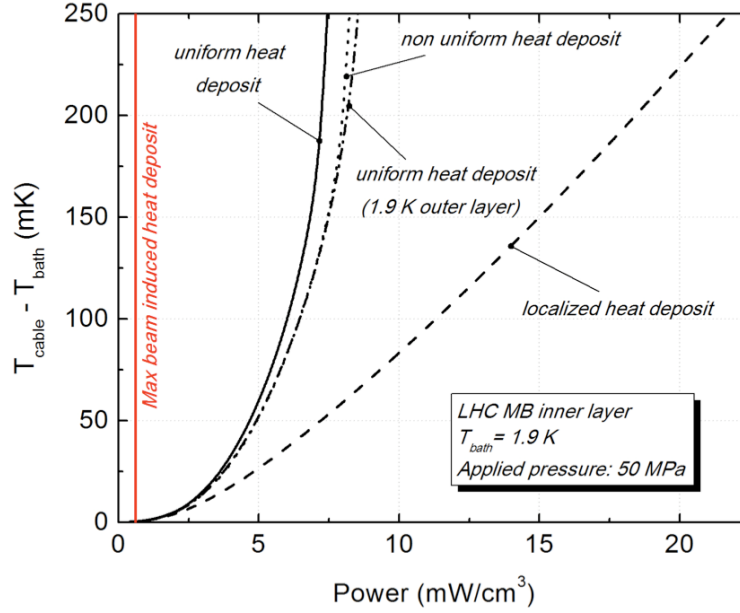


Figure 7.4: Calculated temperature rise of the mid-plane cable vs. heat load for the LHC MB inner layer cable, in the coil configuration. The bath temperature is assumed to be 1.9 K. Different heating and cooling configurations are considered, as described in the text.

due to polyimide solid conduction towards the adjacent (cold) cables, as witnessed by the almost linear behavior. However, this case is not representative of the actual heat deposit. We studied the impact of a closer to reality heat distribution according to Fig. 7.3 (right), i.e. 100% of the heat deposited in the two central cables, 90% in the adjacent ones and 80% in the following ones. Only a slight improvement can be observed with respect to the uniform heating case. An analogous result is obtained in the more optimistic hypothesis of uniform heat deposit over all the cables and polyimide solid conduction also towards the outer layer cables, assumed at 1.9 K. In all cases, the expected beam loss peak power density in the MB inner layer would cause a temperature rise of only few mK.

The bath temperature T_{bath} might vary from the nominal value of 1.9 K. The influence of such variation on the heat extraction until T_λ is shown in Fig. 7.5. The heat extraction capability decreases with increasing T_{bath} and is larger than the maximum beam induced heat deposit, in the considered range of T_{bath} .

The inner layer cables have always been considered more critical than the outer layer ones, because the relevant heat deposit is three times larger. On the other hand the outer layer cables can evacuate a smaller amount of heat, since they are not in direct contact with the bath. The largest of the small faces is in contact with the quench heaters and the ground insulation, whereas the smallest one is in contact with the inner layer through a fishbone structure. Fig. 7.6 reports the heat transfer curve of the MB outer layer in optimistic vs. pessimistic hypothesis of heat transfer mechanisms. In the optimistic case the cables can transfer heat both through He II and polyimide conduction towards the inner layer cables, which are assumed at 1.9 K. In the pessimistic case no heat transfer is assumed in this direction, corresponding to quasi adiabatic conditions. Indeed the only heat extraction from the central cables can occur towards the heated adjacent cables, and adiabatic azimuthal boundary conditions are assumed. The situation is critical in the

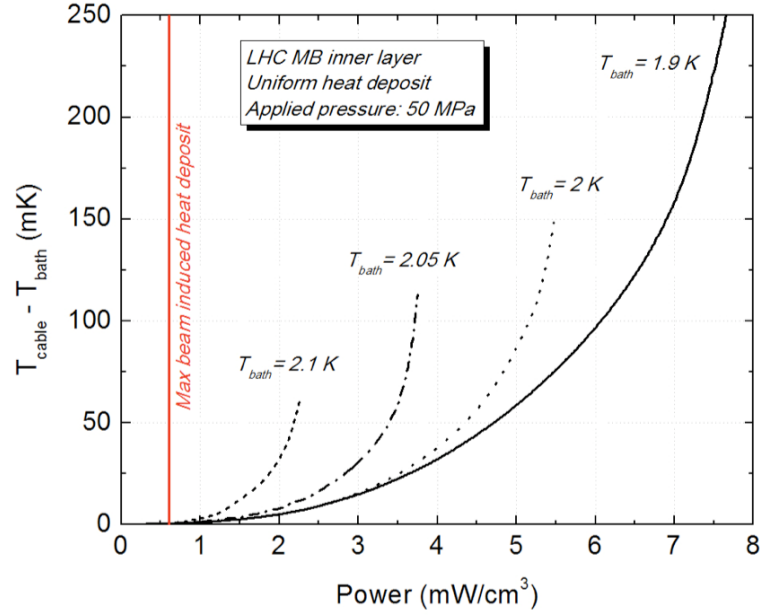


Figure 7.5: Calculated temperature rise of the mid-plane cable vs. heat load for the LHC MB inner layer cable, in the coil configuration. Different bath temperatures are assumed, ranging between 1.9 and 2.1 K.

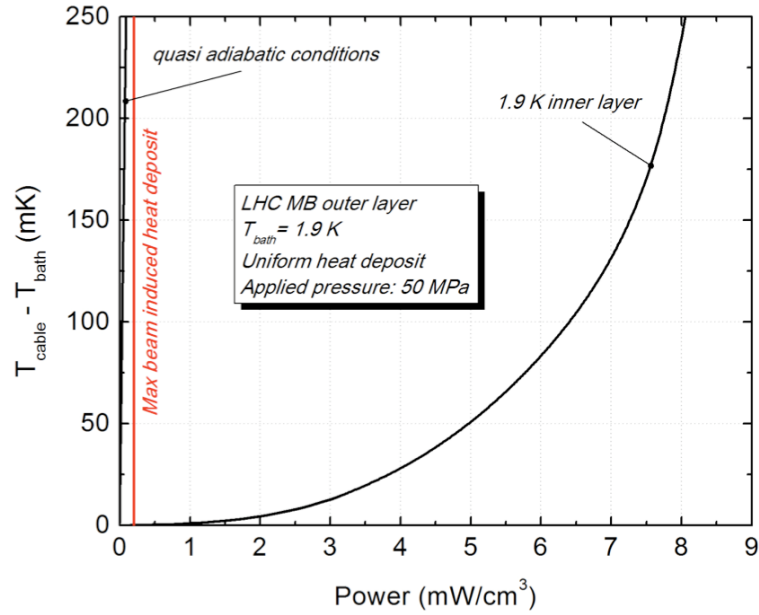


Figure 7.6: Calculated temperature rise of the mid-plane cable vs. heat load for the LHC MB outer layer cable, in the coil configuration. The bath temperature is assumed to be 1.9 K. Different cooling configurations are considered, namely a quasi adiabatic case of no radial heat transfer and a more optimistic scenario of radial heat transfer towards the inner layer cable assumed at 1.9 K.

assumption of such conservative hypothesis. The maximum beam induced heat deposit would cause a temperature rise above T_λ . The actual behavior of the outer layer cables is in between the two calculated curves. Although further investigations are needed to determine it more precisely, this study showed that the outer layer cable should not be neglected while estimating the coil stability.

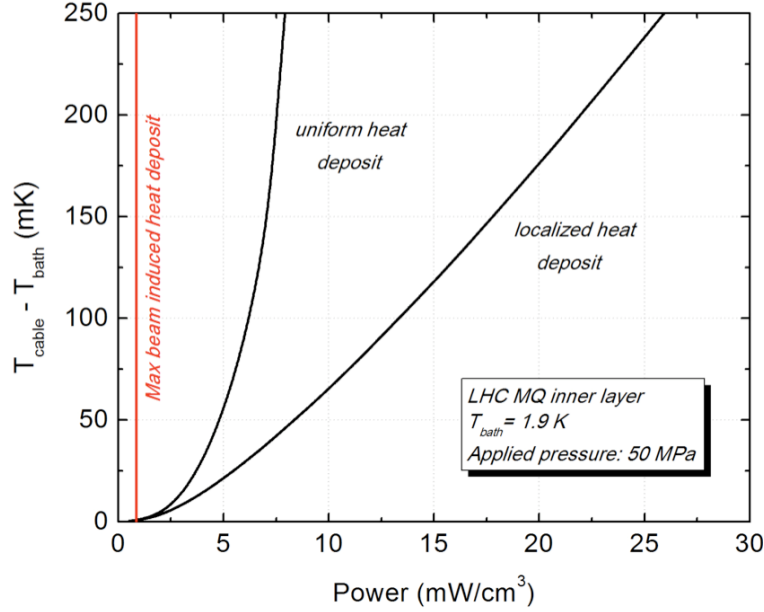


Figure 7.7: Calculated temperature rise of the mid-plane cable vs. heat load for the LHC MQ inner layer cable, in the coil configuration. The bath temperature is assumed to be 1.9 K. The case of uniform heating over all the cables is compared to the localized heat deposit in one single cable.

Fig. 7.7 reports the results of the MQ inner layer. The model parameters are modified to take into account the dimensions of the MQ cable and polyimide tapes. The slits and micro-channels thickness is considered equal to that determined for the MB case. The beam induced heat deposit is slightly larger than for the MB, but still considerably smaller than the allowed heat extraction, both in the uniform and localized heating case.

A good cable electrical insulation should allow enough heat transfer to maintain the cable below T_λ in case of heat deposit. However a further margin is present before the superconducting cables reach the critical temperature determining the quench of the magnet. In the second part of this section, we show how we exploited the experimental results presented in chapter 3 to estimate the steady-state quench margin over the whole beam energy range.

The current sharing temperature T_{cs} was computed in the center and inner edge of the most critical mid-plane cables, according to the Nb-Ti critical surface [135]. The relevant magnetic field values were calculated using the ROXIE computer code [14][136], depending on the magnet current. We determined the heat extracted at T_{cs} in the cable center and edge from the stack experimental data of the LHC MB insulation. The case considered was that of five heated cables at an applied pressure of 50 MPa. The heat was normalized to the smallest of the cable small faces, assuming that above T_λ the heat extraction mainly occurs through the small faces. Fig. 7.8 presents the obtained results, expressed as the quench margin with respect to the magnet operational current I_{op} .

The curves represent the power that can be extracted from the coil as long as the cable center / inner edge is superconducting. The cable center is more stable (lower magnetic field, thus higher T_{cs}) than the inner edge, but the latter is better cooled. For low currents the limiting part of the cable is the center, whereas for high currents the limiting part is the inner edge. The most conservative assumption is to consider the coil quench margin as

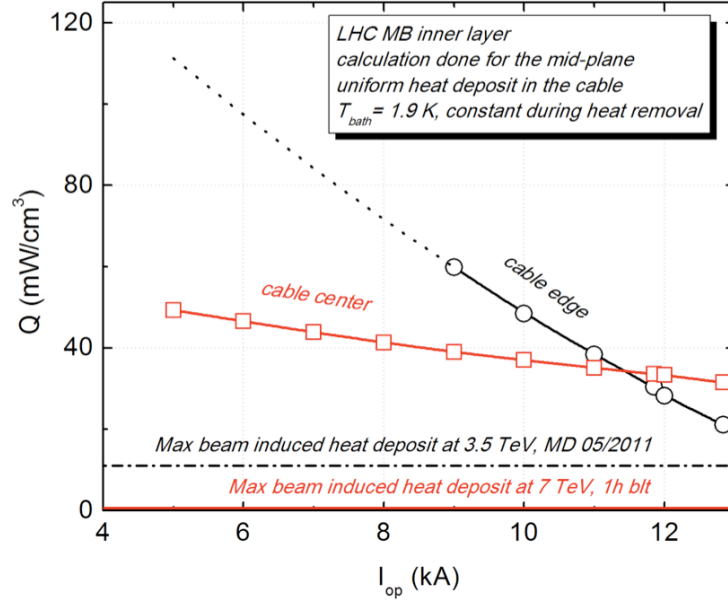


Figure 7.8: Steady-state quench margin of the mid-plane cable of the LHC MB inner layer, as a function of the magnet current. Uniform cable heating and a constant bath temperature of 1.9 K are considered.

the lower envelope of the two curves. The cable edge curve is probably closer to reality because the beam losses are mainly concentrated in that zone. The heat deposit in the tests was uniform over the cable cross-section. The quench margin in case of a non-uniform heating pattern, similar to the beam-loss pattern may be slightly higher.

The maximum beam induced heat deposit is shown as well, according to Fig. 7.1. The case of 7 TeV (11.85 KA) refers to one hour beam life time nominal intensity. The case of 3.5 TeV (5.925 KA) refers to the loss rate of the MD done in May 2011, which did not lead to quench of the magnets. In both cases the quench margin obtained is considerably higher than the maximum beam loss heat deposit.

7.5 HL-LHC magnets

The same studies were applied to the HL-LHC (EI4) insulation. The magnet MQXC that will be built with this new insulation, in the frame of the HL-LHC upgrade, will face a larger heat load than the LHC MB and MQ magnets. Such heat deposit, of the order of 7.5 mW/cm³, could not be withstood by the LHC insulation without losing the superfluid state. This is clearly shown by the LHC MB curve reported in Fig. 7.9.

In the first of the two analyses, the model was built by modifying the relevant stack model presented in chapter 5. We assumed the same hypotheses considered in the previous section. The only difference concerned the applied pressure. We considered 100 MPa (at room temperature), which corresponds to the mid-plane pressure of the MQXC magnet [77]. Fig. 7.9 shows the results for uniform heat deposit over all the cables and for localized heat deposit in one single cable, in 1.9 K bath. Fig. 7.10 shows the results for different bath temperatures from 1.9 to 2.1 K. In all cases, thanks to the efficient HL-LHC insulation, the allowed heat extraction is significantly larger than the maximum beam induced heat deposit.

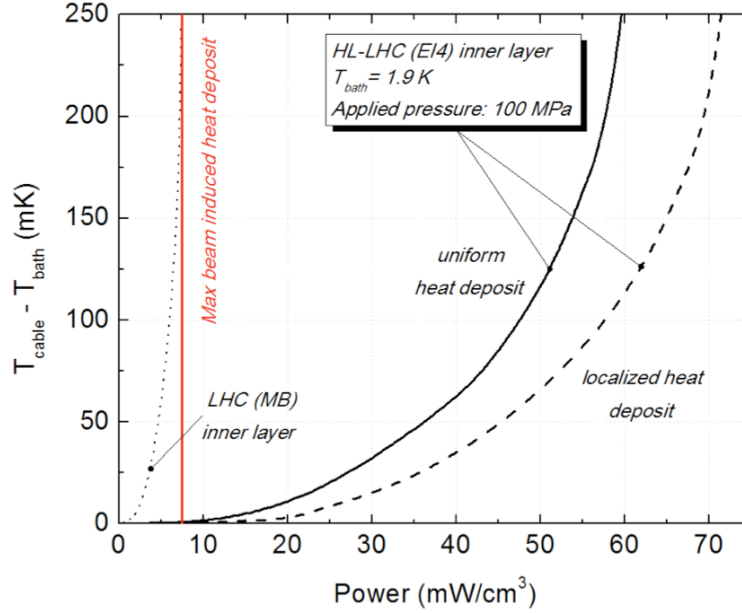


Figure 7.9: Calculated temperature rise of the mid-plane cable vs. heat load for the HL-LHC (EI4) inner layer cable, in the coil configuration. The bath temperature is assumed to be 1.9 K. The case of uniform heating of all the cables is compared to the localized heating case, where one single cable is heated. The LHC (MB) curve is reported for comparison.

It is worth noticing that, in the coil configuration, the improvement of heat extraction of the HL-LHC (EI4) insulation with respect to the LHC MB one is more than four times, as it was the case in chapters 4 and 5. The reason is that the major heat extraction for the LHC insulation occurs through the cable small faces. If one of them becomes adiabatic, as we assumed in the coil configuration, the allowed heat extraction is roughly divided by two. This is not the case for the HL-LHC insulation, where the network of micro-channels responsible for the major heat extraction is located on all the four cable faces. Therefore if one of the small faces becomes adiabatic, the effect on the allowed heat extraction is minor.

The procedure to calculate the quench margin was the same followed in the previous section. For the T_{cs} computation we took into account the MQXC magnetic field map [137]. The HL-LHC (EI4) experimental data from chapter 4 were used to determine the heat extraction, in case of five heated cables at an applied pressure of 100 MPa. The results are reported in Fig. 7.11. The same features of Fig. 7.8 are present, with higher values of the quench margin. The maximum beam induced heat deposit refers to the case of 7 TeV at a luminosity of $5 \cdot 10^{34} \text{cm}^{-2} \text{s}^{-1}$. It corresponds to a magnet current of 12.85 KA, where the estimated quench margin is almost seven times higher.

7.6 Conclusion

The quench margin evaluation carried out using both a modeling and an experimental approach confirmed that the stability margin of the LHC main dipoles is sufficiently higher than the expected beam induced heat deposit. Such magnets would not withstand the larger heat load expected in the HL-LHC interaction regions. The thermally enhanced insulation

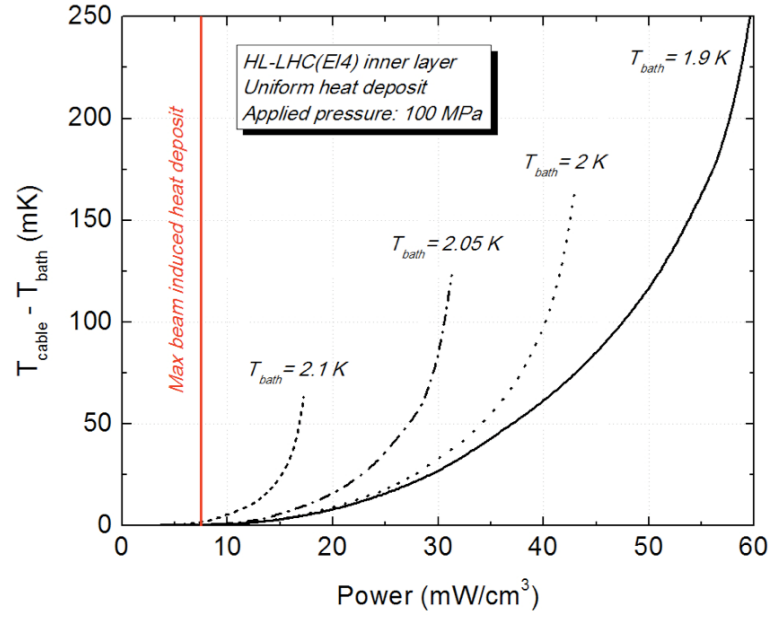


Figure 7.10: Calculated temperature rise of the mid-plane cable vs. heat load for the HL-LHC (EI4) inner layer cable, in the coil configuration. Different bath temperatures are assumed, ranging between 1.9 and 2.1 K.

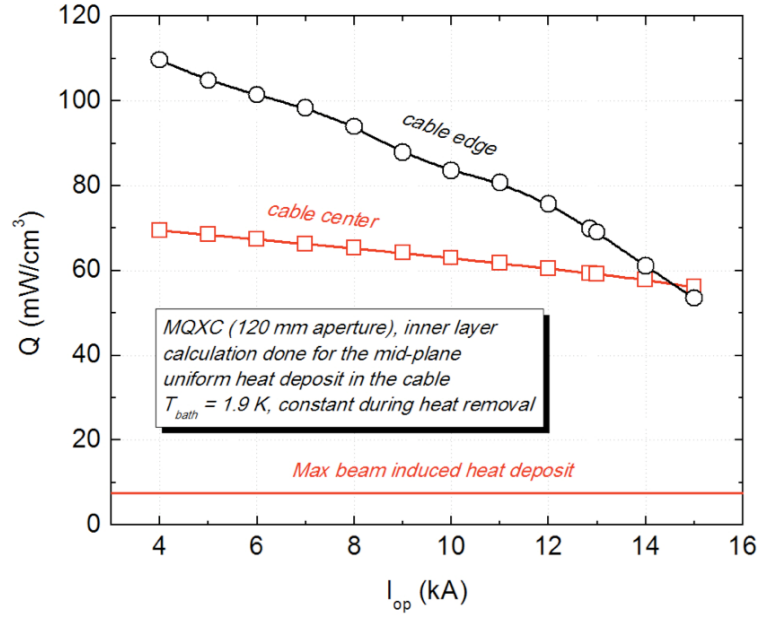


Figure 7.11: Steady-state quench margin of the mid-plane cable of the HL-LHC MQXC inner layer, as a function of the magnet current. Uniform cable heating and a constant bath temperature of 1.9 K are considered.

presented in chapter 4 allows instead a comfortable margin also in this challenging case.

Chapter 8

Conclusion

This thesis work brought original contributions to the theory, modeling and measurement of heat transfer in superconducting magnets cooled by superfluid helium. Our investigations encompassed different aspects of the topic, spanning from the micro-scale of the narrow channels in the cable insulation to the magnet scale. The achieved qualitative and quantitative results allowed to obtain a thorough comprehension of the magnet heat transport and stability mechanisms for the LHC and for its future upgrades.

The heat transport through the cable electrical insulation was first addressed by developing an innovative experimental program. It allowed to understand and quantify a number of thermal features of the LHC *state-of-the-art* insulation. The results of the study mainly highlighted the important role of superfluid helium penetrating inside the cable through the insulation porous structure, and provided indications for the elaboration of a thermal numerical model of the coil. The superfluid helium heat transfer constitutes a significant mechanism for heat extraction that can be further exploited.

A new thermally enhanced insulation scheme (HL-LHC) based on an increased porosity to superfluid helium was developed. The improved thermal performance with respect to the LHC insulation was demonstrated by a spectacular increased heat transfer capacity of at least a factor of four. The performed experiments proved that this improvement does not reduce with the applied pressure, up to the levels typical of magnet operation. Therefore the proposed insulation is a suitable candidate for future superconducting magnets that will deal with large heat loads. This is the case of the inner triplets quadrupoles of the HL-LHC upgrade project, for which the insulation was developed. In this frame the new insulation is currently being used for the prototype of the so-called MQXC magnet. The possibility to use such insulation scheme is also being considered for other LHC and non-LHC related projects.

The experimental measurements highlighted a larger thermal decoupling of adjacent cables wrapped with this new insulation, with respect to the LHC one. A helium micro-channels network exists indeed between the insulation tapes, thus allowing an efficient heat transfer between cables and bath. We also demonstrated that there is potential for further improving the heat extraction relying on the concept of HL-LHC insulation.

The electrical robustness of the HL-LHC insulation was investigated and compared to the LHC one, proving to be satisfactory. A mechanical characterization was performed as well, showing a larger thickness loss and a 10% reduction of the elastic modulus with respect to the LHC insulation. A new experimental setup was developed to measure the stress

relaxation, showing that the largest pressure losses take place during the first days after the application of the initial force. Different stress relaxation behaviors were highlighted, depending on the insulation scheme and on the compactness of the superconducting cable. It was shown that a higher curing pressure helps to limit the stress losses after assembly, by roughly 20%.

We developed a theoretical model that allowed to quantitatively explain the results of the experimental heat transfer tests. By comparison to measurements performed in different heating configurations and at different applied pressures, the model allowed identifying the main mechanisms for heat extraction in the LHC and HL-LHC schemes. The He II micro-channels were confirmed to be responsible for the most significant heat transfer. Their effective dimensions were identified from the thermal analysis, and confirmed to correspond to geometrical dimensions by microscope images. In the LHC insulation, the micro-channels consist of slits created by the tapes overlap. They feature an average thickness of about $7\text{ }\mu\text{m}$ in the non-pressed (small) cable face, permitting the establishment of a turbulent regime. In the pressed (large) cable face the equivalent cross-section of each slit is instead smaller than $2\text{ }\mu\text{m}^2$, resulting in a laminar regime. In the HL-LHC insulation, the micro-channels are located between the wrappings of the intermediate tape. In the mechanical conditions typical of magnet operation they feature an average cross-section of about 40% of their non-pressed geometrical size, which allows the establishment of a fully developed Gorter-Mellink regime.

In the modeling we assumed the validity of the classical laws of the superfluid helium dynamic regimes also in the micro-channels. In order to assess this hypothesis that was never investigated down to such small dimensions, we conceived and developed a new experimental and theoretical activity to investigate the heat transport through micro-channels in pressurized superfluid helium. The first main result of this study was the observation of the Gorter-Mellink regime in channels with equivalent diameter of $\sim 100\text{ }\mu\text{m}$, which confirmed the only study so far carried out in these conditions. In smaller channels of $16\text{ }\mu\text{m}$ thickness we could identify the laminar regime of pure superfluidity, as well as the fully developed turbulent regime. The latter is the most interesting for superconducting magnets applications, as demonstrated by the model. The Gorter-Mellink coefficient characterizing this regime was found to be in agreement with the theoretical one, confirming the independence of the relevant law from the channel geometrical shape and size down to these dimensions.

In the last part of the thesis we addressed the magnets stability against beam-induced heat deposit, that will become a critical issue when the LHC will run at nominal beam energy as well as after the luminosity upgrade. The most unstable part of the magnet was identified, and the quench margin was evaluated using both a modeling and an experimental approach based on the results of the thesis. It was confirmed that the stability margin of the LHC main dipoles is sufficiently higher than the expected beam induced heat deposit. Such magnets would however not withstand the larger heat load expected in the HL-LHC interaction regions. The proposed thermally enhanced insulation allows instead a comfortable margin also in this challenging case.

The work performed in this thesis opens new perspectives and curiosity. The possibility to upgrade the coil-like experimental setup is presently under investigation. The modifications would concern the geometry and the heat deposition, in order to reproduce more precisely the coil thermal behavior and the radial beam loss profile. Future heat transfer

measurements are foreseen to further improve the estimation of the quench margin for the LHC magnets.

The same approach will be followed to investigate heat transfer in coils realized with the promising Nb₃Sn technology.

Another future exploitation of the presented heat transfer measurements is the investigation of the transient regime. The time evolution of the heat extraction through the cable insulation is indeed of relevance for the magnet stability in case of transient beam losses.

The modeling would be refined according to the results of the new measurements and extended at temperature regimes above T_λ . It would also take advantage of further experimental studies on narrow channels that will investigate dimensions of the order of the μm or smaller, the presence of restrictions and networks of interconnected micro-channels, thus reproducing the actual topology of the cables electrical insulations.

List of publications

During the course of the Ph.D. thesis :

Refereed contributions to journals

- P.P. Granieri, P. Fessia, D. Richter and D. Tommasini, “Heat transfer in an enhanced cable insulation scheme for the superconducting magnets of the LHC luminosity upgrade”, *IEEE Trans. Appl. Supercond.*, vol. 20, no. 3, pp. 168–171, 2010.
- P. Fessia, P.P. Granieri, S. Luzieux, D. Tommasini, A. Gerardin, M. Guinchard, F. Regis, S. Sgobba and A. Zaghloul, “Electrical and mechanical performance of an enhanced cable insulation scheme for superconducting magnets”, *IEEE Trans. Appl. Supercond.*, vol. 20, no. 3, pp. 1622–1625, 2010.
- P. Fessia, P.P. Granieri, F. Borgnolutti, F. Regis, D. Richter and E. Todesco, “A 120 mm bore quadrupole for the phase I LHC upgrade”, *IEEE Trans. Appl. Supercond.*, vol. 20, no. 3, pp. 140–143, 2010.
- P.P. Granieri, C. Lorin and E. Todesco, “Slip–Stick mechanism in training the superconducting magnets in the Large Hadron Collider”, *IEEE Trans. Appl. Supercond.*, vol. 21, no. 5, pp. 3555–3560, 2011.
- P.P. Granieri, P. Fessia, D. Richter and D. Tommasini, “Thermally enhanced cable insulation for the Nb-Ti high luminosity LHC inner triplet model”, *IEEE Trans. Appl. Supercond.*, vol. 23, no. 3, 7700404, 2012.
- P.P. Granieri, M. Casali, M. Bianchi, M. Breschi, L. Bottura and G.P. Willering, “Analysis of defective interconnections of the 13 kA LHC superconducting bus bars”, *IEEE Trans. Appl. Supercond.*, vol. 23, no. 3, 4000504, 2012.
- P.P. Granieri, “Heat transfer through cable insulation of Nb-Ti superconducting magnets operating in He II”, *Cryogenics*, accepted for publication.
- P.P. Granieri, M. Breschi, M. Casali, L. Bottura and A. Siemko, “Thermo-electric analysis of the interconnection of the LHC main superconducting bus bars”, *Cryogenics*, accepted for publication.
- D. Richter and P.P. Granieri, “Heat transfer measurements through superconducting cable electrical insulation”, *Cryogenics*, to be submitted for publication.
- P.P. Granieri, “Zero-dimensional stability analysis of the LHC cables”, *Cryogenics*, to be submitted for publication.
- A. Mapelli, P. Petagna and P.P. Granieri, “Manufacturing of Pyrex micro-channels for cryogenic applications”, *J. of Micromech. Microeng.*, to be submitted for publication.

Refereed conferences proceedings

- P.P. Granieri and D. Richter, “Heat transfer measurements through thermally enhanced insulation schemes for Nb-Ti superconducting magnets operating in He II”, *Proceedings of ICEC 23 - ICMC 2010*, Wroclaw, Poland, pp. 893–898, 2010.
- P.P. Granieri, M. Casali and D. Richter, “Heat transfer in the LHC main superconducting bus bars”, *Proceedings of ICEC 23 - ICMC 2010*, Wroclaw, Poland, pp. 411–416, 2010.
- P.P. Granieri, B. Baudouy, A. Four, F. Lentijo, A. Mapelli, P. Petagna and D. Tommasini, “Steady-state heat transfer through micro-channels in pressurized He II”, *Advances in Cryogenic Engineering*, accepted for publication.

Non-refereed conferences proceedings, notes

- P. Fessia, P.P. Granieri *et al.*, “Qualification of Magnet Component”, SLHC-PP Work Package 6 Milestone Report, in the frame of the FP7 European program for the development of new inner triplets for the phase I of the LHC luminosity upgrade, 2008.
- P.P. Granieri, “Stability analysis of the ITER poloidal field insert conductor”, CERN/ITER Internal Note, EDMS 936182, 2008. Presented at the workshop ITER PF Insert Coil, October 2008, Naka JAEA, Japan.
- P. Fessia, P.P. Granieri *et al.*, “LHC upgrade phase I: status of the development of the magnet system in the frame of an FP7 EU project”, EDMS 1002559, 2009.
- P.P. Granieri, M. Casali, D. Richter, L. Bottura, M. Breschi and A. Verweij, “Preliminary analysis of the heat extraction from the LHC main superconducting bus bars”, CERN TE Internal Note, EDMS 1090724, 2010.
- P.P. Granieri, L. Bottura, M. Casali and M. Breschi, “Protection estimates for the 13 kA bus bars interconnections at 3.5 - 4.5 TeV”, CERN Memorandum, EDMS 1185034, 2012.
- P.P. Granieri, “Mechanical measurements of enhanced cable insulation schemes for Nb-Ti superconducting magnets of the HL-LHC upgrade”, CERN Internal Note, to be published.

Before the Ph.D. thesis :**Refereed contributions to journals**

- M. Breschi, P.P. Granieri, M. Calvi, M. Coccoli and L. Bottura, “Quench propagation and stability analysis of Rutherford resistive core cables”, *Cryogenics*, vol. 46, no. , pp. 606–614, 2006.
- M. Calvi, P.P. Granieri *et al.*, “Analytical model of thermoelectrical behavior in superconducting resistive core cables”, *IEEE Trans. Appl. Supercond.*, vol. 16, no. 2, pp. 1208–1211, 2006.
- P.P. Granieri *et al.*, “Stability analysis of the LHC cables for transient heat depositions”, *IEEE Trans. Appl. Supercond.*, vol. 18, no. 2, pp. 1257–1262, 2008.

Non-refereed conferences proceedings, notes

- L. Bottura, P.P. Granieri and M. Breschi, “Analysis of the stability margin of force-flow cooled superconducting cables for superferic accelerator magnets”, Report of the GSI-INTAS Grant 03-54-4964, EDMS 585062, 2005.

List of presentations

During the course of the Ph.D. thesis :

International conferences or workshops

- *Transient heat transfer model and stability analysis of helium-cooled superconducting cables*, CHATS-AS workshop on Applied Superconductivity 2008, October - November 2008, KEK, Tsukuba, Japan.
- *Evaluation of stability and quench*, ITER PF Insert Coil workshop, October 2008, Naka JAEA, Japan.
- *Heat transfer in superfluid He through porous cable insulation*, workshop on Thermal Modeling & Thermal Experiments for Accelerator Magnets, September-October 2009, Geneva, Switzerland.
- *Heat transfer in an enhanced cable insulation scheme for the superconducting magnets of the LHC luminosity upgrade*, conference on Magnets Technology MT-21, October 2009, Hefei, China.
- *Heat transfer measurements through thermally enhanced insulation schemes for Nb-Ti superconducting magnets operating in He II*, International Cryogenic Engineering / International Cryogenic Materials Conference ICEC 23-ICMC 2010, July 2010, Wroclaw, Poland.
- *Heat transfer in the LHC main superconducting bus bars*, International Cryogenic Engineering / International Cryogenic Materials Conference ICEC 23 - ICMC 2010, July 2010, Wroclaw, Poland.
- *Thermally enhanced cable insulation for the Nb-Ti high luminosity LHC inner triplet model*, conference on Magnets Technology MT-22, September 2011, Marseille, France.
- *Analysis of defective interconnections of the 13 kA LHC superconducting bus bars*, conference on Magnets Technology MT-22, September 2011, Marseille, France.
- *Heat transfer through cable insulation of Nb-Ti superconducting magnets operating in He II*, CHATS-AS workshop on Applied Superconductivity 2011, October 2011, CERN, Geneva, Switzerland.
- *Stability analysis of the interconnection of the LHC main superconducting bus bars*, CHATS-AS workshop on Applied Superconductivity 2011, October 2011, CERN, Geneva, Switzerland.

Seminars at CERN, Geneva, Switzerland

- *Impact of gaps in the stabilizer of the splices of the LHC main superconducting busbars*, Magnet Operation and Performance Support (MOPS) team meeting, October 15th 2008.

- *Status of the qualification of the enhanced insulation*, LHC Inner Triplets Upgrade Working Group meeting, May 6th 2009.
- *Development of the insulation for the low-beta quadrupoles LHC interaction regions upgrade phase I*, Technology department (TE) Magnet seminar, July 3rd 2009.
- *Heat extraction from the LHC main SC bus bars & impact on the bus bars stability*, meeting 15 of the LHC Splices Consolidation Task Force, March 25th 2010.
- *Stability analysis of the interconnection of the LHC main superconducting bus bars*, Technology department (TE) Magnet seminar, January 14th 2011.

Before the Ph.D. thesis :

International conferences or workshops

- *Analytical model of thermo-electrical behaviour in superconducting resistive core cables*, conference on Magnets Technology MT-19, September 2005, Genoa, Italy.
- *Stability analysis of the LHC cables for transient heat depositions*, conference on Magnets Technology MT-20, August 2007, Philadelphia, USA.
- *Modeling of cable stability margin for transient perturbations*, workshop on Heat Generation & Transfer in Superconducting Magnets THERMOMAG 07, November 2007, Paris, France.

List of contributions to other topics

This list contains the contributions during the course of the Ph.D. thesis to topics that are not directly related to its main subjects:

- a. Energy margin calculations for modeling of the training mechanisms of the LHC superconducting magnets [138];
- b. Analysis of heat transfer in the LHC main superconducting bus bars [139] [140];
- c. Stability analysis of the interconnection of the LHC main superconducting bus bars, modeling of experimental tests of defective interconnections, and protection estimates for LHC operation at 3.5 – 4.5 TeV [141] [142] [143];
- d. Zero-dimensional stability analysis of the LHC cables [144];
- e. Heat extraction measurement from insulated superconducting cables in supercritical helium, for the fast ramped magnets of the SIS300 synchrotron of FAIR, GSI. In collaboration with Istituto Nazionale di Fisica Nucleare (INFN) Genoa, Italy [145];
- f. Heat transfer measurement through the large face of insulated Nb-Ti cables. In collaboration with Wroclaw University of Technology (WUT), Poland [89];
- g. Stability analysis of the ITER poloidal field (PF) insert conductor [146];
- h. Quench analysis of superconducting fast cycles magnet for the PS2 [147].

Bibliography

- [1] CERN official website. [Online]. Available: <http://www.cern.ch>
- [2] O. S. Brüning *et al.*, *LHC design report vol. 1*. CERN, Geneva, Switzerland, 2004.
- [3] P. Collier and O. S. Brüning, “Building a behemoth,” *Nature*, no. 448, pp. 285–289, 2007.
- [4] *The LHC Study Group. Design study of the Large Hadron Collider (LHC): A multiparticle collider in the LEP tunnel*. CERN 91-03, 1991.
- [5] L. Rossi, “Superconductivity: its role, its success and its setbacks in the Large Hadron Collider of CERN,” *Superconductor Science and Technology*, vol. 23, 2010.
- [6] A. Blondel *et al.*, “Physics opportunities with future proton accelerators at CERN,” CERN-PH-TH/2006-175, 2006. [Online]. Available: <http://arxiv.org/pdf/hep-ph/0609102>
- [7] L. Rossi, L. Bottura, G. de Rijk, and E. Todesco, “Advanced accelerator magnets for upgrading the LHC,” *IEEE Trans. Appl. Supercond.*, to be published.
- [8] E. Todesco and F. Zimmermann, Eds., *Workshop on the High-Energy Large Hadron Collider*, October 2010.
- [9] K.-H. Mess, P. Schmuser, and S. Wolff, *Superconducting accelerator magnets*. World Scientific, Singapore, 1996.
- [10] S. W. Van Sciver, *Helium cryogenics*. Plenum Press, New York and London, 1986.
- [11] P. Lebrun and L. Taviani, “The technology of superfluid helium,” in *CERN accelerator school: superconductivity and cryogenics for accelerators and detectors*, 2002, pp. 375–395.
- [12] L. Burnod, D. Leroy, B. Szeless, B. Baudouy, and C. Meuris, “Thermal modelling of the LHC dipoles functioning in superfluid helium,” in *European Particle Accelerator Conference (EPAC 94), London, England, 1994*, pp. 2295–2297.
- [13] R. van Weelderen, B. Vullierme, and T. Peterson, “The cryogenic design of the phase I upgrade inner triplet magnets for LHC,” in *Proceedings of ICEC 23 – ICMC 2010, Wroclaw, Poland, 2010*, pp. 899–903.
- [14] P. Hagen and B. Auchmann, unpublished calculations.
- [15] Y. Ajima *et al.*, “The MQXA quadrupoles for the LHC low-beta insertions,” *Nucl. Instrum. Meth. Sect. A*, vol. 550, no. 3, pp. 499–513, 2005.
- [16] M. Lamm *et al.*, “Test results of Fermilab-built quadrupoles for the LHC interaction regions,” in *European Particle Accelerator Conference (EPAC 06), Edinburgh, Scotland, 2006*, pp. 2637–2639.

- [17] J. P. Koutchouk, L. Rossi, and E. Todesco, “A solution for phase-one upgrade of the LHC low-beta quadrupoles based on Nb-Ti,” LHC Project Report 1000, CERN, Geneva, Switzerland, 2007.
- [18] R. Ostojic *et al.*, “Conceptual design of the LHC interaction region upgrade : phase-I,” LHC Project Report 1163, CERN, Geneva, Switzerland, 2008.
- [19] A. Devred, “Insulation systems for Nb₃Sn accelerator magnet coils manufactured by the Wind and React technique,” *IEEE Trans. Appl. Supercond.*, vol. 12, no. 1, March 2002.
- [20] M. La China and D. Tommasini, “Comparative study of heat transfer from Nb-Ti and Nb₃Sn coils to He II,” *Phys. Rev. ST Accel. Beams*, vol. 8, p. 082401, Aug 2008.
- [21] P. Fessia, P. P. Granieri, F. Borgnolutti, F. Regis, D. Richter, and E. Todesco, “A 120 mm bore quadrupole for the phase I LHC upgrade,” *IEEE Trans. Appl. Supercond.*, vol. 20, no. 3, pp. 140–143, 2010.
- [22] S. Russenschuck, B. Auchmann, J. C. Perez, D. Ramos, P. Fessia, M. Karppinen, G. Kirby, T. Sahner, and N. Schwerg, “Design challenges for a wide-aperture insertion quadrupole magnet,” *IEEE Trans. Appl. Supercond.*, vol. 21, pp. 1674–1678, 2011.
- [23] E. Todesco, “HL-LHC: initial workflow between magnets, beam dynamics and energy deposition,” CERN Hi Lumi collaboration meeting, November 2011.
- [24] J. Billan, “Selection of the insulation of superconducting wires for d.c. magnets,” Int. Symposium on High Voltage Insulation for Low Temperature Application, Wroclaw, Poland. CERN-ISR-LTD-76-15, 1976.
- [25] T. S. Jaffrey *et al.*, “Fermilab-built SSC collider dipoles using low temperature curing insulation systems with and without glass tape,” in *Particle Accelerator Conference, Washington, D.C.*, 1993, pp. 2769–2771.
- [26] C. H. Dustmann, M. Forster, and D. Bonmann, “Series production of the superconducting HERA dipole magnets,” *IEEE Trans. Magn.*, vol. 24, pp. 1338–1341, 1988.
- [27] M. Anerella, A. Ghosh, E. Kelly, J. Schmalzle, E. Willen, J. Fraivillig, J. Ochsner, and D. J. Parish, “Improved cable insulation for superconducting magnets,” in *Particle Accelerator Conference, Washington, D.C.*, 1993, pp. 2790–2792.
- [28] C. Meuris, B. Baudouy, D. Leroy, and B. Szeless, “Heat transfer in electrical insulation of LHC cables cooled with superfluid helium,” *Cryogenics*, vol. 39, pp. 921–931, 1999.
- [29] P. Fessia, H. Kummer, H. Kuribayashi, D. Tommasini, and F. Van de Velde, “Curing of LHC main dipole coils insulated with all polyimide PIXEO® adhesive tape,” *IEEE Trans. Appl. Supercond.*, vol. 16, no. 2, pp. 1782–1785, 2006.
- [30] H. Kummer, “CERN reception tests for the polyimide films for the LHC main dipole and quadrupole magnets,” CERN, EDMS 414022, Tech. Rep., 2000.
- [31] B. Hébral, *Cryogénie: ses applications en supraconductivité*. Institut international du froid et technique de l’ingénieur, 1995.
- [32] “Hepak,” Cryodata Inc., P.O. Box 173, Louisville, CO 80027.
- [33] L. Onsager. *Nuovo cimento*, 1948.

- [34] R. Feynman, "Application of quantum mechanics to liquid helium," *Progress in low temperature physics*, pp. 17—53, 1955.
- [35] I. Khalatnikov, *An introduction to theory of superfluidity*. New York Amsterdam: Benjamin Publishing inc. 206, 1965, vol. 1.
- [36] R. Donnelly, W. Glaberson, and P. Parks, *Experimental superfluidity*. University of Chicago Press, 1967.
- [37] S. J. Putterman, *Superfluid hydrodynamics*. North-Holland / American Elsevier, 1974.
- [38] W. E. Keller, *Helium-3 and Helium-4*. New York: Plenum Press, 1969.
- [39] W. F. Vinen, "Mutual friction in a heat current in liquid helium II. I. Experiments on steady heat currents," *Proc. Roy. Soc.*, vol. A 240, p. 114, 1957.
- [40] C. J. Gorter and J. H. Mellink, "On the irreversible process in liquid helium II," *Physica*, vol. XV, pp. 285–304, May 1949.
- [41] R. Asthony and J. Northby, "Vortex velocity in turbulent He II counterflow," *Phys. rev. Lett.*, p. 1714, 1975.
- [42] J. Tough, "Superfluid turbulence," *Progress in low temperature Physics*, vol. 8, pp. 135—219, 1982.
- [43] W. F. Vinen, "Mutual friction in a heat current in liquid helium II. III. Theory of the mutual friction," *Proc. Roy. Soc.*, vol. 242, pp. 493–515, 1957.
- [44] J. Allen and J. Reekie, "Momentum transfer and heat flow in liquid helium II," *Mathematical proceedings of the Cambridge Philosophical Society*, vol. 35, 1939.
- [45] K. Atkins and H. Fairbank, "Liquid helium," *American Journal of Physics*, vol. 27, p. 672, 1959.
- [46] W. van Alphen *et al.*, "The dependence of the critical velocity of the superfluid on channel diameter and film thickness," *Physics Letters*, vol. 20, no. 5, pp. 474–475, 1966.
- [47] P. Craig, "Critical velocities in superfluid He II," *Physical Letters*, vol. 21, no. 4, p. 385, 1966.
- [48] D. Ladner and J. Tough, "Temperature and velocity dependence of superfluid turbulence," *Physical Review B*, vol. 20, no. 7, pp. 2690–2701, 1979.
- [49] V. Arp, "Heat transport through helium II," *Cryogenics*, vol. 10, pp. 96–105, 1970.
- [50] P. Kapitza, "The study of heat transfer in helium II," *J. Phys. (USSR)*, vol. 4, no. 3, pp. 181–210, 1941.
- [51] C. Meuris, "Heat transport in insulation of cables cooled by superfluid helium," *Cryogenics*, vol. 31, pp. 624–628, 1991.
- [52] B. Baudouy, "Etude des transferts de chaleur dans les isolations électriques de câbles supraconducteurs d'aimant d'accélérateur refroidi par hélium superfluide," Ph.D. dissertation, Université Pierre et Marie Curie and CEA-Saclay, 1996.
- [53] N. Kimura, V. Kovachev, A. Nakamoto, A. Yamamoto, T. Shintomi, A. Terashima, K. Tanaka, and T. Haruyama, "Heat transfer from insulated Rutherford type cables immersed in pressurized He II," *Advances in Cryogenic Engineering*, vol. 43, pp. 1433–1440, 1998.

-
- [54] N. Kimura, V. Kovachev, A. Yamamoto, T. Shintomi, A. Nakamoto, A. Terashima, K. Tanaka, and T. Haruyama, “Improved heat transfer for Rutherford-type insulated cables in pressurized He II,” *Proceedings of MT-15*, pp. 1238–1241, 1998.
- [55] N. Kimura, A. Yamamoto, T. Shintomi, A. Terashima, V. Kovachev, and M. Murakami, “Heat transfer characteristics of Rutherford-type superconducting cables in pressurized He II,” *IEEE Trans. Appl. Supercond.*, vol. 9, no. 2, pp. 1097–1100, 1999.
- [56] D. Richter, J. Fleiter, B. Baudouy, and A. Devred, “Evaluation of the transfer of heat from the coil of the LHC dipole magnet to helium II,” *IEEE Trans. Appl. Supercond.*, vol. 17, no. 2, pp. 1263–1268, 2007.
- [57] D. Richter *et al.*, “DC measurement of electrical contacts between strands in superconducting cables for the LHC main magnets,” *IEEE Trans. Appl. Supercond.*, vol. 7, no. 2, pp. 786–792, 1997.
- [58] D. Richter and P. P. Granieri, “Heat transfer measurements through superconducting cable electrical insulation,” *Cryogenics*, to be submitted for publication.
- [59] T. W. Kerlin, *Practical thermocouple thermometry*. North Carolina, ISA Publishing, 1999.
- [60] G. Claudet, *Handbook of Applied Superconductivity*, 1998, ch. Bath cryostats for superfluid helium cooling, pp. 795–800.
- [61] T. Boutboul, C.-H. Denarié, Z. Charifoulline, L. Oberli, and D. Richter, “Critical current test facilities for LHC superconducting NbTi cable strands,” in *Proceedings of the 5th EUCAS, Copenhagen*, 2001.
- [62] L. G. Rubin, “Cryogenic thermometry: a review of progress since 1982,” *Cryogenics*, vol. 37, no. 7, pp. 341–356, 1997.
- [63] J. G. Hust, R. L. Powell, and L. L. Sparks, *Temperature, its measurement and control in science and industry*. Pittsburgh: Instrument Society of America, 1972, vol. IV, pp. 1525–1535.
- [64] Lake Shore Cryotronics Inc. Appendix G: Sensor temperature response data tables. [Online]. Available: www.lakeshore.com
- [65] L. Chiesa, S. Feher, J. Kerby, M. Lamm, I. Novitski, D. Orris, J. Ozelis, T. Peterson, M. Tartaglia, and A. Zlobin, “Thermal studies of a high gradient quadrupole magnet cooled with pressurized, stagnant superfluid,” *IEEE Trans. Appl. Supercond.*, vol. 11, no. 1, pp. 1625–1628, 2001.
- [66] B. Baudouy, M. X. François, F.-P. Juster, and C. Meuris, “He II heat transfer through superconducting cables electrical insulation,” *Cryogenics*, vol. 40, pp. 127–136, 2000.
- [67] R. Lopez, “Dielectrical test on different kind of kapton wrapping,” unpublished measurements.
- [68] K. Couturier, P. Ferracin, W. Scandale, E. Todesco, and D. Tommasini, “Thermomechanical properties of the coil of the superconducting magnets for the Large Hadron Collider,” *IEEE Trans. Appl. Supercond.*, vol. 12, no. 2, pp. 1804–1812, 2001.
- [69] P. Védrine, B. Gallet, and C. Nouvel, “Measurement of thermo-mechanical properties of NbTi windings for accelerator magnets,” *IEEE Trans. Appl. Supercond.*, vol. 9, no. 2, pp. 236–239, 1999.

- [70] R. B. Meuser, S. Caspi, and W. S. Gilbert, “Measured mechanical properties of superconducting coil materials and their influence on coil prestress,” *IEEE Trans. Magn.*, vol. 17, pp. 2320–2323, 1981.
- [71] M. Reytier, A. Devred, M. Durante, C. Gourdin, and P. Vedrine, “Characterization of the thermo-mechanical behavior of insulated cable stacks representative of accelerator magnet coils,” *IEEE Trans. Appl. Supercond.*, vol. 11, pp. 3066–3069, 2001.
- [72] F. Cerutti, M. Mereghetti, and E. Wildner, “Update of power deposition studies in the LHC upgrade phase I insertion regions,” EDMS 975134, CERN, Geneva, Switzerland, 2008.
- [73] M. W. Wilson *et al.*, “Design studies on superconducting Cos Θ magnets for a fast pulsed synchrotron,” *IEEE Trans. Appl. Supercond.*, vol. 12, no. 1, pp. 313–316, 2002.
- [74] P. P. Granieri, “Mechanical measurements at ambient temperature of thermally enhanced cable insulation schemes for Nb-Ti superconducting magnets of the HL-LHC upgrade,” CERN TE, Tech. Rep., to be published.
- [75] M. La China and D. Tommasini, “Cable insulation scheme to improve heat transfer to superfluid helium in Nb-Ti accelerator magnets,” *IEEE Trans. Appl. Supercond.*, vol. 18, pp. 1285–1288, 2008.
- [76] D. Tommasini and D. Richter, “A new cable insulation scheme improving heat transfer in Nb-Ti superconducting accelerator magnets,” in *Proc. 11th European Particle Accelerator Conference, Genoa, Italy*, 2008.
- [77] G. Kirby *et al.*, “Engineering design and manufacturing challenges for a wide-aperture, superconducting quadrupole magnet,” *IEEE Trans. Appl. Supercond.*, to be published.
- [78] T. Nakamoto, “Conceptual design of the new D1 magnet for HL-LHC upgrade,” CERN Hi Lumi collaboration meeting, November 2011.
- [79] “Cluster of research infrastructures for synergies in physics (CRISP), in the frame of the FP7 european program, 2011.”
- [80] B. Baudouy, C. Meuris, L. Vieillard, and M. X. François, “Steady-state heat transferring through porous superconducting cable insulation,” *Advances in Cryogenic Engineering*, vol. 41, pp. 289–296, 1996.
- [81] B. Baudouy, “Kapitza resistance and thermal conductivity of Kapton in superfluid helium,” *Cryogenics*, vol. 43, pp. 667–672, 2003.
- [82] J. Lawrence, A. Patel, and J. G. Brisson, “The thermal conductivity of Kapton HN between 0.5 and 5 K,” *Cryogenics*, vol. 40, pp. 203–207, 2000.
- [83] National Institute of Standards and Technology (NIST). [Online]. Available: <http://www.nist.gov/index.html>
- [84] Eckels Engineering Inc., “Cryocomp version 3.”
- [85] M. Barucci, E. Gottardi, I. Peroni, and G. Ventura, “Low temperature thermal conductivity of Kapton and Upilex,” *Cryogenics*, vol. 40, pp. 145–147, 2000.
- [86] D. J. Benford, T. J. Powers, and S. H. Moseley, “Thermal conductivity of Kapton tape,” *Cryogenics*, vol. 39, pp. 93–95, 1999.

-
- [87] A. Bejan, *Convection heat transfer*, second edition ed. John Wiley & Sons, Inc., New York, 1995.
- [88] E. Gmelin, M. Asen-Palmer, M. Reuther, and R. Villar, "Thermal boundary resistance of mechanical contacts between solids at sub-ambient temperatures," *J. Phys. D: Appl. Phys.*, vol. 32, pp. 1622–1625, 1999.
- [89] M. Chorowski, J. Polinski, and M. Strychalski, "Heat transfer through Rutherford superconducting cable with novel pattern of polyimide electrical insulation in pressurized superfluid helium environment," *Advances in Cryogenic Engineering*, submitted for publication.
- [90] D. Bocian, unpublished calculation.
- [91] E. Bielert, A. Verweij, and H. ten Kate, "Finite element modeling in 3D of the impact of superfluid helium filled micro-channels on the heat transfer through LHC type cable insulation," *IEEE Trans. Appl. Supercond.*, accepted for publication.
- [92] C. Lorin, E. Todesco, and D. Bocian, "Numerical simulation of micro-channel deformation in enhanced insulation for Nb-Ti superconducting accelerator magnets," *IEEE Trans. Appl. Supercond.*, to be submitted for publication.
- [93] W. M. De Rapper, "Heat treatment and impregnation of the Nb3Sn SMC cable FRESCA sample," CERN, EDMS 1011308, Tech. Rep., 2009.
- [94] N. Kimura, H. Nakai, M. Murakami, A. Yamamoto, and T. Shintomi, "A study of the heat transfer properties of pressurized helium II through fine channels," *Advances in Cryogenic Engineering*, vol. 51, pp. 97–104, 2006.
- [95] C. Linnet and T. H. K. Frederking, "Thermal conditions at the Gorter-Mellink counterflow limit between 0.01 and 3 bar," *Journal of Low Temperature Physics*, vol. 21, no. 3–4, pp. 447–462, 1975.
- [96] A. Khalil, "Effect of channel restrictions on the axial heat transport in subcooled superfluid helium," *Cryogenics*, vol. 23, pp. 67–71, 1983.
- [97] S. W. a. Van Sciver, "Developments in He II heat transfer and applications to superconducting magnets," *Advances in Cryogenic Engineering*, vol. 27, pp. 375–398, 1981.
- [98] B. Helvensteijin, B. S. R., and S. W. Van Sciver, "Heat transfer in He II in microbore tubing," *Advances in Cryogenic Engineering*, vol. 27, pp. 485–492, 1982.
- [99] B. Helvensteijin *et al.*, "Heat flow in He II in microbore channels," *Advances in Cryogenic Engineering*, vol. 29, pp. 343–350, 1984.
- [100] B. Helvensteijin and S. W. Van Sciver, "Metastable heat flow phenomena and dropping pressure differences in he ii using multiple channel configurations," *Advances in Cryogenic Engineering*, vol. 33, pp. 399–406, 1988.
- [101] EPFL Center of MicroNanoTechnology in Lausanne, Switzerland. [Online]. Available: <http://cmi.epfl.ch>
- [102] Pyrex®, Corning, NY, USA. [Online]. Available: www.corning.com
- [103] S. Franssila, *Introduction to micro fabrication*. John Wiley & Sons, Inc., New York, 2004.

- [104] M. Elwenspoek and H. Jansen, *Silicon micromachining*. Cambridge University Press, 1998.
- [105] M. Madou, *Fundamentals of microfabrication*. CRC Press, Boca Raton, USA, 1997.
- [106] H. Wensink, “Fabrication of microstructures by powder blasting,” Ph.D. dissertation, University of Twente, Enschede, The Netherlands, 2002.
- [107] A. Mapelli, P. Petagna, and P. P. Granieri, “Manufacturing of pyrex micro-channels for cryogenic applications,” *J. of Micromech. Microeng.*, to be submitted for publication.
- [108] P. P. P. M. Lerou, “Micromachined Joule-Thomson cryocooler,” Ph.D. dissertation, University of Twente, Enschede, The Netherlands, 2007.
- [109] J. Burger, “Cryogenic microcooling. A micromachined cold stage operating with a sorption compressor in a vapor compression cycle,” Ph.D. dissertation, University of Twente, Enschede, The Netherlands, 2001.
- [110] B. Baudouy and J. Polinski, “Thermal conductivity and kapitza resistance of epoxy resin fiberglass tape at superfluid helium temperature,” *Cryogenics*, vol. 49, pp. 138–143, 2009.
- [111] R. A. Fisher, G. E. Brodale, E. W. Hornung, and W. F. Giaque, “Thermal conductivity and heat capacity of 7740 Pyrex below 4 °K and in magnetic fields to 90 kG,” *The Review of Scientific Instruments*, vol. 39, pp. 108–114, 1968.
- [112] F. Lentijo, “Etude des transferts de chaleur en hélium superfluide dans des micro-canaux,” Master’s thesis, ENSTA ParisTech and CEA–Saclay, 2011.
- [113] C. E. Chase, “Thermal conduction in liquid helium II. I. Temperature dependence,” *Physical Review*, vol. 127, pp. 361–370, 1962.
- [114] W. E. Keller and E. F. Hammel, “Isothermal flow of liquid He II through narrow channels,” *Physics*, vol. 2, no. 5, p. 221, 1966.
- [115] D. J. Griffiths, *Phil. Mag.*, vol. 17, p. 1109, 1968.
- [116] B. K. Jones, “High speed vortices in helium,” *Physical Review*, vol. 177, p. 292, 1969.
- [117] M. Sapinski, “Quench limits,” *Proceedings of the Chamonix 2012 Workshop on LHC*, 2012.
- [118] List of LHC beam induced quenches. [Online]. Available: <http://cern.ch/biq>
- [119] J. B. Jeanneret, D. Leroy, L. Oberli, and T. Trenkler, “Quench levels and transient beam losses in LHC magnets,” LHC Project Report 44, CERN, Geneva, Switzerland, 1996.
- [120] A. Verweij, “Quenches: will there be any ?” *Proceedings of the Chamonix 2012 Workshop on LHC*, 2012.
- [121] P. P. Granieri *et al.*, “Stability analysis of the LHC cables for transient heat depositions,” *IEEE Trans. Appl. Supercond.*, vol. 18, no. 2, pp. 1257–1262, 2008.
- [122] B. Dehning *et al.*, “Design of the beam loss monitoring system for the LHC ring,” LHC Project report 781, CERN, Geneva, Switzerland, 2004.
- [123] A. Fassò *et al.*, “The FLUKA code: Present application and future development,” CHEP03, La Jolla, CA, USA, March 24–28, 2003.

-
- [124] A. Fassò, A. Ferrari, J. Ranft, and P. Sala, “FLUKA: a multi-particle transport code,” CERN-2005-10, INFN/TC-05/11, SLAC-R-773.
- [125] G. Battistoni, S. Muraro, P. R. Sala, F. Cerutti, A. Ferrari, S. Roesler, A. Fassò, and J. Ranft, “The FLUKA code: description and benchmarking,” proceedings of the Hadronic Shower Simulation Workshop 2006, Fermilab 6th –8th September 2006, M. Albrow, R. Raja eds., AIP Conference Proceeding 896, 31-49, 2007.
- [126] F. Cerutti, B. Dehning, A. Ferrari, H. C., M. Mauri, A. Mereghetti, M. Sapinski, and E. Wildner, “Estimation of threshold for the signals of the blms around the lhc final focus triplet magnets estimation of threshold for the signals of the BLMs around the LHC final focus triplet magnets,” ATS-Note-2012-014, CERN, Geneva, Switzerland, 2012.
- [127] V. Boccone for the FLUKA team, “Energy deposition with and without IR3 upgrade,” Collimation Review, 14th June 2011.
- [128] D. Wollman, “Collimation setup and performance,” Collimation Review, 14th June 2011.
- [129] A. Rossi, “Proton beam performance with and without IR3 upgrade,” Collimation Review, 14th June 2011.
- [130] F. Cerutti, private communication.
- [131] L. S. Esposito and F. Cerutti, unpublished calculation.
- [132] N. Mokhov, I. Rakhno, J. Kerby, and S. J.B., “Protecting LHC IP1/IP5 components against radiation resulting from colliding beam interactions,” LHC Project Report 633, CERN, Geneva, Switzerland, 2003.
- [133] F. Cerutti and A. Mereghetti, “Results of the sLHC-IRP1 energy deposition studies - optics sLHCv2.0,” SLHC-IRP1, TDG Meeting, CERN, 10th December 2009.
- [134] P. Ferracin, “Superconducting accelerator magnets. Unit 14: Construction methods and support structures. Episode II,” US Particle Accelerator School (USPAS), 2007.
- [135] L. Bottura, “A practical fit for the critical surface of NbTi,” *IEEE Trans. Appl. Supercond.*, vol. 10, no. 1, pp. 1054–1057, 2000.
- [136] S. Russenschuck, “ROXIE - a computer code for the integrated design of accelerator magnets,” in *Proc. European Particle Accelerator Conference, Stockholm, Sweden*, 1998.
- [137] Hilumi project - workpackage 3: magnets. [Online]. Available: <https://espace.cern.ch/HiLumi/wp3/SitePages/Home.aspx>
- [138] P. P. Granieri, C. Lorin, and E. Todesco, “Slip–Stick mechanism in training the superconducting magnets in the Large Hadron Collider,” *IEEE Trans. Appl. Supercond.*, vol. 21, no. 5, pp. 3555–3560, 2011.
- [139] P. P. Granieri, M. Casali, and D. Richter, “Heat transfer in the LHC main superconducting bus bars,” in *Proceedings of ICEC 23 – ICMC 2010*. Wroclaw, Poland, 2010, pp. 411–416.
- [140] P. P. Granieri, M. Casali, D. Richter, L. Bottura, M. Breschi, and A. Verweij, “Preliminary analysis of the heat extraction from the LHC main superconducting bus bars,” CERN TE, EDMS 1090724, Tech. Rep., 2010.

- [141] P. P. Granieri, M. Breschi, M. Casali, L. Bottura, and A. Siemko, “Stability analysis of the interconnection of the LHC main superconducting bus bars’,” *Cryogenics*, submitted for publication.
- [142] P. P. Granieri, M. Casali, M. Bianchi, M. Breschi, L. Bottura, and G. P. Willering, “Analysis of defective interconnections of the 13 kA LHC superconducting bus bars,” *IEEE Trans. Appl. Supercond.*, accepted for publication.
- [143] P. P. Granieri, L. Bottura, M. Casali, and M. Breschi, “Protection estimates for the 13 kA bus bars interconnections at 3.5 - 4.5 TeV,” CERN TE, EDMS 1185034, Tech. Rep., 2012.
- [144] P. P. Granieri, “Zero-dimensional stability analysis of the LHC cables,” *Cryogenics*, to be submitted for publication.
- [145] F. Alessandria, S. Angius, G. Bellomo, P. Fabbriatore, S. Farinon, U. Gambardella, R. Marabotto, R. Musenich, R. Repetto, M. Sorbi, and G. Volpini, “Technical design report of a superconducting model dipole for FAIR SIS300,” INFN/TC-09/4, Tech. Rep., 2009.
- [146] P. P. Granieri, “Stability analysis of the iter poloidal field insert conductor,” CERN-ITER, EDMS 936182, Tech. Rep., 2008.
- [147] T. Salmi, “Quench analysis for the PS2 fast cycled magnet,” CERN TE, EDMS 1029854, Tech. Rep., 2009.

Pier Paolo GRANIERI

Date of Birth: January 3rd, 1982
Civil Status: Married, no children
Citizenship: Italian

Address: route de Rougemont 24, 1286 Soral, Switzerland
Mobile: +41 (0) 76 220 40 21 / +39 328 30 37 192
E-mail : pgranier@cern.ch ; granieri_pierpaolo@yahoo.fr

RESEARCH AND WORK EXPERIENCE

May 11 – Present *Cryogenics group (TE-CRG), CERN, Switzerland*

Senior fellow

- Experimental tests of thermal model coils for the Large Hadron Collider (LHC) and the High Luminosity LHC (HL-LHC) superconducting (SC) magnets
- Calculation of magnets quench limit for LHC and HL-LHC upgrade
- Supervision of 3 MS students thesis: Thermal modeling of Nb-Ti and Nb₃Sn SC coils

Apr 08 – Apr 11 *Magnets superconductors and cryostats group (TE-MSG), CERN, Switzerland*

Ph.D. student

- Conception and experimental validation of a heat transfer model between superconducting cables and He II, in the frame of the LHC accelerator
- Development (thermal, electrical and mechanical tests) of a thermally enhanced cable insulation for the HL-LHC upgrade, in the frame of the FP7 European program
- Experimental and theoretical investigation of He II heat transport through micro-channels
- Thermo-electrical analysis of the LHC SC bus bars interconnections
- Stability analysis of the Poloidal Field (PF) insert coil for the nuclear fusion reactor ITER
- Scientific collaborations with: CEA Saclay, France; University of Bologna, Italy; INFN Genoa, Italy; Wroclaw University of Technology, Poland
- Supervision/mentoring of 4 MS students thesis: Stability of the LHC bus bars, Analysis of the LHC defective splices tests, Quench analysis for the PS2 Fast Cycled Magnet (FCM)

Dec 06 – Jan 08 *Magnets tests and measurements group (AT-MTM), CERN, Switzerland*

Technical student

- Stability analysis of the LHC magnets with respect to transient beam loss
- Theoretical development of a transient heat transfer model between SC strands and helium

Oct 04 – Nov 05 *Electrical engineering department, University of Bologna, Italy*

Internship

- Design of a Rutherford resistive core SC cable for high field accelerator magnets
- Quench propagation studies in the above mentioned cable
- Stability analysis of force-flow cooled SC cables for superferic accelerator magnets

July – Sept 04 *Magnets tests and measurements group (AT-MTM), CERN, Switzerland*

Internship

- Numerical calculation of stability margins of an innovative design of Cable-in-Conduit Conductor for the SIS-100 ring, Intern. Accelerator Facility, GSI-Darmstadt, Germany

EDUCATION

May 12

Particle accelerator physics laboratory (LPAL), EPFL, Switzerland

Doctoral program

- *Thesis:* Heat transfer between the superconducting cables of the LHC accelerator magnets and the superfluid helium bath
- *Courses:* SC accelerator magnets, *US Particle Accelerator School, Lansing MI, US*
Low-beta linear accelerator, *US Particle Accelerator School, Lansing MI, US*
Cryogenics, *Société Française du Vide, Paris, France*
Introduction to particle accelerators, *EPFL Doctoral School, Switzerland*
Fundamentals of microscale Heat Transfer, *EPFL Doctoral School, Switzerland*
Cryogenic engineering, *US Particle Accelerator School, Boston MA, US*

May 08

Mechanical engineering, University of Bologna, Italy

Master of Science

- *Thesis:* Stability analysis and quench propagation in SC magnets for particle accelerators
- *Major:* Power plants and energetic Systems
- *Erasmus Program:* Sept 03 - June 04, *EPF Ecole d'ingénieurs Sceaux (Paris), France*

SKILLS

Languages: *Italian:* Native *English:* Fluent (working language)
 French: Fluent (working language) *Spanish:* Good

Computer skills: *Operating Systems:* Windows, UNIX
 MS Office, LaTeX
 Programming: C, Fortran, MATLAB
 CAD: Pro-Engineer
 Project management: MS Project
 Modelling with multi-physics finite elements codes

PUBLICATIONS, CONFERENCES, AWARDS AND QUALIFICATIONS

- ✓ 11 publications in international refereed journals (*Cryogenics, IEEE Transactions on Applied Superconductivity*)
- ✓ Conferences/workshops: 2005 (MT-19, Italy), 2007 (MT-20, USA; THERMOMAG, France), 2008 (ITER PF Insert Coil; CHATS-AS, Japan), 2009 (MT-21, China), 2010 (ICEC-ICMC, Poland), 2011 (MT-22, France; CHATS-AS, Switzerland)
- ✓ Several seminars / talks at CERN, Geneva, Switzerland
- ✓ Awards: Prize for MS Thesis, offered by Edison SpA in memory of Eng. L. Priori (1st classified)
 Prize for MS Thesis, offered by Accenture SpA and University of Bologna (1st classified)
- ✓ Technical editor for the international journal *IEEE Transactions on Applied Superconductivity*
- ✓ Referee for the international journals *Cryogenics, IEEE Transactions on Applied Superconductivity, Advances in Cryogenic Engineering*
- ✓ Italian qualification to the engineer profession since December 2009

INTERESTS

Tennis player and instructor, teaching physics and mathematics, volunteer work with ISF (Ingénieurs Sans Frontières).